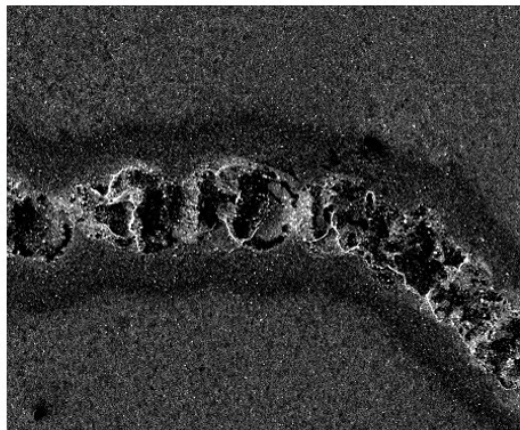
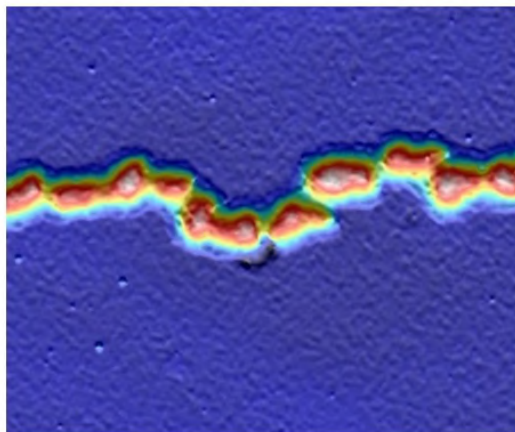
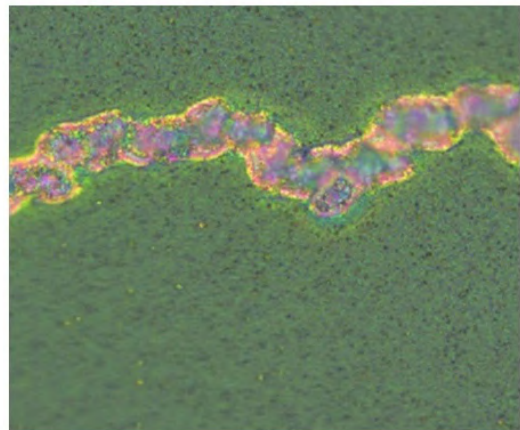
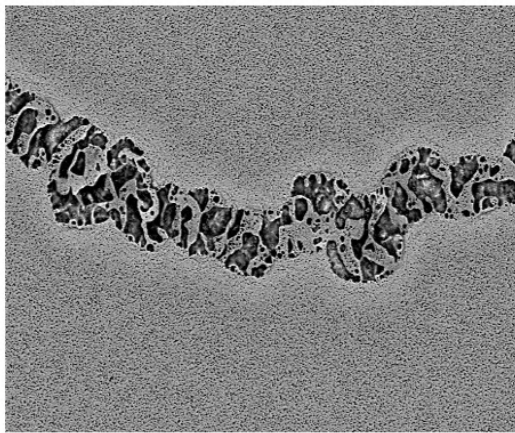


Reverse Bias Induced Worm-like Defects in Cu(In,Ga)Se_2 Thin-Film Solar Cells

MSc Thesis - Material Science & Engineering

Cornelis Peter Aantjes

Delft University of Technology



Reverse Bias Induced Worm-like Defects in *Cu(In,Ga)Se₂* Thin-Film Solar Cells

by

Cornelis Peter Aantjes

to obtain the degree of Master of Science in Material Science & Engineering
at the Delft University of Technology,
to be defended publicly on Tuesday September 17, 2019 at 14:00.

Student number:	4228928	
Project duration:	February 1, 2019 – September 17, 2019	
Thesis committee:	dr. A. J. Böttger,	TU Delft, supervisor
	K. Bakker,	TNO-Solliance, supervisor
	Prof. dr. A.W. Weeber,	TU Delft
	Dr. ir. W.G. Sloof,	TU Delft

This thesis is confidential and cannot be made public until 17 September, 2021.

An electronic version of this thesis is available at <http://repository.tudelft.nl/>.

Abstract

Environmental factors in the field cause partial shading of $Cu(In, Ga)Se_2$ (CIGS) thin-film photovoltaic modules. Partial shading forces shaded cells into reverse bias leading to irreversible efficiency loss. The origin of the irreversible efficiency loss is the formation of defects in the shaded cell. The defects are going by the name of 'worm-like defects'. Understanding the mechanisms involved during the formation of worm-like defects can result in preventive measures to mitigate negative effects of partial shading.

The formation of worm-like defects involves a moving hot-spot across the cell. The exact mechanisms involved in the movement of a hot-spot is unknown. The problem in studying the mechanisms present in these hot-spots is an unknown current density and temperature. After rapid formation of worm-like defects severe changes in the solar cell are observed.

This work expands the knowledge on changes in geometry, composition and crystal structure after worm-like defect formation. X-ray diffraction results shows crystal structure of CIGS below worm-like defects has not changed. Energy dispersive X-ray results show Cu rich areas near the back contact and areas with high Ga and O content near the transparent conductive oxide. A band outside the worm-like defects is observed where Se is exchanged with S while Cu, In or Ga is exchanged with Cd.

Furthermore, a new experimental method is presented that allows control over locally applied conditions. The new method shows applied conditions can be controlled inducing features while resistive heating is suppressed. This enables future research on involved mechanisms.

Based on experimental results multiple possible mechanisms are proposed. In the authors view a plausible and major mechanism is electromigration of Cu towards the back contact. This migration is enhanced by the electromagnetic field and elevated temperature. Cu migration initiates a phase transformation of CIGS into a Cu rich and Cu poor phase. Subsequent to this phase transformation is a reaction of Ga and O. Further testing with this method is needed to investigate in which order mechanisms occur during worm-like defect formation.

Acknowledgements

This thesis project marks the end of time as a student. For this milestone I would like to thank the people who contributed to the final leap.

First of all I would like to thank Klaas Bakker and Mirjam Theelen for providing the opportunity to write my master thesis at Solliance. I had a great time finding out what being a researcher in the photovoltaic industry is like. Thank you Klaas, for being my daily supervisor. Although the weekly meetings were sometimes more of an open discussion hours with no strict agenda resulting in more questions than answers, they were always interesting and very useful. In the end I am sure most of the open questions are answered. Thank you for all the helping me improve my scientific skills. Without your experience, knowledge and help I would not have been able to make such progress with this thesis. I wish you the best of luck while continuing your research and am convinced you will earn the postgraduate doctoral degree.

A special thanks to Amarante Böttger, my TU Delft supervisor. Thank you for your interest in the topic and trust in my capabilities. Thank you for helping me to zoom out and oversee the total picture of my thesis. I often forgot about the complete picture due to all the interesting details from experiments. This really helped me out while writing the final parts of this work.

I would like to thank all the employees I worked with at Solliance for helping me out with instructions, interpreting data and measurements.

A special thanks goes out to all my family. So thank you, mom, dad, Eline, Marjan & Petra. I sometimes might have been unreachable in the past years but thank you for supporting me. Without your unconditional support I would not be where I am standing now.

Ana, although I sometimes might not have been able to talk with you about specific details, you were always there to help me out while writing my thesis. I cannot thank you enough for unconditional support and understanding. I am sorry if I was too stubborn while being wrong.

*Cornelis Peter Aantjes
Delft, September 2019*

Contents

1	Introduction	1
1.1	Motivation for research on degradation of CIGS thin-film solar cells	1
1.2	Objective	2
1.3	Outline of thesis.	3
2	Background	5
2.1	Basic CIGS thin-film technology, operation and material properties	5
2.1.1	Working principle of a CIGS solar cell	5
2.1.2	Soda-lime glass substrate	5
2.1.3	Molybdenum back contact.	6
2.1.4	CIGS absorber layer	7
2.1.5	CdS buffer-layer	8
2.1.6	Aluminium doped ZnO window layer	9
2.2	Semiconductor physics, doping, diode properties and electronics	9
2.2.1	Semiconductor physics	9
2.2.2	Doping.	10
2.2.3	The pn-junction	11
2.2.4	Biasing.	12
2.2.5	Loss mechanisms	14
2.3	Defects and element migration in CIGS.	15
2.3.1	Defects in CIGS	16
2.3.2	Diffusion.	18
2.3.3	Electromigration.	19
2.3.4	Thermal and stress migration	20
2.3.5	Chemical reactions	20
3	Worm-like defects	23
3.1	Literature study	23
3.2	Relevant research at Solliance.	25
3.2.1	'Nantes' samples.	25
3.2.2	EDS by Eurofins	26
3.2.3	Raman	28
3.2.4	(Spectral) Photoluminescence	29
3.2.5	Confocal Microscopy	30
3.3	Summary	31
4	Methodology	33
4.1	Production method	34
4.1.1	Nantes samples	34
4.1.2	Sample with and without AZO	34
4.2	Scanning ElectronMicroscopy(SEM) with Energy Dispersive X-ray Spectroscopy (EDS).	34
4.2.1	Measured elements	34
4.2.2	Penetration of electrons	34
4.2.3	Settings	35
4.3	Point probe experiment.	35
4.4	Raman Spectroscopy and (Spectral) Photoluminescence	38
4.5	Etching	38
4.6	Confocal microscopy	38
4.7	X-ray Diffraction (XRD)	38
4.8	IV-measurement & worm-like defect formation.	38

5	Post-mortem study on worm-like defects	39
5.1	XRD	39
5.2	SEM analysis	40
5.2.1	EDS colour maps.	40
5.2.2	EDS point analysis	42
5.2.3	Discussion on DS results.	44
5.3	Summary	45
6	Point probe experiment	47
6.1	Experimental setup	47
6.1.1	RB diode characteristics	47
6.1.2	Measurement scheme	48
6.2	General observation: applied conditions, SEM, OM and CM	49
6.2.1	Features > 15 μm (nuggets)	49
6.2.2	Features < 15 μm (Seeds).	51
6.2.3	Stain-like features	53
6.3	Raman	54
6.4	EDS	57
6.5	Samples with AZO.	58
6.6	Discussion of results	59
6.7	Summary	60
7	Discussion & Conclusions	63
7.1	Discussion	63
7.2	Conclusions.	67
8	Future work and recommendations	69
	Bibliography	71
A	Eurofins SEM-EDS linescans and colour maps	79
B	Raman peak positions overview	89
C	Monte-Carlo simulation with 'Casino v2'	93
D	Nantes samples EDS and mapping	97
D.1	Nantes EDS	98
D.2	Nantes mapping	112
E	Point probe without AZO experimental results	119
E.1	Feature categories.	120
E.2	Confocal microscopy	124
E.3	Raman spectroscopy	129
E.4	EDS	134

Nomenclature

μ_h or μ_e	Hole or electron mobility
G	Gibbs free energy
N_e	Free-electron density
N_h	Hole density
AZO	Aluminium doped Zinc Oxide
BEC	Backscattered Electron Composition
CB	Conduction band
CC	Constant Current experiment
CGS	$CuGaSe_2$
CIGS	$Cu(In,Ga)Se_2$
CIS	$CuInSe_2$
CM	Confocal Microscope
CV	Constant Voltage experiment
DOS	<i>Density – of – States</i>
EBIC	Electron Beam Induced Current
EDS	Energy Dispersive X-ray Spectroscopy
EDX	Energy Dispersive X-ray Spectroscopy
FB	Forward Bias
i-Zno	Intrinsic Zinc Oxide
ODC	Ordered Cefect Compound or Chalcopyrite
OM	Optical microscope
OVC	Ordered Vacancy Compound
RB	Reverse Bias
SCR	Space Charge Region
SEI	Secondary Electron Images
SEM	Scanning Electron microscope
SLG	Soda-Lime Glass
SPL	Spectral Photo-Luminescence
SRH	Shockley-Read-Hall
TCO	Transparent Conductive Oxide
VB	Valence Band
XRD	X-ray Diffraction

Introduction

1.1. Motivation for research on degradation of CIGS thin-film solar cells

Humanity has 12 years to act or we will face catastrophic effects of climate change. This is a clear message from the Intergovernmental Panel on Climate Change (IPCC) released in October 2018 [1]. Human activities are estimated to have caused approximately 1.0°C of global warming above pre-industrial levels. This increase is likely to reach 1.5°C between 2030 and 2052. As a result of global warming the sea level will continue to rise well beyond 2100. The magnitude and rate of this rise depends on future emission pathways. On land, the global warming has an impact on biodiversity and ecosystems, including species loss and extinction. Limiting global warming to 2°C is projected to lower the impact on sea level, ocean temperature, ecosystems (on land and in oceans), livelihood of humans, food security, water supply and economic growth [1]. To limit the global warming and its impact 195 countries have pledged to limit the amount of greenhouse gases in the Paris agreement [2]. Current energy production with fossil fuels need to reduce and is to be replaced with sustainable energy to reach the goals of the Paris agreement. A key aspect in this transition is reducing the cost of renewable energy production. The sun is a major source of inexhaustible free energy. In theory, solar energy possesses the potential to provide energy for the entire world. This potential gives rise to the development of photovoltaic technology to convert solar energy into electricity. The conversion of solar energy into electricity has already been proven and widely practised all over the world but has room for improvement [3].

In the photovoltaic industry crystalline silicon technology implemented in modules has a market share over 90% [4]. The second biggest technology on the market is thin-film technology with market share of 4%. Cu(In,Ga)Se_2 (CIGS) is $I-III-IV_2$ semiconductor material suitable for thin-film technology. CIGS modules cover 50% of the thin-film market share. A CIGS lab record efficiency of 23.35% and commercially available module efficiency 17.9% has been achieved with CIGS technology [5, 6]. Thin-film solar cells have an absorber layer thickness in the range of approximately $1.5\text{--}2.5\text{ }\mu\text{m}$ compared to crystalline silicon with thicknesses in the range of $150\text{--}200\text{ }\mu\text{m}$ [4, 7]. Despite the small market share, thin-film technology has the advantage of minimal material use and being able to produce light weight, coloured or flexible modules for special applications. This can not be done with crystalline silicon technology due the required thicker absorber layer [8]. For solar energy the Levelised Cost Of Electricity (LCOE) is a result of three main factors: initial costs, operation costs, maintenance costs and total energy yield over its lifetime. The total energy yield of a project using photovoltaic modules depends on the initial module conversion efficiency and the efficiency development over time. Improving long-term performance and stability of thin-film solar cells thus increases total yield during its lifetime and reduce the LCOE. Research on cell efficiency, cell and module configuration combined with production techniques and degradation mechanisms of solar cells can optimise yield and finally minimise cost of solar energy.

At Solliance, part of TNO, research is done on production, quality, stability and degradation of thin-film solar cells and modules. Insight in mechanisms causing degradation can be used to produce thin-film solar cells and modules with long term stability and performance. A combination of partial shading, cell and module configuration result in a potential applied over one or more cells. This potential is called the reverse bias

potential. The current as a result of this potential is able to induce defects as shown in Figure 1.1 on the CdS/CIGS interface. The defected sites are sometimes visible without magnification and appear as if a worm travelled through the material. These defects are referred to as 'worm-like defects'. Worm-like defects have a negative effect on individual cell efficiency. The damage in one cell is not limited as the bad performance also negatively affects the string of cells in the module. Meaning one damaged cell decreases module efficiency significantly [9–11]. In depth details on worm-like defects will be provided in Chapter 3.

Worm-like defect formation and propagation is a complex process as all mechanisms take place in seconds. In addition, the local conditions are unknown and the formation is influenced by 5 different layers (in the stacking) having a total thickness under $3.5\ \mu\text{m}$. A chain reaction of unknown mechanisms is present during formation. Local parameters such as temperature, current density, applied potential, local composition and defect densities are all involved in the process. The individual effects and contribution of these parameters on worm-like defect formation and propagation is yet unknown. This study tries to attribute specific parameters to specific mechanisms. More specifically: what conditions activate specific mechanisms. An extensive study on these worm-like defects contributes to understanding of the formation and propagation mechanisms. This knowledge can be used to mitigate the negative effects or to prevent worm-like defects from forming and improve the CIGS thin-film technology performance. This eventually leads to a lower LCOE.

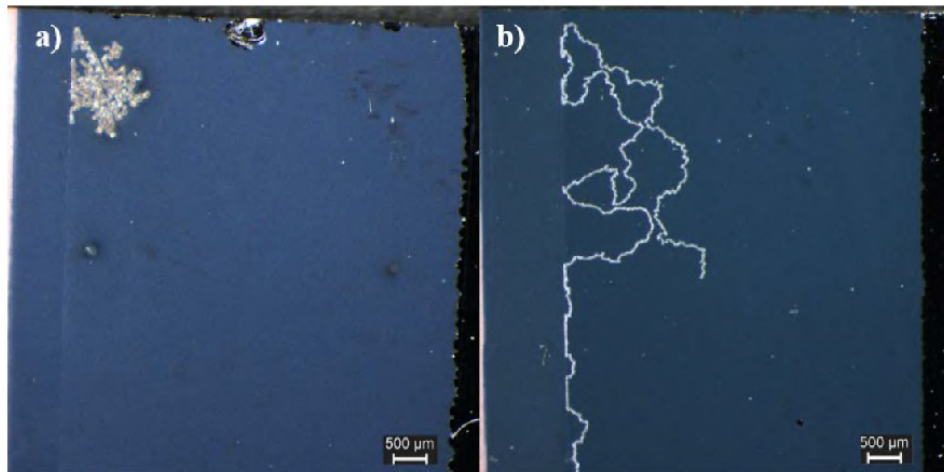


Figure 1.1: Optical microscope images of worm-like defects in a) sample 1602_2J showing local worm-like defect behaviour and in b) sample 1605_3B showing mobile worm-like defect behaviour [12].

1.2. Objective

The objective of this research is gaining knowledge about mechanisms involved in worm-like defect formation and propagation. It is essential to have proper knowledge on the mechanisms involved before it is possible to take measures preventing or reducing damage induced by worm-like defects. Looking at methods to prevent or reduce the effects of worm-like defect is not possible with the current knowledge. The main research question of this thesis is as follows:

What are possible mechanisms involved in reverse bias induced worm-like defects in CIGS solar cells?

It is not fully documented what changes occur in the cell during worm-like defect formation. The worm-like defects must be studied as knowing exactly what has formed is essential before possible mechanisms can be proposed. To get a well established view on the changes in the cell the first sub-question is: f

1. What are the changes in composition, geometry and structure observed at reverse bias induced defects in CIGS solar cells?

The following problem arises in studying worm-like defect formation and propagation. Different mechanisms like diffusion, electromigration, chemical reactions and phase changes might be involved. These individual mechanisms are influenced by the electromagnetic field, current and/or temperature. Worm-like

defect formation appears to be a chain reaction of multiple different mechanisms in a few seconds where an individual mechanism can not be discriminated. Additionally the local parameters are unknown due to lateral conduction of the front and back contact of the cell. An experiment is set up to gain control over the local parameters. With this new setup the second sub-question arises:

2. Is it possible to mimic partial mechanisms involved in worm-like defect formation by controlling applied parameters locally?

A new experiment is developed to apply local conditions. With the experiment different features are observed for different conditions. The features and their conditions are documented. The next step of this research is comparing locally induced features to worm-like defects with the third sub-question:

3. What are the differences and similarities between worm-like defects observed in CIGS solar cells and locally induced features on a sample with no aluminium doped zinc oxide?

The three sub-questions together aim at answering the main research question. The next section presents the outline of this thesis and briefly explains what is described in each chapter.

The scope of this work is limited to solar cells with the following stacking: soda lime glass substrate, Mo back contact, CIGS absorber layer, CdS buffer layer and a aluminium doped zinc oxide window layer. This work does not focus on any intrinsic or extrinsic means (e.g. bypass diodes) to prevent worm-like defect formation. The current knowledge on the topic is not sufficient enough to start thinking about preventive measures. Therefore, this work focuses on only on possible mechanisms involved in worm-like defect formation. However, results presented in this work is relevant and contributes to preventive measures in the future.

1.3. Outline of thesis

Chapter 2 provides the reader with background information about CIGS thin-film technology, topology, semiconductor physics and possible element migration relevant for this thesis.

Chapter 3 contains the information available from literature and relevant research at Solliance about worm-like defects.

Chapter 4 contains the methodology used in this thesis. The how and why of the new experiment is documented in this chapter. This includes findings and experiences during the development of the experiment. All experimental setups used for analysis and corresponding settings are documented.

Chapter 5 is a continuation of Chapter 3. It presents results of Energy Dispersive X-ray Spectroscopy (EDS or EDX) to identify the migration of all elements in the cell. X-ray diffraction (XRD) results are presented to gain information on crystallographic properties and composition. The results are used to answer sub-question 1.

Chapter 6 presents the results of the experiment described in Chapter 4. The locally induced features are divided into categories. Results of analysis with Raman, Scanning Electron Microscope (SEM) and Energy dispersive X-ray Spectroscopy (EDS or EDX) is presented. The applied conditions with observed locally induced features are compared with worm-like defects. The results presented in this chapter are focussed on sub-question 2 and 3.

Chapter 7 covers a discussion on all the research questions. The discussion combines findings from literature with results presented in this work. Conclusions are drawn addressing the research questions.

Chapter 8 presents the future work & recommendations. The experiment developed shows potential for further research. Recommendations regarding the next steps in this experiment are given. This recommendations can directly be used to gain more insight in worm-like defect formation and propagation.

2

Background

This chapter provides the reader with all the relevant background information required to understand the research presented in this work. It starts with the working principles of a solar cell and details on the materials and layers relevant for this work. To understand the conditions where worm-like defects are formed basic knowledge on semiconductor physics, biasing, pn-junctions and breakdown mechanisms is required. It also provides the reader with information on possible mechanisms involved to understand the discussion and conclusions.

2.1. Basic CIGS thin-film technology, operation and material properties

2.1.1. Working principle of a CIGS solar cell

This section introduces the reader with the basic working principle of a solar cell. In addition the function and material properties of the individual layers are addressed. The working principle of solar cells is based on the photovoltaic effect. The photovoltaic effect is the generation of a potential difference at the junction of two materials in response to electromagnetic radiation [13]. By using this effect properly, solar cells are able to convert sunlight into electricity. The three major steps in the photovoltaic effect and its conversion to usable energy are as follows: [13]

- 1 Electron hole pair generation caused by absorption of photons in the absorber layer. Incident photons of sunlight are absorbed and excite an electron into a higher energy state leaving behind a void with a positive charge called a hole.
- 2 Separation of charge carriers in CIGS by the Space Charge Region (SCR). The SCR acts like a membrane separating the electron-hole pair.
- 3 Collection of the charge carriers by an external circuit where work is extracted.

Figure 2.1 schematically shows the general working principle of a photovoltaic cells. In addition to the previous mentioned mechanisms it involves recombination of the electron-hole pairs. More detailed information on this process is found in Subsection 2.2.5. A common topology used in CIGS thin-film technology is shown in Figure 2.2 where the absorber material is $Cu(In,Ga)Se_2$ (p-type). This is also the topology used in this work. The specific function and essential properties of individual layers are presented in the next paragraphs. An overview of important quantified parameters of CdS and CIGS can be found in Table 2.1. The next sections will provide basic information on the layers presented in Figure 2.2.

2.1.2. Soda-lime glass substrate

Soda-lime glass (SLG) is commonly used substrate for CIGS thin-film technology. The reason for its use are favourable thermal expansion coefficients, material availability and the presence of 15-20% sodium oxide (NaO). When deposition techniques are implemented right, Na diffuses through the Mo into the CIGS absorber layer enhancing electronic properties. Na is known to enhance p-type doping in CIGS by inhibiting donor defects in the bulk and grain boundaries [16]. Typically, glass thicknesses between 1 and 3 mm are used.

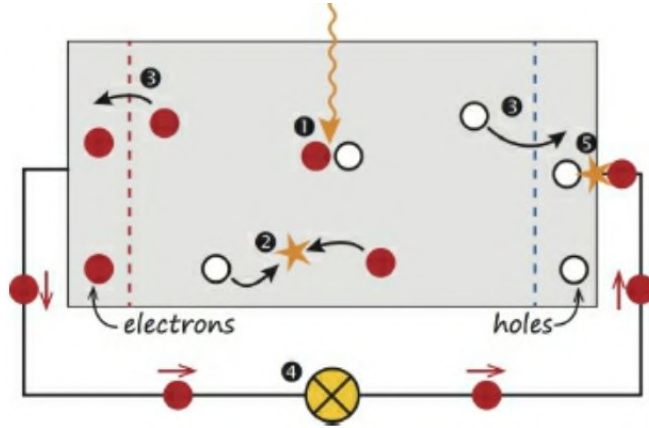


Figure 2.1: A very simple solar cell model. (1) Absorption of a photon leads to the generation of an electron-hole pair. (2) Usually, the electrons and holes recombine. (3) With semipermeable membranes the electrons and holes are separated. (4) the separated electrons are used to drive an electrical circuit. (5) after the electrons have passed through the circuit they recombine with holes [13].

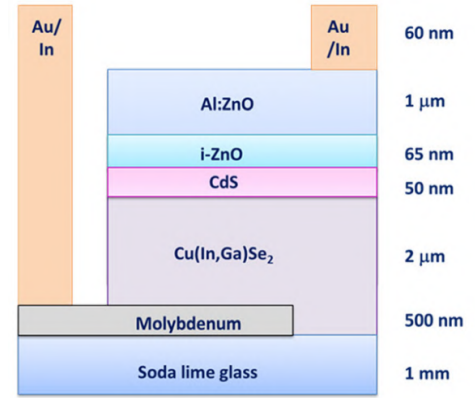


Figure 2.2: Layer stacking of Solliance CIGS test structures (not to scale) deposited on soda lime glass samples [14]. The same stacking of layers is used in this work.

Table 2.1: Overview of device parameters in a CIGS solar cell topology with p-type CIGS, n-type CdS [15].

Parameters	N-CdS	P-CIGS
Thickness (μm)	0.05	3
Dielectric constant	8.28	13.6
Refractive index	3.16	3.67
Band gap (eV)	2.42	1.15
Electron affinity (eV)	4.4	4.5
Electron mobility (cm^2/Vs)	350	100
Hole mobility (cm^2/Vs)	50	25
Conduction band effective density of states (cm^{-3})	1.7×10^{19}	2×10^{18}
Valence band effective density of states (cm^{-3})	2.4×10^{18}	1.6×10^{19}
Donor concentration (cm^{-3})	1×10^{18}	0
Acceptor concentration (cm^{-3})	0	2×10^{16}
Electron lifetime (s)	2×10^{-8}	1×10^{-8}
Hole lifetime (s)	6×10^{-8}	5×10^{-8}
Absorption file	cds.a	cigs.a

The material and electrical properties of each layer have been elicited from some reliable sources of numerical simulations and experimental works (Gloeckler et al. 2003; Chelvanathan et al. 2010; Bouloufa et al. 2007; Schlenker et al. 2007; Balboul et al. 2008; Hossain et al. 2011; Repins et al. 2009; Gloeckler et al. 2005; Jackson et al. 2007)

2.1.3. Molybdenum back contact

The most used back contact material in CIGS thin-film technology is molybdenum. It is used for its low resistivity and high stability at the elevated temperatures present during the growth process of the absorber layer. The thickness of the Mo-layer is in the range of $0.3\text{-}1.0 \mu\text{m}$. Deposition parameters of the Mo-layer are crucial in controlling diffusion process of Na through the barrier layer into the CIGS absorber layer [14]. The use of Mo as back contact has some drawbacks. Mo poorly reflects long wavelengths and is a relatively scarce metal. On the CIGS/Mo interface an intermediate layer of MoSe_2 is formed. This layer is proven to be beneficial serving as quasi-Ohmic contact [17].

2.1.4. CIGS absorber layer

Crystal structure & phase diagram

CIGS can also be described as $I-III-VI_2$ semiconductor material. The absorber used in CIGS thin-film technology is a $Cu(In_{1-x},Ga_x)Se_2$ layer. This layer is p-doped by being Cu deficient. Doping is a subject which is addressed in detail in Subsection 2.2.2. For CIGS cells at Solliance x (in stated chemical composition) is approximately 0.3. The crystal structure of the layer is chalcopyrite(α). The unit cell of chalcopyrite CIS is shown in Figure 2.3(a). In the case of CIGS the In atoms in the unit cell are replaced with Ga atoms. For CGS all the In atoms in the unit are replaced with Ga atoms. Chalcopyrite is in the $I4_2d$ space group exhibiting tetragonal bonding.

As CIGS is a quaternary compound the phase diagram is very complex. For simplicity the example of CIS is used. Figure 2.4 shows the phase diagram of CIS. In this phase diagram only the chalcopyrite, denoted as α , is present at room temperature for a Cu content between 23 and 25 at.%. Lowering the Cu content gives an additional phase called Ordered Defect Chalcopyrite (ODC) denoted as β . In literature this phase is also called Ordered Vacancy Compound (OVC). The unit cell of the ODC is shown in Figure 2.3(b). It looks different but still is chalcopyrite with a large number of ordered defects. Examples of these defect phases are $Cu(In_{1-x},Ga_x)_3Se_5$ and $Cu(In_{1-x},Ga_x)_5Se_8$. On the Cu rich side of the diagram, phases segregate in chalcopyrite and Cu_2Se . Cu_2Se is p-type semiconductor material with a high hole conductivity [18, 19]. In addition, in CIGS it is also observed Cu_2Se occurs in solid solution at temperatures above 873 K [20]. The addition of Na and Ga is known to broaden the stability of α -chalcopyrite [17, 21]. This means a higher change in Cu content is required to initiate phase changes.

The device performance depends little on the grain size compared to other semiconductors attributed to a charge neutral barrier in the grain boundary [22]. The usual grain size of CIGS therefore ranges from 0.5-2 μm , which is in the same order of magnitude of the absorber layer thickness [17, 23]. Numerical and experimental research on properties of different layers including CIGS is summarised by Asaduzzaman et al. [15] and represented in Table 2.1.

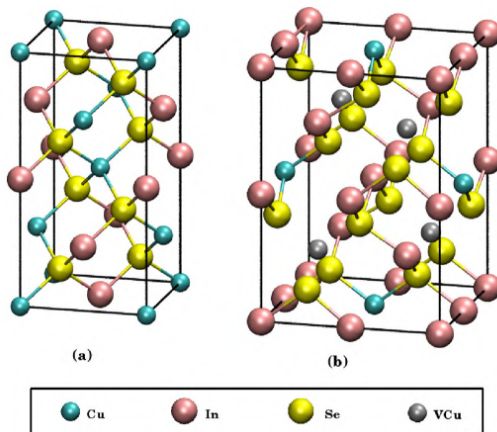


Figure 2.3: Crystal structure showing the conventional tetragonal unit cell of (a) $CuInSe_2$ (α) and (b) chalcopyrite polytype of $CuIn_5Se_8$ (β or ODC) [24].

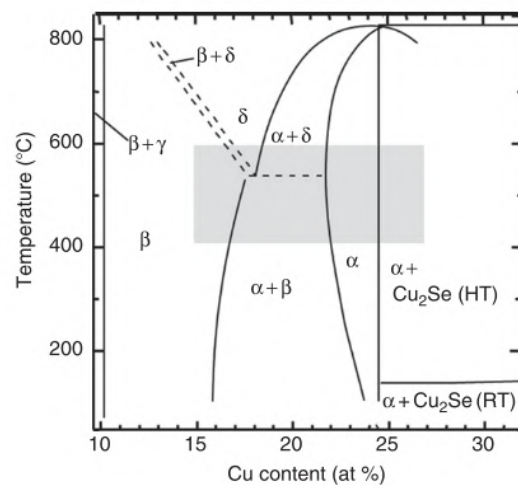


Figure 2.4: Pseudo-binary phase diagram for In_2Se_3 - Cu_2Se tie-line. The shaded area indicates the regions in the phase diagram relevant to multistage co-evaporation of high-efficiency chalcopyrite solar cells [17].

A ternary phase diagram between Cu_2Se , In_2Se_3 and Ga_2Se_3 is shown in Figure 2.5. This pseudo-ternary shows that in the case of CIGS with Ga involved similar observations are present compared to Figure 2.4. When moving from α chalcopyrite to a lower Cu content a region with β chalcopyrite or ODC exists. In the area with a higher concentration of Cu compared to α chalcopyrite shows the existence of Cu_2Se .

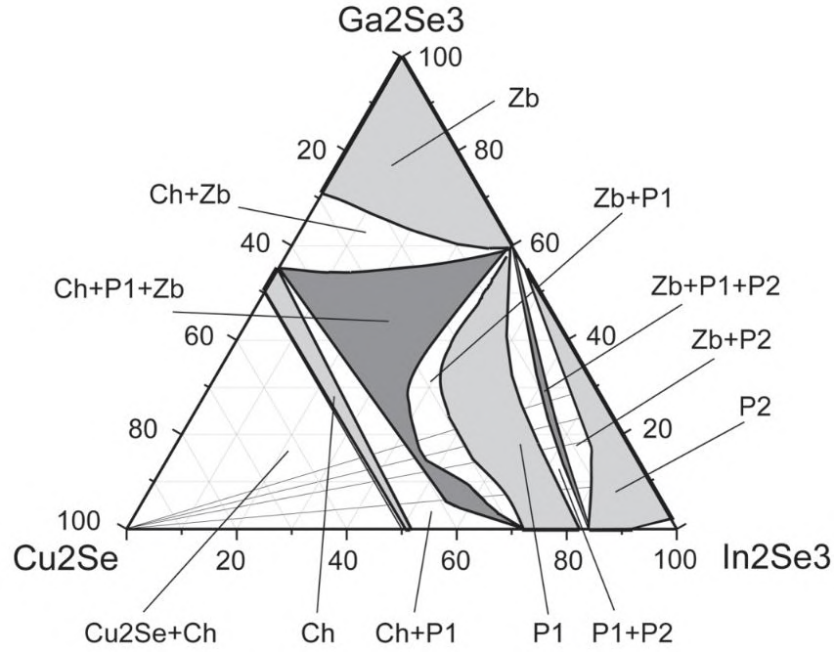


Figure 2.5: Predominance diagram for the $\text{Cu}_2\text{Se}-\text{In}_2\text{Se}_3-\text{Ga}_2\text{Se}_3$ pseudo-ternary phase field at room temperature. Ch denotes the α phase, P1 is the β phase or ODC, P2 is the γ phase (Wurtzite), and Zb is the δ phase (Zincblende) [21].

The bandgap for CIS is approximately 1.0 eV . For CGS the bandgap is approximately 1.7 eV . By replacing the indium atoms of CIS with Ga atoms it is possible to tune the bandgap to desired values [25]. For this reason the ratio between elements In and Ga directly holds information on the bandgap. The following ratios are used in CIGS thin-film technology.

$$GGI = \frac{Ga}{Ga + In} \quad (2.1)$$

$$CGI = \frac{Cu}{Ga + In} \quad (2.2)$$

$$Se/CIG = \frac{Se}{Cu + Ga + In} \quad (2.3)$$

Where all values are in at.%. In the case of stoichiometric CIGS ($\text{Cu}(\text{In}, \text{Ga})\text{Se}_2$) the values for CGI and Se/CIG are equal to 1.

Thermal properties

Neumann [26] studied the properties of CIS poly-crystals and observed the following properties. A thermal expansion coefficient, α_{th} , in the range of $7.0 - 10.7 \times 10^{-6} \text{ K}^{-1}$. A molar heat capacity, C_p , of approximately $98 \text{ J} \cdot \text{mol}^{-1} \text{ K}^{-1}$ at 300 K increasing almost linear to $108 \text{ J} \cdot \text{mol}^{-1} \text{ K}^{-1}$ at 500 K . The thermal conductivity, λ , is $0.1 \text{ W} \cdot \text{cm}^{-1} \cdot \text{K}^{-1}$ at 300 K and $0.035 \text{ W} \cdot \text{cm}^{-1} \cdot \text{K}^{-1}$ at 500 K . The properties of CGS have the same order of magnitude but slightly differ [26, 27].

2.1.5. CdS buffer-layer

The primary role the CdS buffer layer is to form a hetero-junction with the CIGS absorber layer while being as transparent as possible [28]. The CdS layer is a highly doped buffer layer (Carrier density $\sim 1 \times 10^{20} \text{ cm}^{-3}$). The bandgap of CdS is between 2.4 and 2.5 eV [29]. It passivates macroscopic or microscopic defects on the chalcopyrite absorber surface. It may provide proper band alignment between absorber and window layer and it may cause type inversion at the hetero-interface through surface donors at or close to the interface [17]. For plasma enhanced vapour deposition of CdS layer a hexagonal Wurtzite crystal structure was found having a high mismatch with the CIGS absorber layer compared with chemical bath deposition. The grain size of CdS is in the range of $70-80 \text{ nm}$ [30]. To get insight in the order of magnitude of doping, thicknesses, carrier lifetime and other properties for CdS Table 2.1 is inserted.

2.1.6. Aluminium doped ZnO window layer

For current extraction a window layer is needed. This layer needs to be transparent and electronically conductive. An Al:ZnO (AZO) is the most common used Transparent Conductive Oxide (TCO) in CIGS thin-film technology. The band gap of ZnO is 3.3 eV and the Conduction Band (CB) is reasonably aligned with the CIGS absorber and the CdS buffer layer [17]. Between the CIGS and AZO an i-ZnO layer is deposited it acts as a insulating layer because it is not highly doped. It helps prevent shunting through pinholes or other defects in the absorber layer and protects the absorber layer in the high temperature deposition of the AZO [17]. The CIGS solar cell parameters were found to depend significantly on the i-ZnO thickness [31]. Table 2.1 shows properties of n-type ZnO layer.

2.2. Semiconductor physics, doping, diode properties and electronics

2.2.1. Semiconductor physics

Materials in solid state have an electronic band structure. The electrons in material where the electrons are too tightly bound to the atom to carry electric current are in the so called the **Valance Band** (VB). Electrons which are free to move are in the so called the **Conduction Band** (CB). In conducting material available bands in the CB have overlap with the VB. An electron can move from the VB to the CB without requiring additional energy. In the case of semiconducting material there is a relatively narrow energy gap (E_g) between the VB and CB. For isolating materials the E_g between the VB and CB is high [32]. A schematic representation of the CB and VB is shown in Figure 2.6.

At 0 K the CB is completely empty. As temperature increases electrons are thermally excited to the CB leaving behind a hole in the VB. The Fermi energy is the hypothetical energy level of an electron, such that at thermodynamic equilibrium the energy level has a 50% probability of being occupied. In semiconductors the Fermi energy (E_F) lies between the VB and CB. The electron distribution of intrinsic semiconductor material is shown in Figure 2.6 where it is shown the number of electrons in the CB is a function of temperature and the band gap [33]. $Z(E)$ is the density of electron states in the CB. A result of electrons in the CB is the possibility to transport current when a potential is present. For intrinsic CGS and CIS at room temperature the hole- (N_h) and free-electron density (N_e) is in the order of 10^{19} and 10^{17} cm^{-3} , respectively [34].

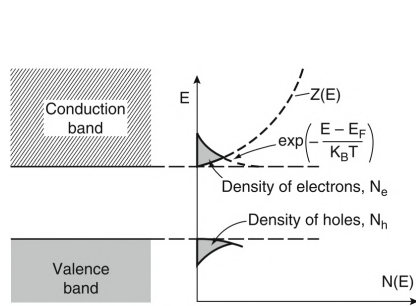


Figure 2.6: Density of free electrons (N_e) and holes (N_h) for an intrinsic semiconductor [33].

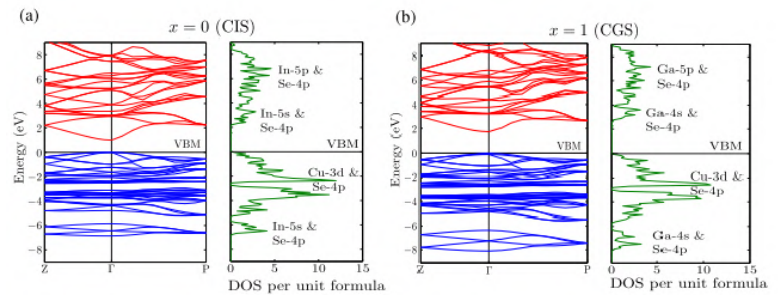


Figure 2.7: Band structure and density of states (DOS) per unit formula containing 4 atoms - of (a) CIS and (b) CGS, obtained using the tuned HSE06 functional. The band structure is plotted along the Z-Γ-P path in reciprocal space. The valence band maxima (VBM) are set to 0 eV. The character of the bands, as obtained from the study of the projected density of states, is added in the vicinity of the DOS [25].

The Density-Of-States (DOS), shown in Figure 2.7, represent the number of quantum states as a function of energy. Figure 2.7 shows the energy bands and DOS of CGS and CIS where clearly the band gap described in this section is visible.

Absorber layer materials in photovoltaic technology are divided in two categories: direct bandgap and indirect bandgap. In direct bandgap material a photon directly creates an electron-hole pair by transferring its energy. For indirect bandgap material the momentum of charge carriers in the VB is different than in the CB. An electron requires momentum to get into the CB. This momentum is provided by phonons from the lattice. The extra required energy decreases the absorption coefficients of indirect bandgap materials. CIGS is classified as a direct bandgap material. This can be seen in Figure 2.7 where the lowest part of the CB has

the same momentum as the highest energy level of the VB. CIGS therefore is direct bandgap material with a higher absorption coefficient making it suitable for thin-film photovoltaic technology. The conductivity, σ , of a semiconductor is given in Equation 2.4.

$$\sigma = N_e e \mu_e + N_h e \mu_h \quad (2.4)$$

Where σ is a function of charge carrier densities of holes (N_h) and electrons (N_e). In Equation 2.4 e is the elementary charge of 1.602×10^{-19} C. μ_h and μ_e denote the carrier mobility ($\text{cm}^2 \cdot \text{V}^{-1} \cdot \text{s}^{-1}$) of electrons or holes, respectively. The carrier mobility represents how easy a charge carrier moves through the material in the presence of an electromagnetic field. As said, with increasing temperature the amount of charge carriers increase and thus the conductivity increases initially. However, the mobility of carriers is reduced by lattice vibration at higher temperatures reducing the conductivity. Schematic curves of the carrier mobility, carrier density and conduction is shown in Figure 2.8. The conductivity increases with increasing temperature showing in conductivity the carrier density dominates over the scattering by lattice vibrations.

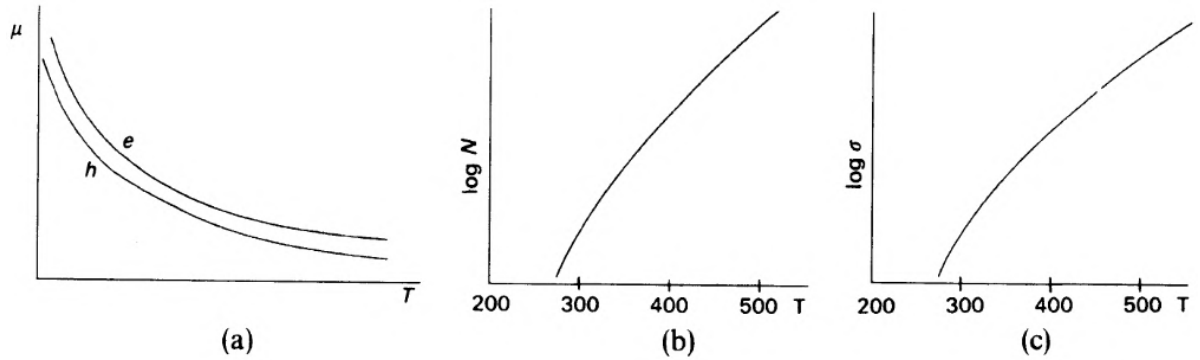


Figure 2.8: Schematic representation of the temperature dependence of (a) electron and hole mobility's (μ), (b) number of carriers in an intrinsic semiconductor (N), and (c) conductivity for an intrinsic semiconductor σ Where T is given in K [33].

The conductivity of semiconductors at desired operating temperatures (<373 K) are artificially modified by using dopants. In this case added elements or non-stoichiometry extrinsically increases the charge carrier density in the material to increase conductivity at a desired temperature. Figure 2.9 schematically shows the effect of extrinsic doping on the conductivity as a function of temperature. It also shows a decrease in mobility due to lattice scattering. Further details of this doping relevant for CIGS is provided in the next section.

2.2.2. Doping

As mentioned in the previous paragraph, the conductivity of semiconductor material is a function of the carrier density. It is possible to produce CIGS Cu deficient (non-stoichiometric). In Cu deficient CIGS the crystal lattice is missing electrons. This material is called a p-type material as the material has an excess of holes (+) and thus has an enhanced hole conductivity. In the opposite way production with an excess of Cu compared to stoichiometric CIGS causes an excess of electrons and be negative charged. This is called n-type semiconductor material which has an enhanced electron conductivity. The conductivity, carrier mobility and hole density are shown in Figure 2.10 as a function of temperature for co-evaporated CIGS. The increase in conductivity at 300 K is attributed to an increase in carrier concentration and current transport in extended states of the CB [35]. Figure 2.10 shows the conductivity rapidly increases above 300 K.

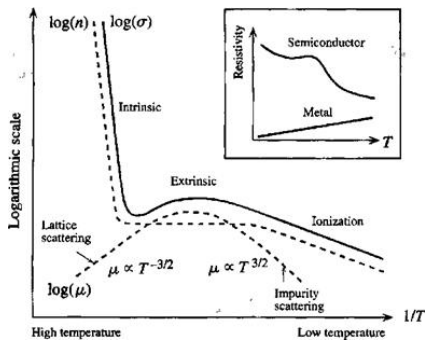


Figure 2.9: Schematic representation on the effect of extrinsic doping on the conductivity at different temperature. Image taken from [36].

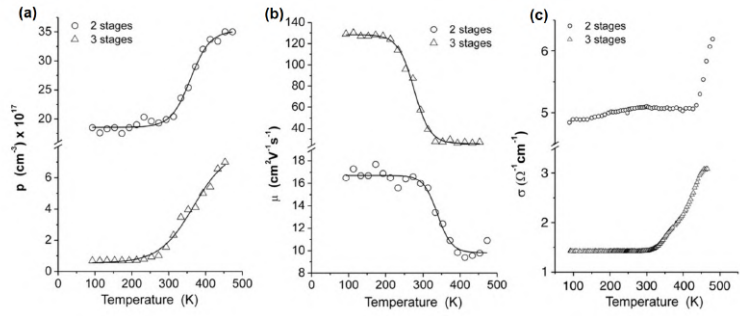


Figure 2.10: Curves of (a) hole density (p), (b) hole mobility (μ) and (c) conductivity (σ) versus Temperature corresponding to CIGS films deposited in two and three stages [35].

2.2.3. The pn-junction

A pn-junction is used to create the SCR which functions as a membrane for charges. It is required in PV technology for electron-hole pair separation as mentioned in Section 2.1. A common way of creating a pn-junction in CIGS technology is bringing p-type CIGS absorber layer material in contact with a CdS buffer layer. When a p-type semiconductor material is in Ohmic-contact with an n-type semiconductor material the following mechanisms occur:

- The hole concentration difference of in p-type material generates a diffusion current ($I_{diffusion}$) of holes towards the n-type material. The same holds for the electrons except the movement is in the opposite direction.
- The movement of these charge carriers exposes positive ion cores in the n-type side while in the n-type material negative ion cores are exposed. This results in an electromagnetic field at the junction and forming the SCR (or depletion region).
- Minority carriers being thermally generated in the SCR are swept across the junction due to the electromagnetic field. This is called the drift current (I_{drift}).
- Once equilibrium is reached the net current in the diode is zero and I_{drift} equals $I_{diffusion}$.

The above process is schematically shown in Figure 2.11. In p-type semiconductor material the holes are majority carriers and electrons minority carriers. The opposite holds for an n-type semiconductor material. The electrochemical potential is constant and independent of position. The contact between the p-type and n-type material results in band bending near the surface. Figure 2.14(a) schematically shows the band structure (VB and CB) within the cell in equilibrium conditions (without bias or light). In CIGS solar cells with a CdS buffer layer and a GGI ratio of 0.32 the width of the SCR is in the range of 0.4-0.6 μm . The width of the SCR increases with lower Ga content and decreases with higher Ga content [37].

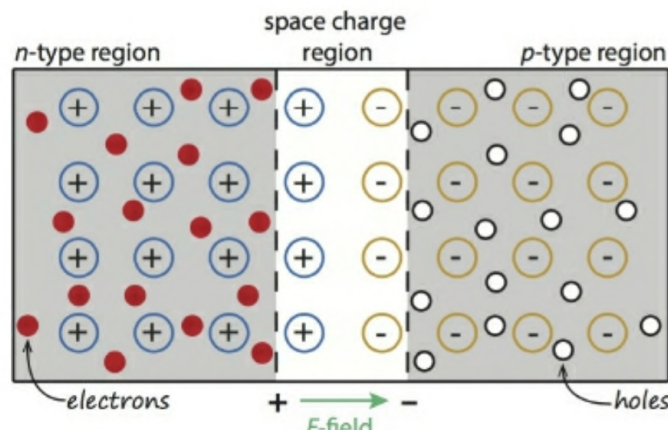


Figure 2.11: The formation of a space-charge region when n-type and p-type semiconductors are brought together. The white band in the middle represents the space-charge region. Image taken from [13].

2.2.4. Biasing

It is possible to apply an external potential over the SCR in two ways. When the positive terminal of the external potential is connected to the p-type material this is called a **Forward Bias (FB)**. When the positive terminal of the applied potential is connected to the n-type material this is called a **Reverse Bias (FB)**. These two situations are schematically represented in Figure 2.12.

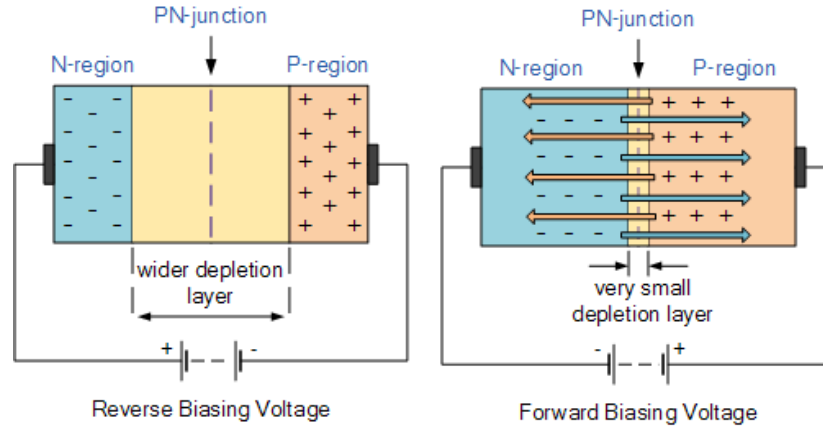


Figure 2.12: Schematic representation of forward and reverse biasing conditions applied on semiconductor material with a pn-junction. Image taken from <https://www.electronics-tutorials.ws/diode>

The most common way to look at solar cell characteristics is the IV-curve. A schematic solar cell(diode) IV-curve is shown in Figure 2.13(a). This curve shows the diode curve for RB and FB conditions including the short circuit current (I_{SC}), open circuit potential (V_{OC}) and maximum power point voltage (V_{MPP}). The dashed lines are under illuminated conditions.

In addition to the IV-curve shown in Figure 2.13(a) it is possible to, theoretically, represent a solar cell in an equivalent circuit. The equivalent circuit has to reflect the electrical characteristics of a solar cell. Figure 2.13(b) shows the equivalent circuit of a solar cell in light equilibrium, dark RB and dark FB. The circuits consist of one diode and a shunt resistance. For simplicity the series resistance also relevant in PV-technology is left out. When the V_{cell} equals V_{MPP} in light equilibrium the power output of the cell reaches it maximum. It is seen from the equivalent circuit that a low shunt resistance R_{shunt} results in a large shunt current I_{shunt} resulting in current losses and a lower power output per cell. Biasing conditions effect the electronic band structure described in Section 2.1.1. Schematic band diagrams under equilibrium, FB, RB under dark and illuminated conditions is shown in Figure 2.14.

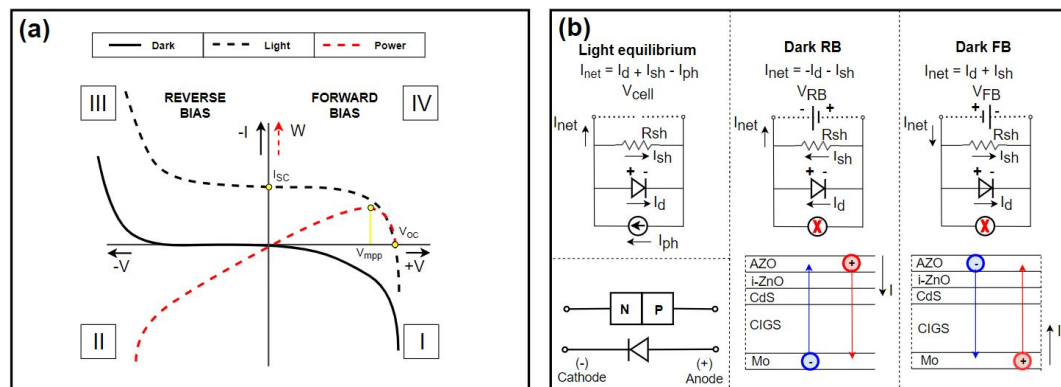


Figure 2.13: (a) Schematic solar cell IV-curve with illuminated and dark conditions. Including an additional power curve ($Power = I * V$) (b) Equivalent circuit for solar cell in light equilibrium, dark RB and dark FB conditions. This figure is composed out of multiple articles found in literature [9, 38, 39].

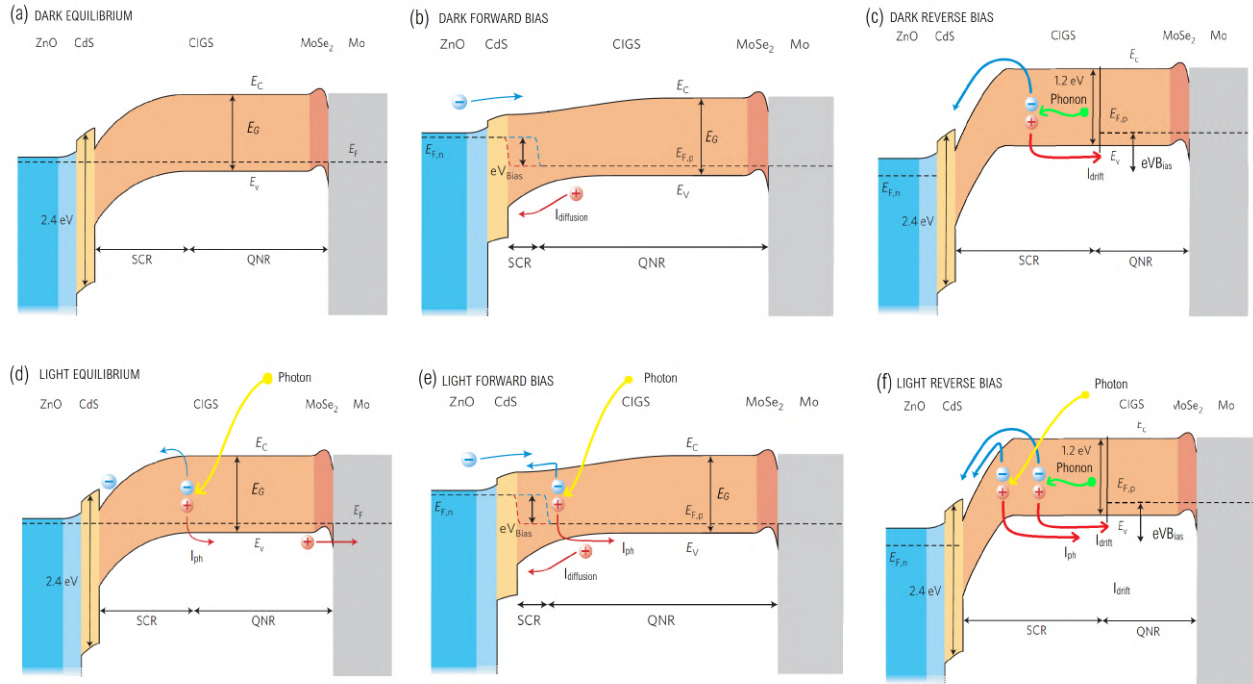


Figure 2.14: Schematic band diagram of a CIGS solar cell under (a) light, (b) dark Forward Bias, (c) light forward Bias, (d) dark reverse Bias and (e) light reverse bias conditions. This figure is based on the band structure image of Chirila et al. [40] in combination with figures from [17, 41].

The next paragraphs explain the relevant mechanisms during biasing with the help of Figures 2.12, 2.13 and 2.14. In **FB**, the potential applied moves majority carriers, from p-side and n-side, into the depletion region where they recombine. This is shown with arrows in Figure 2.12. The SCR width decreases and the energy barrier over the junction is lowered, shown in Figure 2.14(b). There is a big concentration difference in carrier densities over the junction. The lowered barrier results in an increase of diffusing majority carriers through the junction. When a hole from the p-side (majority carrier) reaches the other side of the junction it becomes a minority carrier and is likely to recombine due to the larger electron concentration. This is why the FB current is also called a recombination current. When the potential is increased it is possible for more holes to reach the end of the n-type region recombining with an electron in the metal contact. The net current is dependant on the applied potential shown in Figure 2.13 where the current directly increases when a FB is applied. The same holds for the electrons in the opposite direction. Due to the recombination of charge carriers the hole concentration will not equalise and current continues to flow. Once the FB reaches the built in field of the junction the barrier diminishes and current starts increasing rapidly. This characteristic is shown in Figure 2.13(a) where the current rapidly increases when a dark FB is applied. The net current under illuminated condition depends on the photocurrent and the applied FB potential. At low FB potential the induced recombination current reduces the net current. The recombination current increases with an increase in FB potential. Eventually the potential is reached where the current under illuminated conditions will be larger compared to the photocurrent and the direction of current is reversed.

The potential barrier for diffusion increases if a **RB** is applied. If thermal generation of an electron-hole pair occurs in SCR, the electromagnetic field present moves the charge carriers and thus a drift current is present. An electron is swept across the SCR from p-side where it is a minority carrier to the n-side where it is majority carrier. The opposite is true for the hole. Initially, drift current is not dependant on the applied voltage because this does not influence the amount of thermally excited electron-hole pairs in the SCR. The junction width increases, shown in Figure 2.12 due to an applied potential forcing the majority carriers to move away from the junction. Mind the number of thermally generated electron-hole pairs is low and thus this drift current is low compared to the currents present in operating conditions.

When a RB potential is applied, a low drift current is initiated. It is observed the dark RB part of the curve, shown in Figure 2.13(a), initially shows no dependency on the applied potential as the curve is almost horizontal. It is not visible in this graph but increasing the potential slightly increases the RB current. The RB increases the width of the SCR (or depletion region) shown in Figure 2.12. This allows for more thermal generation of electron-hole pairs in the SCR increasing the drift current. In CIGS the SCR is wide compared to photovoltaic technology using silicon due to lower doping concentrations. In addition the thin absorber layer generates a high electromagnetic field for a relatively low potential.

At an increased RB potential, in light or in dark, the current suddenly increases. This is called the transition potential. This sudden increase in current can be attributed to two distinct mechanisms in the junction.

- 1 Zener breakdown
- 2 Avalanche breakdown

When Zener breakdown occurs the electromagnetic field present in the junction is so high that it is able to pull an electron out of VB on the p-side into the CB on the n-side of the junction creating an additional drift current [42]. Once the threshold of potential is reached the increase of current causes more electrons being pulled through the junction. In CIGS, Zener breakdown happens at lower potential than Avalanche breakdown [39].

In the case of avalanche breakdown the initial process of charge carrier generation is caused by thermal electron-hole pair generation. The electron (or hole) generated in the SCR is accelerated by the electromagnetic field. The drifting electrons collide with an atom during transport. If the electromagnetic field is strong enough, the electron gains sufficient energy to ionise an electron when colliding with the atom. The field accelerates this extra electron which collides and creates another electron in the CB. This process is called carrier multiplication creating an electron avalanche like effect. The current density increases towards the TCO. The multiplication of the charge carriers must be suppressed or it is capable of damaging semiconductor devices [43]. The ionisation rate decreases with increasing band-gap. For that reason high band gap materials have higher breakdown potentials. The ionisation rate decreases with an increase in temperature at a given electromagnetic field [44].

The potential where the RB transition takes place is affected by light and temperature. With increasing temperature the transition shifts to a lower potential. Defects are less active at lower temperatures, it is plausible they are involved in the transition potential [9, 39, 45]. Illuminating a CIGS cell with red light, being only absorbed in the CdS, does not influence the transition voltage. While blue light, being absorbed in the CdS and CIGS layer causes a decreased breakdown potential [9, 46]. Meta-stable defects in the CdS buffer/CIGS interface region are tentatively proposed as the source of this effect. The thickness of the CdS buffer layer has a very weak impact on the transition potential [9].

The main focus of this thesis is the dark RB condition. Dark RB involves tunneling mechanisms and processes which are not yet fully understood for CIGS. It is an aspect in the whole process but it is not in the scope of this thesis to study this in detail. For now, the most important point from this section is the direction of movement for holes and electrons in the dark RB. As shown in Figure 2.13(b) the electrons move from the molybdenum back contact towards the AZO, while holes move in the opposite direction.

2.2.5. Loss mechanisms

Recombination mechanisms strongly determine the conversion efficiency of solar cells. An electron-hole pair which recombines within the absorber layer cannot be extracted from the cell power output. The three main recombination mechanisms are:

- Direct recombination
- Shockley-Read-Hall recombination (SRH)
- Auger recombination

Direct recombination is a bandgap-to-bandgap process where an electron from the CB recombines with a hole in the VB generating a photon. SRH recombination is facilitated by an impurity atom or lattice defects creating trap states for an electron within the bandgap. An electron can be trapped at such a location and recombine with a hole that is attracted to the trapped electron. SRH recombination also occurs at surfaces. At

the interface between different materials trap states are present due to dangling bonds. Auger recombination involves three particles, where an electron in the CB recombines with an hole in the VB and transferring its momentum to the second electron in the CB which reaches a higher energy state. When the second electron relaxes, it releases its energy to vibration energy of the lattice or phonon modes. This results in heating up of the material. Auger recombination is not very relevant for CIGS material due to the direct bandgap [13].

As shown in Figure 2.12 possible leakage current (shunt) inside the cell can be present. Literature presents the following possible causes for this leakage current. Micro-scale pinholes in individual layers where no CIGS absorber layer is present between the Mo and other layers of the stack [47]. It is also possible low resistance pathways along grain boundaries exist. These pathways are induced by conductive elements shunting the cell at the grain boundary. The pin-holes and grain boundaries are Ohmic shunts. Two other shunts are possible. It is possible the TCO is in direct contact with the CIGS. This allows electrons to get injected in the CIGS. This results in a Space Charged Limited Current (SCLC). The next presented shunt pathway is a trap assisted tunnelling mechanism. A local high density of trap states enables tunneling of charge carriers through the material [48, 49]. All the described shunt pathways are shown in Figure 2.15.

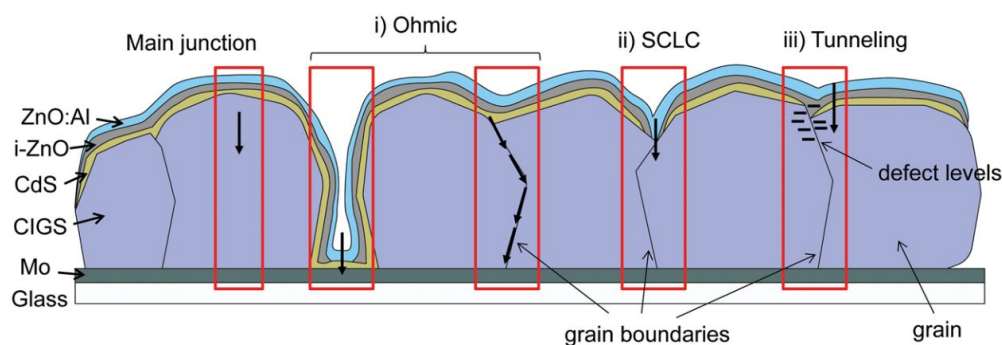


Figure 2.15: Possible shunt pathways in a ZnO:Al/i-ZnO/CdS/CIGS/Mo solar cell. SCLC refers to space-charge limited current [50].

2.3. Defects and element migration in CIGS

Worm-like defects are the main focus of this thesis and are separately described in Chapter 3. Material migration is a general term describing forced element or particle transport mechanisms in solids. Migration of elements occurs due to one or more of the following: (1) a concentration gradient (chemical diffusion), (2) temperature gradient inside the solid, (3) mechanical stress and (4) an electromagnetic field. During worm-like defect formation and propagation all conditions are present and migration of elements is observed. For example: (1) the concentration gradient at interfaces and in depletion region, (2) local Ohmic heating as a result of current at shunts or weak spots, (3) mechanical stress as a result of local temperature differences and differences in thermal expansion between layer and (4) an external applied potential in the form of a reverse bias and the internal electromagnetic field of the junction.

The following quotation from Stanbery describes the problem very well:

"Even one of the most basic assumptions made in conventional semiconductors, that electronic and ionic transport are decoupled, does not apply under some typical circumstances. Consequently, more complex models that borrow concepts from the theories of disordered materials and electrochemistry must be employed to understand the behaviour of CIGS photovoltaic devices. " [21]

To have more insight in the behaviour of material migration in CIGS information found in literature is presented on the following topics: defects, diffusion, electromigration, thermal migration, stress migration and chemical reactions.

2.3.1. Defects in CIGS

There is a wide variety of defect pairs possible in a CIGS absorber layer. It is not relevant to discuss them all in detail so only the most important defects are listed and described. CIGS consists of four constituent elements. In solids, the number of point defects grows exponentially with the number of constituents thus increasing the number of ways for the system to minimise its free energy [51]. In general, the vacancy equilibrium concentration increases exponentially with temperature [32]. This is evident from the following formula:

$$N_v = N * \exp\left(-\frac{Q_v}{kT}\right) \quad (2.5)$$

Where N is the total number of atomic sites, Q_v is the formation energy of a vacancy, k is the Boltzmann constant and T is the temperature in K [32]. In the case for CIGS this results in an increase of Cu vacancies with increasing temperature. The Cu vacancy is a simple example but other defects also increase in concentration with increasing temperatures.

The Ordered Defect Compound (ODC) where In and Ga take the place of Cu atoms (e.g. $CuIn_3Se_5$, shown in the phase diagram of Figure 2.4, is believed to be the result of many $2V_{Cu} + (In, Ga)_{Cu}$ orderly present in the bulk [52]. The lower boundary for energy of formation of several possible defects in CIGS are shown in Table 2.2.

Table 2.2: Lower boundaries for some defect free energies of formation (eV) from [51].

V_{Cu}	V_{In}	V_{Se}	In_{Cu}	Cu_{In}	Se_{In}	$In_{Cu} + 2V_{Cu}$	$Cu_{In} + 2Cu_i$	$V_{Se} + Cu_{In}$	Se_{Cu}	In_{Se}	Cu_{Se}
0.75	1.88	2.21	0.22	1.47	1.88	0.65	0.89	2.35	0.75	2.21	2.1

The Cu and In atoms in Cu deficient CIS were studied by Nakamura et al. et al. [53]. The activation energy of Cu migration was found to be 1.05 eV experimentally. The position of transition state is between the centre of the octahedral site and Se atom in the unit cell shown in Figure 2.3. The activation energy of In migration was found to be 1.70 eV [53]. In CGS and Cu poor CIS, it seems to be the $V_{Cu} - V_{Se}$ divacancy dominating, whereas, the single V_{Cu} dominates in Cu rich CIS [54].

Lany and Zunger [55] theoretically studied the $V_{Cu} - V_{Se}$ defect pair in the SCR and under RB in dark and light conditions. This pair occurs as acceptor $[V_{Cu} - V_{Se}]^-$ or as donor $[V_{Cu} - V_{Se}]^+$ complex where the defects create a shallow donor or acceptor electron energy levels between the VB and CB. When electrons excited by photons are caught by the defect, this changes the configuration from donor to the acceptor complex, thus light increases the concentration of acceptor complexes. Red light is capable of this change in configuration. In pure CIS and low Ga content CIGS, the donor configuration produces a shallow n-conductive donor level (charge states 0 and 1+). Three different regions are distinguished.

- 1 Near the junction the complex exists in the acceptor(-) configuration. No configuration change is caused by the RB potential.
- 2 Further away from the junction the complex exist in the donor(+) configuration. This complex converts towards the acceptor configuration by electron capture or hole emission as a result after reverse bias treatment increasing the the net acceptor density and increasing the junction capacitance.
- 3 Even further away from the junction, under zero bias a p-type condition exists. The reverse bias converts acceptor- to donor complexes. Thus decreasing the net acceptor density [55].

The concentration of complexes is shown in Figure 2.16 showing an increased temperature result in an increased acceptor complex concentration, while the donor complex concentration decreases. This shows light and temperature effect the defect state (donor or acceptor) in the CIGS absorber layer. This example shows the defect concentrations are dependant on the bias potential of the SCR.

Combining the findings of Lany and Zunger [55] with the observed change in RB transition voltage seen in blue and red illumination is by Szaniawski et al. [9] gives rise to the importance of the acceptor-density on RB diode transition characteristics.

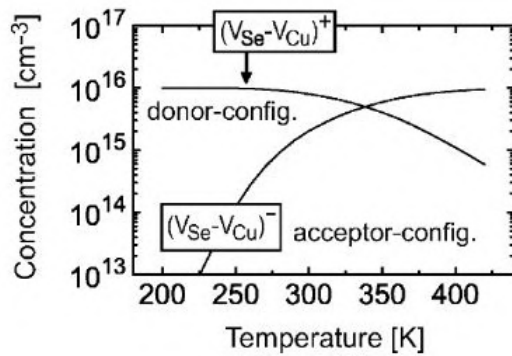


Figure 2.16: The corresponding equilibrium distribution between the donor and the acceptor configuration of $[V_{Cu} - V_{Se}]$, as a function of temperature [55].

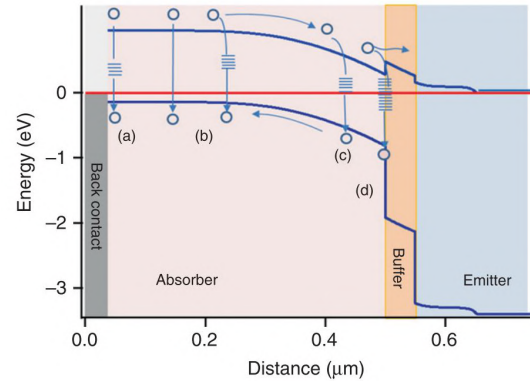


Figure 2.17: Band diagram for chalcopyrite-type heterojunction device indicating recombination mechanisms: (a) back contact recombination; (b) bulk recombination; (c) space-charge region recombination; (d) interface recombination [17].

RB diode characteristics, defects and temperature

General RB diode characteristics, defects and temperature have been described in this chapter. It is a complex situation as the following things occur:

- Increase in temperature increases defect concentration.
- Increase in temperature increases thermal electron hole pair generation.
- RB potential affects the nature of defects.
- RB potential increases the width of the SCR.

These mechanisms all have their influence on the RB current. The RB current is a result of thermal excitation of electrons in the SCR. Assuming thermal excitation is equivalent everywhere in the CIGS layer this means increasing the width of the SCR also increases the RB current as the electromagnetic field of the SCR 'collects' more thermally excited carriers. Gap states, already mentioned in Subsection 2.2.5, are schematically represented in Figure 2.4. The image shows recombination mechanisms at these gap states. The reverse process, electron-hole pair generation, is possible at these gap states. The energy required for an electron to move from the VB to a gap state and from a gap state to the CB is lower than the energy required for band-to-band excitation. Gap states are present at interfaces and in the crystal lattice. The concentration of defects increase with temperature, increasing the concentration of gap states and increase the RB current. It is also shown in Figure 2.4 at surfaces a high concentration of gap states is present. Defects at the CdS/CIGS interface and in the SCR (shown in Figure 2.4(c) and (d)) contribute to the RB current. Gap states present are also present at grain boundaries shown in Figure 2.15. It is possible, given a sufficient RB potential, for the SCR to include the whole CIGS layer. This allows thermal excitation taking place at the defects on the Mo/CIGS (shown in Figure 2.4(a)) interface to contribute to the RB current. The movement of carriers by the electromagnetic field of the SCR involves movement and scattering with the lattice. This scattering involves heat dissipation.

2.3.2. Diffusion

The driving force of diffusion is a concentration gradient. This gradient is present due to layers of different materials and the internal gradient to create the depletion region. The volume of atoms inside the crystal lattice is important in diffusion for interchangeability. To have a short overview Table 2.3 was constructed to provide the ionic radii of all relevant elements relevant in CIGS.

Table 2.3: Ionic Radii of relevant Ions in CIGS thin-film technology. Obtained values out the work of Shannon [56]

Element		Cu	Cu	In	Ga	Se	Cd	S	Zn	O	Na	Mo
Ionic charge	[C]	+	2+	3+	3+	2-	2+	2-	2+	2-	+	3+
Crystal Ionic radius	[pm]	91	87	94	76	184	109	170	88	126	116	83
Effective Ionic Radius	[pm]	77	73	80	62	198	95	184	74	140	102	69

The temperature dependence of the diffusion coefficient is shown in the following equation:

$$D = D_0 \exp\left(-\frac{Q_d}{RT}\right) \quad (2.6)$$

Where D_0 is a temperature dependant pre-exponential ($m^2 * s^{-1}$), Q_d is the activation energy for diffusion ($J * mol^{-1}$ or eV per atom), R is the gas constant ($8.31 J * mol^{-1} K^{-1}$ or $8.62 * 10^{-5} eV * K^{-1}$ per atom) and T is the absolute temperature in K [32]. Fick's second law and assuming the temperature dependence of the diffusion coefficient is independent of compositions result in a simple formula for the diffusion length x :

$$x = \sqrt{Dt} \quad (2.7)$$

Where D is the diffusion coefficient at a specific temperature and t is the time [32]. Compared with metals, self-diffusion in semiconductors is a very slow process. The grain boundaries present in a material act as fast diffusion paths [57].

Basol et al. [58] studied the diffusion of S into CIGS. It is found the S distribution profiles were greatly influenced by the Ga content. Where the S concentration profile follows the Ga concentration profile. The bulk diffusion constants of S in Cu rich and Cu poor differ by about two orders of magnitude. Where the inclusion of S is more favourable in Cu rich material. The diffusion constant in Cu poor material was estimated to be about $3 * 10^{-13} cm^2/s$ at $848 K$ [58].

Park et al. [59] studied in-situ diffusion of elements at the CIGS/CdS/ZnO interfaces while annealing. It is found CdS adjacent to CdS/CIGS interface begins to present a porous structure above $473 K$. The pore evolution should be directly correlated with Cd and/or S diffusion out of CdS. The surface of CIGS is known to be Cu deficient making it easy for Cd to diffuse in the CIGS. The continuous Cd in-diffusion is suggested to happen by the assistance of Ga out-diffusion. Ga is known to be very soluble in ZnO. The presence of Ga in the ZnO increases the conductivity [60].

Chen et al. [61] studied diffusion behaviour at the CdS/CIGS interface while annealing at $323 K$ and $473 K$ for 30 minutes. They observed that during annealing Cd diffused $500 nm$ into the CIGS layer. The concentration of S near the CIGS surface also increased showing diffusion length of about $300 nm$. The In decreased at the surface due to its low binding energy. The diffusion of Zn was limited to the CdS layer and did not diffuse into the CIGS [61]. It is not noted in this article but in the SIMS profile Ga and Cu appear as if they diffused into the CdS layer.

The diffusion of Cd into the CIS and Cu into the CdS layer has been studied by Nakada and Kunioka [62] and Yin and Lou [63]. The presence of Cd in the CIGS and a decrease of Cu at the CIGS surface is observed. It is concluded Cu atoms are replaced by Cd. The ionic radii and valance, 0.97 \AA for Cd^{2+} and 0.96 \AA Cu^+ are very similar making the observations found with experiments plausible [62].

Salome et al. et al. [64] show the presence of Cu deprived and Cd enriched areas in the CIGS. The opposite, Cd enriched and Cd deprived is also found. This suggests the segregation of Cd–Se. The results indicate that there is a diffusion process that replaces Cu with Cd in the CIGS layer and Cd with Cu in the CdS layer.

Jones [65] studied the diffusion of Ga into a CdS layer. The Ga diffuses into CdS by occupying cation sites. At 1010 K the diffusion coefficient is in the range of 1×10^{-16} for low Ga concentrations. Combining this data with Equation 2.7 implies Ga diffuses 77 nm in CdS in 60 seconds.

Lei et al. et al. [66] observed spontaneous formation of voids at grain boundaries or in the bulk has been observed in $Cu(In,Ga)Se_2$ films deposited by multistage evaporation processes. The observation is explained with a model involving the Kirkendall effect, inter-diffusion and a solid-phase reaction between Cu_2Se and In or Ga [66].

2.3.3. Electromigration

The migration of elements due to an electromagnetic field is often referred to as electromigration (EM). When current is transported through a material it produces two forces on atoms in the solid. The first is an electrostatic force, F_{field} , caused by the applied electromagnetic field needed for current. The second force, F_{wind} , is a result of momentum transfer between moving electrons and atoms in the crystal lattice. This force therefore acts in the direction of current flow. When the net force on an atom is larger than the activation energy it is able to hop to adjacent positions in the lattice. Figure 2.18 shows the electromigration in the case of a metal (conductor) where $F_{wind} \gg F_{field}$ [67]. The diffusion mechanisms involved in electromigration take place along the grain boundaries, along surfaces or through the lattice. Atoms in the crystal have strong bonding compared to atoms at grain boundaries or surfaces. The atoms at the grain boundaries have a lower activation energy due to asymmetric bonding forces [67]. In the case of CIGS, the contribution F_{wind} is lower due to lower current densities and higher electromagnetic fields [68]. Electromigration is an activated diffusion process, so the rate of migration increases with increasing temperature [69].

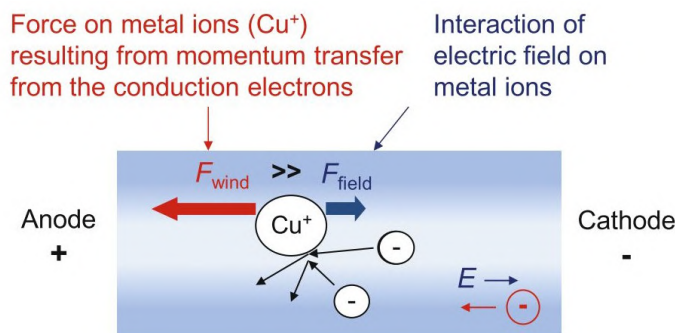


Figure 2.18: Two forces act on metal ions (Cu) that make up the lattice. Electromigration is the result of the dominant force, that in a metal is, the momentum transfer from the electrons that move in the applied electromagnetic field E [67].

Guillemoles et al. [70] studied the self healing effect of CIGS. The most simple defect example is the creation of a $Cu_i^+ - V_{Cu}^-$ (Frenkel) pair. When a Frenkel defect pair is generated in the SCR the Cu interstitial is repelled towards the p-side of the junction interface due to the internal electromagnetic field. The Cu vacancy is repelled to the n-side of the junction. This charge separation results in an electromagnetic field opposing (and thus decreases) the original electromagnetic field. Interestingly, this pair creation followed by charge separation is analogous to the separation of an illumination-induced electron-hole pair in the SCR, which reduces the electromagnetic field in the SCR and produces the photovoltaic effect. The mobile Cu_i migrates until it is trapped in a defect. The remaining Cu vacancy, which is also effectively mobile, is eliminated in another defect process [70, 71]. It is expected that with an external RB potential, thus a wider SCR, higher field and elevated temperature induced by current results in more element migration.

Chernyak et al. [72] and Gartsman et al. [73] researched the effect of electromagnetic field on Cu migration in CIS. Between 483 and 592 K chemical diffusion coefficient for the most mobile species, Cu ions and vacancies, is $10^{-6} - 10^{-7} \text{ cm}^2/\text{s}$. Based on experimental results they calculated that during 50ms Cu ions are displaced over a distance of 130 μm resulting in an ion velocity v_{ion} of 0.26 cm/s. They conclude that the direct electromagnetic field dependence of Cu ion mobility plays a minor role. Rather, indirect electromagnetic field

dependence of mobility due to local Joule heating, dominates [72]. Nádaždy et al. et al. [74] studied the electromagnetic field induced Cu ion migration in bricks and also proposed the electromagnetic field-induced Cu migration takes place via a vacancy mechanism [72].

High voltages and currents are used to produce stable CIS junction devices. Localised heating effects do play a role, albeit a limited one, because no melting occurs. These effects are expected to be strongest around junctions, owing to the injection of hot carriers and electron-phonon interactions. They locally enhance the diffusion of defects or defect reactivity. The external field is used to create bulk junctions. The field induced Cu migration without introduction of a foreign phase and without melting. The migration and redistribution of Cu atoms results in a permanent junction once the external electromagnetic field is switched off [75–78].

2.3.4. Thermal and stress migration

Thermal migration (TM) occurs due to a temperature gradient. In the case of thermal migration the vacancies move to the higher temperature region while the atoms move to the lower temperature region. Thermal migration also contributes to the transport of energy as the moving atoms carry along heat. As a consequence TM lowers its own driving force [67].

Stress migration (SM) is induced by a mechanical stress gradient from external forces or internal. Due to the stress gradient vacancies move from a tensile stress region to a compressive stress region. The atoms move in the opposite direction from a compressive stress region to tensile region [67].

Coupled effects are present in many situations. The temperature (directly related to diffusion coefficients) and concentration differences are involved in EM, TM and SM. All three mechanisms cause a concentration gradient. The **coupled migration effects of EM, TM and SM** are shown in Figure 2.19.

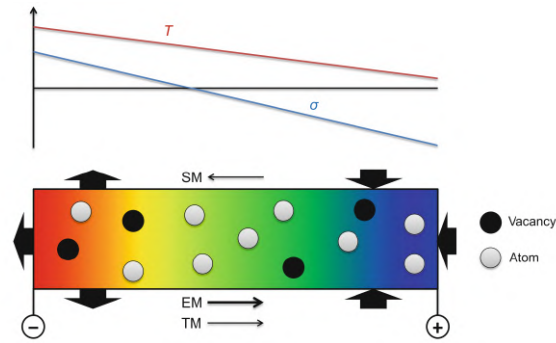


Figure 2.19: Coupled effects of EM, TM and SM in a metal wire segment. T is the temperature and σ is the mechanical stress

2.3.5. Chemical reactions

The previous sections described movement of elements. It is very well possible that chemical reactions at surfaces or in the layers take place during worm-like defect formation. There are two thermodynamic factors in determining if a chemical reaction occurs spontaneous. The first is factor is the enthalpy of the reaction (ΔH). If $\Delta H < 0$ energy in the form of heat is released during the reaction. The second factor is the disorder of the system or the entropy (ΔS). If $\Delta S > 0$ the reaction increases the disorder in the system and the reaction occurs spontaneous. The Gibbs free energy (G) of the system reflects the balance between these two factors and is defined as the enthalpy change of the reaction minus the entropy change of the reaction times temperature. The Gibbs free energy of a reaction at a constant temperature can be written as follows:

$$\Delta G = \Delta H - T\Delta S \quad (2.8)$$

When $\Delta G < 0$ the reaction is favourable or spontaneous and when $\Delta G > 0$ the reaction is unfavourable. As this work is not a study on thermodynamics the presented information is sufficient to understand the next paragraph.

The standard free energy (G°) of a compound is a combination of the energy released or required and the change in disorder during formation out of its constituent pure elements. More negative G° or ΔG means a more spontaneous reaction. As a rule of thumb, reactions with a low ΔG or G° are spontaneous and a measure for the stability of end products.

Table 2.4 shows the G° of relevant compounds in CIGS solar cells. In addition to this table the G° of $CuGaSe_2$ is $-283 \text{ kJ} \cdot \text{mole}^{-1}$ [71]. The general observations from Table 2.4 is Cu poor CIS ($CuIn_2Se_5$ or $CuIn_5Se_8$), Ga_2O_3 and In_2O_3 have a low ΔG . Thus are relatively stable compounds.

It is also possible look at the reactions between compounds. The ΔG of some relevant reactions in CIGS solar cells shown in Table 2.5. It is observed reactions between the CdS and ZnO are not favoured thermodynamically [51]. This is in contrast reactions where Ga is present in one of the compounds. All the reactions where Ga is present in one of the compounds have a $\Delta G < 0$ and are thermodynamically favourable. Table 2.5 and a lower G° for $CuGaSe_2$ compared with $CuInSe_2$ suggests Ga is very reactive.

Table 2.4: Standard free energies (298 K) of some compounds of the Mo/CIGS/CdS/ZnO system [51].

Compound	G° (kJ/mole)	Compound	G° (kJ/mole)
Cu $^\circ$	-9.9	CdO	-274.7
In $^\circ$	-17.2	CdS	-176.8
Se $^\circ$	-12.6	CdSe	-170.7
Cu $_2$ Se	-103.9	Cu $_2$ O	-198.2
Cu $_7$ Se $_4$	-351	Cu $_2$ S	-115.6
Cu $_3$ Se $_2$	-173	CuO	-168.8
CuSe	-65.2	CuS	-73.6
CuSe $_2$	-81	In $_2$ O $_3$	-957.0
In $_2$ Se $_3$	-360	In $_2$ S $_3$	-414.4
InSe	-130	MoSe $_2$	-180.2
In $_3$ Se $_4$	-416.5	Mo $^\circ$	-8.5
Cu $_{11}$ In $_9$	-410	ZnO	-363.6
Cu $_2$ In	-61.5	ZnS	-222.2
CuInSe $_2$	-280	ZnSe	-193.5
Cu $_2$ In $_7$ Se $_4$	-942.5	SnO $_2$	-596.43
CuIn $_3$ Se $_5$	-661.5	SnS $_2$	-179.62
CuIn $_5$ Se $_8$	-1041.6	SnSe $_2$	-154.89
Ga $_2$ Se $_3$	-462.4	Ga $_2$ O $_3$	-1114.4
Ga $^\circ$	-12.17	Ga $_2$ S $_3$	-558.7

Enthalpy of formation at 298 K at $1 \cdot 10^5 \text{ Pa}$. Entropy at 0 K are set to zero

Table 2.5: Free energies of reaction for some of the relevant reactions at the interfaces in the Mo/CIGS/buffer/TCO type of solar cells [51].

Reactions	ΔG (kJ)	Possible
Back contact		
Mo + 2Cu $_2$ Se \Rightarrow MoSe $_2$ + 4Cu	-3.5	Yes
Buffer and Window		
Cu $_2$ Se + CdS \rightarrow Cu $_2$ S + CdSe	-5.6	Yes
In $_2$ Se $_3$ + (Zn,Cd)Cd(S,Se) \rightarrow (Zn,Cd)In $_2$ (S,Se) $_4$	< 0	Yes
In $_2$ Se $_3$ + 3CdS \rightarrow 3CdSe + In $_2$ S $_3$	0.3	?
Ga $_2$ Se $_3$ + 3CdS \rightarrow 3CdSe + Ga $_2$ S $_3$	-78	Yes
Ga $_2$ Se $_3$ + 3ZnS \rightarrow 3ZnSe + Ga $_2$ S $_3$	-10.2	Yes
CdS + ZnO \rightarrow CdO + ZnS	43.5	No
In $_2$ Se $_3$ + 3ZnO \rightarrow In $_2$ O $_3$ + 3ZnSe	-60.3	Yes
Ga $_2$ Se $_3$ + 3ZnO \rightarrow Ga $_2$ O $_3$ + 3ZnSe	-141.7	Yes
In $_2$ S $_3$ + 3ZnO \rightarrow In $_2$ O $_3$ + 3ZnS	-128.4	Yes

3

Worm-like defects

This chapter consists of two sections. The first section contains the information available from literature. The second section contains relevant research at Solliance on worm-like defects.

3.1. Literature study

The combination of cell configuration (monolithic series interconnection) and partial shading of a CIGS module results in a RB potential difference over one or more cells of a string. As mentioned in Subsection 2.2.4, a RB potential generates a small current through the cell. When a threshold of applied RB potential is met, the current suddenly starts increases. The RB current is one of the most important factors as it dissipates energy in shunts and other parts of the cell heating up the material. To protect each cell with an external bypass diode in a thin-film module is practically (and especially economically) not feasible [79]. The effects of worm-like defects on cell performance varies. In some cases the efficiency drops some percentages, while cases where the efficiency drops over 10% are also seen. Information in literature on formation, propagation and structure of worm-like defects is limited. What is formed and how propagation takes place is still unknown. This section presents the available information in literature regarding worm-like defects.

Observations

Two different types of worm-like defects are shown in SEM image of Figure 1.1. Figure 1.1(a) clearly shows more local behaviour compared with Figure 1.1(b). Both cases involve a discrete process of propagating. Worm-like defects show discrete propagation steps in a chain of linked spheres when looking at surface of the cell area a higher magnification. The spheres of discrete steps are shown in Figure 3.1. In the case of a stationary worm-like defect discrete steps stay confined to the vicinity of the nucleation point whereas in mobile worm-like defects they propagate throughout the cell shown in Figure 3.2. Figure 3.2 shows an Electron Beam Induced Current (EBIC) image where it can be seen poor current collection is present inside the worm. Cross-sectional views of the worm like defects are shown in Figures 3.3 and 3.4. Note that in Figure 3.3 voids are formed above the CIGS layer and light areas near the back contact appear. It is observed the defect is formed between the CIGS and ZnO layer.

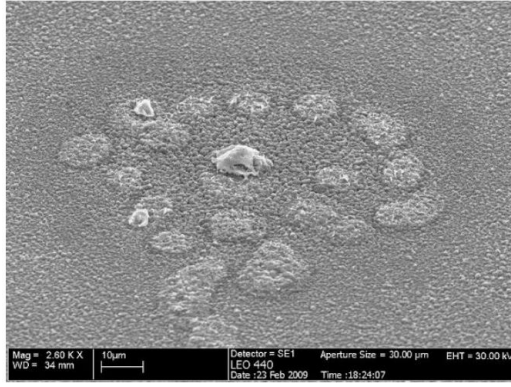


Figure 3.1: Point of origin for worm-like defect. Propagation of the damage appears as adjacent spots [38].

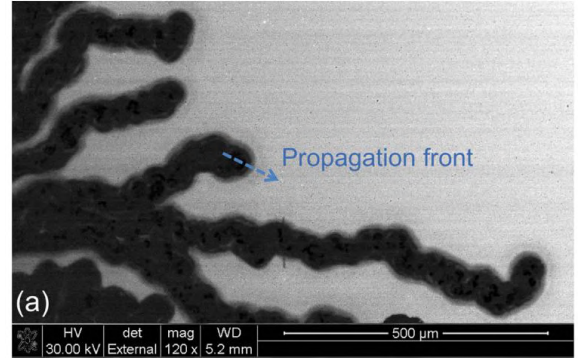


Figure 3.2: An EBIC image from an SEM shows an overhead view of a worm-like defect, where dark areas correspond to poor current collection [80].

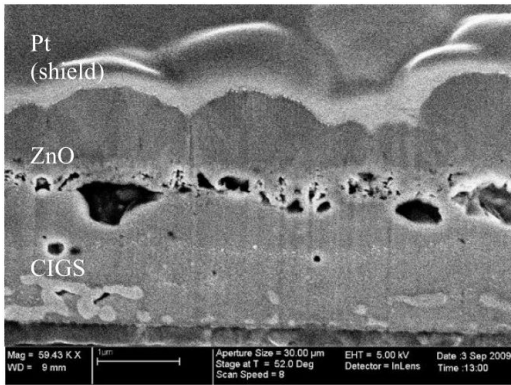


Figure 3.3: Focused Ion Beam cross-section of a worm shows how cavities are formed at the absorber/window interface. Note also the segregation of light areas near the back contact [38].

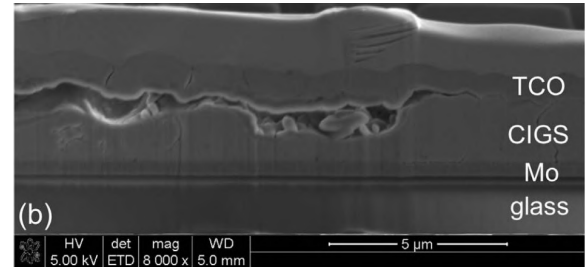


Figure 3.4: An SEM image of FIB-prepared cross-section at the propagating end of a worm-like defect showing voids near the top of the CIGS layer [80].

The conditions in which the worm-like defects are created are important for studying the migration of elements. Compared to the ideal RB diode curve shown in Figure 2.13. The RB part of the IV-curve where worm-like defects form and propagate is different from ideal diode behaviour. An IV-curve where worm-like defects are formed is shown in Figure 3.5 where clearly jumps in current are present compared to the ideal smooth line. Chernyak et al. [72] reported when a constant voltage is applied and current over time shows spikes, similar to the spikes seen in Figure 3.5, the spikes are attributed to changes in the material. A Focused Ion Beam (FIB) with Energy Dispersive X-Ray (EDS or EDS) was used to determine composition profiles per elements before and after worm-like defect formation. The result is shown in Figure 3.6. It is observed by Westin and Zimmermann [38] that the observation of 'islands' near the back contact are Cu rich. Note in Figure 3.6 the decrease in width where Se was detected.

Guthrey et al. [81] studied local resistive heating in CIGS solar cells. Non-uniformities in the CIGS absorber layer are identified as the origin of worm-like defects. The energy dissipation in the form of heat at these non-uniformities initiates thermal runaway breakdown resulting in damaging of the cell. An equivalent circuit is derived to model the temperature of shunts. Different R_{shunt} are used as input for this model. It is assumed the TCO and molybdenum back contact heat up as a result of current crowding around the shunt. The temperature increase is dependant on the volume around the shunt supporting the RB current. Small shunts therefore heat up more as the supporting volume is smaller. The model estimates a cell temperature of over 320 K at a RB potential of -3 V. At this potential the temperature of a shunt with a resistance of 10 Ω reaches over 1200 K. It is important to note that this model is based on a lot of assumptions and not validated with experiments. However, it is one of the most thorough published models generating insights in local electrical behaviour around shunts.

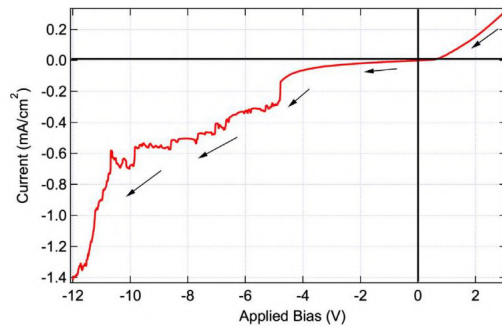


Figure 3.5: Measured IV-curve during an applied reverse bias. The applied voltage begins in FB and progresses towards higher RB. The graph shows jumps in reverse current as worm-like defects form and propagate [80].

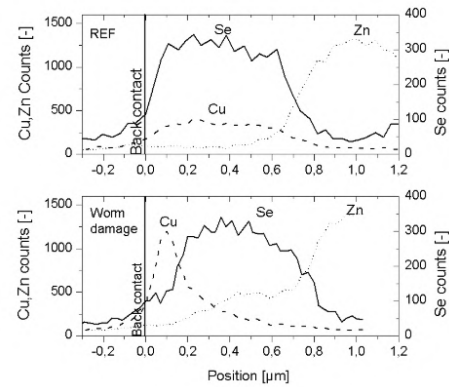


Figure 3.6: EDS scan across the layers from Figure 3.3. Mo peak (not present in the graph) set as "0" position. Cross section of damaged area shows Cu rich areas near the back contact and Zn appears to have intermixed with the CIGS layer [38].

3.2. Relevant research at Solliance

This thesis is part of a bigger study on worm-like defects at Solliance. In recent research worm-like defects are created on samples with a varying AZO thickness. The samples are designed according to the Nantes-Solliance design, imitating a monolithic interconnected cell. The main results from recent studies at Solliance by Nilsson's [12] and Klaas Bakker is presented

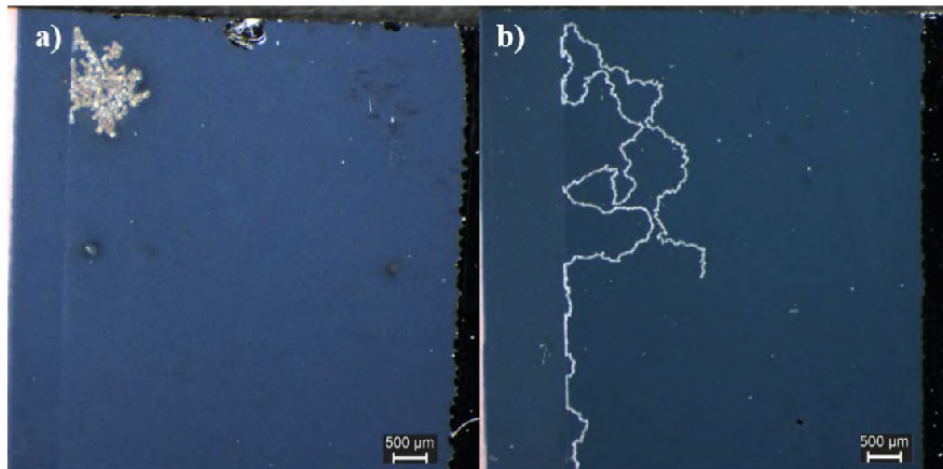


Figure 3.7: Optical microscope images of worm-like defects in a) sample 1602_2J showing local worm-like defect behaviour and in b) sample 1605_3B showing mobile worm-like defect behaviour [12].

3.2.1. 'Nantes' samples

An overview of the samples used in this chapter is shown in Table 3.1. The Mo, CIGS and CdS were deposited at Nantes University of Technology. The AZO was deposited at Solliance in Eindhoven or at the University of Nantes. The resulting cells have different AZO thicknesses. Worm-like defects were formed on all samples except 1602_3B by applying a RB voltage sweep in the dark, using a Keithley 2400 Source Meter. An initial FB potential of 0.7 V was applied, the voltage then decreased in steps of 50 mV, with a speed of 100 mV * s⁻¹. The IV-curves of the formation of samples are shown in Figure 3.8. As shown in Table 3.1 the thickness of the AZO is related to the behaviour of the worm-like defect. The samples with 2 μm have local worm-like defect behaviour. The samples with 1 μm AZO have worm-like defects are mobile and travel through the sample.

Table 3.1: Overview of 'Nantes' samples used from Nilsson [12] partially used in this work

		Active area cm^2	AZO thickness μm	AZO deposition location	behaviour
1602	2J	0.43	2	Nantes	local
	4B	0.36	2	Nantes	local
	4D	0.45	2	Nantes	local
	3B	0.34	1	Eindhoven	mobile
	3C	0.38	1	Eindhoven	mobile
	4H	0.49	1	Eindhoven	mobile
	4I	0.29	1	Eindhoven	mobile

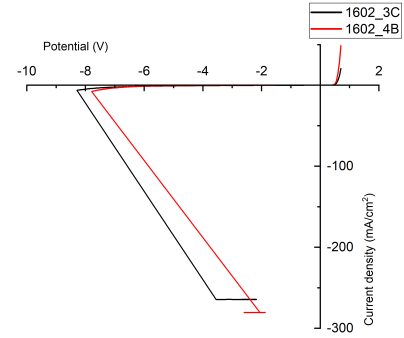


Figure 3.8: Reverse bias IV-curves during worm-like defect formation on the 'Nantes' samples [12].

3.2.2. EDS by Eurofins

A part of the characterisation was outsourced to Eurofins Scientific.¹ A trench under a specific angle is made with a Focused Ion Beam (FIB) using Ga ions. A SEM under an angle compared to the plane normal to the surface area of the cell was used to analyse the trench. On sample 1602_4H and 1602_4B two trenches were made and named spot 1 and spot 2. The result are cross-sectional images of worm-like defects. The exact locations are placed Appendix A. The resulting SEM image of 1602_4H is shown in Figure 3.9. This section shows a selected part of result and presents major observations. For additional information see Appendix A.

Visual observation

It is clear from Figure 3.9 that the AZO layer has been pushed up. The pushed up parts of the worm-like defect are discrete 'bubbles'. The following things are observed at all locations:

- A pushed up AZO layer
- Many small and a couple of large ($1\text{-}10\ \mu\text{m}$) cavities below the AZO.
- A layer of approximately $0.25\ \mu\text{m}$ between the large cavities and the AZO.
- Lighter areas near on the interface between CIGS and the back-contact.

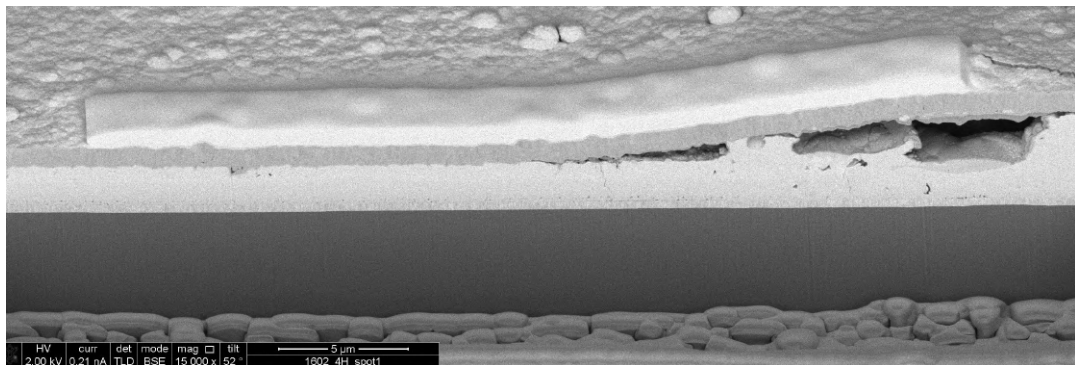


Figure 3.9: 1602_4H spot 1 SEM image of the trench with a crack in the AZO and cavities between on the CIGS/CdS interface. The white layer on the TCO (grey) is a deposited Pt layer to protect the sample from focused ion beam milling.

Element analysis

EDS (line-) scans and colour maps are used for visual observations and elemental analysis. Performing EDS on large surfaces allows colour maps of specific areas to be made. An example of one of these colour maps is shown in Figure 3.10. High Cu content areas in the CIGS near the back contact are found. These areas also have a low Se content.

¹The Eurofins facility in Eindhoven specialises material analysis and reliability investigation of consumer products, medical equipment, lighting products and other high-tech products. It has specific expertise in gas analysis and 'facility cleanliness' for high-tech manufacturing.

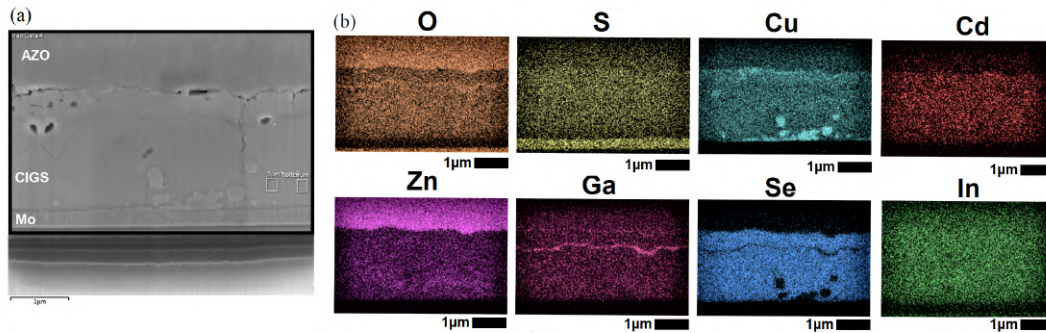


Figure 3.10: (a) The SEM image of a cross-section with the black box shows measurement area of (b) the colour map showing relevant elements at 1602_B spot 1.

A line-scan creates an element content across a drawn line over the sample. The element profiles outside worm-like defect are in Appendix A. In the undamaged part of the solar cell the profiles of Se, Cu, Mo are, as expected, flat. The Ga profile has a higher concentration near the back contact. From there it lowers towards approximately $0.2 \mu\text{m}$ from the CdS interface. Further toward the CdS interface it starts increasing again. This Ga profile is deliberately applied. A notch-type Ga profile commonly used for high current density due to absorption in the low bandgap region (low Ga region). A high voltage is maintained due to a larger bandgap in the SCR [82]. Figure 3.11 shows a line scan of sample 1602_4B spot 2 on a worm-like defect. For 1602_4B spot 2 the Cu concentration increases in both ways meaning from the middle of the CIGS layer towards the CIGS/CdS and towards the CIGS/Mo interface.

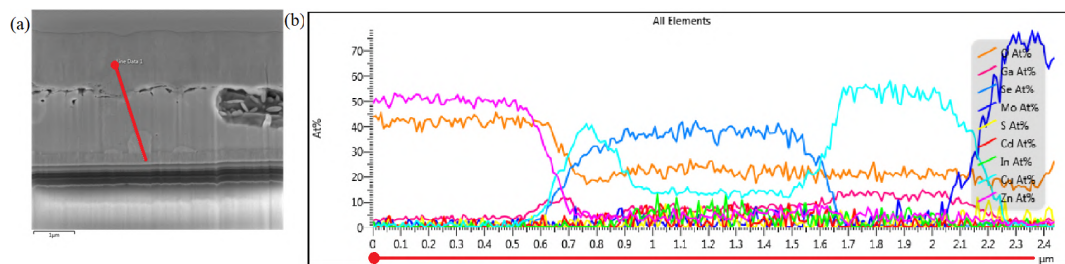


Figure 3.11: EDS line scan result at sample 1602_4B spot 2. With (a) SEM image of the cross-section indicating the line scan and (b) all element EDS profiles along the line.

After EDS line-scans and colour maps the samples were etched to remove the ZnO and CdS. Again, EDS was used to create colour maps. The results are shown in Figure 3.12. After etching it is observed that gallium has an increased concentration at the surface. The EDS maps at Figure 3.12, again, show a Cd and S band around the worm-like defect but only near the TCO.

It is redundant to show all information here. An overview of the observations is provided in Table 3.2 where more detailed images like Figures 3.10 and 3.11 of the other location can be found in Appendix A.

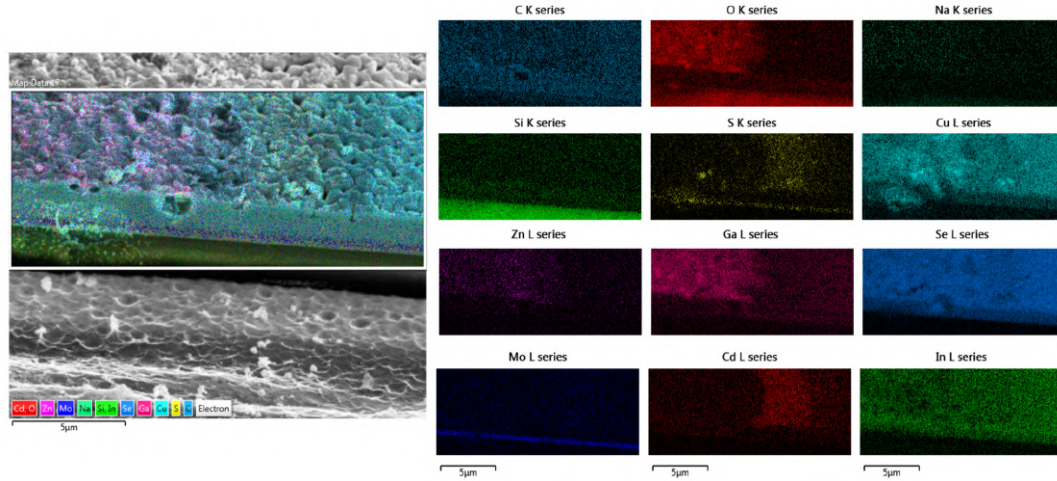


Figure 3.12: EDS colour map results after etching sample 1602_4B spot 2 with left: a SEM image with super-imposed colour maps of all elements and right: colour maps of individual elements.

Table 3.2: Observations from Eurofins SEM EDS and MAP results summarised in one Table

Location	Line-scan	MAP
1602_4H Spot 1	<ul style="list-style-type: none"> • Towards TCO Cu increases & Se decreases. • Higher value and more extreme Ga profile compared with other observations in and outside worm-like defects. 	<ul style="list-style-type: none"> • Cu migration towards TCO • Appears like S migrated in CIGS layer • Small Cd line visible
1602_4H Spot 2	n.a.	<ul style="list-style-type: none"> • Cu rich parts near back contact • Cavities show less Cu, In, Se but more Cd and S
1602_4B Spot 1	n.a.	<ul style="list-style-type: none"> • Cu rich and Se poor areas near the AZO and back contact
1602_4B Spot 2	<ul style="list-style-type: none"> • Cu moved towards the AZO and back contact. Near the back contact Se starts decreasing when Cu increases. • Ga profile more a step function increasing near the TCO compared to the smooth line outside defect 	<ul style="list-style-type: none"> • Small Ga rich line above cavity. • Cu rich areas near back contact. • Cu rich areas near TCO. • Cu rich 'trail' visible. • Cavities are Cd and Se rich.

3.2.3. Raman

For interpretation of Raman data on CIGS solar cells, peaks have to be attributed to vibration modes of atomic bonds. Theelen and Schiepers [83] recently published a paper including a table with Raman peak positions for CIGS material. This table is a summary from literature. The data and its references are included in Appendix B. A summary of the table extracted from Appendix B is shown in Table 3.3. Additional to the work from Nilsson [12], Theelen and Schiepers [83] peak positions of relevant atomic bonds of chemical reactions shown in Table 2.5 are added.

Nilsson [12] did Raman spectroscopy experiments with a green ($\lambda = 533 \text{ nm}$) and a red ($\lambda = 614 \text{ nm}$) laser. Initial Raman spectroscopy was done on the samples before worm-like defects were formed. After worm-like defect formation Raman spectroscopy on worm-like defects was done before after etching the samples with 3 wt.% Hydrochloric acid (HCl). The etching step removed the AZO and the CdS layer.

Outside worm-like defects the initial red laser Raman results for were comparable for all samples from Table 3.1. This was expected since AZO is principally transparent to red light and samples from batch 1602 are deposited alike. The changes towards the worm-like defect include an increase in FWHM of the CIGS A1 peak at

Table 3.3: Raman shift peak values for relevant atomic bonds

$Cu(In,Ga)Se_2$	Raman shift cm^{-1}		$Cu(In,Ga)S_2$	Raman shift cm^{-1}		Other	Raman shift cm^{-1}	
OVC	150-160	[83]	$Al - CuInS_2$	290-305	[83]	$InSe$	120-130	[83]
$Al - CuInSe_2$	173-176	[83]	$Al - CuGaS_2$	310	[83]	$InSe_3$	150	[83]
$Al - CuGaSe_2$	182-188	[83]	Shoulder Al-S	318	[83]	CdS	304, 600, 900	[84]
B2/E	215-225, 261, 273	[83]	$Cu_{2-x}S$	460	[83]	$CdSe$	211	[85]
Se	230-260	[83]	MoS_2	180-220-380-400-460	[83]	Ga_2O_3	155, 250, 300	[86]
$Cu_{2-x}Se$	260-263	[83]				In_2O_3	136, 365, 495, 590, 625	[87]
$B1 - CIGSe$	115-130	[83]				$ZnSe$	250, 500, 750, 1000	[88]
						ZnS	278, 351	[89]

175 cm^{-1} and peak position shifts towards lower values around the visible band outside a worm-like defect. It is possible a decrease in Ga or increase in Cu content is responsible for this shift [90, 91]. The Raman shifts for the red laser outside the worm-like defect are shown in Figure 3.13. It is not possible to draw any conclusion regarding the different elements present but the increase in Full Width at Half Maximum (FWHM) indicates a defected structure [12].

At the same location the green laser results shown in Figure 3.14 a higher background signal near the worm-like defect compared with the bulk is observed. Near the worm-like defect an additional peaks at 304 cm^{-1} , 600 cm^{-1} and 900 cm^{-1} are observed. These peaks are attributed to CdS [84].

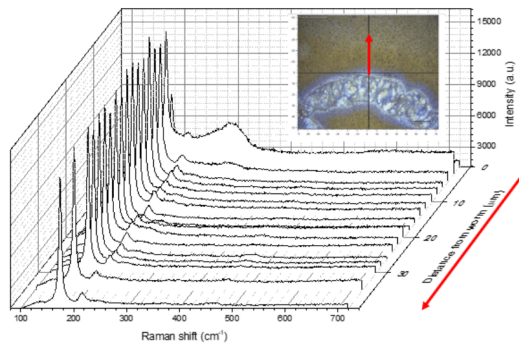


Figure 3.13: Raman spectroscopy with a red laser. Results are after etching. The measurement is done along the shown arrow [12].

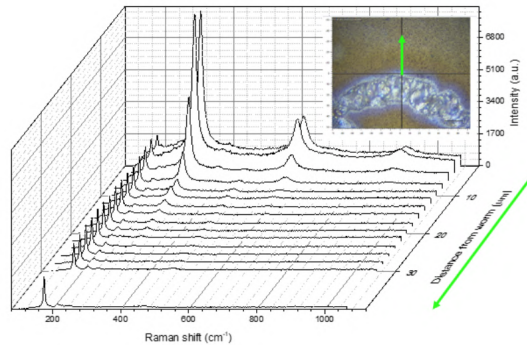


Figure 3.14: Raman spectroscopy with a green laser. Results are after etching. The measurement is done along the shown arrow [12].

The Raman shift **inside** worm-like defects is also measured. Inside the worm-like defect the CIGS A1 shown in Figure 3.15(b) around 178 cm^{-1} is disturbed and broadened. Inside the worm-like defect peaks at 233, 260 and $440/460\text{ cm}^{-1}$ are observed with the red laser. This is shown in Figure 3.15(a). With the green laser, shown in Figure 3.15(c), a Raman shift at 236 and 260 cm^{-1} is observed. The peaks inside the worm-like defect correspond to Cu_2Se and indicate Cu segregation [90, 92]. The results of a green and red laser are shown in Peaks around 233 cm^{-1} and indicate either In-Se or Ga-Se compound being formed [93, 94].

3.2.4. (Spectral) Photoluminescence

Spectral PhotoLuminescence (SPL) measurements were carried out at the same location as the Raman spectroscopy before and after etching. Measurement on worm-like defects resulted in a very low signal. This indicates the material does not function as a solar cell as the bandgap of the material is not in the desired range of wavelengths. The signal before and after etch outside worm-like defect area were comparable. A minor peak at 1.1 eV and a major peak at 1.19 eV are observed. These peaks are related to bandgap energy and represent recombination in the absorber layer [95]. The result near a worm-like defect on 1602_4I is shown in Figure 3.16. The peaks are broadening towards lower energies and can be attributed to recombination between different point defects, vacancies and anti-sites [59, 96–99]. In Figure 3.16 peaks at 0.87 and 0.97 eV appear. The 0.97 eV peaks are attributed to Cd_{Cu} defects [100]. The $V_{Se} + V_{Cu}$ and In_{Cu} give rise to energy transition of these values but the exact nature is not confirmed and varies between sights [96].

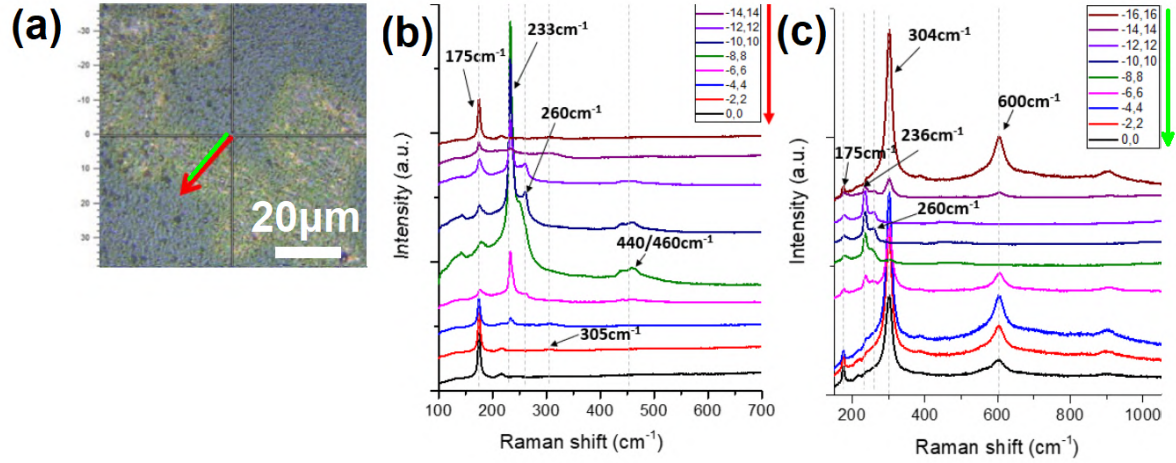


Figure 3.15: Results from red (b) and green (c) Raman spectroscopy measurements on sample 1602_4I. Measurements were done along the arrows in (a). The coordinates for each resulting spectrum are given in the legend [12].

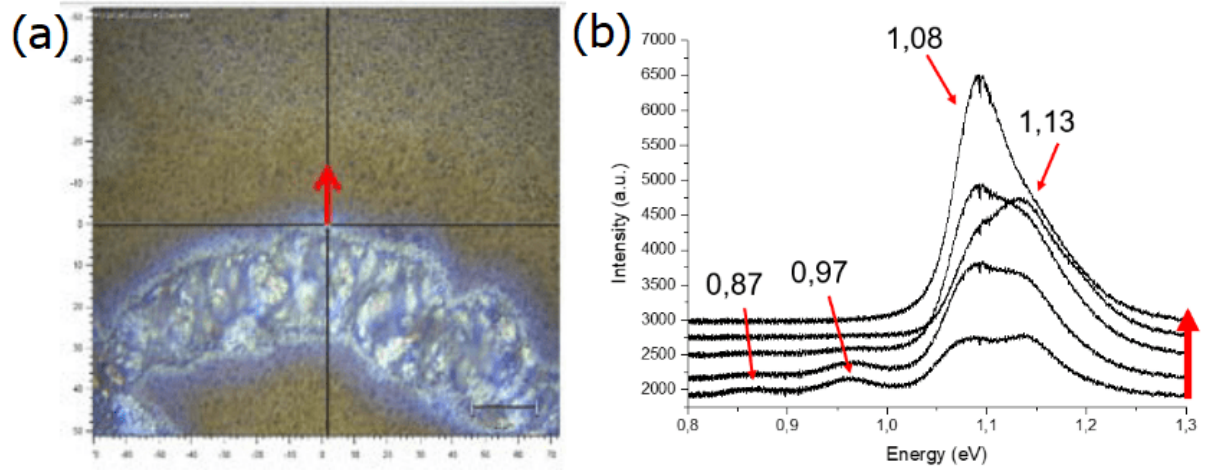


Figure 3.16: (a) OM with red arrow as indication where SPL measurements were done, (b) SPL measurement result on sample 1602_4I next to worm-like defect [12]

3.2.5. Confocal Microscopy

As observed from the cross-sectional SEM images shown in Figures 3.9 and 3.11 the material under the AZO has swollen during worm-like defect formation. To get an idea on the increase in volume and height Confocal Microscopy (CM) was done. The confocal microscopy results at 1402_4I are shown in Figure 3.17. It is found worm-like defects in cells with a $1\ \mu\text{m}$ AZO have a height in the range from $0.1\text{--}1.7\ \mu\text{m}$. The diameter of the discrete steps in the range of $20\text{--}25\ \mu\text{m}$. For the samples with $2\ \mu\text{m}$ AZO the discrete steps were in the range of $50\text{--}80\ \mu\text{m}$. The height of the worm-like defect is in the range of $1.3\text{--}2.1\ \mu\text{m}$.

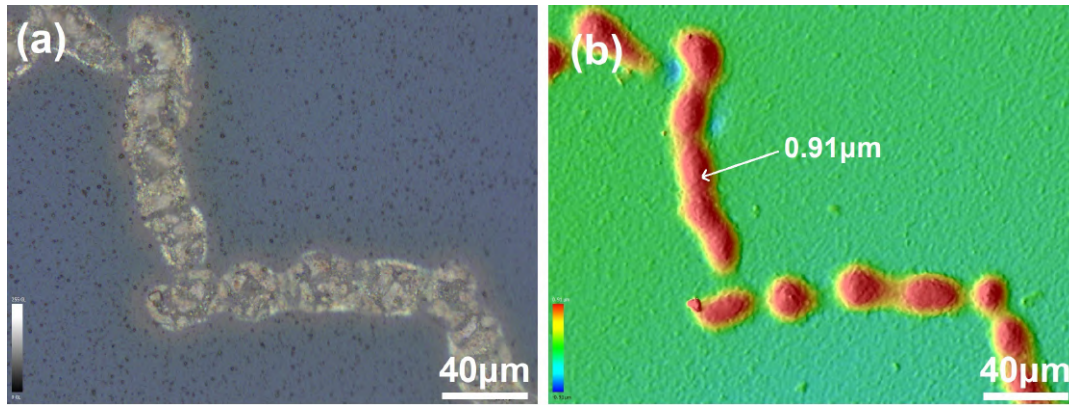


Figure 3.17: (a) Optical microscope image of a worm-like defect at sample 1602_41 location 1. (b) Contour map of Confocal microscopy measurement where the green area is the surface of CIGS at 0. The red area is approximately 1 μm higher than the rest of the surface

3.3. Summary

In multiple articles and research at Solliance similar observations on worm-like defects are found. After formation Cu is found near the back contact, Ga is found near the AZO. Cavities, discrete propagation steps and a pushed up TCO are observed visually. Raman Spectroscopy indicates Cd and S in the band observed around worm-like defects. Information from literature and recent research at Solliance already contains some information to answer the first sub-question. Changes in the band and inside worm-like defects are not fully identified. No thorough investigation is done on the new formed phase near the TCO and Cu rich parts near the back contact. In literature, no theories on possible mechanisms are proposed. The next step in this research is an experiment trying to gain more information on the observations. Before heading into experimental results the methodology of this work is presented in the next chapter.

4

Methodology

This chapter contains the methodology of this work. First the reader is introduced with the reasoning behind the experiments. After the explanation why it is described in detail how the experiment is set up and how the measurements are done. To answer the research questions this work is build up out of two experimental parts.

The **first** part continues the recent research at Solliance presented in Chapter 3. These experiment are set up to investigate the composition and crystal structure of worm-like defects in more detail. It does so by analysing changes in crystal structure after worm-like defect formation (Post-Mortem) with X-Ray Diffraction (XRD). A more thorough chemical analysis on selected elements in the worm-like defects is done under a Scanning Electron Microscope (SEM) with Energy Dispersive X-Ray Spectroscopy (EDS or EDX).

The **second** part of this work is a newly developed experiment with second and third sub-question in mind. The experiment set up specifically to locally control the applied current and potential for a set amount of time. During worm-like defect formation a lot of elements migrate in a short amount of time. The local current density and the increase in local temperature are unknown. Controlling applied condition locally might allow control over temperature due to a lack of shunts, electromigration or chemical reactions.

There is a **problem** in controlling the local conditions. In normal operating conditions current is extracted from the cell via lateral conduction through the AZO and Mo located at front and back, respectively. Under RB the potential is present between the area of the layers. The formation of worm-like defects is most likely to start at one of many weak spots or defects in the CIGS absorber layer [81]. The effects of lateral conduction result in unpredictable location of worm-like defect formation as defects are distributed throughout the cell. A major problem as a result of lateral conduction is an unknown local current density and temperature during the process. The measured current through the cell could have been transported anywhere between the AZO and the Mo layer. This does not necessarily mean at the site where the worm-like defect is formed. The time of worm-like defect formation is in the order seconds where the worm-like defect propagates several millimetre across the cell. During the formation voids appear, a new Ga rich layer is formed at the surface, Cd and S are observed in a band outside the defect and Cu migrates towards the back contact. The **objective** of this experiment is to discriminate applied conditions with observed changes and mechanisms in the cell during or prior to worm-like defect formation. The variable parameters in this experiment are current, RB potential and time.

The **experiment** is set up as follows. A sample with the stacking of Figure 2.2 AZO is produced but **this time without the AZO** layer. On the sample without AZO (so top layer is i-ZnO) a probe is lowered at a specified location. The back contact metal layer is connected to another probe.

The two probes are connected to an electronic device controlling the current and potential. This enables local control over the applied conditions. The changes in the material as a result of the applied conditions is documented in the following order:

- Categorised features with Optical Microscopy, SEM and Confocal Microscopy directly coupled to applied conditions.
- Raman spectroscopy on observed features.
- SEM-EDS analysis on observed features.
- Differences and comparison between features and worm-like defects.

4.1. Production method

4.1.1. Nantes samples

The Nantes samples, from Table 3.1, are produced in collaboration with Nantes university. The samples were not encapsulated and produced with an active area of approximately 5 mm by 7 mm. The layout of these cells is specifically designed to mimic the geometry in a monolithically interconnected module. The layers were build up in the following order: 1 mm soda lime glass substrate, 500 nm DC-sputtered Mo, 2000 nm co-evaporated CIGS, 65 nm DC-sputtered i-ZnO, 1 or 2 μm DC-sputtered AZO and 60 nm thermally co-evaporated gold contacts on the side [101]. A detailed description on the procedures and cell design is found in [102].

4.1.2. Sample with and without AZO

The new cells with and without AZO produced for this research are produced in the baseline production of Solliance. The substrate of the cells is soda-lime glass. The first layer is a 200 nm Mo layer. The 1.6 μm CIGS is co-evaporated onto the Mo. Chemical bath deposition is used to deposit 50 nm CdS. During the production of these samples something went wrong with the chemicals during the chemical bath deposition. The result is a CdS layer with a very low Cd content.

4.2. Scanning Electron Microscopy (SEM) with Energy Dispersive X-ray Spectroscopy (EDS)

A Scanning Electron Microscope (SEM) was used to analyse worm-like defects. High resolution images and surface topology are obtained. The Energy Dispersive X-ray spectroscopy is used to obtain information regarding local composition. A JEOL JSM-6010LA Analytical Scanning Electron Microscope (SEM) combined with InTouchScope(navi) software is used in this work. The EDS detector is not calibrated for composition analysis but it is capable of visualising trends relative to measurement performed on bulk material outside worm-like defect areas. The JEOL SEM has a maximum accelerating voltage of 20 keV and operates in vacuum.

4.2.1. Measured elements

When giving an electron enough energy it is emitted to molecular orbital (or electron shell) with more energy leaving behind an electron vacancy or hole. The excitation requires a minimum amount of energy. When an electron from an outer shell fills the inner shell vacancy it releases X-rays according to the difference in energy between the bands. The band structure is different for elements and thus different characteristic X-rays are produced per element. A summary for relevant elements is extracted from the periodic table provided by JEOL and shown in Table 4.1. From Table 4.1 it is seen the characteristic X-rays of the following elements overlap: In & K, Na & Zn and Mo & S. These paired elements give the same signal and are hard to discriminate.

4.2.2. Penetration of electrons

What is measured during EDS is determined by the penetration depth of the electron beam. The penetration depth of the electrons is dependant on the accelerating voltage. Higher acceleration means more energy and deeper penetration of electrons in the sample. The depth of penetration also depends on the material density. This is important to keep in mind as the samples are multi-layered. The Monte-Carlo simulation program 'Casino V2' was used to estimate penetration depth for different layer stacking and accelerating voltages. The model run for 6, 12 and 18 kV with a beam diameter of 60 nm on two different samples. All the detailed

Table 4.1: Element data for elements relevant for SEM EDS.

Element	Atomic nr.	Characteristic lines in X-ray			Oxidation states	1st Ionization energy ($kJ * mol^{-1}$)	Electronegativity
		K- α (eV)	L- α (eV)	M- α (eV)			
C	6	0.277			4-, 3-, 2-, 1-, 1+, 2+, 3+, 4+	1086.5	2.55
Cd	48	23.173*	3.133		2+	867.4	1.69
Cu	29	8.040	0.93		1+, 2+, 3+, 4+	745.5	1.90
Ga	31	9.241	1.098		1+, 2+, 3+	578.8	1.81
In	49	24.21*	3.286	0.364	1+, 2+, 3+	558.3	1.78
K	19	3.312			1+	418.8	0.82
Mo	42	17.441	2.293		2-, 1-, 1+, 2+, 3+, 4+, 5+, 6+	684.3	2.16
Na	11	1.041			1-, 1+	495.8	0.93
O	8	0.525			2-, 1-, 1+, 2+	1313.9	3.44
S	16	2.307			2-, 1-, 1+, 2+, 3+, 4+, 5+, 6+	999.6	2.58
Se	34	11.204	1.379		2-, 2+, 4+, 6+	941	2.55
Zn	30	8.630	1.012		2+	906.4	1.65

*not detectable with acceleration voltages available of a JEOL JSM-6010LA SEM

Values from: www.unamur.be/services/microscopie/sme-documents/Energy-20table-20for-20EDS-20analysis-1.pdf

settings and information is found in Appendix C. A summary of the acquired results from casino is shown in Table 4.2. From this results it can be concluded that for a stacking with i-ZnO and CdS the penetration is approximately 60 nm in the CIGS. This must be taken in account when looking at images or EDS results. The width of analysis at high accelerating voltages of almost 1 μm is significant comparing it to the 20 μm width of the observed band around worm-like defects.

Table 4.2: Penetration depth of electrons for 2 different sample stacking at different accelerating voltages.

	CIGS/Mo/SLG			i-ZnO/CdS/CIGS/Mo/SLG		
Thickness layer (nm)	2000/500/substrate			50/50/2000/500/substrate		
Accelerating voltage (kV)	6	12	18	6	12	18
Penetration depth (nm)	164	460	814	160	430	880
Width of analysis (nm)	100	305	900	210	500	1000

The penetration depth and width were read of graphs at the point where 90% of the electrons were absorbed.

4.2.3. Settings

Two settings are selected for EDS measurements. Interesting features are observed in worm-like defects near surface and deeper in the cell. For this defects to be measured a high and a low accelerating voltage were chosen as standard setting. The SEM is not calibrated and the settings have a large influence on the resulting values. Manually selected shells and accelerating voltage were changed until empirically the elemental analysis was as close to the expected values for CIGS as possible. This was a GGI of 0.3, a CGI of 0.8 and a Se/CIG of 1.0. The results as close as possible to these ratios resulted in a accelerating voltage of 6 and 18 kV. Both were used at a spot size of 60 nm. At 6 kV the L- α was selected for the following elements: Ga, Se, Cd and Zn. The K- α shell was selected for O, Na and S. For 18 kV experiments the selected shells are identical except for Cu is changed to the K- α . For the 18 kV some possibilities open up in changing measured shells. This can be seen in Table 4.1 where Zn, Se, Ga and Cu have the possibility of measuring the K- α shell. To minimise the difference in settings whilst having values as close to the expected ratios only the Cu shell is changed from the L- α to the K- α shell for the 18 kV setting. The same shells hold for mapping where an additional measurements at 12 kV was added.

4.3. Point probe experiment

The local electrical conditions of a cell are applied with the following setup. Two probes are attached to the cables of a Metrohm Autolab pgstat30 potentiostat/galvanostat (Autolab) shown in Figure 4.3(a). The needle shaped probe, shown in Figure 4.3(b) is connected with the back contact with silver paste while the round shaped probe tip is placed on the measurement location. Nova 2.0 software is used to program specific experiments in the potentiostatic or galvanostatic mode. The Autolab is limited to 10 V or 1 A. The resolution of the potential is 0.3 μV . The accuracy is 0.2 % of current range. The current range is able to work from 10

nA up to $1 A$. Due to the relatively small area of the probe on the i-ZnO the current limit was set at $-30 \mu A$ for all experiments unless specified otherwise. The i-ZnO layer is thin and fragile. In potentiostatic mode a set constant potential is applied where current varies due to material and temperature changes. In galvanostatic mode a set constant current is applied to the cell and voltage changes according to material and temperature changes. Before each measurement a sweep is applied. The sweep goes from 0 up to the set conditions (in steps in potential or current). The sweep gives insight in the local diode properties. The sample holder shown in Figure 4.3(c) and (d) completely darkens the sample and also acts as Faraday cage.

Contact has to be made between the probe and sample while the probe presses lightly at the sample. At first the probe was lowered to much causing the layers to shatter before or during the application of the electrical conditions. An example of a shattered layers with a SEM is shown in Figure 4.1. Contact also damages the sample by only pressing forces of the probe. An example of contact damage is shown in Figure 4.2.

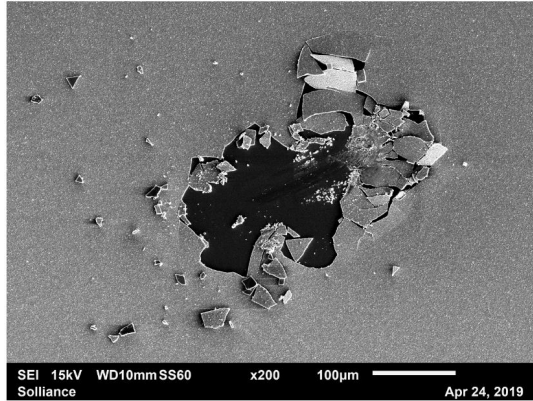


Figure 4.1: SEM image of spot 6G1 where the force of the probe on the layers resulted in shattering of the layers.

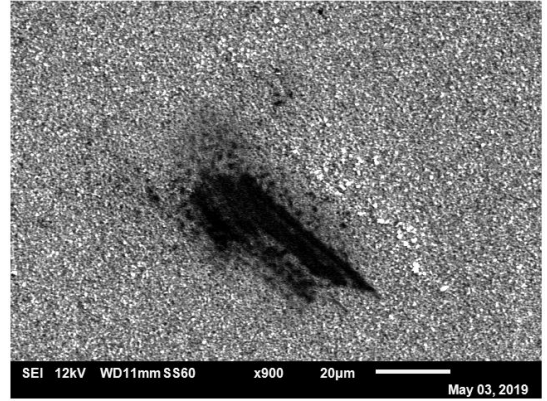


Figure 4.2: SEM image at spot 9D2 showing mechanical damage as a result of the probe pressing the i-ZnO.

This problem is resolved by using the setup as follows: in Nova 2.0 the cell is switched on and the current range set to $10 nA$. By turning the wheels the probe is lowered until the read out of the current suddenly measures approximately $-100 nA$ as a result of contact. The box is still open and light from the surrounding cause the sample to act as a local solar cell explaining the small current when contact is made. After the 'contact check' was initiated it was not possible to find these spots anymore. Figure 4.1 still gives a good indication of the contact area of the probe. In this case it is about $2500 \mu m^2$. It appears as if the probe scratched the surface when lowered. It is expected with the lightest touch as possible whilst having good contact the area is approximately $625 \mu m^2$ ($\frac{1}{4} * 2500$).

The following **measurement notation** was used for locations on the sample. The sample dimension standard at Solliance is a square with 9 columns and 18 rows of cells. The rows are named A-R and the columns are named 1-9. The sample was cut in half. An AZO layer was deposited on column 1-4 as fully functioning reference cells. Column 6-9 were left without AZO. A scan of column 6-9 is shown in Figure 4.4. As an example the used notation of measurement spots in this work is given. Per cell 3 areas were used as measurement spots as shown in Figure 4.4. The notation is described with an example. The notation consists of a number, a letter and again a number. The first number denotes the column, the first letter denotes the row. The combination of those two is a unique cell on the sample. The last number is the location on the specific cell. The cells were divided into three areas as shown in Figure 4.4.

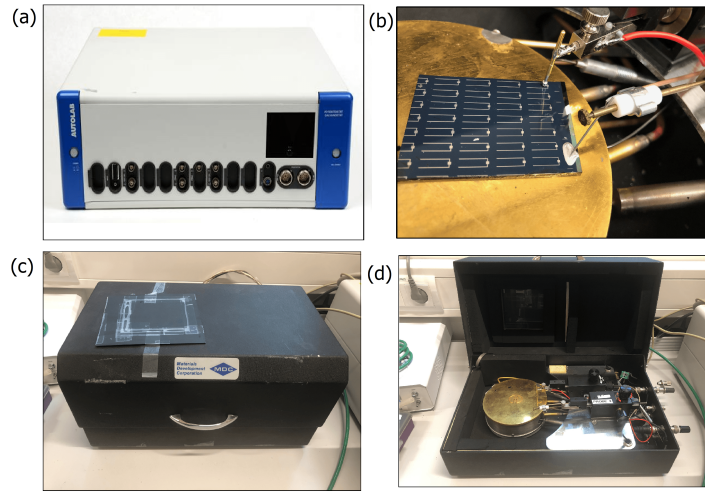


Figure 4.3: (a) Metrohm autolab pgstat30 potentiostat/galvanostat (b) Samples connected with a needle pressed on silver paste connected to the back contact and the point probe directly connected on top of a desired measurement location (c) and (d) are an open and closed image of the sample holder completely darkening the sample and also acts as a Faraday cage.

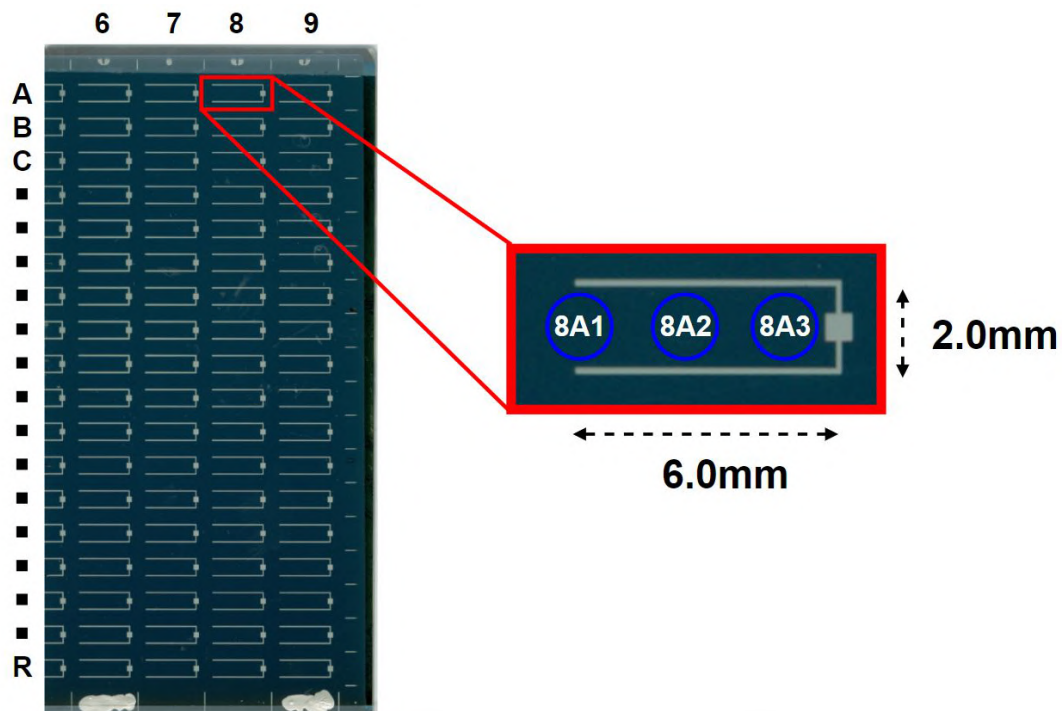


Figure 4.4: Image of column 5-9 showing an example of the notation used in this work during experiments.

4.4. Raman Spectroscopy and (Spectral) Photoluminescence

A Horiba Labram Aramis Raman microscope equipped with a Symphony IR detector and a 532 nm (green) laser was used for Raman spectroscopy LabSpec 6. software is used. A 633 nm (red) laser has a penetration depth of 300 nm in CIGS [83]. Based on this information the penetration depth of the green laser is estimated at 250 nm.

Raman spectroscopy measures the shift, up or down, of laser photons upon inelastic scattering by molecular vibrations (phonons). The shift in energy provides information on the vibration modes present in the system. For Raman measurements the following settings and components are used: 1800 gr/mm grating, 'synapse' mode, '532 edge laser' filter, slit at 100, hole at 200 and a minimum of 5 accumulations. The measurements spectrum range is 100-1000 cm^{-1} . The laser power was set at 10%. The acquisition time was altered per measurement to get significant counts. The maximum counts for this setup is 64000.

4.5. Etching

In order to characterise the samples without AZO or i-ZnO an etching step is performed. If only i-ZnO was present the samples were etched for 5 minutes with Hydrochloric acid 1 M HCL (3wt.%). After the etching the sample are rinsed with demi-water. To remove all the water droplets on the surface the samples were rinsed with Isopropanol (IPA) and dried with air.

4.6. Confocal microscopy

Confocal microscopy (CM) is an optical technique for 3D mapping of surfaces. The technique depends on spatial pinholes to block out-of-focus light. The area in focus on a surface is measured while the point of focus moves up or down for a set height range. Based on these areas combined with the point of focus of the microscope a height map is produced. For confocal microscopy in this work a Leica DCM 3D was used. When the lens with the largest magnification of 50x is used the minimum measured step size in height is 200 nm. During measurements the initial focus was on the surface of the sample. From this surface the point of focus ranged from -5(down) to +10 (up) μm . The minimum amount of good data points is set at 95%. The threshold was set at 5%.

4.7. X-ray Diffraction (XRD)

The XRD experiment were outsourced to employees of Delft University of Technology at the Material Science and Engineering department. The XRD was specifically used due to the possibility of measuring with a small spot size of 0.3 x 0.3 mm. The experimental setup had the following specifications: Bruker D8 Discover diffractometer with Incoatec Microfocus Source (I μS). 50 kV 1000 mA, Cu K α radiation. Montel Optics ELM32 with parallel beam, UBC collimator 0.5 mm and 0.3 mm. UMC 1516 sample stage, Eiger 2 500k detector. Measurements position and sample height were adjusted using laser-video. The following experiment was done: Locked coupled θ - 2θ scan 20° -80°, step size 0.02° 2θ , counting time per step 10 s. The results were processed with the Bruker Diffrac. EVA vs 5.0 software. The X-rays have a penetration depth of over 2.5 μm in the cell. This means the signal penetrates the AZO, CdS and CIGS reaching the Mo back contact.

4.8. IV-measurement & worm-like defect formation

The performance of the cells is an important aspect as the final results of this work must be coupled to fully functioning solar cells. The IV-curves were measured with a Neonsee solar simulator. The measurements were done under the following conditions: AM1.5, with an illumination of 1 $kW * m^{-2}$ at 273 K. The worm-like defects were induced with a Keithley 2400 Source Meter in the same manner as described in Section 3.2.1.

Post-mortem study on worm-like defects

In this chapter the reader is provided with the results of the continued post-mortem study on worm-like defects at Solliance from Section 3.2. To investigate the crystallographic nature of the worm-like defect XRD is used. To gain additional knowledge on the composition of the worm-like defects EDS is performed. SEM-EDS measurements were done of the following samples: 1602_3C, 1602_4B, 1602_4D and 1602_4H. This section presents only selected results. For more data and images of other samples, see Appendix D.

5.1. XRD

XRD experiments were done on sample 1602_2J. The sample was chosen for its local worm-like defect enabling a large fraction of the beam size to be on the worm-like defect. The small X-ray beam is pointed at the worm area and 2 mm outside that area (downwards in Figure 5.1), with a 0.5 mm diameter beam and a 0.3 mm beam. Figure 5.1 is a picture taken with the laser video system. The direction of the X-ray beam is from left to right.

XRD pattern

The XRD pattern on and outside worm-like defect area are almost identical meaning the differences between the two measurement locations very small. This is explained by the small volume of the different material visible in a cross-section SEM image of a worm-like defect shown in Figure 3.9. The patterns outside and on the worm-like defect differ at $2\theta \approx 27$ degrees. This is shown in Figure 5.2 showing a fraction of the full XRD pattern. In Figure 5.2 the left peak is attributed to an In rich phase and the right peak is attributed to a Ga rich phase [103, 104]. The ratio between the peaks is 0.88 (0.85 for 0.3 mm beam) compared to 0.78 (for both beam sizes) on the worm-like defect. The difference in the peak ratio suggests the material has a lower Ga content on the worm-like defect. Combining this information with the high intensity Ga on top of the CIGS in the SEM mapping from Figure 3.10 suggest the Ga moved out of the CIGS matrix towards the ZnO in different material.

The full XRD pattern is shown in Figure 5.3. In this pattern the peak at $2\theta \approx 34.7$ degrees reflects the AZO layer [105]. The peak at $2\theta \approx 40.7$ degrees is attributed to the Mo back contact [106]. Showing the beam fully penetrates the CIGS material. The peak at $2\theta \approx 53.4$ degrees is attributed to the (312) peak of CGS or CIS [103, 104].

This is the first time the crystal structure of the layer underneath a defect has been studied. It is an addition to the subtle differences observed with Raman spectroscopy which also suggested less Ga [12]. The XRD experiment show no clear evidence of a different crystal structure present in the cell after worm-like defect formation. This means the CIGS crystal structure does not change radically in the process of worm-like defect formation. The thin top layer has a relatively small volume compared to the measured volume. The slight changes in the spectrum suggests a movement of Ga out of the CIGS matrix. From the XRD results it is concluded the crystal structure of the material did not change or the volume of the changed material is too low for changes to be observed.

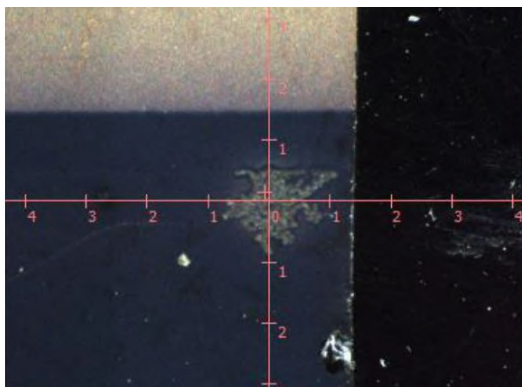


Figure 5.1: Measurement location on sample 1602_2J in the middle of the worm-like defect and at 2 mm below (downwards on axis) the worm-like defect.

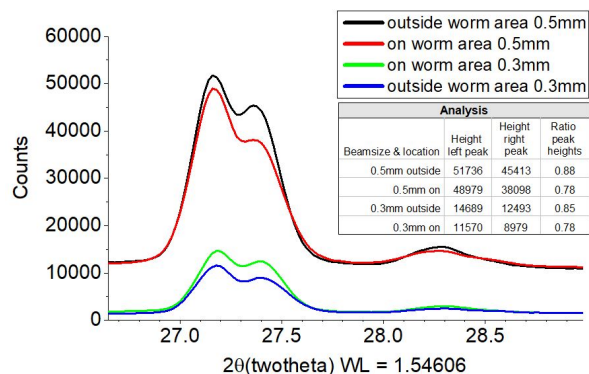


Figure 5.2: XRD pattern results from sample 1602_2J. Measurements are on and outside the worm-like defect. This graph shows is an enlarged part of the complete pattern around $2\theta=27.5$ degrees.

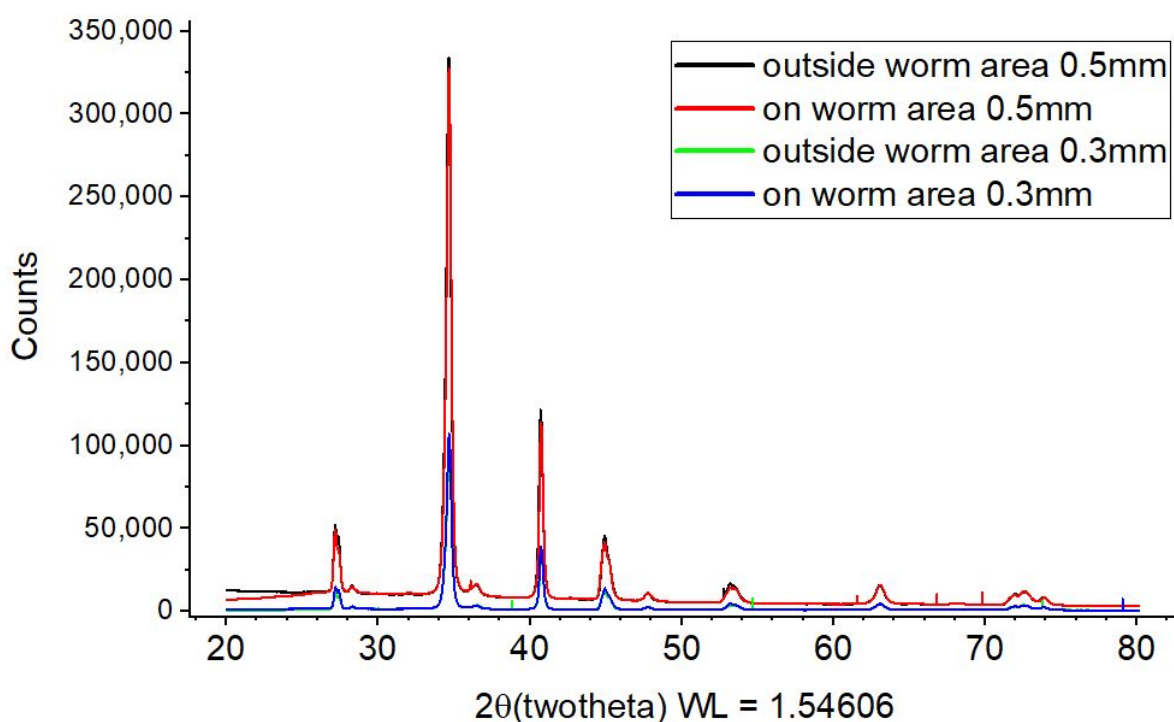


Figure 5.3: XRD pattern on sample 1602_2J. Measurements are done on and outside the worm-like defect. The two measurements outside the worm area overlap with the pattern on the worm-like defect making them not visible.

5.2. SEM analysis

This section presents the results acquired with the SEM on the Nantes samples. It contains Secondary Electron Images (SEI), Backscattered Electron Composition images (BEC), EDS colour maps and EDS point analysis.

5.2.1. EDS colour maps

Colour maps are ideal to get a general idea on the high and low concentration of elements around worm-like defects. The intensity on the images represents the presence of a specific element. Maps were made at 6 and 18 kV on different samples. The penetration depth of the electrons, shown in Table 4.2, is approximately 164 and 814 nm for 6 and 18 kV, respectively. Figures 5.4 and 5.5 show a SEI and colour maps for the following elements: Cu, In, Ga, Se, Cd, S, Zn and O. The SEI shows a worm-like defect with light and dark areas. Around

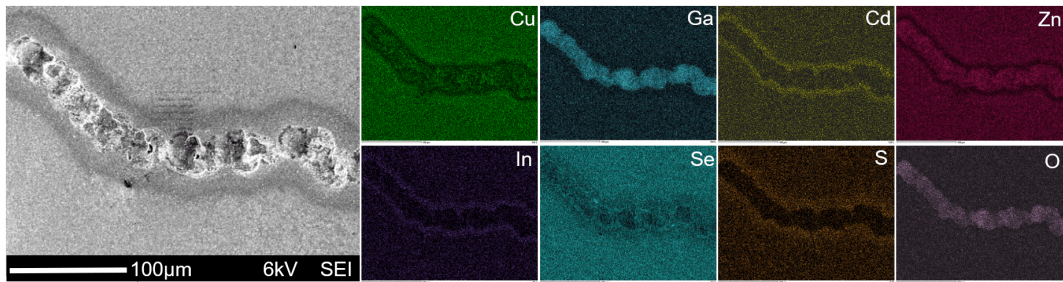


Figure 5.4: 6 kV SEM-EDS colour maps of elements at 1602_3C spot 1 showing a Ga rich worm-like defect with a Cd and S rich band around it.

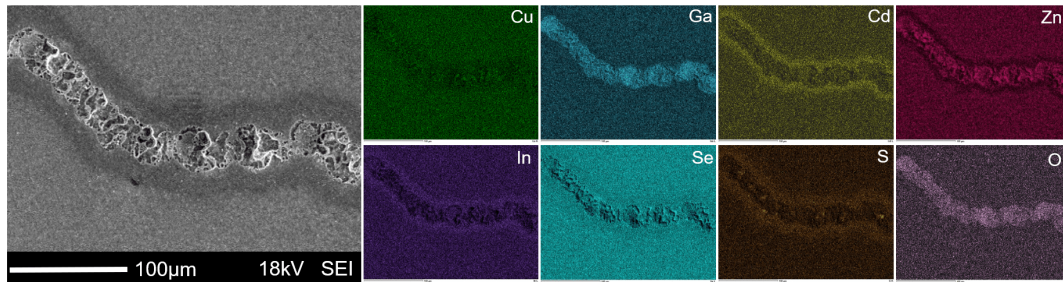


Figure 5.5: 18 kV SEM-EDS colour maps of elements at sample 1602_3C spot 1 showing a Ga rich worm-like defect with a Cd and S rich band around it.

the worm-like defect a dark band is observed. The colour maps reveal that inside the worm-like defect the Cu intensity is lower for 6 kV. This is not the case for 18 kV. The In at 6 kV shows a small visible band around the worm-like defect. For In the band is more clear at 18 kV. In also shows a lower intensity in the worm-like defect compared to bulk material. Ga has a high homogeneous intensity inside the worm-like defect for both accelerating voltages. The Se has areas of high and low intensity within the worm-like defect. A band of Cd around the worm is observed. The S intensity also shows a band around the worm-like defect. The S rich band appears to be wider compared with the Cd band. In the 18 kV measurement high intensity S spots are visible. The Zn shows an increased intensity inside the worm-like defect and a low intensity where the In, Cd and S have an increased intensity. An increased intensity of O is observed inside the worm-like defect for 6 and 18 kV. What is not clearly visible in Figure 5.4 and 5.5 is that the Cu, Ga and In have areas with high and low intensities inside the worm-like defect. Identical observations in mapping results for 1602_4B, 1602_4D and 1602_4H are found and are found in Appendix. D.

Inside the worm-like defects different intensities of elements appear. The band of Cd is broader compared to S around the worm-like defect. These two observations lead to more in-depth research investigating the area inside worm-like defects and the band around it by performing EDS point analysis. This is presented in the next Section.

The 18 kV spots of high intensity S are most likely Mo. Mo and S have overlapping signals in EDS (see Table 4.1). High S intensities are probably caused by higher accelerating voltages in combination with voids underneath the surface resulting in electrons reaching the Mo back contact. The overlap of Zn and Na makes it impossible to draw conclusions on the Zn intensity. It is not clear if Zn present in the AZO moved into the worm-like defect or if all the ZnO has been etched away and the signal is attributed only to Na. The In band in colour maps around the worm-like defect are not reflected by the In values in the EDS results giving rise to questions if the measurement is effected by the presence of K. The limited capabilities of the EDS analysis might be an overlap in signal. The Cd and In signal might be mixed up. From Table 4.1 the $I - \alpha$ ($= 3.286$ eV) is close to the Cd $I - \alpha$ ($= 3.133$ eV) and in Figure 5.4 both elements have a high intensity in the same areas. Guthrey et al. [81] observed similar images where In was on the same place as the Cd.

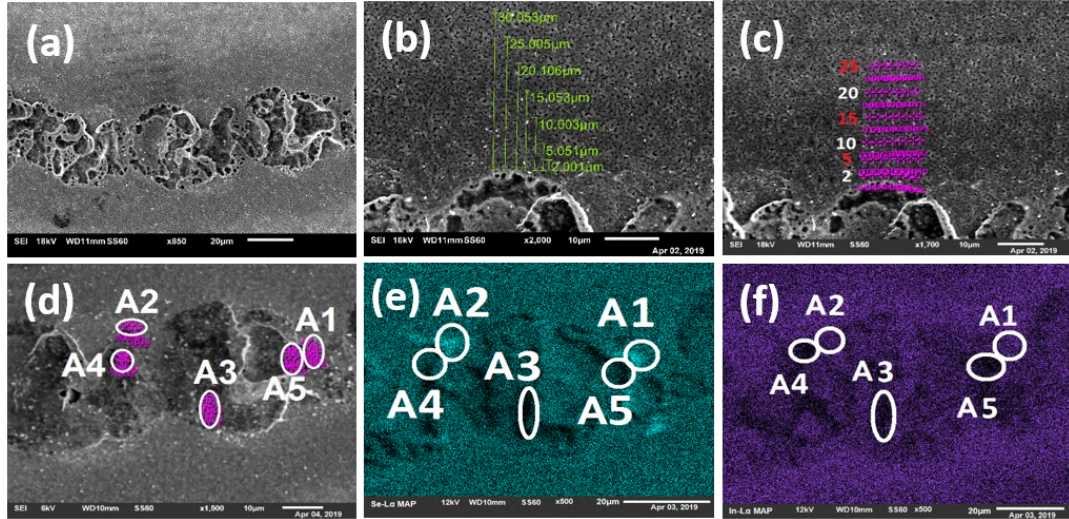


Figure 5.6: Overview of EDS measurement at sample 1602_3C spot 1. (a) SEI of measurement location, (b) measured distances from worm-like defect, (c) 8 points per specified distance from worm-like defect, (d) 8 points inside worm-like defects, (e) measured areas projected on Se colour map and (f) measured areas projected on In colour map.

The Cu intensity inside the worm-like defect area at low voltages is clearly visible. In colour maps at 18 kV intensity of Cu is less visible. The 18 kV colour maps use the Cu-K α shell instead of the L- α at 6 kV. It is possible the difference in Cu intensity inside the worm-like defect changes when changing from 6 to 18 kV. The absorption of the X-ray's within the sample are different for $k - \alpha$ and $l - \alpha$ waves. The Ga and O detected at the surface of the worm-like defect are comparable with EDS-mapping results from Eurofins (Figure 3.12) where Ga was found on the surface of the etched samples. The same holds for the Cd and S.

5.2.2. EDS point analysis

The EDS point analysis function of the SEM is not calibrated and values are not regarded as absolute composition. Nevertheless, the data provides useful details not visible in the colour map images. It is found individual element values between measuring points are deviating. Figure 5.4 and 5.5 show different intensities of Se, In, S and Cd in specific regions. The material is not homogeneous in the worm-like defect, shown in the cross-sectional view of Figure 3.9. Variation in measurements are therefore expected due to a combination of in-homogeneity and limited SEM capabilities. To reduce inaccuracy and reduce the effect of outliers 8 points at a specific distance from the worm-like defect or in specifically selected areas are measured. The specific distances at a location are measured from the edge of the worm. An SEI of sample 1602_3C spot 1 and the measured distances are shown in Figure 5.6(a) and (b). Measuring points are set at this distance shown in Figure 5.6(c). Inside the worm-like defect the maps are used to select specific measurement locations.

The results from the SEM-EDS point analysis at sample 1602_3C spot 1 with 6 kV is shown in Figure 5.7. **Outside the worm-like defect** the Cu, In, Ga and Se content decreases while the Cd and S content increases towards the defect. The element profiles outside the worm-like defect can be described as follows. Compared with bulk values the Cu content increases at 15 and 20 μm . Closer towards the worm-like defect the Cu value starts decreasing. The Se, In and Ga all start decreasing at a distance of 20 μm when moving towards the worm-like defect. The S content starts increasing at a distance of 20 μm while the Cd starts increasing from 15 μm . It is clear the CIGS content around the worm-like defect lowers as the CdS content around the worm increases.

In bulk measurements the GGI, CGI and Se/CIG at 6 kV is 0.32, 0.61 and 1.43. Where the values for GGI, CGI and Se/CIGS should be approximately 0.3, 0.8 and 1.1. This indicates the real values for Cu are expected to be higher and the values for Se to be lower.

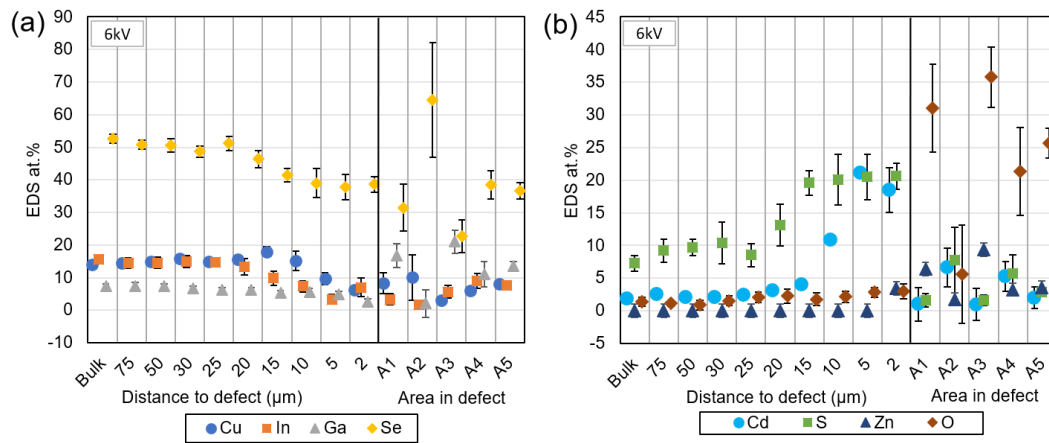


Figure 5.7: Graph with SEM-EDS results at sample 1602_3C spot 1 (a) Cu, In, Ga & Se and (b) Cd, S, Zn & O results with 6 kV. The black vertical line represents the border of the worm-like defect.

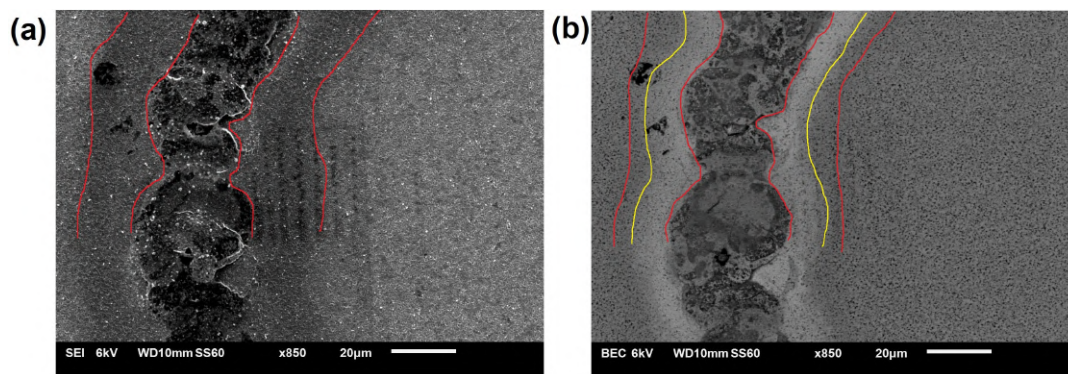


Figure 5.8: (a) SEI and (b) BEC image of sample 1602_3C spot 1 where the edge of the visible band in SEI is marked Red in both images. The additional visible band in the BEC image is drawn with yellow.

The difference in distance from the worm-like defect where Cd and S start increasing is noticeable. This resulted in a closer look on the different areas present in the darker band observed in Figures 5.4 and 5.5. The visible band around the worm-like defect is marked with red at the SEI presented in Figure 5.8(a). When projecting this band edge on the BEC image shown in Figure 5.8 it is found another line, represented with yellow, is visible. Also note the border between the worm-like defect and band is more clear for the BEC image.

The majority of results presented in this section are done at 6 kV experiments. In an 18 kV experiment more volume (width and depth of electron beam) is measured. The results are comparable but the added measured volume of CIGS below the worm-like defect results in less significant changes and variations. It is observed some areas inside the worm-like defect (e.g. at A3 and A4 in Figure 5.7) have a higher Cu content compared to the bulk material at 18 kV. At 6 kV Cu content is generally lower compared to bulk material. This is seen at all measurements inside worm-like defects on various samples presented in Appendix D.

It is possible to combine the the EDS results and the visual observations from SEI and BEC images. A projection of selected elements over an SEI and BEC image is shown in Figure 5.9. The value of Cu, In and Ga is combined. Figure 5.9 shows the dark band in the SEI concurs with the increase of S and decrease of Se. The observed white band in the BEC image concurs with the increase of Cd and decrease of Cu, In and Ga.

Inside the worm-like defect areas with high and low Se intensities from the colour maps are selected. Four out of five (all but A2) areas exhibit a higher Ga value compared to bulk material. The Se, Ga, O and Cu content show large deviations to measurements outside the worm-like defect. The standard deviation is represented by the error bar length in Figure 5.7. The deviation originates from differences between individual points. It is found for individual measurement points that a relatively high Ga content is accompanied with a relatively

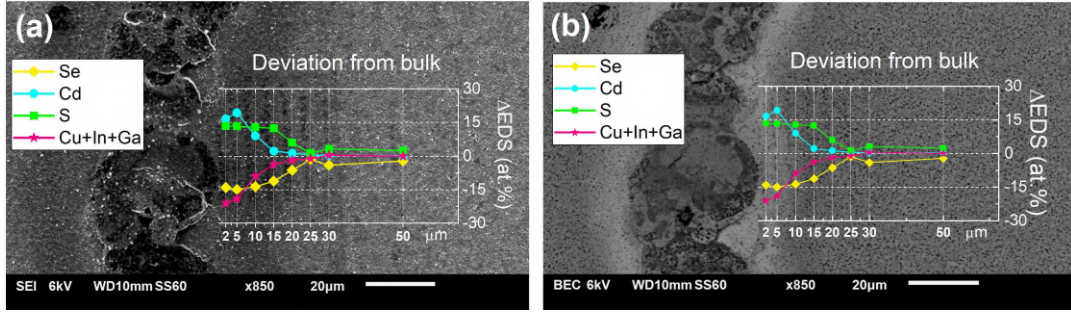


Figure 5.9: Sample 1602_3C spot 1 at 6 kV SEM-EDS results superimposed on a SEI and BEC image taken at 6 kV. The EDS results on the y axis are subtracted from the bulk measurements far away from the degraded area.

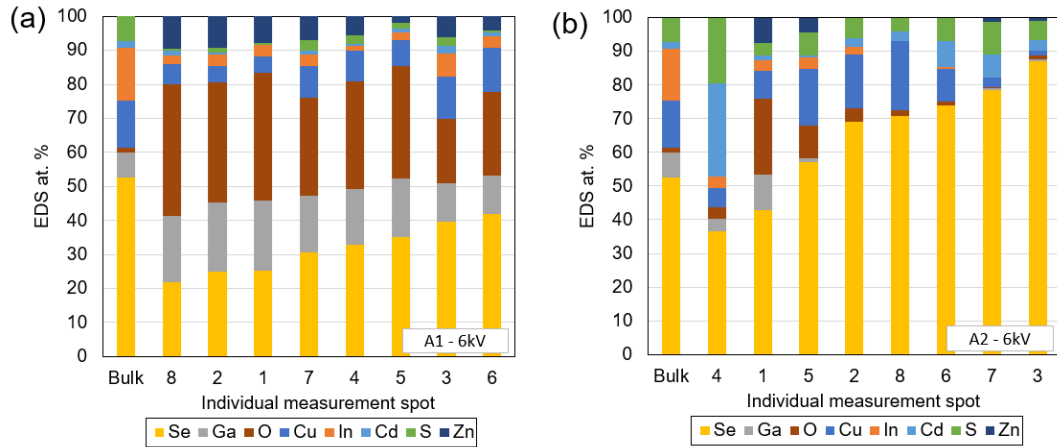


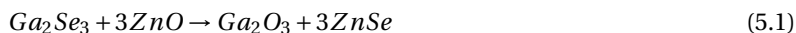
Figure 5.10: Individual SEM-EDS measurement points of sample 1602_3C spot 1 (a) A1 and (b) A2 at 6 kV sorted by increasing Se content showing that low Se content is accompanied with high Ga and O content

high O content. In addition, a low Se content is observed when the Ga and O content are relatively high. In lesser extent a relatively high Se content is accompanied by a higher Cu and lower Zn content. To visualise the this deviation the data of individual measurement points within a specific area were sorted on Se content and plotted in a bar graph. Figure 5.10 shows examples (sample 1602_3C spot 1 A1 and A2) where low Se content is accompanied with a high Ga and O content. This ratio in content between Se, O and Ga is observed inside worm-like defects of other samples and is found in Appendix D. An additional observation in these measurements is the disappearance of Indium. All the EDS measurements at both 6 and 18 kV show a decrease of In inside the worm-like defect. For the 18 kV the ratio between In content measured inside the worm-like defect divided by the In content measured in the bulk is larger.

5.2.3. Discussion on DS results

Note **outside the worm-like defect** at the distance from the worm-like defect where the S starts increasing the Se starts decreasing. Table 2.3 shows the crystal ionic radii of Cu^+ (91pm), In^{3+} (94pm), Ga^{3+} (76), Se^{2-} (184), S^{2-} (170) and Cd^{2+} (109) [56]. Looking only at the valance and atomic radii suggests the the S moves on the Se position in the crystal lattice due to the same valency and size. This suggestion is invigorated by Basol et al. [58] showing S diffuses into CIGS relatively easily and that the diffusion is positively correlated with the high Ga content at the surface. The atomic radius of Cd is larger compared with Cu, In and Ga. Cd does not share the same valence with Cu, In and Ga. This mismatch in valency makes it difficult for Cd to diffuse into the CIGS material at the lattice sites of Cu, In or Ga. The Cd moving into Cu sites is observed in other research [62–64]. The combination of result with findings from literature explains the wider observed band of S compared to Cd around the worm-like defect seen in Figures 5.4, 5.7 and 5.9. It is not clear from where or at what stage in the process the Cd and S come from.

Inside the worm-like defect two different areas with high and low Se content are observed. The areas with low Se content measured a high content of O, Ga content. Looking at the free energies of reactions ΔG from Table 2.5 the reaction with the lowest free energy is as follows:



The free energy of Reaction 5.1, ΔG , is $-141.7 \text{ kJ} \cdot \text{mol}^{-1}$ and is thermodynamically favourable. Presumably this reaction is happening during worm-like defect formation when the CIGS near the TCO is at elevated temperatures and Cu deficient as a result of electromigration. The observed Zn at the location where Ga and O content is measured is conform to this presumption. It cannot be determined in which stage of worm-like defect formation this mechanism is activated. In addition, the out diffusion of Ga into the CdS already happens at relatively temperatures [59, 65]. Besides the reaction Ga is also known to be very soluble in ZnO [60].

5.3. Summary

This paragraph contains a **summary** of SEM-EDS colour mapping and point analysis results. The maps of the Ga, Cd, S, O and Zn agree with the observations found in earlier experiments and literature in Sections 3.1 and 3.2. During worm-like defect formation and propagation Ga moves in the direction of the TCO. The Cu migrates towards the back contact but migration toward the TCO is also observed. Inside the worm-like defect area the In content is lower, but no areas with a high In content are observed. The S (in the band around the worm-like defect) is moving into the CIGS by taking the place of Se in the matrix. The Cd moves into the CIGS matrix at Cu, In or Ga positions. At individual measurements a relation between O and Ga is present. The high Ga and O content is accompanied with low Se and high Zn content.

Where possible the migration of elements is documented. XRD shows the CIGS material below the worm-like defect did not change significantly. Combining information from literature and recent research with the new findings presented in this chapter gives a thorough picture of element migration during worm-like defect formation. The next step is an experiment to gain more insight in the conditions and parameters required to cause the migration of these elements. The local conditions of worm-like defects are unknown due to the lateral conduction of the TCO.

6

Point probe experiment

In this chapter the reader is provided with the results of the point probe. The how and why of this experiment is found in Chapter 4. Mind that the samples are produced without AZO to prevent lateral conduction and possibly resistive heating in shunts. First, the results of the point probe experiment are presented. The maximum potential is applied to know the limitations of the experimental setup. A measurement scheme is set up in an attempt to couple different parameters to observations. The values of the measurement scheme are based on empirical determined local electrical properties. The results of the measurement scheme are presented. First, the observed features are analysed and categorised visually with Confocal Microscopy (CM), Scanning Electron Microscopy (SEM) and Optical Microscopy (OM). The observations are directly coupled to the applied conditions. The follow up of the observation is chemical analysis with Raman spectroscopy and EDS. As reference material worm-like defects induced on cells with an AZO are analysed. Differences and similarities between worm-like defects are presented. The results are discussed and a small summary of the chapter is given.

6.1. Experimental setup

This section presents the initial results with the experiment. With the initial result a measurement scheme is composed.

6.1.1. RB diode characteristics

Limitations of the experiment must be determined to create a measurement scheme within these limits. This is done by repetitive consecutive IV-sweeps from 0 to -9.75 V at different locations. An example of the IV-sweeps in RB at spot 6Q2 is shown in Figure 6.1. In the first 10 repetitions (moving from black to light green) the current increases every sweep. Initially the maximum current is $-10\text{ }\mu\text{A}$ while the current during the 58th sweep is almost $20\text{ }\mu\text{A}$. The initial maximum current of $1.1\text{ }\mu\text{A}$ at -9.75 V is reached at -8.9 V in the 10th repetition. The increase in current for a given potential with increasing sweep number is observed for all locations.

To check if experiments are reproducible a comparison between different spots is required. The RB IV-sweeps for five different spots are presented in Figure 6.2. In all cases the current increases with subsequent sweeps. The deviation between initial sweeps (\square) ranges from $-3\text{ }\mu\text{A}$ to $-12\text{ }\mu\text{A}$. A shift towards higher currents is observed for all samples. Note the 48th sweep of 8A2 (green - ∇). This behaviour is comparable with sudden increase in current in the creation of worm-like defects shown in Figure 3.8. It is observed in other experiments when the RB current is low, samples are more prone to worm-like defect formation. With help of electrical properties shown in Figure 6.2 the measurement scheme was composed. The Autolab has two modes: a potentiostatic or galvanostatic. The applied conditions (-5 to -9.5 V & -5 to $-15\text{ }\mu\text{A}$) of the measurement scheme are based on the values observed in Figure 6.2.

It is interesting to observe local electrical properties of the material enable very high voltages while staying intact. Worm-like defect formation in cells usually occur below a potential of -5 V while the local cell is able to withstand voltages up to -9 V .

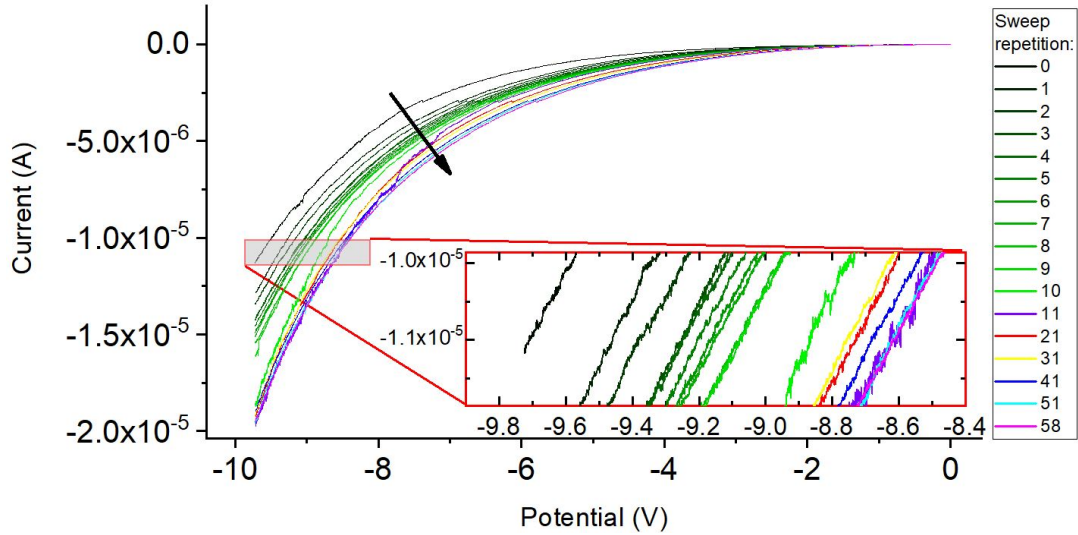


Figure 6.1: Reverse bias IV-curves at location 6Q2 for selected repetitions. The number in the legend corresponds to the n^{th} sweep.

6.1.2. Measurement scheme

The three variables in this experiment are time, RB potential and current. Table 6.1 shows the measurement scheme. The conditions in this measurement scheme are based on the data from the RB diode curves shown in Figure 6.2.

It must be said finding the features showed some difficulties as it was not known what to look for and the area was small. The features might be confused with dust particles or features present are not created by the applied conditions but were already present. Nevertheless, after searching and knowing what to look three different distinguishable features were observed:

- Single feature $> 15 \mu\text{m}$ in diameter with a ring around it
- Multiple features $< 15 \mu\text{m}$
- 'Stain' like features

Table 6.1: Measurement scheme with differences in potential (V), current (μA) and duration (h)

Measurement	Constant	set duration (h)	Spots*
M0	-9.5 V	4	7A3, 6B1, 6B2, 6B3, 8B1
M1	-9 V	4	6C1, 7C1, 8C1,
M2	-7 V	4	7C2, 8C2, 9C2
M3	-5 V	4	7C3, 8C3, 9C3
M4	-5 μA	4	6D2, 7D1, 8D1
M5	-15 μA	4	7D2, 7D3, 9D3
M6	-9 V	0.5, 1, 2, 1	6E1*, 6E2*, 6E3*, 7E1*
M7	-7 V	0.5, 1	7E2*, 7E3*
M8	-5 V	0.5, 1	8E1*, 8E2*
M9	-5 μA	0.5, 1	7F2*, 7F3*
M10	-15 μA	0.5, 1	8F1*, 8F2*

* The first mentioned experiment duration matches the first mentioned spot. The second duration matches the second spot and so on.

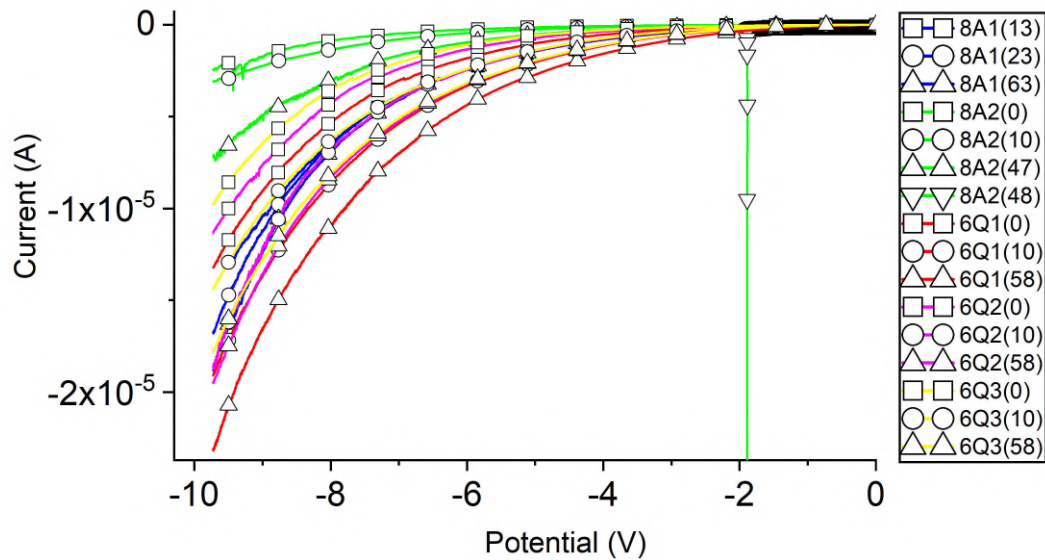


Figure 6.2: Change in RB IV-curves at multiple locations after n repetitions. Where the number between brackets in the legend correspond to the n^{th} sweep

Every feature has its own 'fingerprint' as occasionally all three features are observed at a specific spot making it hard to distinguish them from each other. In the next section the applied conditions are coupled with the observed features by giving one example. To prevent confusion and get an ambiguous report **different features are named as follows**:

- Locally induced features $> 15 \mu\text{m}$ = **nugget**
- Locally induced multiple features $< 15 \mu\text{m}$ = **seeds**
- Locally induced 'Stain' like features = stains or **stain-like features**
- Defects formed with AZO on regular cell = **worm-like defect**

6.2. General observation: applied conditions, SEM, OM and CM

Before the features are presented an introduction to the experiment and graphs is required. A potentiostatic experiments consists of two parts: an initial potential sweep with steps of 0.02 V from 0 to e.g. -7 V and a part where a constant voltage (CV) is applied. In both parts the current as a result of the applied potential is measured. A galvanostatic experiment also consists of two parts: an initial current sweep with steps of $0.05 \mu\text{A}$ from 0 to e.g. $-15 \mu\text{A}$ and a part where a Constant Current (CC) is applied. In this case the potential required to apply the desired current is measured. The applied electrical condition are represented in two graphs. **The first graph** is an IV-sweep similar to curves shown in Figure 6.2. **The second graph** shows the voltage versus time for the CC experiment. In the case of a CV experiment this graph shows the current versus time. The constant condition is mentioned in the legend of the graph. In the next part of this chapter the observations will be presented in the following order:

- Visual observation in OM, SEM and CM.
- Coupling features with applied condition.

6.2.1. Features $> 15 \mu\text{m}$ (nuggets)

The **Visual observation** of a feature bigger than $15 \mu\text{m}$ is shown in Figures 6.3, 6.4 and 6.5. The first big feature observed at spot 6B1 appeared gold in optical microscopy. This images are found in Appendix E and from now on called nuggets.

Now attending another nugget at spot 8C1. Looking at the optical image shown in Figure 6.3 a light blue ring is observed with 3 black spots in it. The biggest black spot is in the centre of the light blue ring. The SEI, shown in Figure 6.4, reveals additional observations. It appears as if a small eruption of material from underneath the i-ZnO occurred. Around the central feature smaller dots appear and one of the black parts from Figure

6.3 appears to be a crater. The ring observed in OM is also observed in the SEI when looking closely to Figure 6.4. In the BEC image, shown in Figure 6.5, the nugget and crater appear darker and no ring is observed. The small dots from the SEI appear as dark spots.

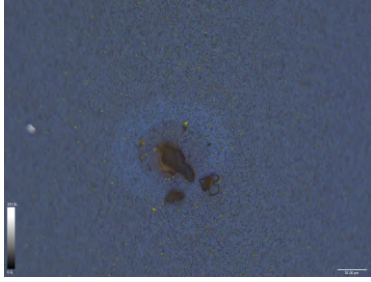


Figure 6.3: Optical microscopy image (50x) at spot 8C1 showing a nugget.

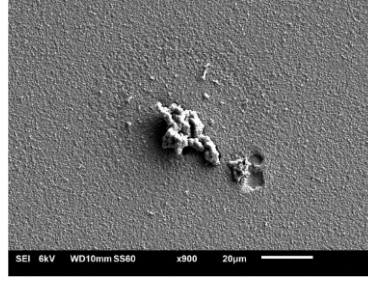


Figure 6.4: 6 kV SEM SEI (300x) at spot 8C1 showing a nugget.

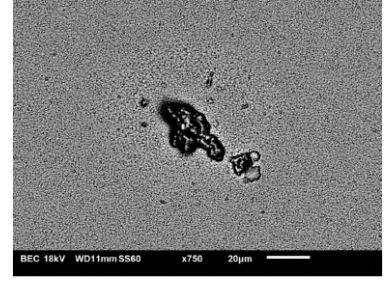


Figure 6.5: 6 kV SEM BEC image (750x) at spot 8C1 showing a nugget.

The **confocal microscope** is used to assess the size and height of the features observed. The observation of 2D images from Figures 6.3, 6.4 and 6.5 appear as if material 'erupted' from the sample but this does not necessarily has to be the case. The height profile graph of a nugget and crater is shown in Figure 6.6(a). This x-axis in the graph is a representation of the line drawn vertically over the defect shown in Figure 6.6(b). The nugget is over $30\ \mu\text{m}$ wide and over $4\ \mu\text{m}$ in height.

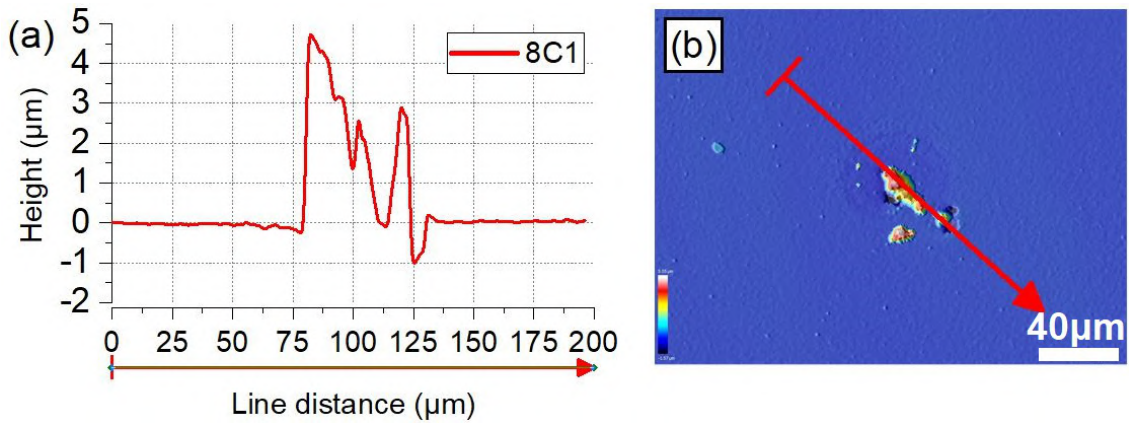


Figure 6.6: Confocal microscopy results at spot 8C1 with (a) a height profile of the defect and (b) a contour map where the annotated arrow reflects the x-axis of (a).

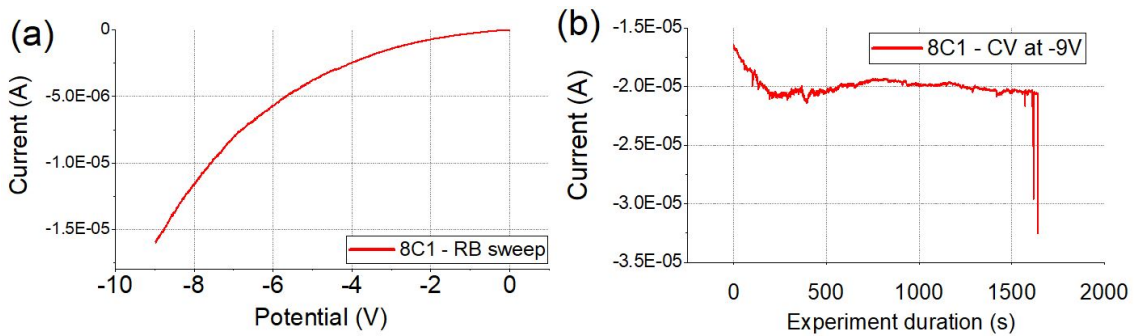


Figure 6.7: Applied conditions during the experiment at spot 8C1 with (a) an IV-sweep from 0 to -9 V and (b) the current as a result of the constant applied potential versus time.

The **applied condition** responsible for creation of features at spot 8C1 is shown in Figure 6.7. Figure 6.7(a) shows the IV-sweep curve and Figure 6.7(b) shows the measured current for constant applied potential versus time. The IV-sweep is a smooth line up to $-15 \mu A$ at $-9 V$. In the CV part current increases from $-15 \mu A$ to $-20 \mu A$ in the first 500s. At this point the current remains approximately $-20 \mu A$ when it suddenly increases after 1600 s when the current limit of $30 \mu A$ and the experiment is stopped.

Correlations between features and applied condition are found. Nuggets only appear if the constant current suddenly increases to the set limit at $-30 \mu A$. If one regards the sudden increase in current as the creation of the nugget the following is observed. Looking at the measurement scheme, nuggets appeared at the following spots: 6B1, 6B2, 6B3, 8B1 and 8C1. Table 6.2 summarises the conditions **prior to** the sudden increase in current. On locations where nuggets are observed the potential applied was $-9 V$ or higher. The current prior to the sudden increase was the lowest for 6B3 at $-8 \mu A$. Averaging all the currents measures prior to the sudden current increase results in $-20 \mu A$. This value is only used to get a general idea and not usable as the contact area is unknown. No relation between the time where the current limit is reached and the current prior to the blow up is found. For all the CV samples where nuggets formed it is found current always increases over time with a constant applied potential. For the CV experiment at spot 8C1 the current increases over time for a constant potential. According to Ohm's law (resistance = voltage/current), the resistance of the material must decrease as the current increases for a constant potential.

6.2.2. Features < $15 \mu m$ (Seeds)

In the second case the **visual observation** features dots smaller than $15 \mu m$. They appear in multiple numbers in OM and SEM images. They are called seeds as they appear like seeds popping up in a field. Spot 7C1 is selected as example where the OM and SEM are shown in Figures 6.8 and 6.9. Figure 6.8 shows white and dark spots. The SEM shows multiple black seeds smaller than $15 \mu m$. When comparing the OM image with the SEM images shown in Figure 6.9 and 6.8 the dark spots are observed as small dots and nothing is seen at the location of the white spots. The seeds observed are probably formed around point probe. When zooming in more on the seeds differences in shape and size are present.

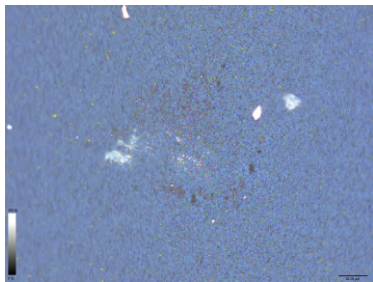


Figure 6.8: Optical microscopy image (50x) at spot 7C1 showing seeds.

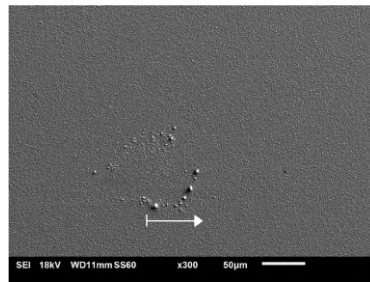


Figure 6.9: 6 kV SEM SEI (300x) at spot 7C1 showing seeds. The drawn white arrow corresponds to the white arrow in Figure 6.10

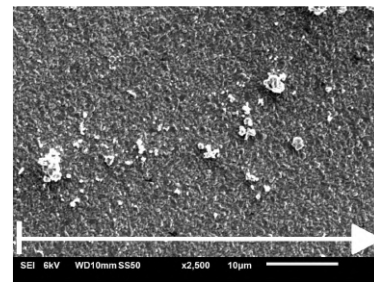


Figure 6.10: 6 kV SEM SEI (2500x) at spot 7C1 showing seeds. The drawn white arrow corresponds to the white arrow in Figure 6.9.

The result of the **CM analysis** is shown in Figure 6.11. Over 25 small dots with a height in the range of 0.5 - $1.0 \mu m$ are observed. The white parts seen in the OM are not visible in the SEM images but are visible in the CM. Their profile shows a height of over $1.0 \mu m$. The white parts in OM are different from the seeds as they do not show up under the SEM but do in CM.

Table 6.2: Table with the conditions before the current limit is reached.

Spot	6B1	6B2	6B3	8B1	8C1
Experiment type	CV	CV	CV	CV	CV
time of reaching current limit (s)	2200	12000	6500	6	1700
Average current before feature formation (μA)	-18	-25	-8	-28	-20
Applied potential (V)	-9.5	-9.5	-9.5	-9.5	-9
Nugget diameter x height (μm)	30 x 1.8	40 x 0.2	20 x 1.2	30 x 1.6	30 x 4

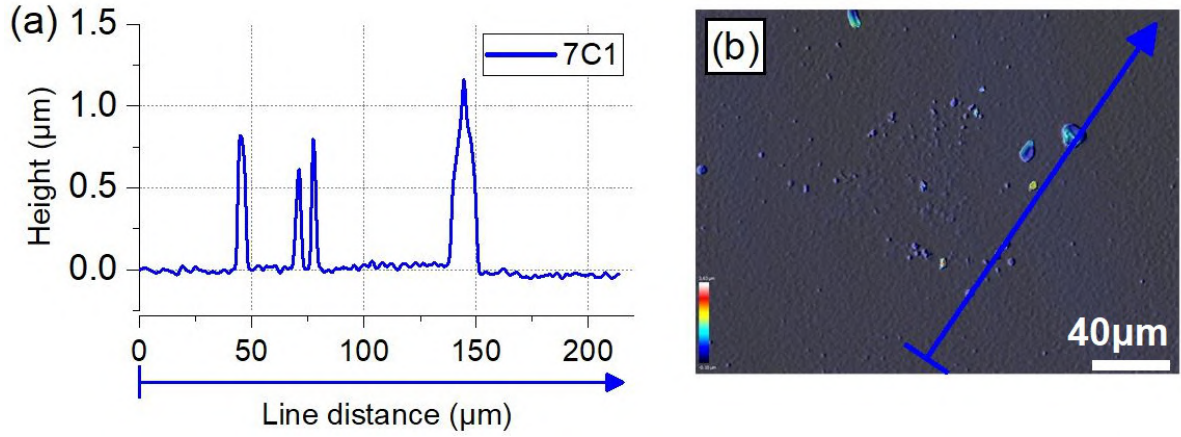


Figure 6.11: Confocal microscopy results at spot 7C1 with (a) a height profile and (b) a contour map where the annotated arrow reflects the x-axis of (a).

The corresponding **applied** conditions for spot 7C1 are shown in Figure 6.12. The initial IV-sweep is the shape expected for a diode in RB. During the first 1000s of the CV part the current increases from $-5 \mu A$ to $-15 \mu A$. After this peak the current decreases again and stays around $-10 \mu A$. In the case of seeds decreasing resistance (by an increase in current for the same potential over time) is observed. This is similar compared to the conditions present when nuggets are observed. The peak around 12000s is caused by a person bumping the table of the setup.

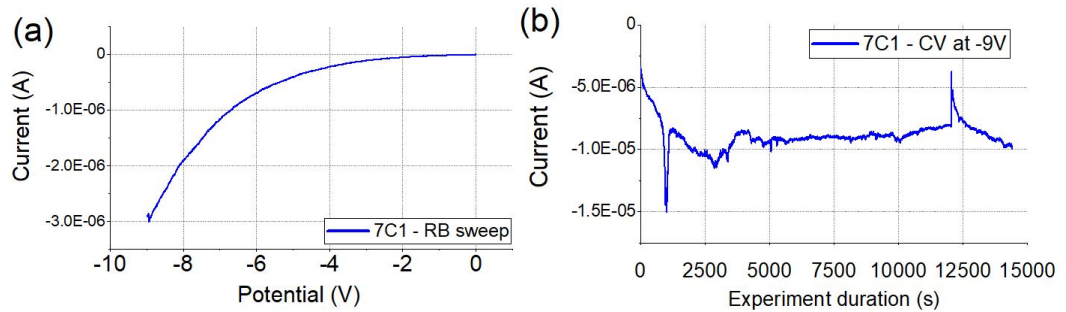


Figure 6.12: Applied conditions during the experiment at spot 7C1 with (a) an IV-sweep from 0 to $-9 V$ and (b) the current as a result of the constant applied potential versus time.

Unfortunately, it is not possible to assign spikes in voltage or current to an individual seed. Table 6.3 is constructed to look into general **correlations** between the seeds and the applied condition. It contains details about the spots where seeds are observed. It is observed seeds appear in the same voltage range as the nuggets. The current applied is in the range between -4.5 and $-15 \mu A$. The average of the maximum current when seeds are observed is $-9.3 \mu A$. Mind again this value is used to get a general idea and not useful as such due to an unknown contact area of individual spots. This is significantly lower compared to the average condition before reaching the current limit $-20 \mu A$ at the nuggets. It shows a minimal current has to be present to initiate nugget formation. In the previous case it was useful to look at the average current prior to the sudden current increase. This sudden increase in current is observed at locations where a nugget formed. Averaging the current has no added value on spots where seeds are observed as they are likely formed when spikes in current occur. It is still relevant to know what the local conditions during the CV or CC part. For that reason the maximum current and potential during the CV and CC are put in Table 6.3. It is noticeable in CV experiments the size of seeds decrease with increasing current spikes (or max current). One can argue that the time of the experiment plays a role in the size of the seeds. However, the nuggets were larger in the experiments with short duration and it appears no correlation is present between the time and seeds dimensions.

Table 6.3: Applied conditions on spots where defects < 15 μm are observed

Spot	6C1	6E1	6E2	6E3	7C1	7E2	8F1	8F2
Experiment	CV	CV	CV	CV	CV	CV	CC	CC
Duration (h)	4	0.5	1	2	4	0.5	1	0.5
Max. potential (V)	-9	-9	-9	-9	-9	-7	-10	-10
Max. current (μA)	-8	-8	-4.5	-4.5	-14	-5.5	-15	-15
largest spike (ΔI)	-4	-4	-0.5	-0.5	-6	-0.2	n.a.	-n.a.
largest spike (ΔV)	n.a.	n.a.	n.a.	n.a.	n.a.	n.a.	-1.2	-0.8
Largest seed diameter (μm)	3.5	7	14	13	4.5	10	14	11

6.2.3. Stain-like features

An example of the third presented feature observed is shown in the OM image of Figure 6.13. This defect appears as a group of discrete individual islands of light grey the OM. In Figure 6.14 light grey spots appear dark in SEI at 6 kV almost like coffee stains on a white piece of paper. This is why they are now referred to as stains or stain-like features. The discrete grey spots overlap more in the SEI compared to the OM image. At 18 kV (shown in Appendix E) the stains are less visible and the diameter of the spots is only 5 μm compared to a diameter over 15 μm . The BEC image at 6 kV shown in Figure 6.15 shows the discrete steps like the SEI and OM image. However, in the BEC image the discrete islands have a dark centre with a grey band around it. Darker areas in a BEC image reflects the presence of heavier elements. The difference in size between 6 and 18 kV indicates the change in material is near measured surface.

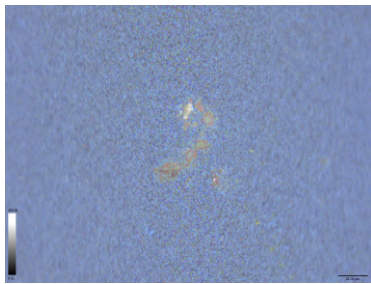


Figure 6.13: Optical microscopy (50x) image of spot

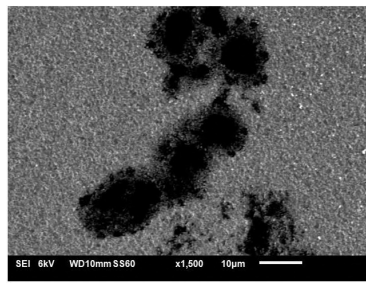


Figure 6.14: 6 kV SEM SEI (1500x) at spot 9C3 showing stains.

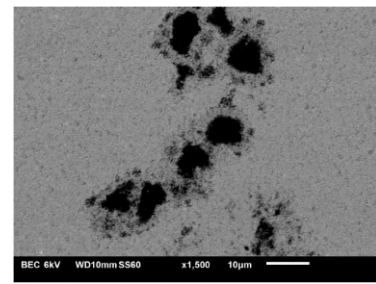


Figure 6.15: 6 kV SEM BEC image at spot 9C3 showing a stains.

The result of the **CM analysis** is shown in Figure 6.16. The discrete islands have a height in the range of 0.1-0.3 μm and are approximately 10 μm wide. Not shown in the profile is the height the dark part below the line in Figure 6.16(b). This is a hole of 0.1 μm deep.

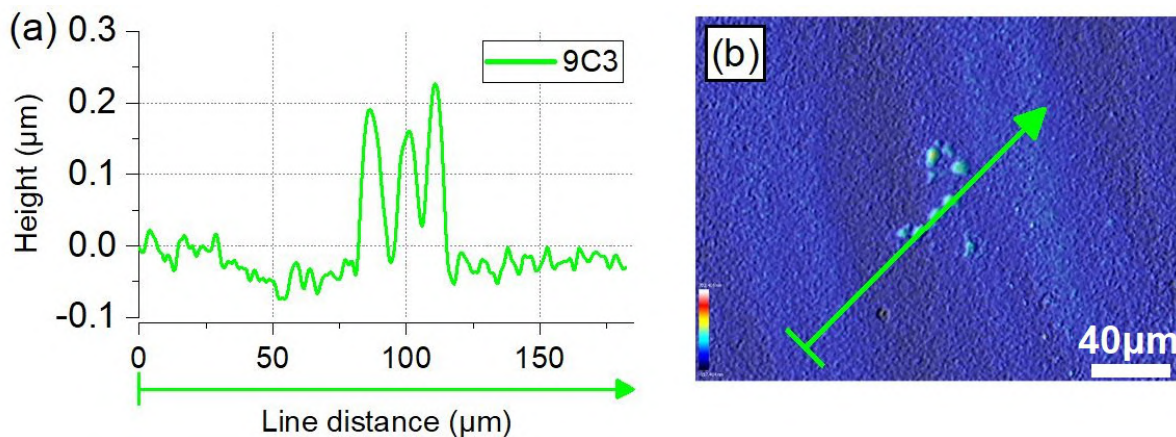


Figure 6.16: Confocal microscopy at spot 9C3 with (a) a height profile and (b) a contour map where the annotated arrow reflects the x-axis of (a).

The electrical properties during the sweep and current during the CV part of the experiment is shown in Figure 6.17. The first interesting observation is a higher current of $-9 \mu A$ at $-5 V$ compared to the currents of approximately $-5 \mu A$ at $-5 V$ in applied conditions for nuggets and seeds in Figures 6.7(a) and 6.12(a). The applied conditions during the CV experiment are shown in Figure 6.17(b). Initially the current shows some spikes in current. In the first 42 minutes (2500 s) the current decreases to $-8 \mu A$. This behaviour is observed in all stain-like features. The decrease in current means an increasing resistance. This is in contrast with the two other type of features (nuggets and seeds) presented earlier where the resistance decreased.

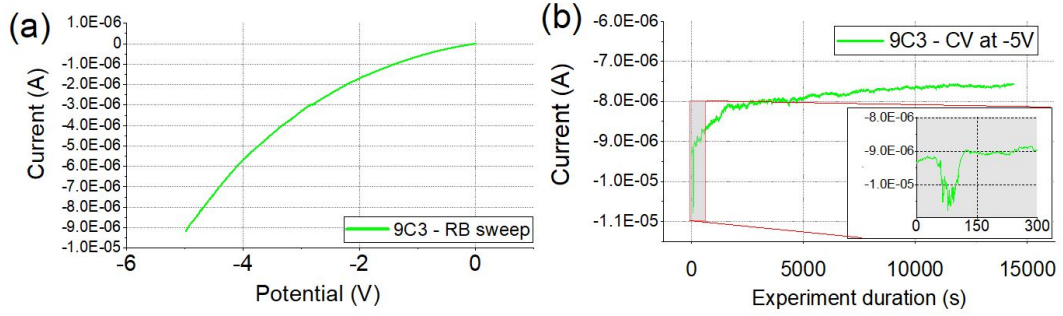


Figure 6.17: Applied conditions during the experiment at spot 9C3 with (a) an IV-sweep from 0 to $-5 V$ and (b) the current as a result of the constant applied potential versus time.

To **correlate** observations with the applied conditions a overview with the samples with stains is constructed in Table 6.4. Most of these stain-like features were formed around $-5 V$. This is significantly lower than the earlier presented features (nuggets and seeds). It is interesting to see while the applied potential is lower, the current is in approximately the same range as the seeds. Meaning that in some cases more power (current * potential) does not automatically leads to the same feature. This shows the potential plays a role in the type of feature formed.

Table 6.4: Applied conditions on spots where stain-like features are observed

Spot	6D2	7C3	7E3	8C3	8E2	9C3
Experiment	CC	CV	CV	CV	CV	CV
Duration (h)	4	4	1	4	0.5	4
Max potential (V)	-5.4	-5	-7	-5	-5	-5
Max current μA	-5	-13	-2	-8.5	-0.5	-11

6.3. Raman

This section contains the Raman spectroscopy results for the three features described in the previous section. The results start with the bulk signal observed in the CIGS. After the Bulk signal Raman spectroscopy results for the three observed features are presented. In addition to the three observed features other interesting observations are presented.

Bulk CIGS

The reference measurement on the bulk is presented in Figure 6.18. In this graph the main observed peak around 178 cm^{-1} is attributed to the CIGS A1 [83]. Three additional peaks are observed. The peaks at 222 and 260 cm^{-1} are attributed to the CIGS B2/E [83]. The peak at 302 cm^{-1} is the CdS peak [84]. This signal is what is expected for CIGS and CdS with a low Cd content. It confirms the accident with the Cd deposition as it shows a low intensity Cd peak when using the green laser. If Cd would be deposited correctly it would give a higher intensity as shown in Figure 3.14.

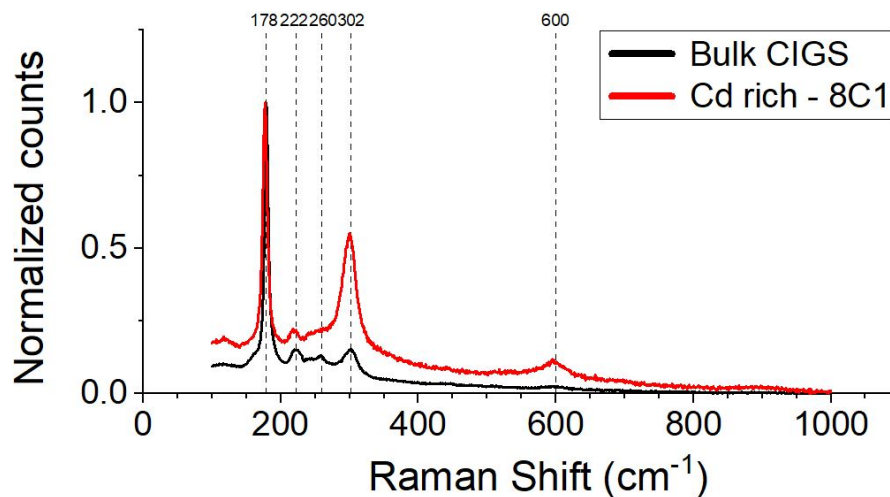


Figure 6.18: Bulk measurement with green laser on sample without AZO with indications on the observed peaks.

In addition to bulk CIGS results Figure 6.18 also shows the curve of a Cd rich signal at 8C1. It is generally found when the CdS peak around 300 cm^{-1} increases compared to the CIGS A1 peak a small peak at 600 cm^{-1} is also observed. In the following graphs this 600 cm^{-1} is left out of the graph but it can be assumed if an intense CdS peak at 300 cm^{-1} a minor peak at 600 cm^{-1} is also present but not shown. This representation increases the details visible between 100 and 400 cm^{-1} .

Stains

This paragraph contains the Raman spectroscopy results observed at the stains shown in Figures 6.13, 6.14 and 6.16. The results of the measurement on the stains are shown in Figure 6.19. In this graph it is observed no changes are present in the Raman signal compared to the bulk material. The same peaks are observed as in the bulk results presented in Figure 6.18. This indicates the features are present at the surface and no change in the CIGS is present. A change in the i-ZnO might not be detected with Raman spectroscopy as the ZnO is transparent for the laser. This indicates subtle changes are present for this feature.

Seeds

When analysing Raman spectroscopy results in Figure 6.20 it is observed the curves exhibit an increase in intensity between 200 and 300 cm^{-1} at the white parts where small seeds are present. The white parts observed in the OM image shown in Figure 6.20(a) at 0 and 44 exhibit the largest deviation from the bulk. This increase is an increase of the 222 , 260 and 300 cm^{-1} . The increase of these peaks is observed in other cases where the white part on the CIGS was observed. The white parts are the places where small seeds are observed. This is seen in the white part with the SEM image shown in Figure 6.9 when knowing the black parts on the bottom are the larger seeds in the SEM image. Unfortunately no Raman measurement was done on the black spots. The increase in intensity of the B2/E peak at 222 and 260 cm^{-1} was also observed on the worm-like defects (results in Figure 3.15)[92]. This increase is attributed to Ga-Se and In-Se atomic bonds [93, 94]. This is important as this shows mechanisms present while inducing these features locally are similar to those in worm-like defect formation.

Nugget

The Raman spectroscopy of a nugget is shown in Figure 6.21. All the curves overlap except the measured spectrum on the nugget (0). The expected CIGS peak in the bulk (at $200\text{ }\mu\text{m}$) is present at 178.8 cm^{-1} . The main peak is shifted to 177 at the nugget ($0\text{ }\mu\text{m}$). This behaviour is also observed in Section 3.2.3 and attributed to a decrease of Ga or increase of Cu [90, 91]. The peak around 302 cm^{-1} increased in intensity. This is attributed to a Cd or S bond [83]. The results are normalised to compare the peak ratio. The additional observed peak at 600 cm^{-1} is attributed to a Cd bond [84]. It is interesting to note the feature is erupted from underneath the i-ZnO layer, verified with CM measurements shown in Figure 6.6, but still exhibits peaks from CIGS. This strong CIGS signal is a big difference with worm-like defects. In the case of worm-like defects the main CIGS A1 peak disappears and peaks around 260 cm^{-1} are observed (see Figure 3.15(c)).

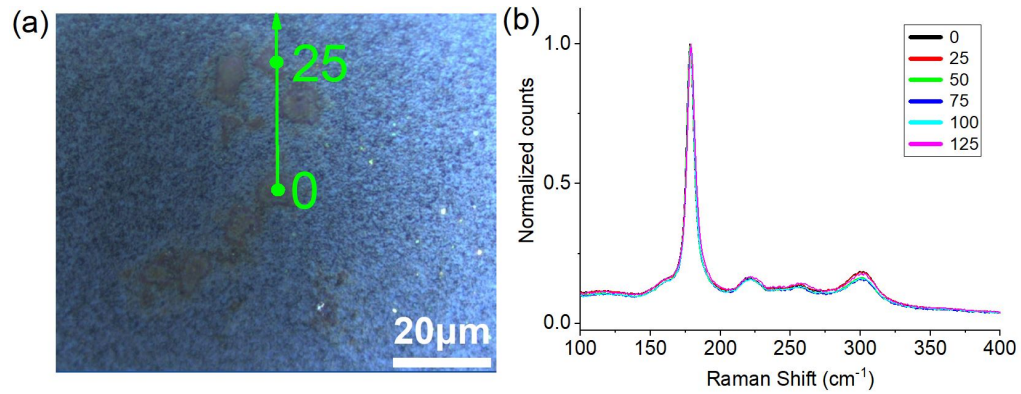


Figure 6.19: Raman spectroscopy results at spot 9C3 (stains) with (a) an OM image representing the direction of the measurement and (b) a graph showing the normalised Raman shift were the number in the legend represents the distance from the origin in μm in the direction of the arrow depicted in (a).

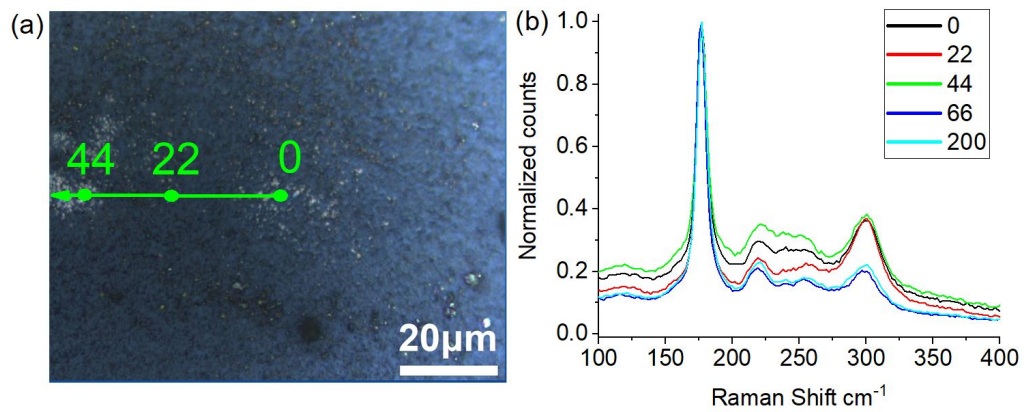


Figure 6.20: Raman spectroscopy results at spot 7C1 (seeds) with (a) an OM image representing the direction of the measurement and (b) a graph showing the normalised Raman shift were the number in the legend represents the distance from the origin in μm in the direction of the arrow depicted in (a).

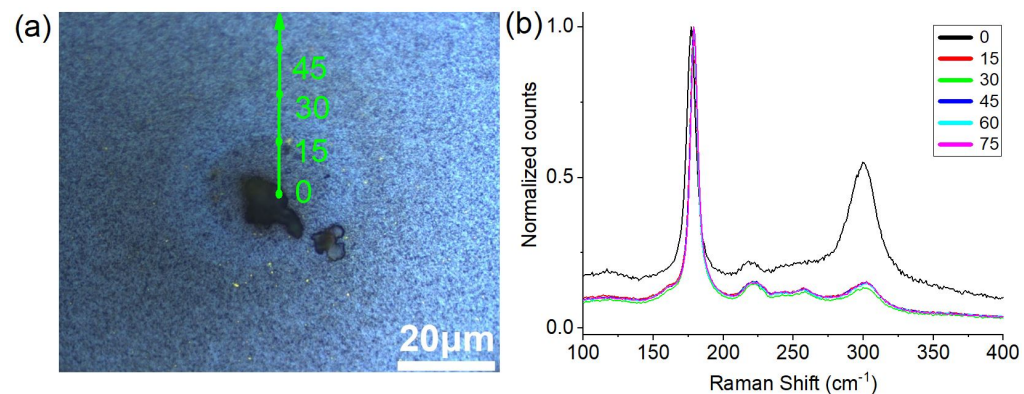


Figure 6.21: Raman spectroscopy results at spot 8C1 (nugget) with (a) an OM image representing the direction of the measurement and (b) a graph showing the normalised Raman shift were the number in the legend represents the distance from the origin in μm in the direction of the arrow depicted in (a).

6.4. EDS

This section contains the EDS analysis of the three examples features presented in previous sections. The EDS analysis at the features is done 18 kV. The signal of CdS (if Cd is present) and CIGS were to low at 6 kV due to the limited penetration depth and the presence of the i-ZnO. In the case of a **stain** the measurement was focused on one dark spot. The results are shown in Figure 6.22 where at the stains the O content increases. The Cu, In, Ga and Se all decrease in content when measuring on the stain (A2 and A3 in Figure 6.22). Combining this with the Raman results from Figure 6.19 indicates a material change of the i-ZnO. The balance between Cu, In, Ga and Se is as expected for CIGS material.

The EDS measurement for the **seeds** at 7C1 are shown in Figure 6.23. From this image the same increase in O content as observed in stain features is observed. The measurement on biggest seed (A5) shows less O and Zn content while the Se and Ga values increase. The Cu and In content in the nugget stays constant.

The EDS result on the **nugget** at spot 8C1 is shown in Figure 6.24. Between the bulk and A1 no changes in content are observed. On the nugget and in the crater (A2 and A3) the values are deviating compared to worm-like defects. Mind that fluctuating content in EDS was also observed in worm-like defects (Figure 5.7. The large deviation in the A2 values is caused by one measurement having a large S content.

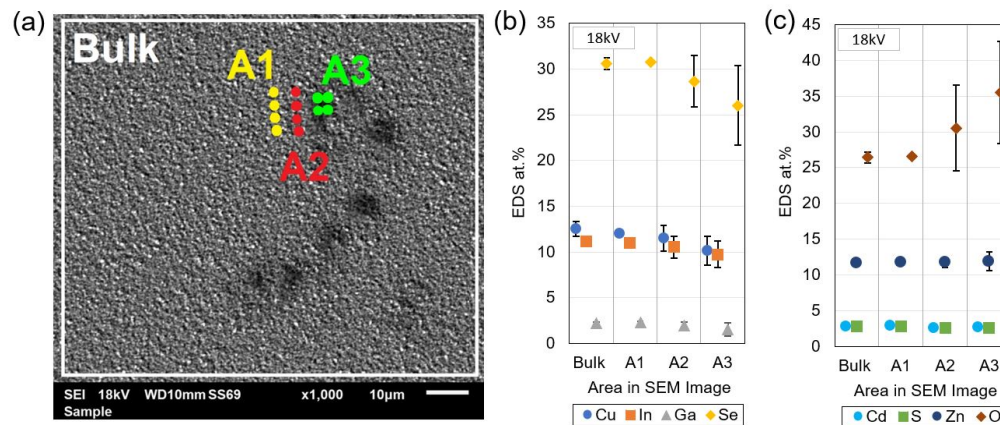


Figure 6.22: SEM-EDS results of stains at spot 9C3 with (a) the notation of the measured locations on a SEI in (b) the EDS results for the different areas.

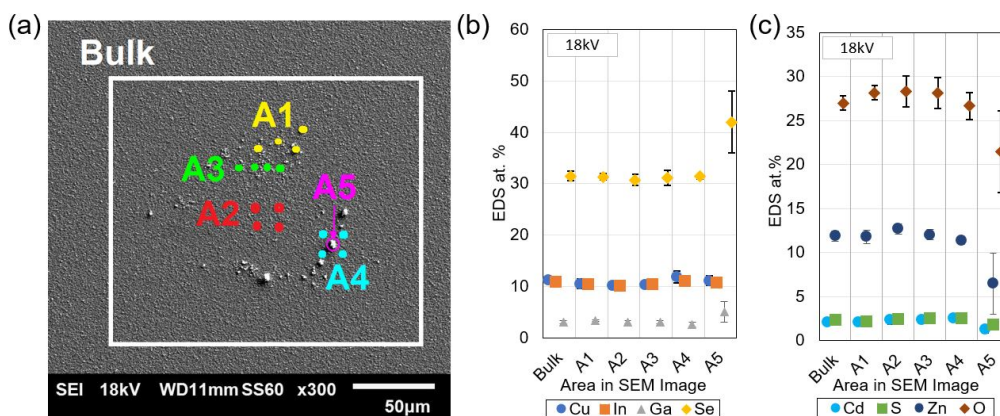


Figure 6.23: SEM-EDS results of seeds at spot 7C1 with (a) the notation of the measured locations on a SEI in (b) the EDS results for the different areas.

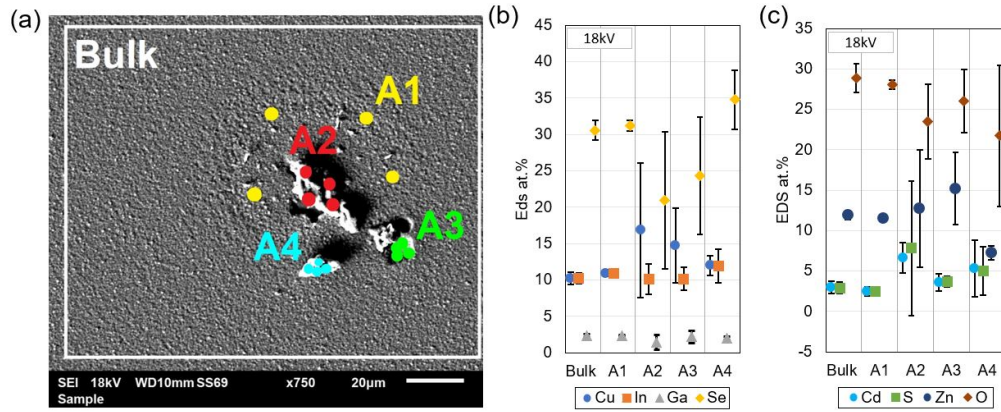


Figure 6.24: SEM-EDS results of the nugget at 8C1 with (a) the notation of the measured location on a SEI and (b) the EDS results for the different areas

In addition to the three defect categories presented, some unique observation are presented. At spot 6B1 the SEM-EDS results after etching showed features also observed in worm-like defects in Chapter 5. The results of 6B1 SEM-EDS results are presented in 6.25. First note the light ring around the big nugget. This nugget looks more solid (less porous) compared to the nugget at 8C1 presented earlier. The EDS results show the bulk does not contain Cd, while the white ring in the BEC image is Cd rich. The white ring with Cd is also seen in EDS on worm-like defects in Figure 5.7. The nugget itself shows an increase in Cd and S compared to the bulk. The deviation for CIGS material are a clear decrease in Cu and Cu. In and Ga do not show large deviation in all areas. The conditions when forming this feature can be found in Table 6.2. Comparing the two nuggets also show similarities. Although measured at 18 kV the nugget at 8C1 the In and Ga values are similar compared to bulk measurements.

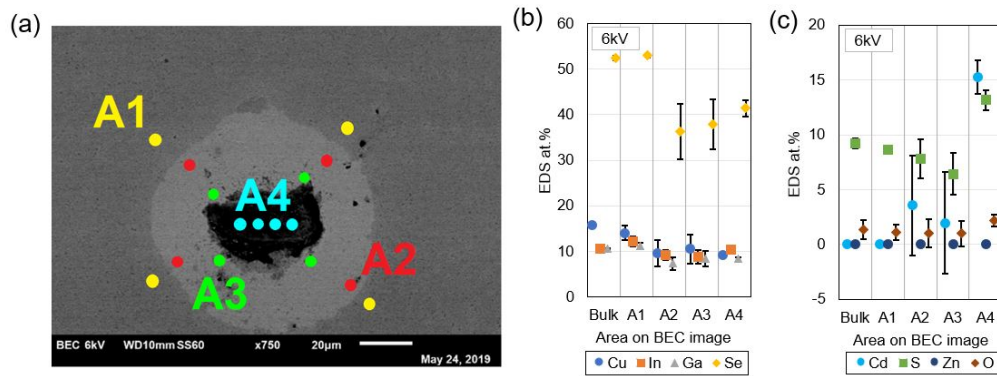


Figure 6.25: SEM-EDS results after etch of the nugget at spot 6B1 with (a) the notation of the measured locations on a SEI in (b) the EDS results for the different areas.

6.5. Samples with AZO

As a reference for the local features worm-like defects are induced on the sample with AZO. The cells have efficiencies in the range from 9.4 to 14.3%. Averaging 11.6%. This low efficiency is due to a low Cd content in the CdS layer. For more information on the production of the cells see Section 4.1. The cells have a open circuit voltage of 0.64 V. The short circuit current is between 28.0 and 34.8 mA. On the sample with AZO 30 worm-like defects were induced. The breakdown potential of the cells is evenly spread between -2.78 and -5.88 V. Figure 6.26 shows an example of the worm-like defects formed. The normalised Raman results from 6.26(c) show an increase in the peak 300 and 600 cm^{-1} . The 300 cm^{-1} peak is attributed to CdS and the 600 cm^{-1} is attributed to Cd [83].

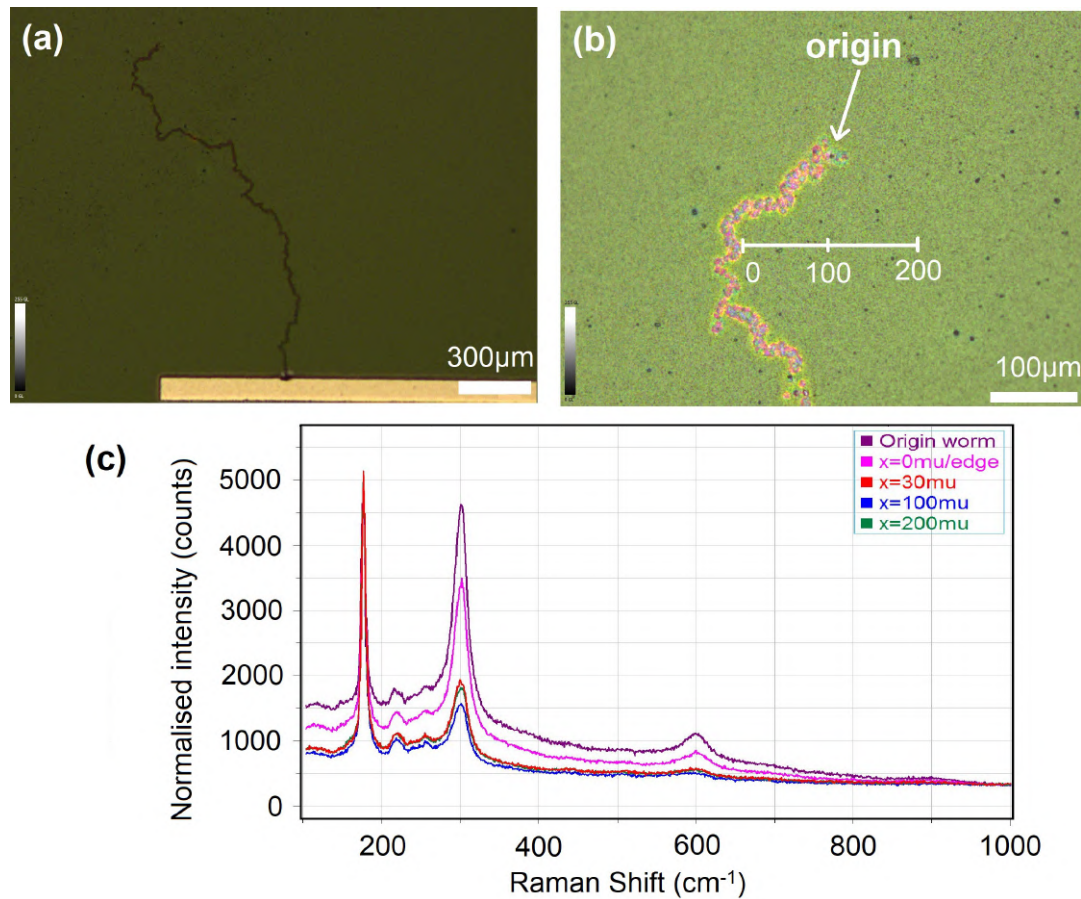


Figure 6.26: Worm-like defect analysis at cell 3B with (a) an optical microscope image (5x) and (b) an optical microscope image (20X with annotations for (c) the normalised Raman spectroscopy results. The Raman spectroscopy results are plotted with an offset for individual curves to be distinguished.

The CM measurements on the worm-like defect at cell 3B is shown in Figure 6.27. The height of the worm-like defects is in the range of 0.5-1.0 μm . The distance between the discrete steps is approximately 15 μm .

6.6. Discussion of results

During the experiments the sample was pushed to an extreme situation. A current of 15 μA on an estimated contact area of a 50 μm diameter circle gives a current density of $0.19 \text{ A} \cdot \text{cm}^{-2}$. The current density during normal cell operation of CIGS thin-film solar cells is approximately $0.025 \text{ A} \cdot \text{cm}^{-2}$. This means the current density locally is a factor 7.6 higher. When a circle with 10 μm diameter is used the current density is 191 times higher. For the set current limit at 30 μA , and thus during the creation of nuggets these factors would double.

Differences and similarities between features and worm-like defects are present. Inducing nuggets or seeds requires higher potential compared with worm-like defect formation. The lack of a shunt might be the explanation for this. In models and experiments shunts heat up as they attract current [45, 81]. When no shunt is present below the probe the local temperature does not increase as much as it does during worm-like defect formation. As migration mechanisms are heavily influenced by temperature the lack of a shunt increases the resilience of the local cell to mechanisms involved in worm-like defect formation. The data from this experiment suggest a better control of temperature is present compared to worm-like defects.

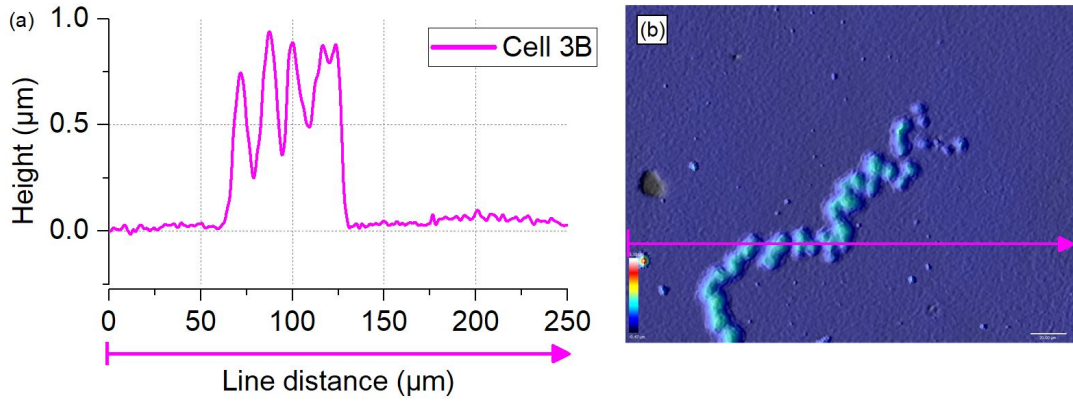


Figure 6.27: Confocal microscopy results at cell 3B with (a) a height profile of the worm-like defect and (b) a contour map where the annotated arrow reflects the x-axis of (a)

Nuggets can be up to $4\ \mu\text{m}$ above the i-ZnO surface. Seeds reach just over $1.0\ \mu\text{m}$. Stain-like features exhibit heights of $0.2\ \mu\text{m}$. On the Nantes samples with $1\ \mu\text{m}$ AZO the height is in the range of 0.1 - $1.7\ \mu\text{m}$. With $2\ \mu\text{m}$ AZO this height is in the range of 1.3 - $2.1\ \mu\text{m}$. All exhibit heights in the same range as worm-like defects. However, the height of nuggets might be related to absence of the AZO layer.

Seeds and nuggets both exhibit additional peaks at 305 and $600\ \text{cm}^{-1}$ with Raman spectroscopy. These peaks are also observed in the band around worm-like defects. In addition the seeds show an increase in peaks around 225 and $260\ \text{cm}^{-1}$. These peaks were also observed in worm-like defects in recent research at Solliance presented in Chapter 3 [12]. The additional peaks are not observed for stain-like features. EDS and BEC images show a ring around the nuggets with a high concentration of Cd. This band is comparable with the Cd rich band in worm-like defects. It is strange Raman spectroscopy shows a peak at $600\ \text{cm}^{-1}$ and a high Ga content in EDS while the CdS layer was deposited with a very small amount of Cd.

EDS on the nuggets at 8C1 shows a higher Cu content compared to the bulk material. It must be taken in account that the CIGS material erupted through the i-ZnO layer. In the bulk, this layer is measured below a i-ZnO layer suppressing the measured CIGS content. It does show that both the nugget at 8C1 and 6B1 are accompanied with Cd and S. The seeds shows an increase in Se content. In nuggets no higher Ga values are observed compared to the bulk material before and after etching this is in contrast with worm-like defects.

The unknown phase of the nuggets has a volume not seen in worm-like defects. Stain-like features show similar discrete adjacent spots compared with worm-like defects. These discrete steps are also observed in worm-like defects. All features have different similarities with worm-like defects but are not exactly the same.

An estimation on the volume of the nugget presented in this thesis at spot 8C1 is $400\ \mu\text{m}^2$ ($2 \times 20 \times 10\ \mu\text{m}$). Without a cross-sectional analysis of the sample no comparison can be done on the volumetric expansion. The size of the seeds and stains is more comparable with the height of worm-like defects. This difference is most probably caused by absence of an AZO layer constraining the 'eruption' of material.

6.7. Summary

The observed **conditions** shows nugget features only appear if a sudden increase to the set current limit is present during the experiment. Prior to the moment where the limit is reached the current is between -8 and $-25\ \mu\text{A}$. The minimum potential is $-9.0\ \text{V}$. Seeds are observed at same potential as nuggets. The difference in applied conditions between seeds and nuggets is current. This is significantly lower for seeds. Stain-like features appeared when a potential around $-5\ \text{V}$ was applied while the current was in the same range where seeds formed. The seeds and stain-like features differ in required voltage even though the power is in the same range.

Similarities between worm-like defects with locally induced features are present. Assuming the seeds and nuggets are created during peaks in current or voltage. They are formed in a couple of seconds. The same holds for worm-like defect formation. In both cases it appears as if a very porous expanded phase has formed.

Analysing both worm-like and locally induced features. Nuggets show similar Cd rich band as worm-like defects in BEC images and EDS. In Raman spectroscopy the peak observed in the edge of worm-like defects is also found on spots with seeds and nuggets. In addition the B2/E peaks increase at the white parts observed in OM. This is also observed inside worm-like defects. This suggests similar mechanisms of worm-like defect formation are present when inducing features locally.

Differences between worm-like defect formation and locally inducing features are present. The potential of worm-like defect formation is lower compared to the potential where seeds and nuggets are formed. A possible explanation is the lack of shunts locally for initiation of the process. Ohmic current through a shunt heats up the material. The heat of a shunt possibly initiates mechanisms like electromigration, diffusion or chemical reactions.

It is concluded it is not possible to induce features locally that exactly match worm-like defect characteristics based on results presented in this chapter. All features show differences and similarities compared with worm-like defects. This shows similar mechanisms are present in worm-like defect formation. The newly developed experiment provides a method able to locally simulate different mechanisms by applying different conditions. This enables the possibility of researching the mechanisms in a way not possible before.

Discussion & Conclusions

The first part of this chapter contains a general discussion on possible mechanisms involved in worm-like defect formation that are able to explain the element migration and observations. The second part of this chapter presents conclusions from this work addressing the research questions from Chapter 1.

7.1. Discussion

This section discusses the main research question based on results presented in this work. The following mechanisms might be involved in worm-like defect and feature formation: electromigration, diffusion, chemical reactions and/or phase transformations. It might very well be possible multiple mechanisms are active at the same time making the problem complex. The discussion tries to elaborate on individual mechanisms that are able to explain the material migration observed.

The following subjects are addressed in this discussion:

- Temperature, current, RB potential and shunts.
- Electromigration of Cu.
- Phase transformation in CIGS as a result of Cu migration.
- Heat as a result of Cu_2Se and ODC.
- Diffusion and chemical reactions related to Ga.
- Electromigration of Ga
- RB breakdown mechanisms
- High electromagnetic field and ionisation

Temperature, current, RB potential and shunts

As described in Chapter 2 increasing RB potential increases the width of the SCR. The RB potential, increasing the SCR, increases the area where thermally excited electron hole-pairs are separated. At elevated temperature the defect concentration goes up. Defects increase the number of gap states resulting in more thermal excitation and thus a larger RB current. The combination of potential and temperature has a significant influence on the RB current. The TCO or CIGS heats up due to joule heating as the shunt draws current. As a result of thermal conduction the temperature of the material around the shunt heats up. The heated CIGS then allows for more RB current in the vicinity of the shunt as thermal excitation of electron-holes is increased. Movement of electrons or holes is associated with heat dissipation. If the RB current increases more heat will be dissipated increasing the temperature locally initiating a self-reinforcing effect. This is the first of two possible heating mechanisms suggested.

Features during point probe experiments are formed a higher potential compared to worm-like defects. In almost all cases the local solar cell material is able to withstand high current densities compared to regular RB current densities in cells. Assuming the point probe experiment lacks an initial heat source (shunt) explains higher required potentials to initiate mechanisms. This stresses importance of temperature change in undamaged parts of the cell for propagation. If this holds, the point probe experiment is able to partially exclude heat from mechanisms in worm-like defect formation.

Electromigration of Cu

When combining background information from Chapter 2 with results it is possible to explain Cu migration towards the back contact. It is unknown where the dissipation of heat takes place it is assumed all layers heat up as a result of current but it is assumed shunts are the main source of heat. In operating condition of a solar cell current is a flow of electrons and holes. In reverse bias electron-hole pairs are thermally generated and separated by the electromagnetic field shown in 7.1(a). Two possible analogies are used to describe mechanisms which might be the reason for Cu migration towards the back contact. Keep in mind the direct electromagnetic field dependence of Cu ion mobility plays a minor role. Rather, indirect electromagnetic field dependence of mobility due to local Joule heating, dominates [72].

The **first analogy** is from a majority carrier (holes in CIGS) perspective. The number of V'_{Cu} increases with an increase of temperature [32]. Analogous to this increase V'_{Cu} the hole concentration in p-type CIGS material increases with an increase in temperature shown in Figure 2.10. The increase in temperature increases the mobility of Cu^+ ions. At a given temperature the F_{direct} from the applied potential acts on Cu^+ pulling them toward the back contact shown in Figure 7.1(e). It is possible the heat from the shunt is conducted to the CIGS around it enabling this Cu migration. The flow of electric charge in this situation can be accommodated by a movement of Cu^+ -ions towards the back contact instead holes.

The **second analogy** is from a minority carrier perspective. The V'_{Cu} concentration increases with an increase in temperature. The F_{direct} on V'_{Cu} is a result of applied potential. The mobility of electrons in CIGS is low. The flow of electric charge in this analogy can be the movement of V'_{Cu} towards the CdS.

A small calculation to back up this theory is done to give insight in the possibility of current transport by V'_{Cu} or Cu^+ instead of holes or electrons. One unit cell of stoichiometric CIS ($CuInSe_2$) has a volume of $a^2 * c = (5.784 * 10^{-10})^2 * (11.616 * 10^{-10}) m^3 = 3,89 * 10^{-21} cm^3$ where a and c are the lattice parameters [7]. This unit cell contains 4 Cu, 4 In and 8 Se atoms. In total gives 16 atoms in a single unit cell. Combining this with the volume of a unit cell gives an atomic density of $3 * 10^{21} cm^{-3}$ atoms of which $7.4 * 10^{20} cm^{-3}$ atoms are Cu atoms. Lets now assume p-type doped CIGS material used with the following stoichiometry $Cu_{0.9}(In,Ga)Se_2$. Missing Cu atoms in the lattice in this material is $7.4 * 10^{19} cm^{-3}$ this is directly related to V'_{Cu} density. This is at least three orders of magnitude higher compared to the hole carrier density of $2 * 10^{16} cm^{-3}$ from Table 2.1.

Phase transformation in CIGS as a result of Cu migration

Looking at the phase diagram of CIS shown in Figure 2.4 it is observed the increase in Cu content allows for the formation of a mix of Cu_2Se and α -chalcopyrite. Decreasing the Cu content shows that the α -chalcopyrite is existing together with the β -chalcopyrite or ODC. This might very well explain the Cu rich islands observed near the back contact as this requires small changes in Cu concentration. SEM-EDS measurements in the worm-like defect with SEM-EDS show Cu deficiency. Raman spectroscopy inside the worm-like defects and on white areas (OM Figure 6.20 show an increased ratio between the B2/E peaks and CIGS A1 peaks suggesting Cu deficient material or Cu_2Se . These findings suggest the segregation of Cu inside the CIGS layer and possibly forming ODC and Cu_2Se .

Heat as a result of Cu_2Se and ODC

The is the second of two possible heating mechanisms involves the Cu migration. Local heating increases the Cu migration towards the back contact. The previous paragraph suggests a phase transformation chalcopyrite with Cu_2Se near the back contact and ODC near the TCO. Cu_2Se is an excellent hole conductor. This locally increases the conductivity. As a result of this higher conductivity the location where Cu_2Se is formed attracts more current similar to the mechanism involved in shunt heating.

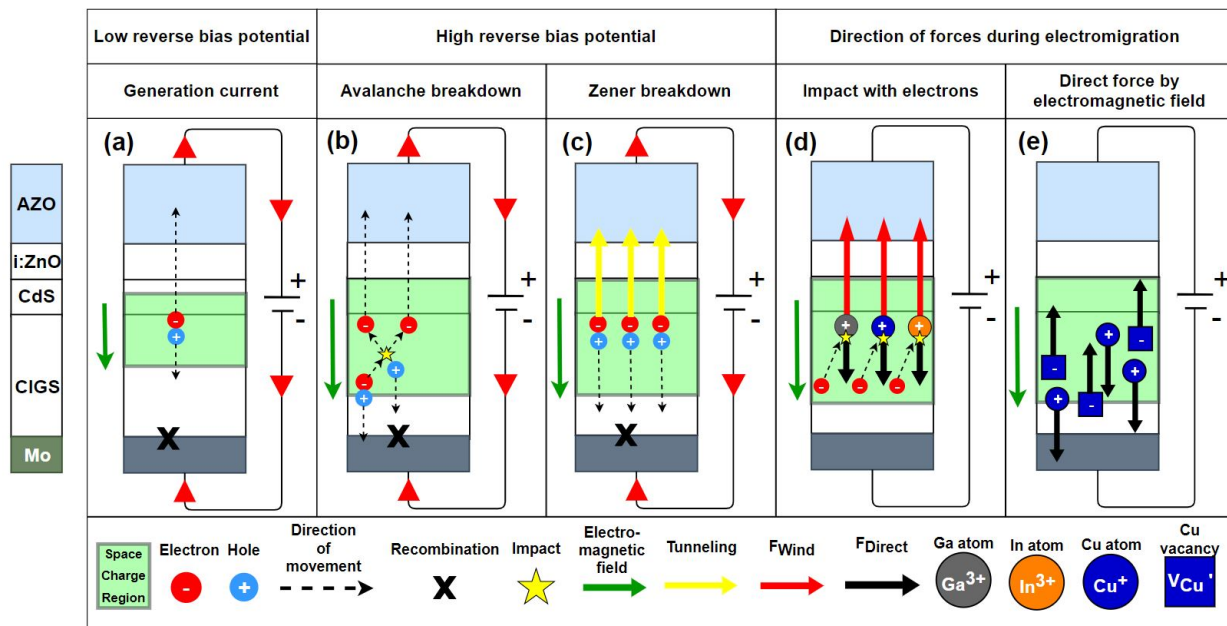


Figure 7.1: Overview to visualise mechanisms (in the dark) described in the discussion with: (a) the drift current due to thermal generation of electron-hole pairs in the SCR at a low reverse bias potential, (b) avalanche breakdown involving impact ionisation of electrons, (c) Zener breakdown with tunnelling mechanism through the SCR, (d) impact and momentum transfer (F_{direct}) between electrons and atoms in the lattice and (e) the F_{direct} on V_{Cu}^{+} and Cu^{+} -ions.

Diffusion and chemical reactions related to Ga

It is possible a chemical reactions takes place prior, subsequent or parallel to Cu migration. When taking the following in account: the G° of CGS is lower than that of CIS [51], Cd is able to diffuse in Cu deficient CIGS assisted by Ga out diffusion [59], Ga is soluble in ZnO [60], the reaction of Ga_2Se_3 with ZnO is thermodynamically favourable [51] and Ga increases the conductivity of ZnO [60]. All this information emphasise the possibility of a chemical reaction.

Assuming Cu migration towards the back contact occurs first, this mechanism increases the diffusion of Cd into the CIGS and out diffusion of Ga. This Ga diffuses through the CdS into the i-ZnO increasing its conductivity which attracts more current. It is also possible this diffusion mechanisms are just a result of heat and has nothing to do with the Cu migration.

When assuming Cu migration towards the back contact occurs and the all of the CdS moves into the CIGS layer or melts, bringing the Ga_2Se_3 in the vicinity of the ZnO initiating a chemical reaction. The products of this reaction are Ga_2O_3 and $ZnSe$. SEM-EDS results inside worm-like defects showed the presence of both Ga_2O_3 and $ZnSe$. In the experiment with the point probe no higher Ga content was observed at the features. The eruption of material and/or the small i-ZnO layer possibly inhibited this chemical reaction during worm-like defect formation.

In the extent of Ga diffusion there is a possibility to explain the the band observed around worm-like defects and nuggets containing a higher Cd and S content. The relative content of Ga is higher near the TCO. The diffusion of S in the CIGS positively correlated with Ga rich CIGS [58]. It is also found the diffusion of Cd in CIGS is accompanied by out diffusion of Ga into the CdS [59]. As mentioned, Cd diffusion into CIGS is also related to Cu deficiency [59].

Electromigration of Ga

Areas with a high Ga concentration are observed near the TCO. This migration of Ga might be caused by the F_{wind} of electromigration or diffusion. Effective wind valencies in electromigration are a complex subject as it involves momentum transfer of electrons with atoms [67]. Transfer of moment between electrons and

atoms involves quantum mechanical physics not yet fully understood in CIGS semiconductor material. Electrons in p-type CIGS are minority carriers. CIGS is a mix of CGS and CIS. By looking at individual properties of CIS and CGS might point in the right direction. The following is observed: minority carrier diffusion length of light excited minority carriers in CIGS is $0.5 \mu\text{m}$ for CGS and well above $1.0 \mu\text{m}$ for CIS [22]. This diffusion length is determined by scattering of electrons by atoms in the lattice. Simplifying the problem by assuming Ga scatters more electrons in CIGS than In could explain why Ga atoms move towards the TCO as F_{wind} is larger for Ga atoms than In. With this assumption the electrons colliding with atoms during an applied RB push the Ga towards the TCO. This mechanism is visualised in Figure 7.1(d). Although it is expected that Ga^{3+} -ion exhibits a higher F_{direct} as the valency is higher than that of a Cu^{+} -ion. The Ga movement caused by the applied potential is also dependant on the mobility of the atoms. The high V'_{Cu} concentration increases mobility of Cu^{+} -ion which might need a lower F_{direct} for migration. In addition to the phase transformation by Cu migration, if Ga moves due to the F_{wind} this reduces the stability of α -chalcopyrite CIGS stimulating the phase transformation [17, 21].

RB breakdown mechanisms

During experiments it is observed in the formation of worm-like defects, seeds and nuggets do not form if the reverse bias curve exhibits high currents at low potential [12]. This behaviour is seen in Figure 6.2. The RB current is complex as it is affected by defects, potential and temperature. As discussed in Subsection 2.2.4 also involves two breakdown mechanisms: Zener and Avalanche.

Zener breakdown occurs at lower RB potential compared with Avalanche breakdown [42]. Seeds are observed at a high potential and low current. Increasing current at a high voltage results in an eruption. Lowering potential leads to the formation of only stains. This indicates Avalanche breakdown might play a role in the features and maybe in worm-like defect formation. Avalanche breakdown involves ionisation impact on atoms shown in Figure 7.1(d). The impact of avalanche electrons increases the F_{wind} and current density in the SCR [67]. When assuming the impact of avalanche electrons is transferring momentum on atoms this might effect element migration. E.g. pushing specific elements towards the front contact. This mechanism is shown in Figure 7.1(d).

In addition to the previous paragraph the following observation stresses the role of the breakdown mechanism. It is observed that light illumination decreases the junction barrier between the CdS and i-ZnO layer [107]. In solar cells it is observed the breakdown potential shifts to lower values under illumination of especially green and blue light [9]. It is also observed a thicker CdS exhibit a higher breakdown potential [9]. It is observed it is more difficult to induce worm-like defects under illuminated conditions. This stresses breakdown mechanisms play an important role in worm-like defect formation in dark conditions.

Stain-like defects occur at lower potential but not necessarily at low power. Low potential suggests avalanche breakdown is not involved. This shows other mechanisms before avalanche breakdown are present and need not to be neglected as they happen at a low bias potential.

High electromagnetic field and ionisation

The applied potential is present over a very thin layer. This part of the discussion elaborates on possible effects of the electromagnetic field. When putting -3 V over a $3 \mu\text{m}$ layer, this results in an electromagnetic field of $3 \cdot 10^6 \text{ V} \cdot \text{m}^{-1}$. Air has an ionisation potential of $10^6 \text{ V} \cdot \text{m}^{-1}$. It must be said ionisation of elements in solids is more difficult. However, the high electromagnetic field shows ionisation is a mechanism not to be neglected in studying worm-like defect formation.

7.2. Conclusions

The conclusion of this thesis consists of two parts. First, conclusions are drawn on the three sub-questions. After the sub-questions the main research question will be addressed.

Starting with the **first sub-question** on the changes in composition, geometry and structure. The following is observed visually after worm-like defect formation:

- Voids/holes between the AZO and CIGS layer.
- Thin visible layer just below AZO on the place the CdS used to be.
- Discrete propagation steps
- Band around worm-like defects
- Cu rich phase near back contact

Additional to the visual observations XRD and SEM-EDS measurements are done. It is found:

- based on XRD results there is no evidence for a change in CIGS crystal structure;
- after worm-like defect formation Cu migration towards the back contact is observed;
- inside worm-like defects areas with a high Ga and O content are observed. These areas show also low Se and high Zn content;
- the band around worm-like defects increase in Cd and S content while decreasing in Cu, In, Ga and Se content;
- the S present in the band around worm-like defects moves into the CIGS matrix at Se positions.
- the Cd present in the band around worm-like defects moves into the CIGS matrix at Cu, In and Ga positions;

First the **third** sub-question on the differences and similarities between locally induced features and worm-like defects induced in CIGS solar cells will be answered.

It is found possible to induce features by applying a RB on a CIGS solar cell with no AZO. Three different locally induced feature categories are observed as a result of the applied conditions:

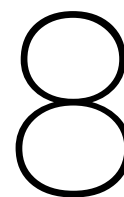
- stain-like features or Stains, induced at low potential and low current
- features $< 15 \mu\text{m}$ or seeds, induced at high potential and low current
- features $> 15 \mu\text{m}$ or nuggets, induced at high potential and high current

While inducing stains the resistance increases during the experiment. In the case for nuggets and stains the resistance decreases. Inducing nuggets involves a sudden increase in current.

Differences and similarities between features and worm-like defects are present. Three different features are observed for distinct applied conditions and the experiment is less affected by local heating of shunts. The OM, CM, SEM-EDS and Raman results show the nugget, seed and stain-like features all have similarities and differences compared to worm-like defects. The required RB potential for inducing local features is higher compared to the potential required to induce worm-like defects. The higher required potential is due to a lack of shunt and thus local heat dissipation. With this information it is possible to answer the **second** sub-question. It can be concluded it is possible to apply controlled conditions and mimic partial mechanisms in worm-like defect formation. This experiments enables further research on worm-like defect formation.

The main research question on **possible mechanisms** involved in reverse bias induced worm-like defects is extensively discussed in the previous section. With results from this research it is not possible to draw conclusions on initial and subsequent mechanisms. Comparing two breakdown mechanisms discussed avalanche breakdown is the most relevant as it involves impact ionisation and momentum transfer of electrons with atoms. The following order of mechanisms appear viable: heat as a result of shunts, temperature activated Cu migration in combination with the applied RB potential, phase transformation of chalcopyrite into Cu_2Se with ODC, subsequent chemical reactions and diffusion related to the Cu poor ODC, CdS and ZnO.

The pin-pointed mechanisms during formation in this work combined with the developed experiment enabling controlled applied conditions are very useful for future research on worm-like defects in CIGS thin-film solar cells.



Future work and recommendations

Throughout this work data was generated and analysed to understand the direct the mechanisms involved in worm-like defects. This chapter presents the next steps for further use of the developed experiment and a general outlook on researching worm-like defects. In the continuation of this research it is essential to gain direct evidence which relate applied parameters to possible mechanisms. Especially separating the initial mechanism from subsequent mechanisms. This is the most important step as this possibly enables measures to inhibit worm-like defect formation and propagation.

Continuing the developed experiment

To study element migration SEM-EDS, secondary ion milling spectroscopy or X-ray photoelectron spectroscopy analysis can be used on cross-sections of the features induced in this work. Combining observations with applied conditions is essential as the direction of migration is the most relevant along the direction of current and applied field. The analysis on cross-sections of features is essential. The main focus in element migration at the cross-sectional analysis is on Cu and Ga.

The initial SEM images of cross-sections of the induced features are already available. Unfortunately the measurements were not finished in time to include the results in this work. the first SEM images are presented in Figures 8.1, 8.2, 8.3 and 8.4 as an appetiser.

The measurement scheme in this work consisted of 3 set potentials and 2 set currents. Most of experiments stabilised' or 'blew-up' in the first hour. To get more thorough knowledge on which conditions create which defect more data is required at more set voltages and potentials. A more extensive measurement scheme results in a better determination of the contact area, which results in a better estimation of the current density.

The RB potential at which features are formed is different from worm-like defects. This was explained by the lack of a shunt. This enables to study the mechanisms as a function of heat. With this experiment it is possible to heat the substrate to desired temperatures while applying the same conditions. This enables applying realistic conditions which are present during worm-like defect formation.

After applying local conditions, it often occurred the spot where the probe was in contact with the i-ZnO could not be found. The measurement points presented in the methodology are not suitable for finding the contact area as little changes are not visible. A suggestion to solve this problem is to remove the grids and replace this with a laser patterned grid. The lowering of the probe on the sample is quite accurate when references on the cell are present. A grid would enable the point probe to be in contact with the sample in the middle of a laser patterned square. This square can be used as orientation under OM and SEM simplifying the search to the contact area.

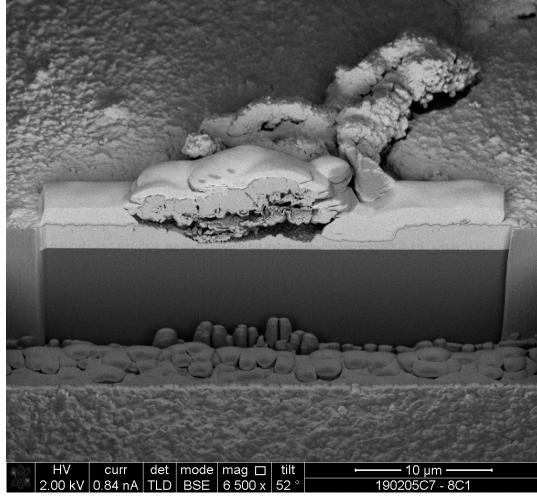


Figure 8.1: Cross-Section SEM image of the nugget at spot 8C1.

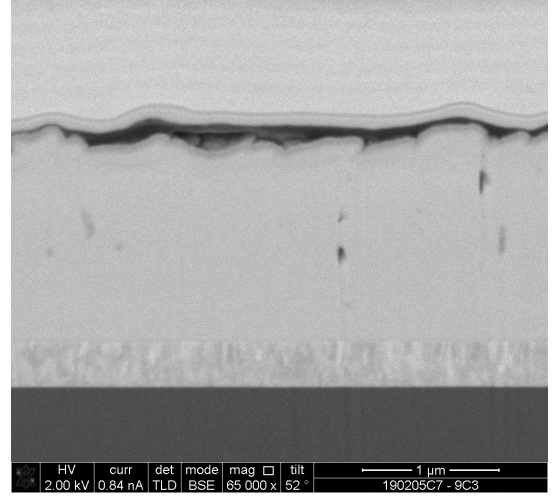


Figure 8.2: Cross-section SEM image of the stain at spot 9C3.

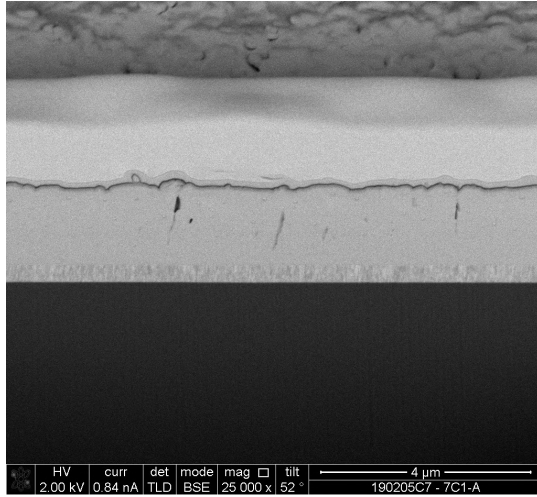


Figure 8.3: Cross-section SEM image of the seeds in the middle of the affected area at spot 7C1.

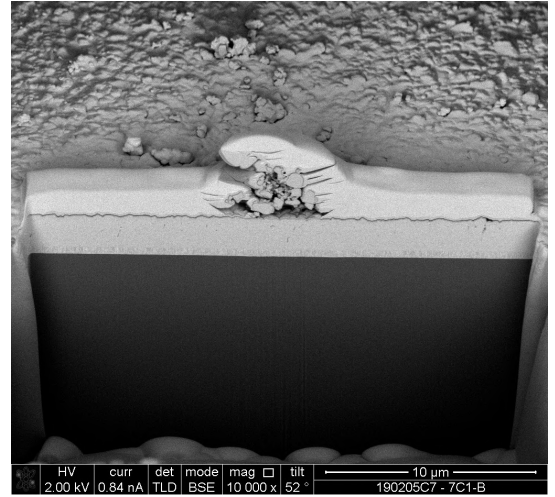


Figure 8.4: Cross-section SEM image of a seeds at spot 7C1.

It is not fully determined what the new Cu rich phase in worm-like and locally induced features is. Analysing these defects with calibrated SEM-EDS or XPS gives insight in their composition from which more details on the reaction during the transformation can be deducted. Electron Back-scatter Diffraction (EBSD) can be used to gain insight in grain orientation. Cu trails are observed in the CIGS. EBSD enables confirmation of Cu migration along grain boundaries or through the crystal lattice.

From all the above observations, discussions and conclusions it arises electromigration plays a big role in worm-like defect formation. Electromigration is mainly studied in metals or Si (semiconductor). No research on electromigration in CIGS is found yet. Understanding electromigration physics in semiconductors and alloys might find differences in F_{wind} on individual Cu, In, Ga or Se elements. This knowledge can be used to explain why certain elements are migrating.

Bibliography

- [1] M. Allen, M. Babiker, and Y. Chen. Summary for policy makers. Report, Intergovernmental Panel on Climate Change (IPCC), 2018.
- [2] A. Rose, D. Wei, N. Miller, and T. Vandyck. Equity, emissions allowance trading and the Paris agreement on climate change. *Economics of Disasters and Climate Change*, 1(3):203–232, 2017. ISSN 2511-1280. doi: 10.1007/s41885-017-0012-3.
- [3] E. Kabir, P. Kumar, S. Kumar, A. Adelodun, and K. Kim. Solar energy: Potential and future prospects. *Renewable and Sustainable Energy Reviews*, 82:894–900, 2018. ISSN 13640321. doi: 10.1016/j.rser.2017.09.094.
- [4] B. Burger. Photovoltaics report presentation with support of PSE conferences and consulting GMBH. Report, 2018.
- [5] M. Hutchins. Solar Frontier hits new CIS cell efficiency record. *PVMagazine*, 2019. URL <https://www.pv-magazine.com/2019/01/21/solar-frontier-hits-new-cis-cell-efficiency-record/>.
- [6] N. Feldman, J. Hoskins, and R. Margolis. Q4 2017/Q1 2018 Solar industry update. Report, NREL, 2018.
- [7] N. Amin. Promises of $Cu(In,Ga)Se_2$ thin film solar cells from the perspective of material properties, fabrication methods and current research challenges. *Journal of Applied Sciences*, 11:401–410, 2011. ISSN 1812-5654. doi: 10.3923/jas.2011.401.410.
- [8] M. Imamzai, M. Aghaei, Y.H. Thayoob, and M. Forouzanfar. A review on comparison between traditional silicon solar cells and thin- film cdte solar cells. *National Graduate Conference*, 2012.
- [9] P. Szaniawski, J. Lindahl, T. Törndahl, U. Zimmermann, and M. Edoff. Light-enhanced reverse breakdown in $Cu(In,Ga)Se_2$ solar cells. *Thin Solid Films*, 535:326–330, 2013. ISSN 00406090. doi: 10.1016/j.tsf.2012.09.022.
- [10] S. Johnston, E. Palmiotti, and A. Gerber. Thin-film module reverse-bias breakdown sites identified by thermal imaging. *Institute of Electrical and Electronics Engineers: Photovoltaic Specialist Conference*, 2018. doi: 978-1-5386-8529-7/18.
- [11] M. Nardone, S. Dahal, and J. M. Waddle. Shading-induced failure in thin-film photovoltaic modules: Electrothermal simulation with nonuniformities. *Solar Energy*, 139:381–388, 2016. ISSN 0038092X. doi: 10.1016/j.solener.2016.10.006.
- [12] H. Nilsson. Morphology and composition of wormlike defects, occurring in CIGSe solar cells under reverse bias conditions. Report, Lulea University of Technology, 2018.
- [13] A. Smets, O. Isabella, R. Van der Swaaij, M. Zeman, and K. Jäger. *Solar Energy*. UIT camebridge Ltd., 2016. ISBN 9781906325.
- [14] M. Theelen, A. Liakopoulou, V. Hans, F. Daume, H. Steijvers, N. Barreau, Z. Vroon, and M. Zeman. Determination of the temperature dependency of the electrical parameters of CIGS solar cells. *Journal of Renewable and Sustainable Energy*, 9(2), 2017. ISSN 1941-7012. doi: 10.1063/1.4979963.
- [15] M. Asaduzzaman, M. Hasan, and A. N. Bahar. An investigation into the effects of band gap and doping concentration on $Cu(In,Ga)Se_2$ solar cell efficiency. *Springerplus*, 5:578, 2016. ISSN 2193-1801 (Print). doi: 10.1186/s40064-016-2256-8.
- [16] M. Bodegard, L. Stol, and J. Hedstrom. The influence of sodium on the grain structure of $CuInSe_2$ films for photovoltaic applications. In *12th European Photovoltaic Solar Energy Conference and Exhibition*, pages 1743–1746. Amsterdam, 1994.

- [17] T. Unold and C. A. Kaufmann. *Chalcopyrite Thin-Film Materials and Solar Cells*, pages 399–422. Elsevier LTD., 2012. ISBN 9780080878737. doi: 10.1016/b978-0-08-087872-0.00121-9.
- [18] G.B. Abdullaev, Z.A. Aliyarova, and G.A. Asadov. Preparation of Cu_2Se single crystals and investigation of their electrical properties. *Physica Status Solidi*, 21, 1967.
- [19] F. El Akkad, B. Mansour, and T. Hendeya. Electric and thermoelectric properties of Cu_2Se and Cu_2S . *Material Research Bulletin*, 16, 1981.
- [20] H. Jitsukawa, H. Matsushita, and Takizawa T. Phase diagrams of the $(\text{Cu}_2\text{Se}, \text{CuSe})\text{-CuGaSe}_2$ system and the crystal growth of CuGaSe_2 by the solution method. *Journal of Crystal Growth*, 186, 1998.
- [21] B. Stanbery. Copper indium selenides and related materials for photovoltaic devices. *Critical Reviews in Solid State and Materials Sciences*, 27(2):73–117, 2002. ISSN 1040-8436 1547-6561. doi: 10.1080/20014091104215.
- [22] S. Siebentritt, M. Igalson, C. Persson, and S. Lany. The electronic structure of chalcopyrites-bands, point defects and grain boundaries. *Progress in Photovoltaics: Research and Applications*, 18:390–410, 2010. ISSN 10627995. doi: 10.1002/pip.936.
- [23] T. Feurer, P. Reinhard, E. Avancini, B. Bissig, J. Löckinger, P. Fuchs, R. Carron, T. Weiss, J. Perrenoud, S. Stutterheim, S. Buecheler, and A. Tiwari. Progress in thin film CIGS photovoltaics - research and development, manufacturing, and applications. *Progress in Photovoltaics: Research and Applications*, 25(7):645–667, 2017. ISSN 10627995. doi: 10.1002/pip.2811.
- [24] E. Ghorbani, J. Kiss, H. Mirhosseini, G. Roma, M. Schmidt, J. Windeln, T. Kühne, and C. Felser. Hybrid-functional calculations on the incorporation of na and k impurities into the CuInSe_2 and CuIn_5Se_8 solar-cell materials. *The Journal of Physical Chemistry*, 119(45):25197–25203, 2015. ISSN 1932-7447. doi: 10.1021/acs.jpcc.5b07639.
- [25] J. Bekaert, R. Saniz, B. Partoens, and D. Lamoen. Native point defects in $\text{Cu}(\text{In}_{1-x}\text{Ga}_x)\text{Se}_2$: hybrid density functional calculations predict the origin of p- and n-type conductivity. *Physical Chemistry Chemical Physics*, 16(40):22299–308, 2014. ISSN 1463-9084 (Electronic). doi: 10.1039/c4cp02870h. URL <https://www.ncbi.nlm.nih.gov/pubmed/25219948>.
- [26] H. Neumann. Lattice vibrational, thermal and mechanical properties of CuInSe_2 . *Solar Cells*, 16:399–418, 1985.
- [27] A. S. Verma. Thermal properties of chalcopyrite semiconductors. *Philosophical Magazine*, 89:183–193, 2009. ISSN 1478-6435 1478-6443. doi: 10.1080/14786430802593814.
- [28] B. McCandless and S.S. Hegedus. Influence of CdS window layer on thin film CdS/CdTe solar cell performance. *Institute of Electrical and Electronics Engineers: Journal of Photovoltaics*, 1991.
- [29] M. Theelen. *Degradation of CIGS Solar Cells*. Thesis, 2015.
- [30] D. Abou-Ras, G. Kostorz, A. Romeo, D. Rudmann, and A. N. Tiwari. Structural and chemical investigations of CBD- and PVD-CdS buffer layers and interfaces in $\text{Cu}(\text{In}, \text{Ga})\text{Se}_2$ -based thin film solar cells. *Thin Solid Films*, 480-481:118–123, 2005. ISSN 00406090. doi: 10.1016/j.tsf.2004.11.033.
- [31] S. Ishizuka, K. Sakurai, A. Yamada, K. Matsubara, P. Fons, K. Iwata, S. Nakamura, Y. Kimura, T. Baba, H. Nakanishi, T. Kojima, and S. Niki. Fabrication of wide-gap $\text{Cu}(\text{In}_{1-x}\text{Ga}_x)\text{Se}_2$ thin film solar cells: a study on the correlation of cell performance with highly resistive i-ZnO layer thickness. *Solar Energy Materials and Solar Cells*, 87(1-4):541–548, 2005. ISSN 09270248. doi: 10.1016/j.solmat.2004.08.017.
- [32] W. D. Callister and D.G. Rethwisch. *Material science and Engineering 8th edition*. Wiley, 2011. ISBN 978-0-470-50586-1.
- [33] R. Hummel. *Electronic Properties of Materials*, volume 4. Springer, 2011. ISBN 978-1-4419-8163-9. doi: 10.1007/978-1-4419-8164-6.

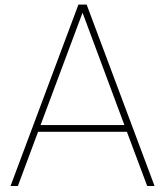
- [34] D. Schroeder, J. Hernandez, G. Berry, and A. Rockett. Hole transport and doping states in epitaxial $\text{Cu}(\text{In}_{1-x}\text{Ga}_x)\text{Se}_2$. *Journal of Applied Physics*, 83(3):1519–1526, 1998. ISSN 0021-8979 1089-7550. doi: 10.1063/1.366860.
- [35] F. Mesa, C. Calderón, and G. Gordillo. Study of electrical properties of CIGS thin films prepared by multistage processes. *Thin Solid Films*, 518(7):1764–1766, 2010. ISSN 00406090. doi: 10.1016/j.tsf.2009.09.028.
- [36] <https://physics.stackexchange.com/questions/347970/differences-in-conductivity-as-temp-rises-for-intrinsic-vs-extrinsic-semiconductor?rq=1>. Differences in conductivity as temperature rises for intrinsic vs extrinsic semiconductors, acces date: 04-06-2019.
- [37] S. R. Kodigala. $\text{Cu}(\text{In}_{1-x}\text{Ga}_x)\text{Se}_2$ and $\text{CuIn}(\text{Se}_{1-x}-\text{S}_x)_2$ Thin Film Solar Cells. Thin Films and Nanostructures. Elsevier, 2010. doi: 10.1016/b978-0-12-373697-0.00008-0.
- [38] P. O. Westin and U. Zimmermann. Reverse bias damage in CIGS modules. In *24th European Photovoltaic Solar Energy Conference*. Uppsala University, 2009.
- [39] X. Sun and M. Alam. A physics-based compact model for CIGS and cdte solar cells from voltage-dependent carrier collection to light-enhanced reverse breakdown. In *42nd Institute of Electrical and Electronics Engineers: Photovoltaic Specialists Conference*, 2015.
- [40] A. Chirila, S. Buecheler, and F. Pianezzi. Highly efficient $\text{Cu}(\text{In},\text{Ga})\text{Se}_2$ solar cells grown on flexible polymer films. *Nat Mater*, 10(11):857–61, 2011. ISSN 1476-1122. doi: 10.1038/nmat3122. URL <https://www.ncbi.nlm.nih.gov/pubmed/21927005>.
- [41] M. Lu, J. Xu, and J. Huang. Non-ionizing energy loss calculations for modeling electron-induced degradation of $\text{Cu}(\text{In},\text{Ga})\text{Se}_2$ thin-film solar cells. *Chinese Physics B*, 25(9), 2016. ISSN 1674-1056. doi: 10.1088/1674-1056/25/9/098402.
- [42] S. Mahadevan, S.M. Hardas, and G. Surya. Electrical breakdown in semiconductors. *Physica Status Solidi*, 8:335–374, 1971.
- [43] M. Rudan. *Physics of Semiconductor Devices 2nd edition*. Springer, Bologna, 2018. ISBN 978-3-319-63153-0. doi: 0.1007/978-3-319-63154-7.
- [44] S. M. Sze and K. Kwok. *Physics of Semiconductor Devices 3rd edition*. John Wiley and Sons, 2006.
- [45] P. Szaniawski, P. Zabierowski, J. Olsson, U. Zimmermann, and M. Edoff. Advancing the understanding of reverse breakdown in $\text{Cu}(\text{In},\text{Ga})\text{Se}_2$ solar cells. *Institute of Electrical and Electronics Engineers: Journal of Photovoltaics*, 7(4):1136–1142, 2017. ISSN 2156-3381 2156-3403. doi: 10.1109/jphotov.2017.2699860.
- [46] S. Puttnins, S. Jander, A. Wehrmann, G. Benndorf, M. Stölzel, A. Müller, H. von Wenckstern, F. Daume, A. Rahm, and M. Grundmann. Breakdown characteristics of flexible $\text{Cu}(\text{In},\text{Ga})\text{Se}_2$ solar cells. *Solar Energy Materials and Solar Cells*, 120:506–511, 2014. ISSN 09270248. doi: 10.1016/j.solmat.2013.09.031.
- [47] M. Tessema and D. Giolando. Pinhole treatment of a cdte photovoltaic device by electrochemical polymerization technique. *Solar Energy Materials and Solar Cells*, 107:9–12, 2012. ISSN 09270248. doi: 10.1016/j.solmat.2012.07.025.
- [48] A. Bosio, N. Romeo, S. Mazzamuto, and V. Canevari. Polycrystalline CdTe thin films for photovoltaic applications. *Progress in Crystal Growth and Characterization of Materials*, 52(4):247–279, 2006. ISSN 09608974. doi: 10.1016/j.pcrysgrow.2006.09.001.
- [49] A. Kaminski, J.J. Marchand, H. El Omar, and A. Laugier. Conducting processes in silicon solar cells. *Institute of Electrical and Electronics Engineers: Photovoltaic Specialist Conference*, 25, 1996. doi: 0-7803-3166-4196.
- [50] B. Williams, S. Smit, B. Kniknie, K. Bakker, W. Keuning, W. Kessels, R. Schropp, and M. Creatore. Identifying parasitic current pathways in CIGS solar cells by modelling darkj-vresponse. *Progress in Photovoltaics: Research and Applications*, 23(11):1516–1525, 2015. ISSN 10627995. doi: 10.1002/pip.2582.

- [51] F. Guillemoles. Stability of $Cu(In,Ga)Se_2$ solar cells: a thermodynamic approach. *Thin Solid Films*, pages 361–362, 2000.
- [52] A. Stokes, M. Al-Jassim, D. Diercks, B. Egaas, and B. Gorman. 3-d point defect density distributions in thin film $Cu(In,Ga)Se_2$ measured by atom probe tomography. *Acta Materialia*, 102:32–37, 2016. ISSN 13596454. doi: 10.1016/j.actamat.2015.09.035.
- [53] S. Nakamura, T. Maeda, and T. Wada. First-principles study of diffusion of Cu and In atoms in $CuInSe_2$. *Japanese Journal of Applied Physics*, 52(4S), 2013. ISSN 0021-4922 1347-4065. doi: 10.7567/jjap.52.04cr01.
- [54] E. Korhonen, K. Kuitunen, E. Tuomisto, A. Urbaniak, M. Igalson, J. Larsen, L. Gütay, S. Siebentritt, and Y. Tömm. Vacancy defects in epitaxial thin film $CuGaSe_2$ and $CuInSe_2$. *Physical Review B*, 86(6), 2012. ISSN 1098-0121 1550-235X. doi: 10.1103/PhysRevB.86.064102.
- [55] S. Lany and A. Zunger. Light- and bias-induced metastabilities in $Cu(In,Ga)Se_2$ based solar cells caused by the $(V_{Se}-V_{Cu})$ vacancy complex. *Journal of Applied Physics*, 100(11), 2006. ISSN 00218979. doi: 10.1063/1.2388256.
- [56] R.D. Shannon. Revised effective ionic radii and systematic studies of interatomic distances in halides and chalcogenides. *Acta Crystallographica*, 32:751–767, 1976.
- [57] H. Mehrer. *Diffusion in solids*. Solid State Science. Springer, 2007. ISBN 978-3-540-71486-6.
- [58] B.M. Basol, A. Halani, and G. Leidholm. Studies on sulfur diffusion into $Cu(In,Ga)Se_2$ thin films. *Progress in Photovoltaics: Research and Applications*, 2000.
- [59] S. Park, E. Lee, S. Lee, S. Park, W. K. Kim, S. Lee, W. Lee, B. Lee, H. Bae, J. Yoo, and C. Jeon. Investigation of $ZnO/CdS/Cu(In_x, Ga_{1-x})Se_2$ interface reaction by using hot-stage TEM. *Current Applied Physics*, 10(3):S399–S401, 2010. ISSN 15671739. doi: 10.1016/j.cap.2010.02.043.
- [60] V. Bhosle, A. Tiwari, and J. Narayan. Electrical properties of transparent and conducting Ga doped ZnO. *Journal of Applied Physics*, 100(3), 2006. ISSN 0021-8979 1089-7550. doi: 10.1063/1.2218466.
- [61] S. Chen, W. Lin, S. Chan, S. Tseng, C. Kuo, S. Hu, W. Peng, and Y. Lu. Photoluminescence analysis of CdS/CIGS interfaces in CIGS solar cells. *ECS Journal of Solid State Science and Technology*, 4(9):P347–P350, 2015. ISSN 2162-8769 2162-8777. doi: 10.1149/2.0041509jss.
- [62] T. Nakada and A. Kunioka. Direct evidence of Cd diffusion into $Cu(In,Ga)Se_2$ thin films during chemical-bath deposition process of CdS films. *Applied Physics Letters*, 74(17):2444–2446, 1999. ISSN 0003-6951 1077-3118. doi: 10.1063/1.123875.
- [63] B. Yin and C. Lou. (112) surface of $CuInSe_2$ thin films with doped Cd atoms. *Advances in Condensed Matter Physics*, 2015:1–7, 2015. ISSN 1687-8108 1687-8124. doi: 10.1155/2015/206501.
- [64] P. Salome, R. Ribeiro-Andrade, J. Teixeira, J. Keller, T. Torndahl, N. Nicoara, M. Edoff, J. Gonzalez, J. Leitao, and S. Sadewasser. Cd and Cu interdiffusion in $Cu(In,Ga)Se_2/CdS$ hetero-interfaces. *Institute of Electrical and Electronics Engineers: Journal of Photovoltaics*, 7(3):858–863, 2017. ISSN 2156-3381 2156-3403. doi: 10.1109/jphotov.2017.2666550.
- [65] E.D. Jones. Diffusion of gallium into cadmium sulphide. *Physics in Chemical Solids*, 41:1261–1265, 1980.
- [66] C. Lei, A. Rockett, I. M. Robertson, W. N. Shafarman, and M. Beck. Void formation and surface energies in $Cu(In,Ga)Se_2$. *Journal of Applied Physics*, 100(7), 2006. ISSN 0021-8979 1089-7550. doi: 10.1063/1.2357422.
- [67] J. Lienig and M. Thiele. *Fundamentals of electromigration - Aware integrated circuit design*, volume 1. Springer, 2018. ISBN 978-3-319-73557-3. doi: 10.1007/978-3-319-73558-0.
- [68] M. Dresselhaus, H. Kamumura, and K. Müller. *Ordering at surfaces and interfaces*. Springer-Verlag, 1992.

- [69] M Neklyudova. *In situ TEM electrical measurements of semiconductor and metal nanowires*. Thesis, 2016.
- [70] F Guillemoles. *Cu(In,Ga)Se₂ solar cells: Device stability based on chemical flexibility*. *Advanced Materials*, 11, 1999.
- [71] F Guillemoles. Stability issues of *Cu(In,Ga)Se₂*-based solar cells. *Published on web*, 1999. doi: 10.1021/jp993143k.
- [72] L. Chernyak, K. Gartsman, D. Cahen, and O. Stafsudd. Electronic effects of ion mobility in semiconductors: Semionic behaviour of *CuInSe₂*. *Physics in Chemical Solids*, 56:1165–1191, 1995.
- [73] K. Gartsman, L. Chernyak, V. Lyahovitskaya, D. Cahen, V. Didik, V. Kozlovsky, R. Malkovich, E. Skoryatina, and V. Usacheva. Direct evidence for diffusion and electromigration of Cu in *CuInSe₂*. *Journal of Applied Physics*, 82(9):4282–4285, 1997. ISSN 0021-8979. doi: 10.1063/1.366252.
- [74] V. Nádaždy, M. Yakushev, E. H. Djebbar, A. E. Hill, and R. D. Tomlinson. Switching of deep levels in *CuInSe₂* due to electric field-induced Cu ion migration. *Journal of Applied Physics*, 84(8):4322–4326, 1998. ISSN 0021-8979 1089-7550. doi: 10.1063/1.368651.
- [75] D. Cahen, L. Chernyak, and K. Gartsman. Room-temperature, electric field-induced creation of stable devices in *CuInSe₂* crystals. *Science*, 28, 1992.
- [76] G. Dagan. Ion migration in chalcopyrite semiconductors. *American Chemical Society*, 1992. doi: 10.1021/j100205a073aÅŽ.
- [77] A. Jakubowicz. Electric-field-induced room-temperature doping in *CuInSe₂*. *Advanced Materials*, 11, 1992.
- [78] I. Lubomirsky, K. Gartsman, and D. Cahen. Space charge effects on dopant diffusion coefficient measurements in semiconductors. *Journal of Applied Physics*, 83(9):4678–4682, 1998. ISSN 0021-8979. doi: 10.1063/1.367254.
- [79] T. Walter. *Reliability Issues of CIGS-Based Thin Film Solar Cells*, pages 111–150. Semiconductors and Semimetals. Elsevier Inc., 2015. ISBN 9780128010211. doi: 10.1016/bs.semsem.2015.05.001.
- [80] E. Palmiotti, S. Johnston, A. Gerber, H. Guthrey, A. Rockett, L. Mansfield, T. Silverman, and M. Al-Jassim. Identification and analysis of partial shading breakdown sites in *Cu(In_x,Ga_{1-x})Se₂* modules. *Solar Energy*, 161:1–5, 2018. ISSN 0038092X. doi: 10.1016/j.solener.2017.12.019.
- [81] H. Guthrey, M. Nardone, S. Johnston, J. Liu, A. Norman, J. Moseley, and M. Al-Jassim. Characterization and modeling of reverse-bias breakdown in *Cu(In,Ga)Se₂* photovoltaic devices. *Progress in Photovoltaics: Research and Applications*, 2019. ISSN 1062-7995 1099-159X. doi: 10.1002/pip.3168.
- [82] C. Frisk, C. Platzer-Björkman, J. Ollson, and P. Szaniawski. Optimizing Ga-profiles for highly efficient *Cu(In,Ga)Se₂* thin film solar cells in simple and complex defect models. *Journal of Physic*, 47, 2014.
- [83] M. Theelen and E. Schiepers. Raman analysis of *Cu(In,Ga)(Se,S)₂* absorbers obtained from atmospheric selenium-sulfur annealing of electrodeposited precursors. *Institute of Electrical and Electronics Engineers: Journal of Photovoltaics*, 2018. doi: 978-1-5386-8529-7/18.
- [84] J. Gu, E. Fahrenkrug, and S. Maldonado. Analysis of the electrodeposition and surface chemistry of CdTe, CdSe, and CdS thin films through substrate-overlayer surface-enhanced raman spectroscopy. *Langmuir*, 30(34):10344–53, 2014. ISSN 1520-5827 (Electronic) 0743-7463 (Linking). doi: 10.1021/la502403q. URL <https://www.ncbi.nlm.nih.gov/pubmed/25105710>.
- [85] P. Y. Yu. Resonant raman study of LO + acoustic phonon modes of CdSe. *Solid State Communications*, 19:1087–1090, 1976.
- [86] A. Yamada. Raman study of epitaxial *Ga₂Se₃* films grown by molecular beam epitaxy. *Journal of Applied Physics*, 31, 1992.

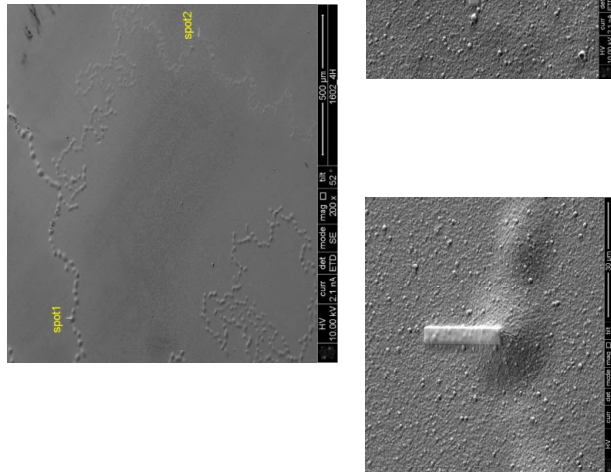
- [87] D. Liu, W. W. Lei, and B. Zou. High-pressure x-ray diffraction and raman spectra study of indium oxide. *Journal of Applied Physics*, 104(8), 2008. ISSN 0021-8979 1089-7550. doi: 10.1063/1.2999369.
- [88] D. Nesheva. Raman scattering from ZnSe nanolayers. *Acta Physica Polonica A*, 2008.
- [89] Y. C. Cheng, C. Q. Jin, F. Gao, X. L. Wu, W. Zhong, S. H. Li, and Paul K. Chu. Raman scattering study of zinc blende and wurtzite ZnS. *Journal of Applied Physics*, 106(12), 2009. ISSN 0021-8979 1089-7550. doi: 10.1063/1.3270401.
- [90] W. Witte, R. Kniese, and M. Powalla. Raman investigations of Cu(In,Ga)Se_2 thin films with various copper contents. *Thin Solid Films*, 517(2):867–869, 2008. ISSN 00406090. doi: 10.1016/j.tsf.2008.07.011.
- [91] W. Witte and R. Kniese. Influence of the Ga content on the Mo/Cu(In,Ga)Se_2 interface formation, 2006.
- [92] C. Insignares-Cuello, C. Broussillou, V. Bermúdez, E. Saucedo, A. Pérez-Rodríguez, and V. Izquierdo-Roca. Raman scattering analysis of electrodeposited Cu(In,Ga)Se_2 solar cells: Impact of ordered vacancy compounds on cell efficiency. *Applied Physics Letters*, 105(2), 2014. ISSN 0003-6951 1077-3118. doi: 10.1063/1.4890970.
- [93] G. Lucovsky, A. Mooradian, W. Taylor, G.B. Wright, and R.C. Keezer. Identification of the fundamental vibrational modes of trigonal alpha-monoclinic and amorphous selenium. *Solid State Communications*, 5:113–117, 1967.
- [94] J. Han, L. Ouyang, D. Zhuang, C. Liao, Ji. Liu, M. Zhao, L. Cha, and M. Besland. Raman and XPS studies of CIGS/Mo interfaces under various annealing temperatures. *Materials Letters*, 136:278–281, 2014. ISSN 0167577X. doi: 10.1016/j.matlet.2014.08.087.
- [95] Y. Nam, J. Yoo, S. Chang, J. Wi, W. Lee, D. Cho, and Y. Chung. Photoluminescence of sulfur-incorporated CIGS solar cells through post-annealing. *Journal of Luminescence*, 188:595–599, 2017. ISSN 00222313. doi: 10.1016/j.jlumin.2017.05.012.
- [96] P. Guha. Electron transport processes in $\text{Cu(In}_{1-x}\text{Ga}_x\text{)Se}_2$ films prepared by four source co-evaporation technique. *Materials Chemistry and Physics*, 74, 2002.
- [97] K. Yoshino and H. Yokoyama. Crystal growth and photoluminescence of $\text{Cu(In}_x\text{Ga}_{1-x}\text{)Se}_2$ alloys. *Journal of Crystal Growth*, 211, 2000.
- [98] J. Yang, H. W. Du, Y. Li, M. Gao, Y. Z. Wan, F. Xu, and Z. Q. Ma. Structural defects and recombination behavior of excited carriers in Cu(In,Ga)Se_2 solar cells. *AIP Advances*, 6(8), 2016. ISSN 2158-3226. doi: 10.1063/1.4961701.
- [99] F. Wang, M. Z. Wu, Y. Y. Wang, Y. M. Yu, X. M. Wu, and L. J. Zhuge. Influence of thickness and annealing temperature on the electrical, optical and structural properties of AZO thin films. *Vacuum*, 89:127–131, 2013. ISSN 0042207X. doi: 10.1016/j.vacuum.2012.02.040.
- [100] P. Gečys, E. Markauskas, A. Žemaitis, and G. Račiukaitis. Variation of P2 series interconnects electrical conductivity in the CIGS solar cells by picosecond laser-induced modification. *Solar Energy*, 132:493–502, 2016. ISSN 0038092X. doi: 10.1016/j.solener.2016.03.027.
- [101] K. Bakker, H. Nilsson, K. Aantjes, N. Barreau, M. Theelen, and A. Weeber. Material property changes in defects caused by reversed bias exposure of CIGS solar cells. *Institute of Electrical and Electronics Engineers: Journal of Photovoltaics*, 2019.
- [102] M. Theelen, K. Bakker, H. Steijvers, S. Roest, P. Hielkema, N. Barreau, and E. Haverkamp. In situ monitoring of the accelerated performance degradation of solar cells and modules: A case study for Cu(In,Ga)Se_2 solar cells. *J Vis Exp*, 2018. ISSN 1940-087X (Electronic) 1940-087X (Linking). doi: 10.3791/55897. URL <https://www.ncbi.nlm.nih.gov/pubmed/30346379>.
- [103] S.C. Abrahams and J.L. Bernstein. Piezoelectric nonlinear optic CuGaSe_2 and CdGeAs_2 : Crystal structure, chalcopyrite microhardness, and sublattice distortion. *J. Chem. Phys.*, 61, 1974.

- [104] K. Nagata, Y. Miyamoto, and K. Takarabe. Refinement of the crystal structure of CuInSe_2 . *Fukuoka Daigaku Rigaku Shuho*, 19, 1989.
- [105] Z. Deng, C. Huang, J. Huang, M. Wang, H. He, H. Wang, and Y. Cao. Effects of al content on the properties of ZnO:Al films prepared by Al_2O_3 and ZnO co-sputtering. *Journal of Materials Science: Materials in Electronics*, 21(10):1030–1035, 2010. ISSN 0957-4522 1573-482X. doi: 10.1007/s10854-010-0084-0.
- [106] H. Khatri and S. Marsillac. The effect of deposition parameters on radiofrequency sputtered molybdenum thin films. *Journal of Physics: Condensed Matter*, 20(5), 2008. ISSN 0953-8984 1361-648X. doi: 10.1088/0953-8984/20/05/055206.
- [107] X. Geng, C. Zhang, and M. Debligny. Cadmium sulfide activated zinc oxide coatings deposited by liquid plasma spray for room temperature nitrogen dioxide detection under visible light illumination. *Ceramics International*, 42(4):4845–4852, 2016. ISSN 02728842. doi: 10.1016/j.ceramint.2015.11.170.

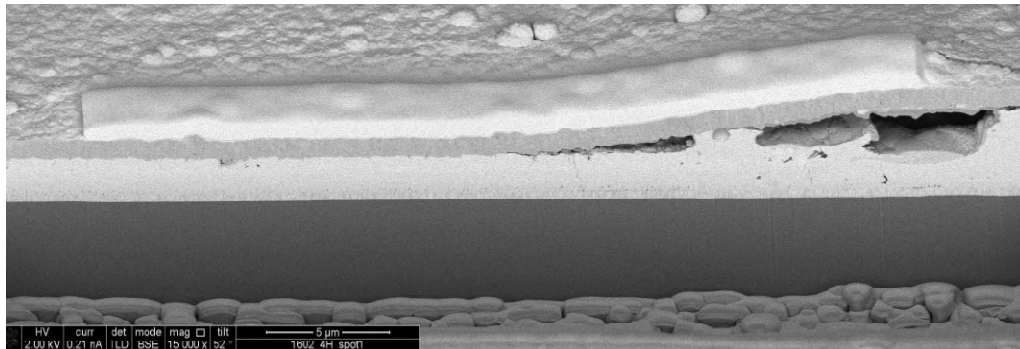


Eurofins SEM-EDS linescans and colour maps

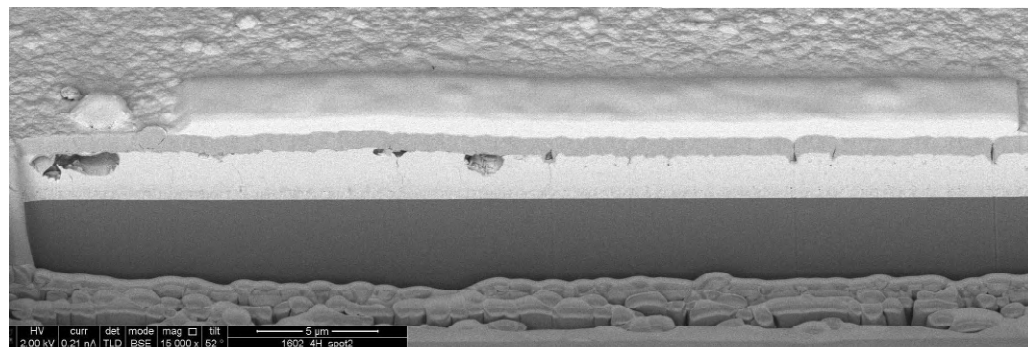
1602_4H - Overview



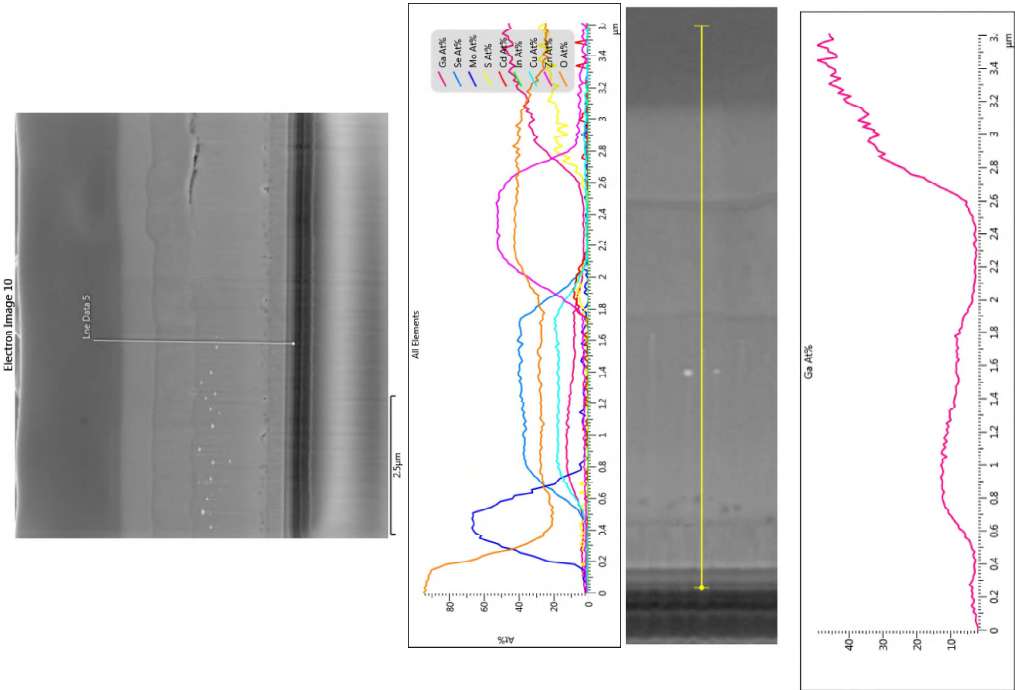
1602_4H Spot 1 - SEM image



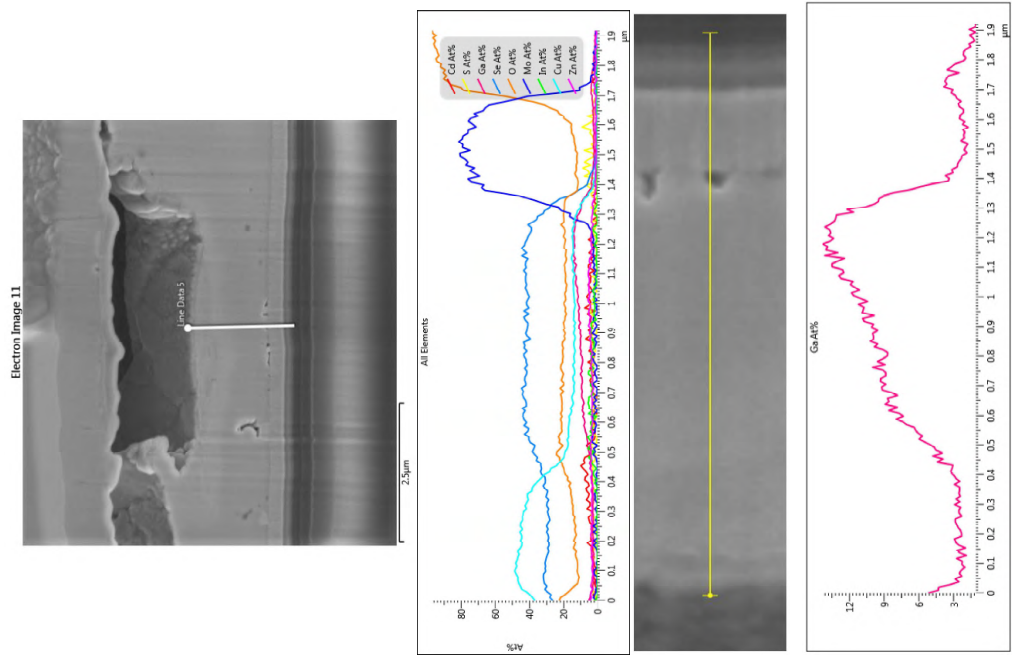
1602_4H Spot 2 - SEM image



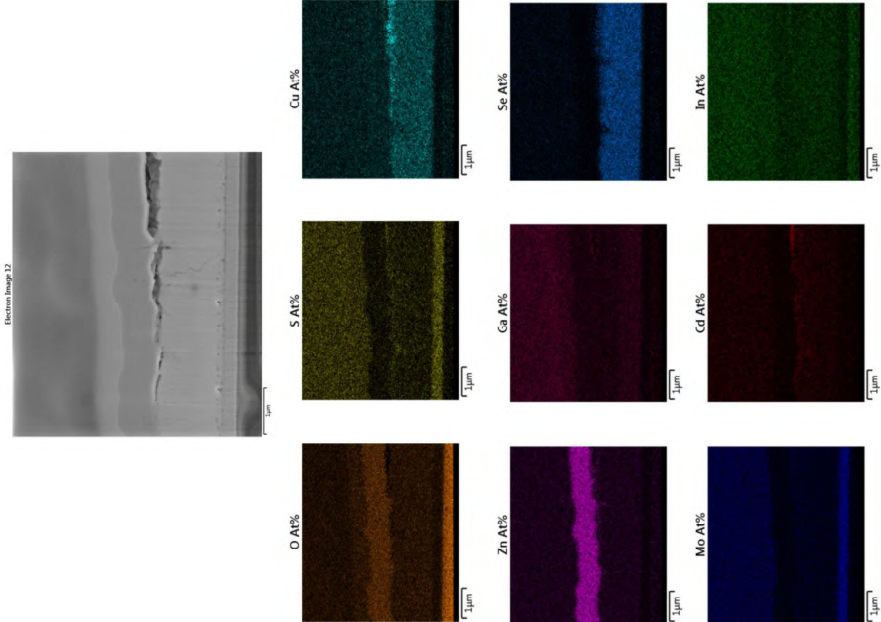
1602_4H Spot 1 – line EDS outside worm (1/2 from left)



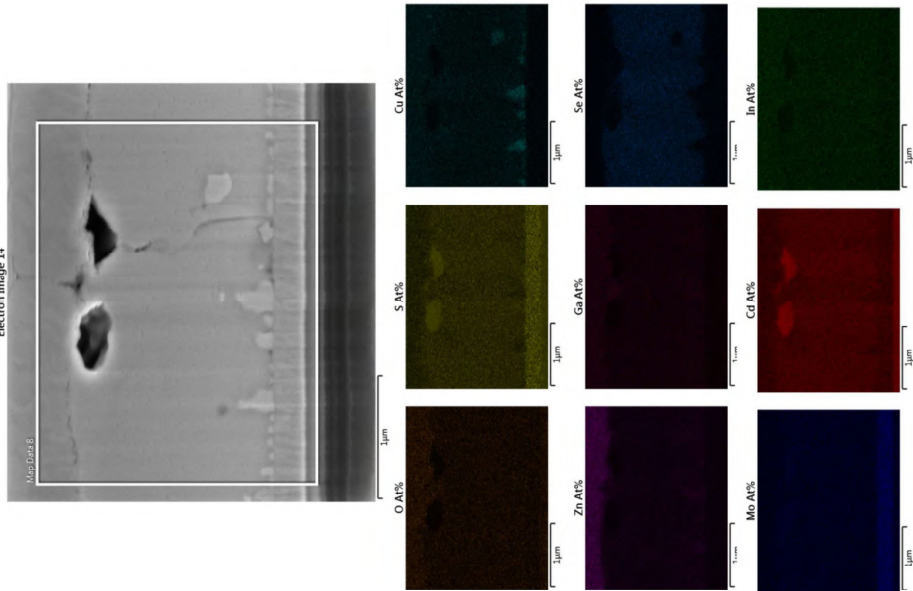
1602_4H Spot 1 – line EDS on worm (8/9 from left)



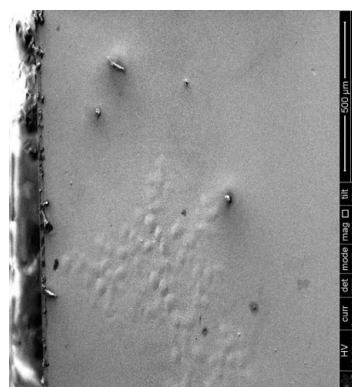
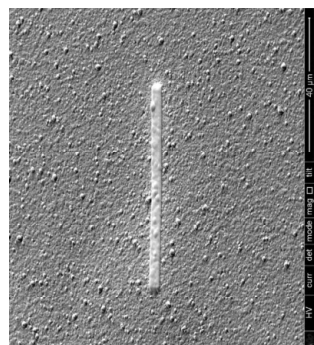
1602_4H Spot 1 – MAP on worm (1/2 from left)



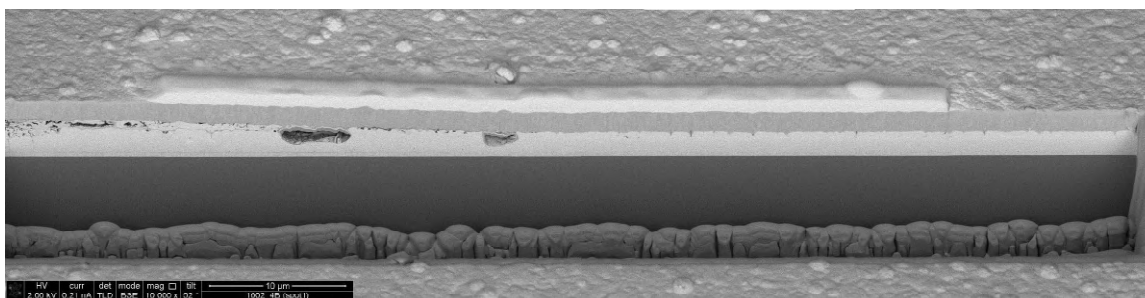
1602_4H Spot 2 – MAP on worm (1/3 from left)



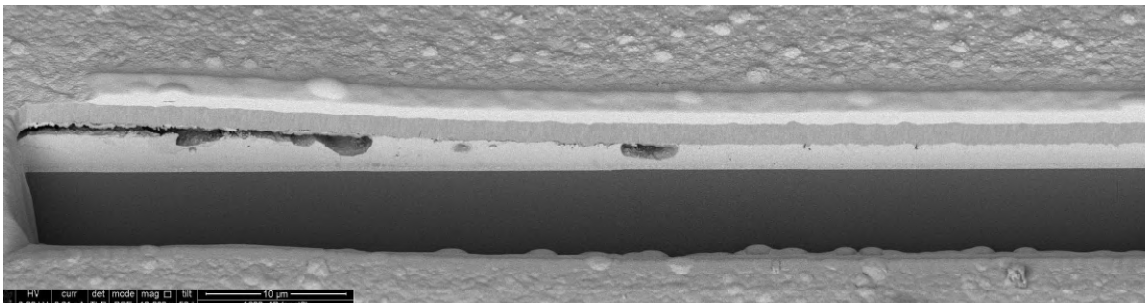
1602_4B – Overview



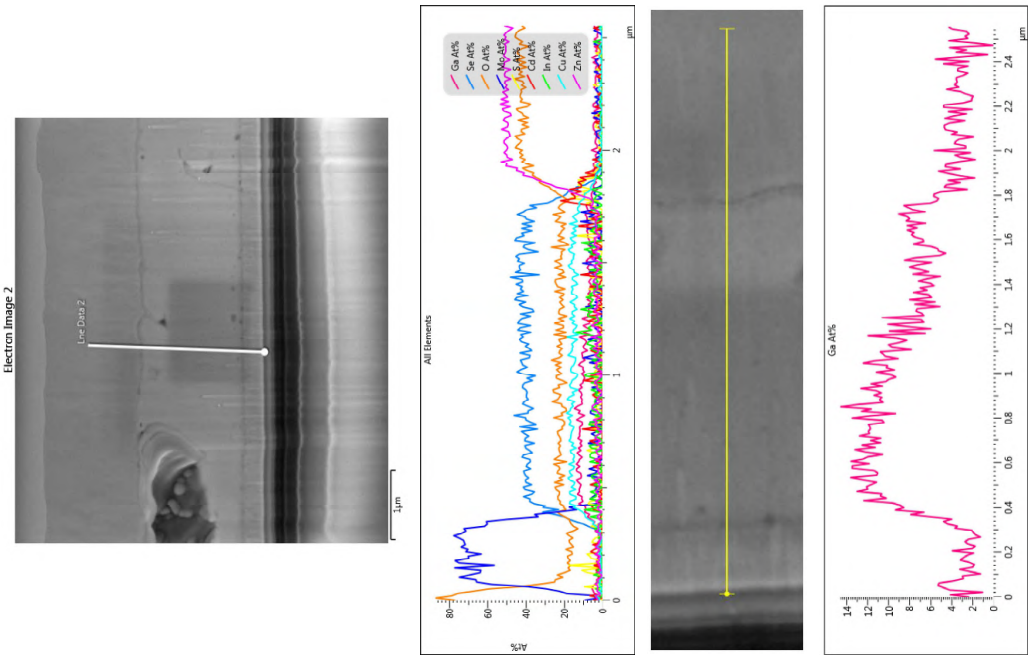
1602_4B Spot 1 – SEM image



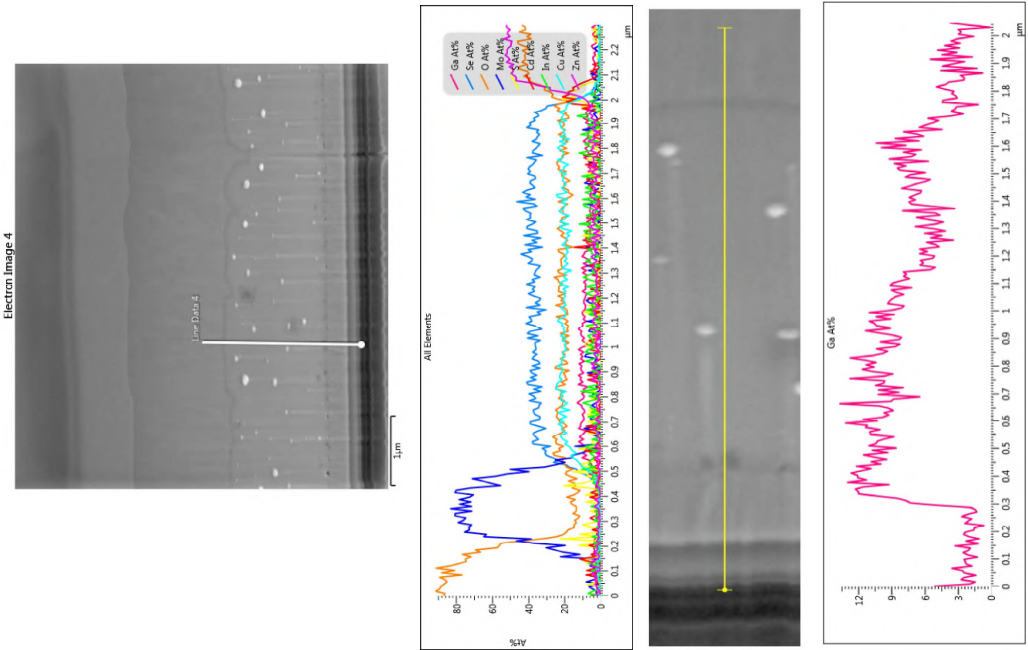
1602_4B Spot 2 – SEM image



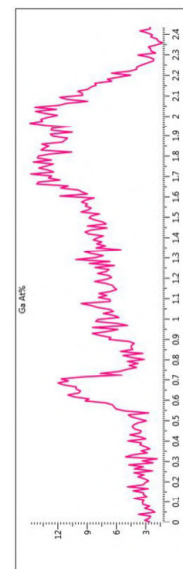
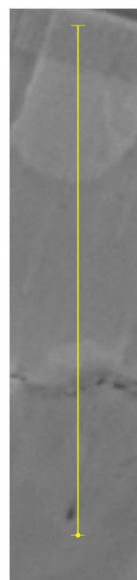
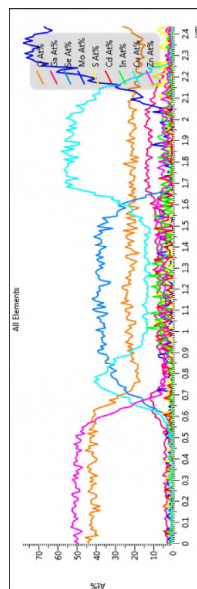
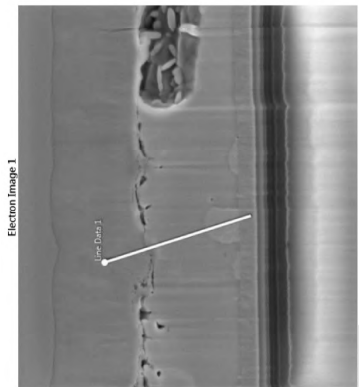
1602_4B Spot 2 – line EDS near defect (5/8 from left)



1602_4B Spot 2 – EDS away from worm

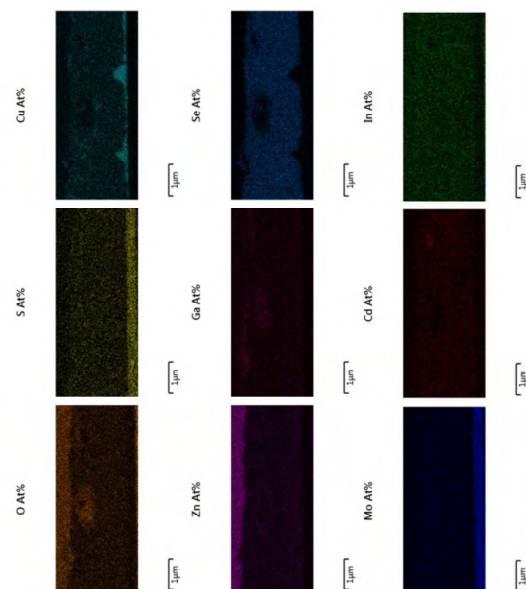


1602_4B Spot 2 – Line EDS on worm (1/2 from left)



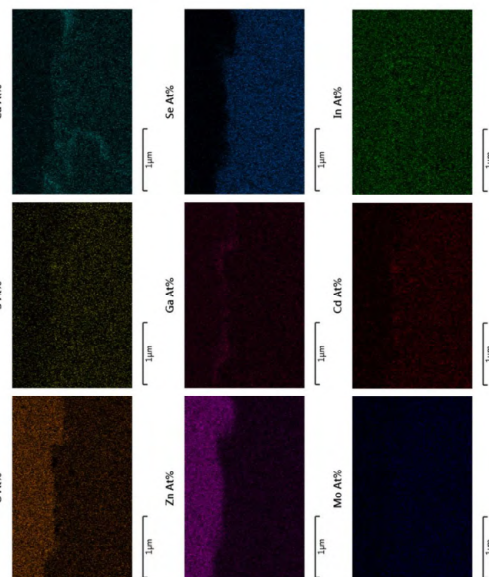
Electron Image 5

This grayscale micrograph shows a cross-section of a material with a layered structure. A central region of interest is labeled "Spectrum 1" with a small square box. A scale bar in the bottom right corner indicates a length of 1 μm. The text "Mag. Data 1" is visible in the bottom left corner.

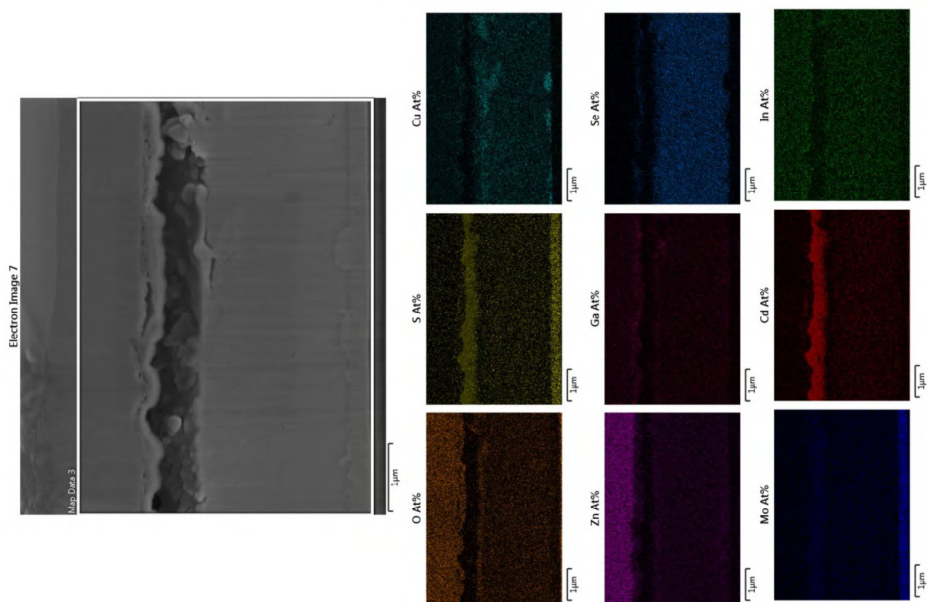


Electron image 6

Micrograph showing a crack in a polymer film. The crack is a vertical line running through the center of the image. The film is labeled $M_w = 20,000$ on the left. A scale bar at the bottom indicates 1 μm .



1602_4B spot 2 left



B

Raman peak positions overview

Cu(In,Ga)Se ₂										Cu(In,Ga)S ₂					
										Al CuInS ₂	Al CuGaS ₂	shoulder Al-S	Cu ₂ S	MoS ₂	
B1	InSe	InSe ₃	OVC	Al	Al	B2/E	Se	Cu ₂ -Se	Al CuInS ₂	Al CuGaS ₂					
CIIGSe	120-130	150	150-160	173-176	182-188	215-225, 261, 273	230-260	260-263	290-305	310	318	460	180-220-380-400-460		
115-130			155	174-175	188	212-273	263								
[4]				173-175					300(290, 305)						
[5]				173	186	200-250									
[6]				175		214		260	290		338	460			
[7]				174	185	212, 231		248, 271							
[8]			155	173											
[9]				173											
[10]	128	200	220, 235	173		215		260							
[11]				173					290						
[12]									290				378-403		
[13]			160	177			240	260	290				180-220-380-400-460		
[14]			150-160	173	183	212-240	240	260	290	310					
[15]				175 CIIGSe		CIIGSe 215, 228; CIGS 240, 266			300 CIGS						
[16]	116, 179, 228	152		175, 178 CIIGSe		215, 232 /220, 250	248		302 CIGS						
[17]			161		181	214, 225			290		321				
[18]				177-180 CIIGSe		213, 227									
[19]				175 single crystal CIIGSe											
[20]			150-160	175 CIIGSe		210-230			300-340 CIGS						
[21]	116, 124			174	184	206, 215, 199, 239, 168, 231, 259, 261, 279									
[22]			150	174		212-220	257	257							
[23]			150	173-174		220, 250		260							
[24]		120, 225		177, 8 CIIGSe				265							

- [4] M. Ahmadi, S. Pramana, C. Boothroyd and Y. Lam, "Elucidating the relationship between crystallo-chemistry and optical properties of CIGS nanocrystals," *Nanotechnology*, vol. 28 (4), p. 45708, 2017
- [5] J. Alvarez-García, B. Barcones, A. Pérez-Rodríguez, A. Romano-Rodríguez, J. R. Morante, A. Janotti, S.-H. Wei and R. Scheer, "Vibrational and crystalline properties of polymorphic CuInC_2 (C = Se, S) chalcogenides," *Phys. Rev. B*, vol. 71 (5) p. 54303, 2005
- [6] T. Bai, C. Liu, N. Wang and S. Liu, "Effects of sputtering voltage and current on the composition and microstructure of the CIGS films prepared by one-step pulsed DC magnetron sputtering," *J. Alloys Compounds*, vol. 646, 532–540, 2015
- [7] M. Beres, K. Yu, J. Syzdek, S. Mao, "Improvement in the electronic quality of pulsed laser deposited $\text{CuIn}_{0.7}\text{Ga}_{0.3}\text{Se}_2$ thin films via post-deposition elemental sulfur annealing process," *Thin Solid Films*, vol. 608 p. 50–56, 2016
- [8] X. Chuan-Ming, S. Yun, L. Feng-Yan, Z. Li, X. Yu-Ming, H. Qing and L. Hong-Tu, "Composition-induced structural modifications in the quaternary $\text{CuIn}_{1-x}\text{Ga}_x\text{Se}_2$ thin films: bond properties versus Ga content," *Chinese Phys.*, vol. 16 (3) p. 788–794, 2007
- [9] X. Fontané, V. Izquierdo-Roca, L. Calvo-Barrio, A. Pérez-Rodríguez, J. R. Morante, D. Guettler, A. Eicke and A. Tiwari, "Investigation of compositional inhomogeneities in complex polycrystalline Cu(In,Ga)Se_2 layers for solar cells," *Appl. Phys. Lett.*, vol. 95 (26) p. 261912, 2009
- [10] Y. Huang, Y. Tang, W. Yuan, X. Zhang, W. Wen and Q. Wang, "Growth and characterization of CIGS thin films by plasma-assisted and thermal-assisted Se vapor selenization process," *Journal of Alloys and Compounds*, vol. 701, p. 732-739, 2017
- [11] C. Insignares-Cuello, F. Oliva, M. Neuschitzer, X. Fontané, C. Broussillou, T. Goisard de Monsabert, E. Saucedo, C.M. Ruiz, A. Pérez-Rodríguez and V. Izquierdo-Roca, "Advanced characterization of electrodeposition-based high efficiency solar cells: Non-destructive Raman scattering quantitative assessment of the anion chemical composition in Cu(In,Ga)(S,Se)_2 absorbers," *Sol. Energy Mater. Sol. Cells*, vol. 143, p. 212–217, 2015
- [12] V. Izquierdo-Roca, A. Pérez-Rodríguez, J. R. Morante, J. Álvarez-García, L. Calvo-Barrio, V. Bermudez, P. P. Grand, L. Parissi, C. Broussillou and O. Kerrec, "Analysis of S-rich CuIn(S,Se)_2 layers for photovoltaic applications: Influence of the sulfurization temperature on the crystalline properties of electrodeposited and sulfurized CuInSe_2 precursors," *J. Appl. Phys.*, vol. 103 (12), p. 123109, 2008
- [13] V. Izquierdo-Roca, E. Saucedo, C. M. Ruiz, X. Fontané, L. Calvo-Barrio, J. Álvarez-García, P.-P. Grand, J. S. Jaime-Ferrer, A. Pérez-Rodríguez, J. R. Morante, and V. Bermudez, "Raman scattering and structural analysis of electrodeposited CuInSe_2 and S-rich quaternary CuIn(S,Se)_2 semiconductors for solar cells," *Phys. status solidi*, vol. 206 (5), p. 1001–1004, 2009
- [14] V. Izquierdo-Roca, X. Fontane, E. Saucedo, J. S. Jaime-Ferrer, J. Alvarez-Garcia, A. Perez-Rodríguez, V. Bermudez and J. Ramon Morante, "Process monitoring of chalcopyrite photovoltaic technologies by Raman spectroscopy: an application to low cost electrodeposition based processes," *New J. Chem.* vol. 35, p. 453–460, 2011
- [15] S. Kim and J. Kim, "Fabrication of CIGS thin films by using spray pyrolysis and post-selenization," *J. Korean Phys. Soc.*, vol. 60 (12) p. 2018–2024, 2012
- [16] I. Klugius, R. Miller, A. Quintilla, T. Friedlmeier, D. Blázquez-Sánchez, E. Ahlswede and M. Powalla, "Rapid thermal processing for printed Cu(In,Ga)(S,Se)_2 solar cells: Comparison of precursor materials," *Thin Solid Films*, vol. 535, p. 107–111, 2013
- [17] Y. Lin, W. Yen, Y. Chen, L. Wang and F. Jih, "Influence of annealing temperature on properties of Cu(In,Ga)(Se,S)_2 thin films prepared by cosputtering from quaternary alloy and In_2S_3 targets," *Physica B* vol. 406, p. 824–830, 2011
- [18] L. Minkevičius, S. Balakauskas, M. Šoliūnas, R. Suzanovičienė, J. Uzėla, G. Molis, R. Juškėnas, A. Selskis, G. Niaura, G. Valušis and V. Tamošiūnas, "Far infrared spectroscopy and imaging of Cu(In,Ga)Se_2 layers," *Lith. J. Phys.*, vol. 53 (4), p. 219–226, 2013
- [19] A. Nagaoka, Y. Nose, H. Miyake, M. Scarpulla, K. Yoshin, "Solution growth of chalcopyrite compounds single crystal," *Renewable Energy*, vol. 79, p. 127-130, 2015
- [20] F. Oliva, S. Kretzschmar, D. Colombara, S. Tombolata, C. M. Ruiz, A. Redinger, E. Saucedo and C. Broussillou, "Optical methodology for process monitoring of chalcopyrite photovoltaic technologies: Application to low cost Cu(In,Ga)(S,Se)_2 electrodeposition based processes," *Sol. Energy Mater. Sol. Cells*, vol. 158 (2), pp 168-183 (2016)
- [21] C. Rincon, F. Ramirez, "Lattice vibrations of CuInSe_2 and CuGaSe_2 by Raman microspectrometry," *J. Appl. Phys.*, vol. 72 (9), p. 4321-4324, 1992
- [22] W. Wei, "Fabrication of CuInGaSe_2 thin film solar cells using low-cost air-stable inks," dissertation, 2012
- [23] W. Witte, R. Knieese, and M. Powalla, "Raman investigations of Cu(In,Ga)Se_2 thin films with various copper contents," *Thin Solid Films*, vol. 517 (2), p. 867–869, 2008
- [24] S. Zakel, B. Pollakowski, C. Streeck, S. Wundrack, A. Weber, S. Brunken, R. Mainz, B. Beckhoff and R. Stosch, "Traceable Quantitative Raman Microscopy and X-ray Fluorescence Analysis as Nondestructive Methods for the Characterization of Cu(In,Ga)Se_2 Absorber Films," *Appl. Spectroscopy*, vol. 70 (2), p. 279–288, 2016

C

Monte-Carlo simulation with 'Casino v2'

Monte-Carlo simulation with 'CASINO V2'

Stacking without ZnO and CdS

Settings:

20000 Trajectories
6, 12 and 18kV
Standard model settings
Beam radius 60nm

Stack of layers:

CIGS - 2000nm

Atomic fractions: Cu = 0,24, In = 0,17, Ga = 0,08, Se = 0,51
Density 5,88g/cm²

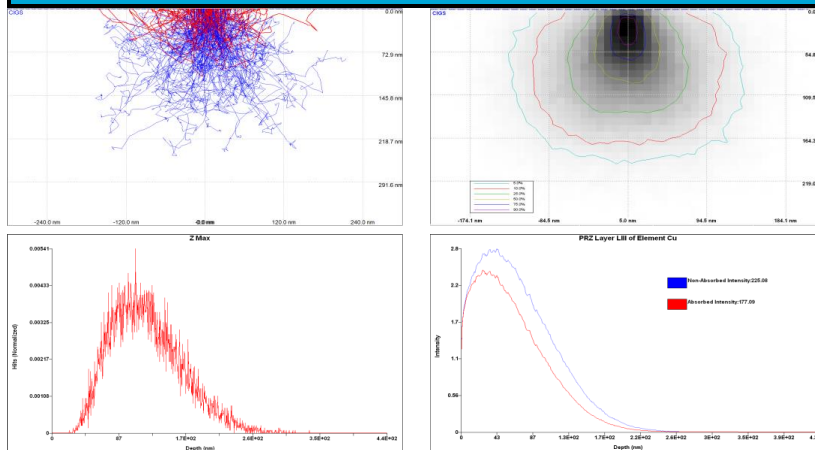
Mo - 500nm

Atomic fractions: Mo = 1,0
Density 10,2g/cm²

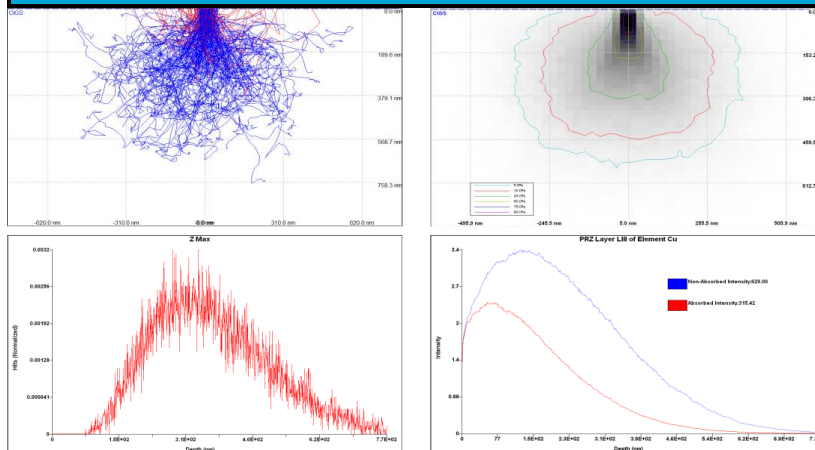
Soda lime glass - Substrate

Atomic fractions: Si = 0,182, O = 0,732, Ca = 0,01, Na = 0,068
Density 5,52g/cm²

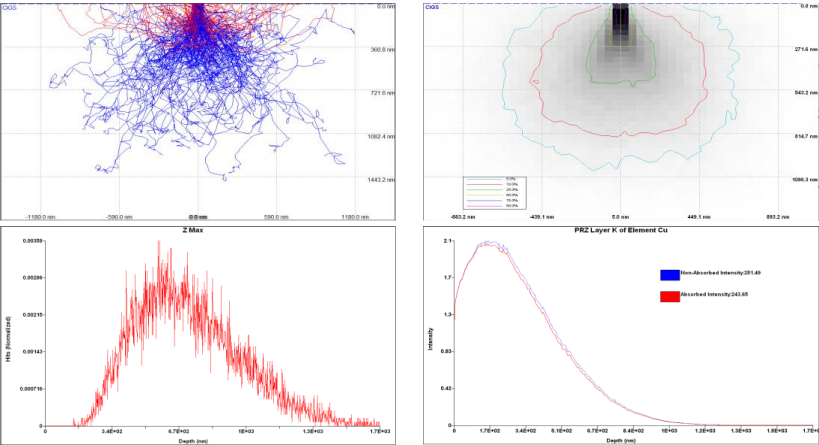
6kV



12kV



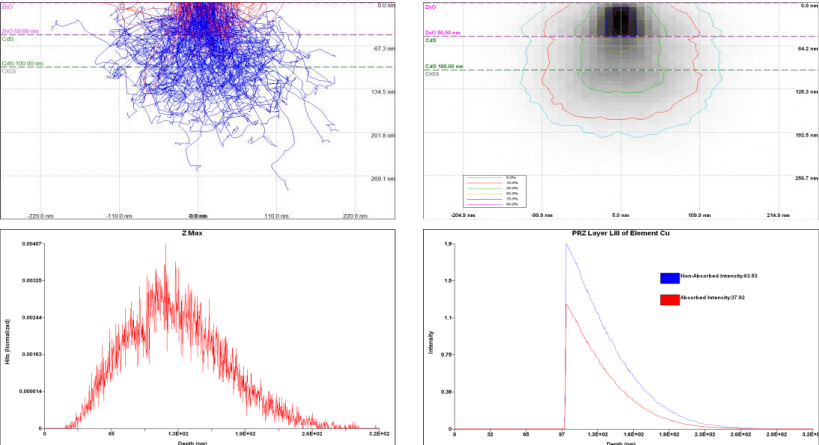
18kV

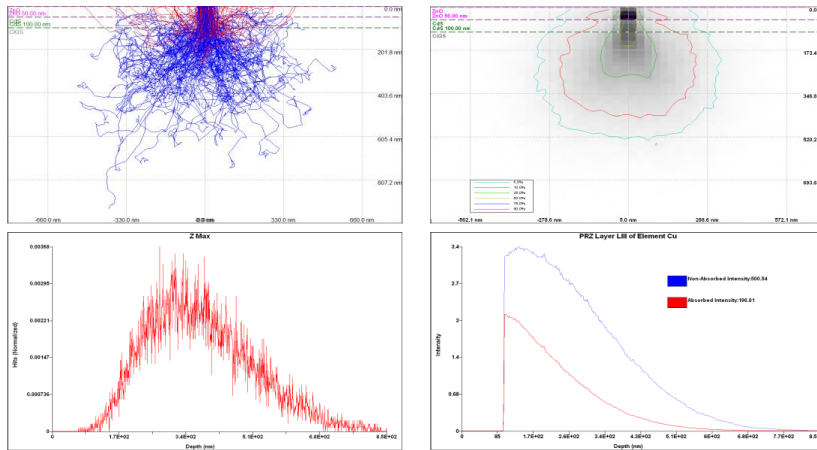
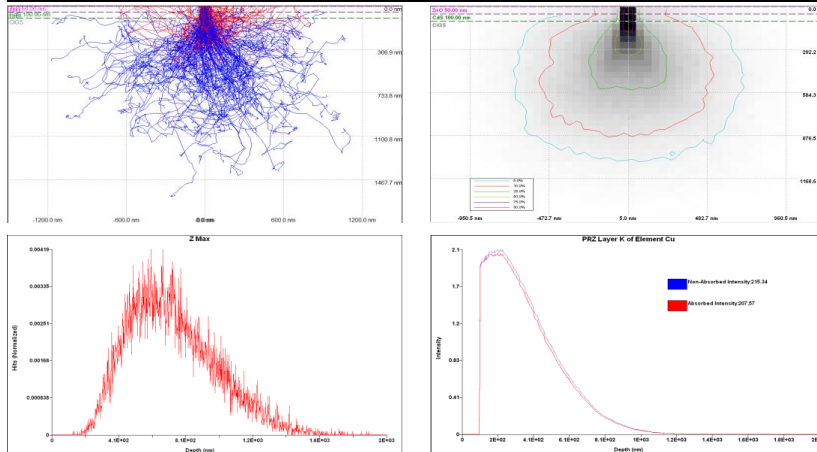


Stacking with i:ZnO and CdS

Settings: 20000 Trajectories 6, 12 and 18kV Standard model settings Beam radius 60nm	CIGS - 2000nm Atomic fractions: Cu = 0.24, In = 0.17, Ga = 0.08, Se = 0.51 Density 5.88g/cm ²
Stack of layers: ZnO- 50nm Atomic fractions: Zn = 0.5, O = 0.5 Density 5.61g/cm ²	Mo - 500nm Atomic fractions: Mo = 1,0 Density 10.2g/cm ²
CdS - 50nm Atomic fractions: Cd = 0.5, S = 0.5 Density 4.82g/cm ²	Soda lime glass - Substrate Atomic fractions: Si = 0.182, O = 0.732, Ca = 0.01, Na = 0.068 Density 5.52g/cm ²

6kV

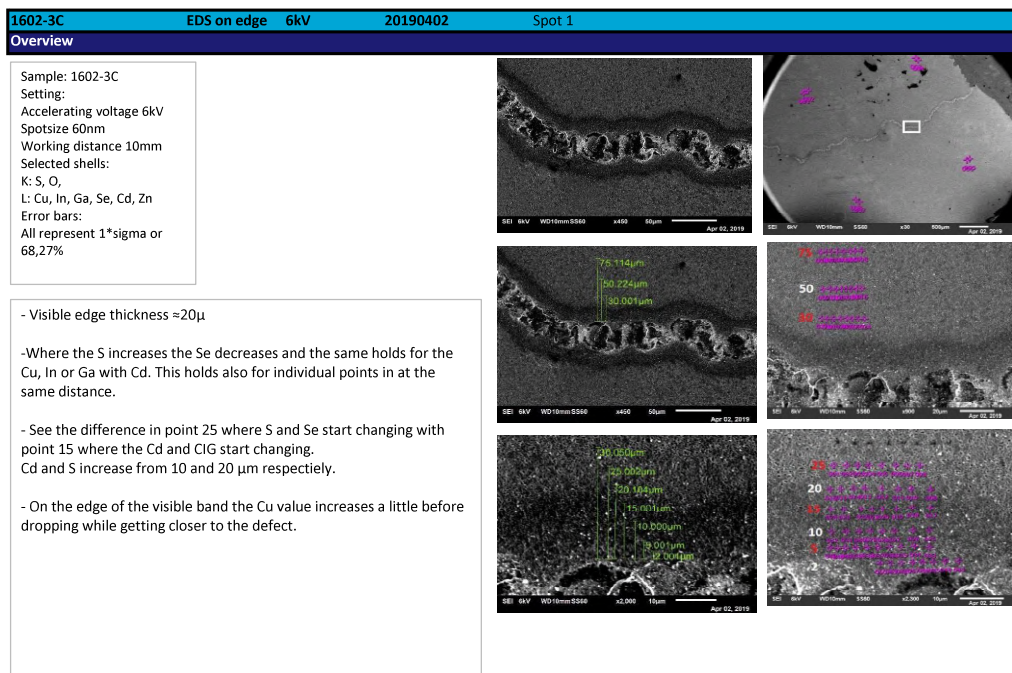


12kV**18kV**

D

Nantes samples EDS and mapping

D.1. Nantes EDS



1602-3C		EDS on edge		6kV		20190402		Spot 1											
At%																			
Measurement		Cu	In	Ga	Se	Cd	S	Zn	O	Meas.	GGI	CGI	S/cd	Se/CIG	NGGI	NCGI	NS/cd	NSe/CIG	
Bulk		14.0	15.5	7.4	52.6	1.9	7.3	0.0	1.3	Bulk	0.32	0.61	4.79	1.43	1.00	1.00	1.00	1.00	
75		14.5	14.5	7.4	50.8	2.5	9.2	0.0	1.1	75	0.34	0.67	8.45	1.40	1.04	1.10	1.76	0.98	
50		15.0	14.5	7.4	50.6	2.0	9.7	0.0	0.9	50	0.34	0.69	4.72	1.37	1.05	1.12	0.99	0.96	
30		15.8	14.9	6.7	48.6	2.1	10.4	0.0	1.5	30	0.31	0.74	27.95	1.30	0.96	1.21	5.83	0.91	
25		15.0	14.6	6.2	51.2	2.4	8.5	0.0	2.1	25	0.30	0.72	4.44	1.43	0.92	1.18	0.93	1.00	
20		15.7	13.3	6.1	46.4	3.1	13.1	0.0	2.3	20	0.32	0.82	4.41	1.32	0.99	1.34	0.92	0.92	
15		18.0	9.8	5.3	41.5	4.0	19.6	0.0	1.7	15	0.36	1.20	7.03	1.27	1.11	1.97	1.47	0.89	
10		15.2	7.3	5.5	39.0	10.8	20.1	0.0	2.1	10	0.43	1.24	2.12	1.41	1.34	2.02	0.44	0.99	
5		9.7	3.4	4.8	37.7	21.2	20.5	0.0	2.8	5	0.61	1.29	0.97	2.13	1.88	2.11	0.20	1.49	
2		6.3	7.0	2.5	38.6	18.5	20.6	3.5	3.0	2	0.29	0.71	1.17	2.48	0.89	1.15	0.24	1.74	

Mass%									Standard deviation								
Measurement	Cu	In	Ga	Se	Cd	S	Zn	O	Meas.	GGI	CGI	S/cd	Se/CIG	NGGI	NCGI	NS/cd	NSe/CIG
Bulk	10.8	25.0	6.8	50.3	4.3	2.3	nd	0.6	Bulk	0.02	0.06	2.91	0.09	0.00	0.00	0.00	0.00
75	12.9	20.5	6.9	54.4	1.6	3.7	nd	nd	75	0.04	0.09	10.06	0.07	0.13	0.15	2.10	0.05
50	11.0	23.3	6.1	52.0	3.7	3.9	nd	0.0	50	0.04	0.07	3.78	0.09	0.11	0.12	0.79	0.06
30	13.0	23.5	6.2	51.2	0.8	5.0	nd	0.4	30	0.02	0.10	60.47	0.04	0.07	0.16	12.61	0.03
25	12.2	23.3	5.2	53.1	2.4	3.3	nd	0.5	25	0.03	0.07	2.15	0.05	0.09	0.12	0.45	0.03
20	15.9	12.8	6.7	47.9	6.5	9.2	nd	1.0	20	0.06	0.16	0.83	0.04	0.20	0.26	0.17	0.03
15	17.7	18.0	5.2	43.5	5.0	10.4	nd	0.3	15	0.06	0.15	3.71	0.20	0.19	0.25	0.77	0.14
10	11.4	7.2	4.3	38.9	27.4	10.3	nd	0.6	10	0.04	0.35	0.90	0.18	0.11	0.58	0.19	0.13
5	7.2	3.6	4.9	37.7	36.7	9.0	nd	0.9	5	0.09	0.59	0.09	0.19	0.28	0.96	0.02	0.13
2	5.3	5.5	3.3	38.5	37.8	9.3	nd	0.3	2	0.13	0.19	0.26	0.34	0.41	0.31	0.05	0.24

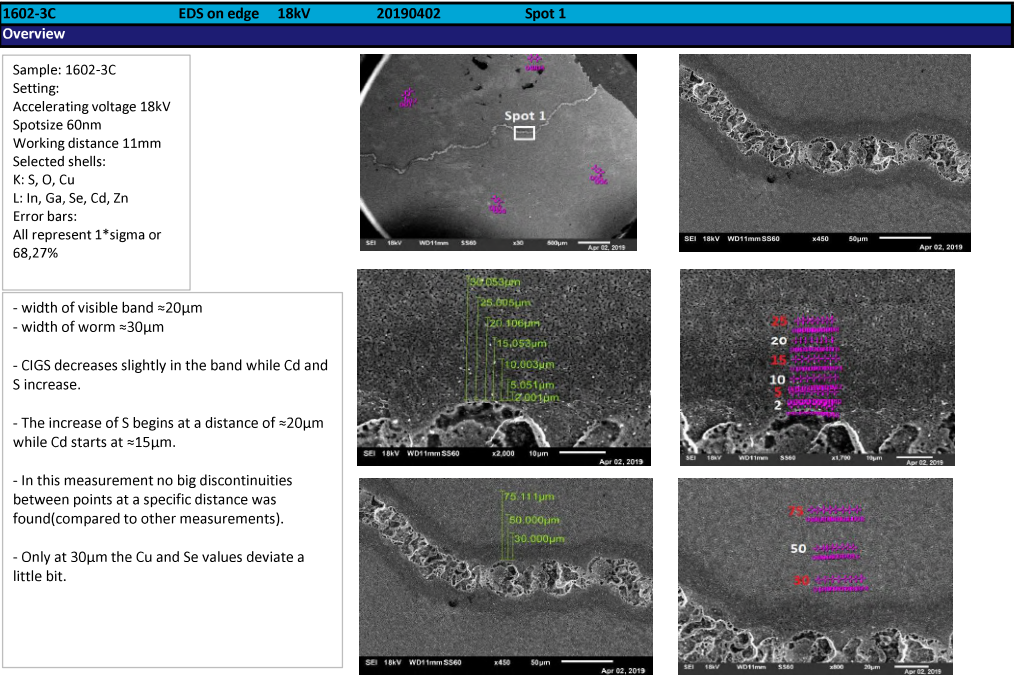
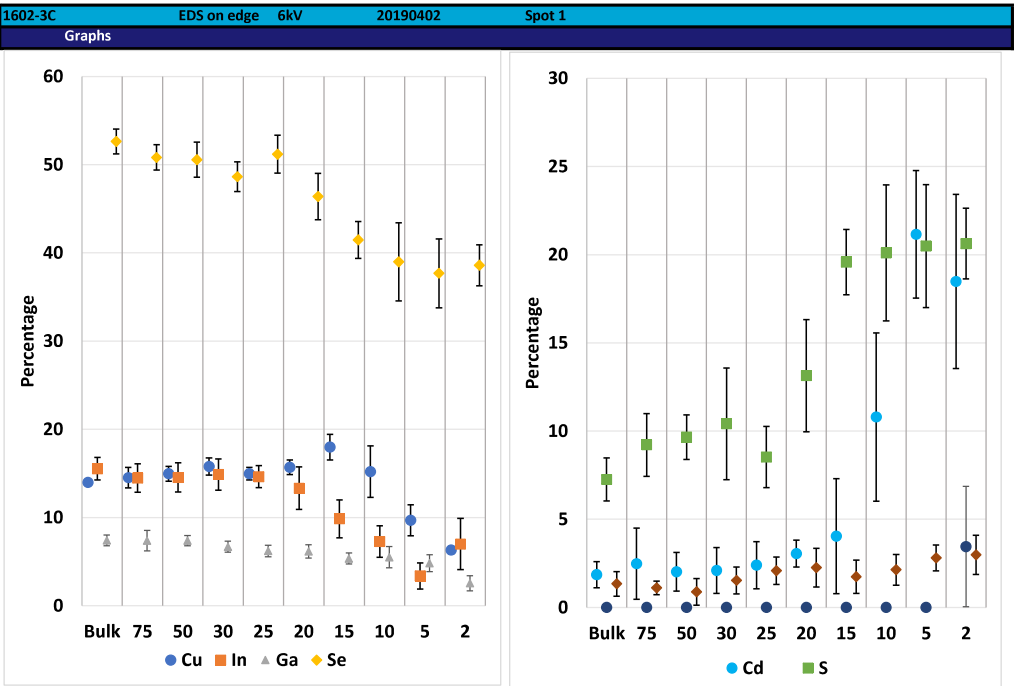


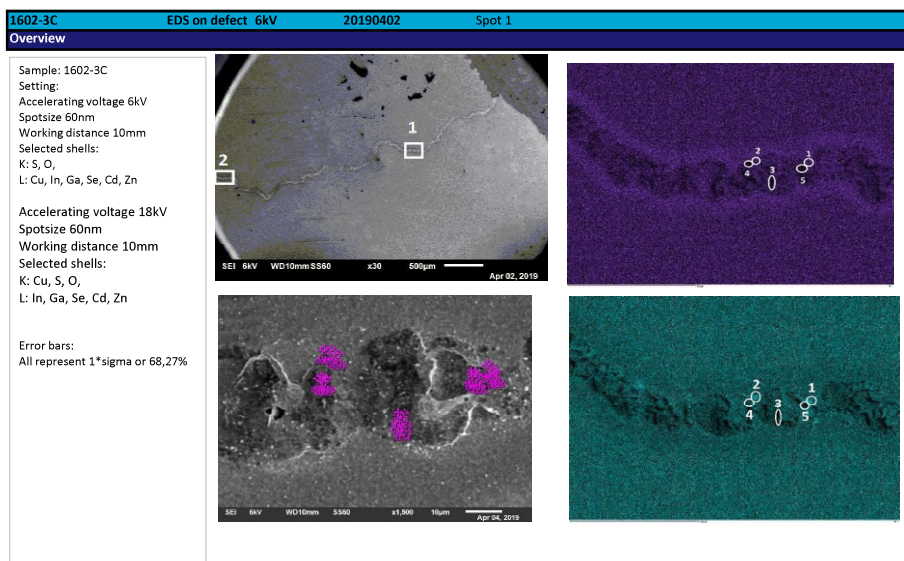
Figure 1 consists of two scatter plots showing the percentage of elements in the bulk and surface of the EDS on edge. The left plot shows the percentage of Cu, In, Ga, and Se. The right plot shows the percentage of Cd, S, Zn, and O. Both plots show a general trend of increasing percentage with increasing distance from the surface (Bulk to 2).

Left Plot: Percentage of Cu, In, Ga, and Se

Distance	Cu (%)	In (%)	Ga (%)	Se (%)
Bulk	24	17	7	49
75	24	17	7	50
50	24	17	6	49
30	24	17	6	49
25	25	17	6	49
20	24	17	6	49
15	25	16	6	49
10	24	16	6	46
5	22	16	6	46
2	21	16	5	46

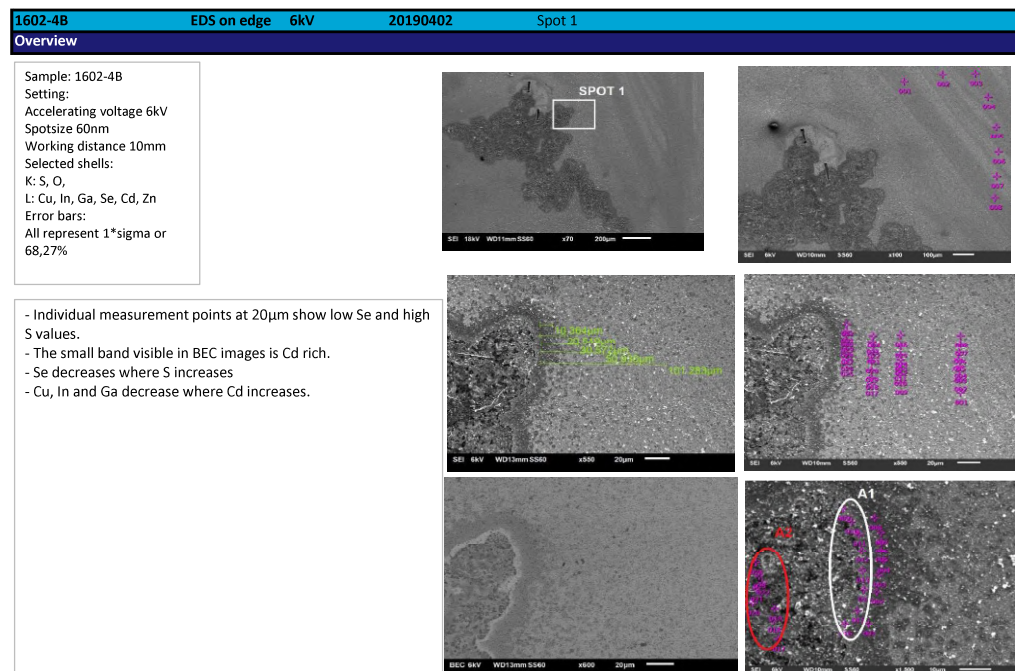
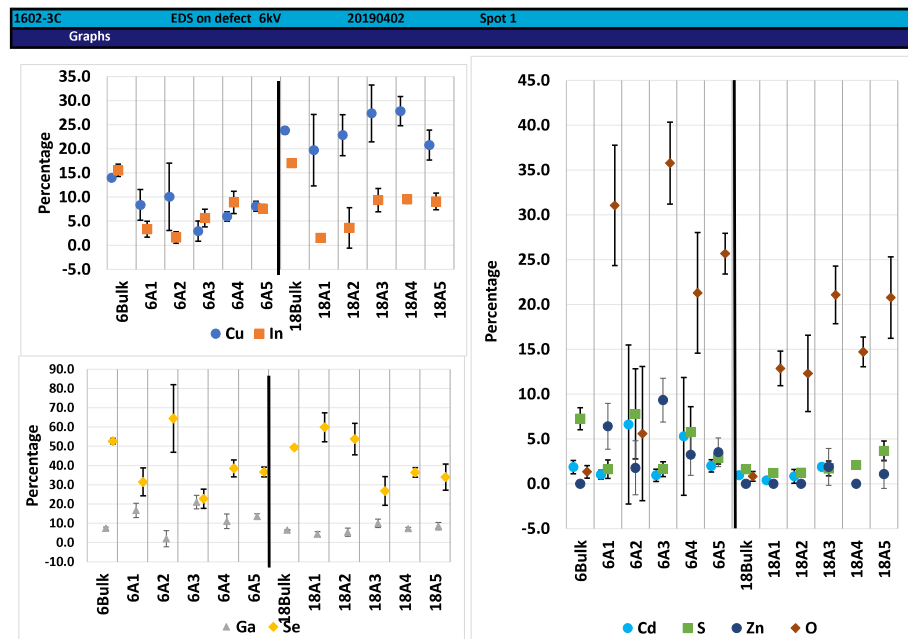
Right Plot: Percentage of Cd, S, Zn, and O

Distance	Cd (%)	S (%)	Zn (%)	O (%)
Bulk	1.0	1.6	0.0	0.9
75	1.1	2.0	0.0	0.5
50	1.4	2.3	0.0	1.1
30	1.1	1.9	0.0	1.2
25	0.9	2.2	0.0	1.2
20	1.1	2.4	0.0	0.8
15	1.7	3.9	0.0	0.7
10	4.5	4.9	0.0	0.9
5	5.4	4.8	0.0	1.5
2	6.8	5.1	0.0	1.9



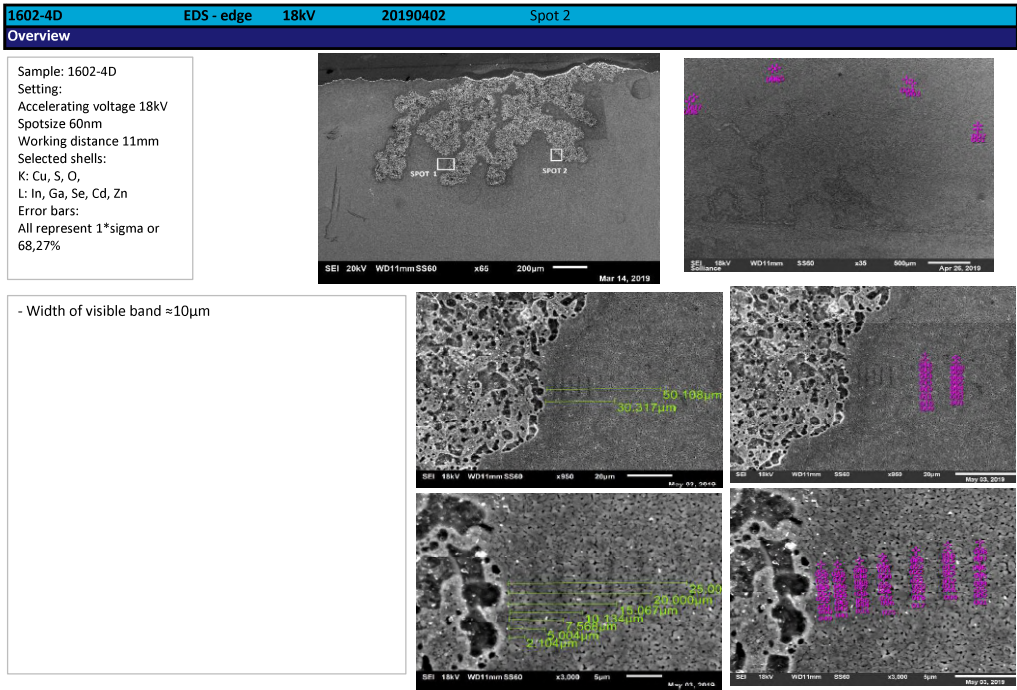
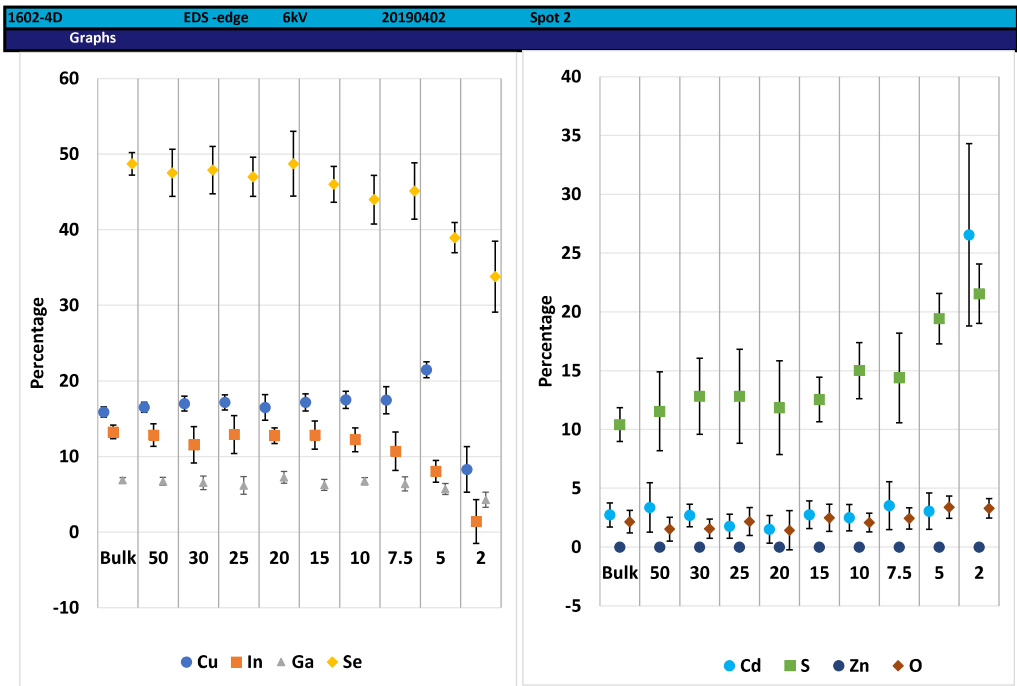
1602-3C		EDS on defect 6kV							20190402		Spot 1									
At%													Normalized ratio's							
Measurement	Cu	In	Ga	Se	Cd	S	Zn	O	Meas.	GGI	CGI	S/cd	Se/ClG	NGGI	NCGI	NS/Cd	NSe/ClG			
6Bulk	14.0	15.5	7.4	52.6	1.9	7.3	0.0	1.3	6Bulk	0.32	0.61	4.79	1.43	1.00	1.00	1.00	1.00			
6A1	8.4	3.3	16.7	31.5	1.0	1.6	6.4	31.1	6A1	0.83	0.45	1.52	1.11	2.57	0.73	0.32	0.78			
6A2	10.1	1.6	2.0	64.5	6.6	7.8	1.8	5.6	6A2	0.19	0.64	2.57	0.94	0.60	1.05	0.54	0.66			
6A3	2.9	5.7	21.0	22.8	0.9	1.6	9.3	35.8	6A3	0.79	0.12	1.65	0.77	2.43	0.19	0.34	0.54			
6A4	6.0	8.9	11.0	38.5	5.3	5.8	3.2	21.3	6A4	0.54	0.35	1.62	1.60	1.67	0.57	0.34	1.12			
6A5	8.1	7.6	13.6	36.6	2.0	2.9	3.5	25.7	6A5	0.64	0.38	1.80	1.25	1.99	0.63	0.37	0.88			
18Bulk	23.8	17.0	6.5	49.3	1.0	1.6	0.0	0.8	18Bulk	0.28	1.01	1.82	1.04	0.28	1.01	1.82	1.04			
18A1	19.7	1.5	4.4	59.9	0.4	1.2	0.0	12.9	18A1	0.74	3.36	3.51	2.73	2.69	3.32	1.92	2.62			
18A2	22.8	3.6	5.4	53.7	0.8	1.2	0.0	12.3	18A2	0.67	3.22	3.64	1.74	2.42	3.18	1.99	1.66			
18A3	27.3	9.4	10.0	26.8	1.9	1.7	1.9	21.1	18A3	0.52	1.45	0.88	0.59	1.87	1.42	0.47	0.57			
18A4	27.8	9.5	7.2	36.4	2.2	2.1	0.0	14.7	18A4	0.75	1.51	1.18	1.07	2.70	1.49	0.65	1.02			
18A5	20.8	9.1	8.5	34.0	2.1	3.7	1.1	20.8	18A5	0.48	1.18	1.69	0.90	1.75	1.16	0.90	0.87			

Mass%									Standard deviation								
Measurement	Cu	In	Ga	Se	Cd	S	Zn	O	Meas.	GGI	CGI	S/cd	Se/ClG	NGGI	NCGI	NS/Cd	NSe/ClG
6Bulk	10.8	25.0	6.8	50.3	4.3	2.3	nd	0.6	6Bulk	0.02	0.06	2.91	0.09	0.00	0.00	0.00	0.00
6A1	7.3	6.1	26.4	33.2	2.7	0.4	12.0	12.0	6A1	0.10	0.24	1.18	0.26	0.30	0.40	0.25	0.18
6A2	17.5	nd	nd	76.0	4.3	1.8	nd	0.4	6A2	0.30	1.30	2.81	1.32	0.91	2.12	0.59	0.93
6A3	5.5	14.4	18.1	40.7	4.0	1.5	7.9	7.9	6A3	0.07	0.09	1.14	0.19	0.23	0.15	0.24	0.13
6A4	7.3	15.4	11.1	49.7	6.1	2.7	2.7	5.0	6A4	0.09	0.22	0.70	0.68	0.29	0.37	0.15	0.47
6A5	7.4	13.4	16.1	47.7	3.3	1.2	4.5	6.5	6A5	0.04	0.07	1.42	0.10	0.12	0.12	0.30	0.07
18Bulk	19.7	24.3	5.6	48.6	1.0	0.7	nd	0.1	18Bulk	0.01	0.03	0.59	0.03	1.00	1.00	1.00	1.00
18A1	24.3	4.2	4.2	63.5	0.8	0.7	nd	2.3	18A1	0.11	1.29	1.21	1.56	0.39	1.27	0.66	1.50
18A2	14.0	22.6	10.3	43.5	3.9	0.7	nd	5.0	18A2	0.18	1.33	4.24	0.45	0.67	1.31	2.32	0.43
18A3	29.8	16.2	8.8	37.1	2.9	0.8	nd	4.4	18A3	0.10	0.43	0.28	0.21	0.35	0.42	0.16	0.20
18A4	0.0	0.0	0.0	0.0	0.0	0.0	0.0	0.0	18A4	0.21	0.50	0.16	0.24	0.76	0.49	0.09	0.23
18A5	17.8	19.3	5.8	46.8	4.6	2.0	nd	3.7	18A5	0.10	0.16	0.38	0.23	0.36	0.16	0.23	0.22

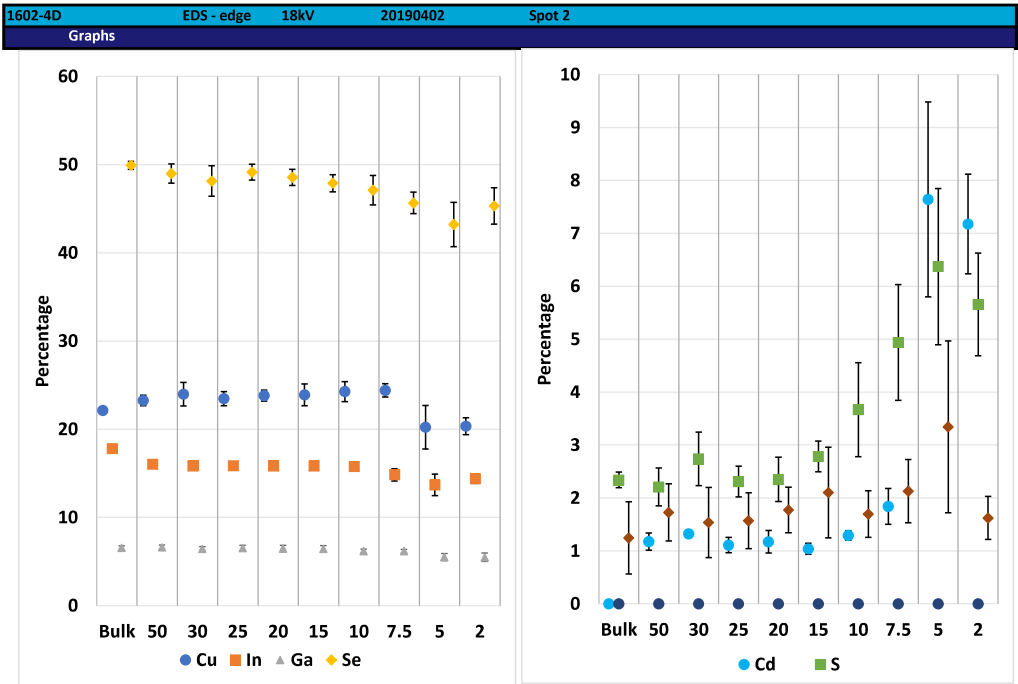


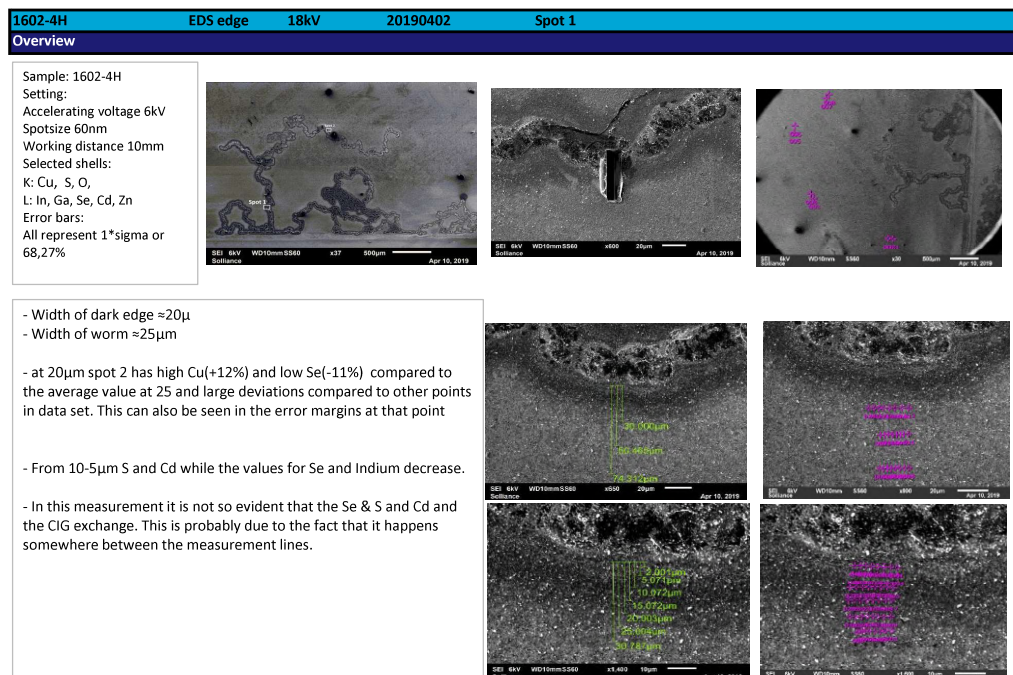
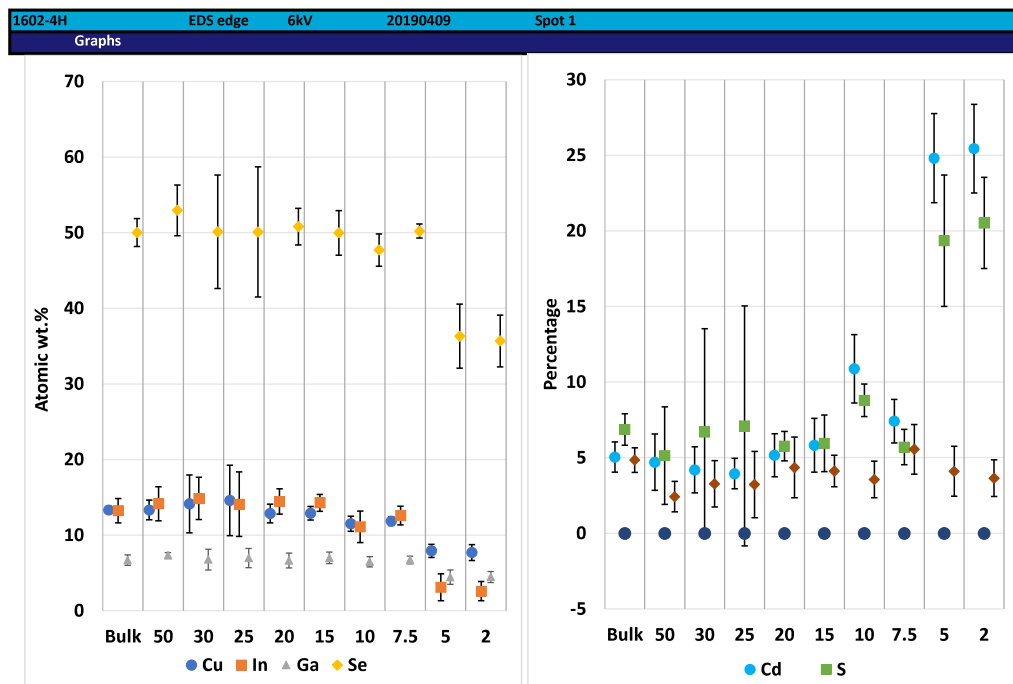
1602-4D		EDS-edge		6kV		20190402		Spot 2										
At%									Normalized ratio's									
Measurement		Cu	In	Ga	Se	Cd	S	Zn	O	Meas.	GGI	CGI	S/cd	Se/CIG	NGGI	NCGI	NS/cd	NSe/CIG
	Bulk	15.9	13.2	6.9	48.7	2.7	10.4	0.0	2.2	Bulk	0.34	0.79	4.20	1.35	1.00	1.00	1.00	1.00
	50	16.5	12.8	6.7	47.5	3.4	11.5	0.0	1.5	50	0.34	0.85	5.51	1.32	1.01	1.08	1.31	0.97
	30	17.0	11.5	6.5	47.9	2.7	12.8	0.0	1.6	30	0.36	0.98	5.29	1.37	1.07	1.24	1.26	1.01
	25	17.2	12.9	6.2	47.0	1.8	12.8	0.0	2.2	25	0.33	0.92	4.00	1.30	0.96	1.16	0.95	0.96
	20	16.5	12.7	7.3	48.7	1.5	11.8	0.0	1.4	20	0.36	0.83	1.94	1.34	1.06	1.05	0.46	0.99
	15	17.2	12.8	6.2	46.0	2.7	12.5	0.0	2.5	15	0.33	0.91	5.59	1.27	0.96	1.15	1.33	0.94
	10	17.5	12.2	6.7	44.0	2.5	15.0	0.0	2.1	10	0.36	0.93	7.52	1.21	1.05	1.17	1.79	0.89
	7.5	17.4	10.7	6.4	45.1	3.5	14.4	0.0	2.4	7.5	0.38	1.05	3.90	1.32	1.11	1.33	0.93	0.98
	5	21.5	8.0	5.7	38.9	3.1	19.4	0.0	3.4	5	0.42	1.59	8.40	1.11	1.22	2.01	2.00	0.82
	2	8.3	1.4	4.3	33.8	26.6	21.5	0.0	3.3	2	0.36	0.77	0.87	1.08	1.05	0.97	0.21	0.80

Mass%									Standard deviation									
Measurement		Cu	In	Ga	Se	Cd	S	Zn	O	Meas.	GGI	CGI	S/cd	Se/CIG	NGGI	NCGI	NS/cd	NSe/CIG
	Bulk	13.2	20.9	6.2	52.4	3.1	3.6	nd	0.5	Bulk	0.02	0.06	1.26	0.07	0.00	0.00	0.00	0.00
	50	14.6	17.3	6.2	53.8	2.0	5.6	nd	0.7	50	0.03	0.10	4.33	0.08	0.08	0.12	1.03	0.06
	30	15.0	16.8	6.6	52.6	2.5	6.3	nd	0.2	30	0.04	0.28	2.18	0.12	0.11	0.35	0.52	0.09
	25	15.6	17.2	5.7	49.6	4.7	6.2	nd	1.0	25	0.06	0.18	3.14	0.10	0.17	0.23	0.75	0.07
	20	12.3	17.9	6.6	54.5	3.9	3.9	nd	1.0	20	0.03	0.11	2.42	0.15	0.09	0.14	0.58	0.11
	15	17.1	18.3	5.8	47.4	3.6	6.6	nd	1.2	15	0.05	0.12	3.27	0.09	0.14	0.16	0.78	0.07
	10	14.3	20.1	6.4	48.9	4.2	5.3	nd	0.9	10	0.05	0.09	4.10	0.13	0.13	0.12	0.98	0.10
	7.5	18.2	13.3	6.6	53.0	nd	8.3	nd	0.6	7.5	0.06	0.23	2.95	0.20	0.17	0.29	0.70	0.15
	5	19.7	15.9	5.5	42.7	5.1	10.1	nd	0.9	5	0.05	0.26	5.25	0.06	0.16	0.33	1.25	0.04
	2	13.1	0.0	4.8	41.7	20.5	8.6	nd	0.4	2	0.42	1.06	0.27	1.20	1.22	1.34	0.06	0.89

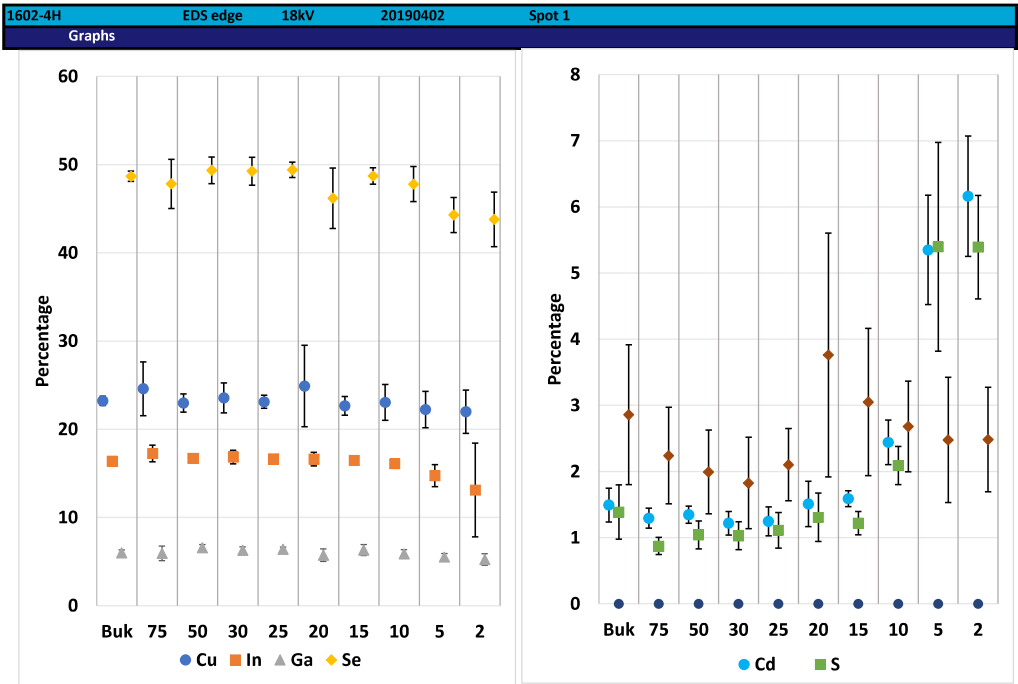


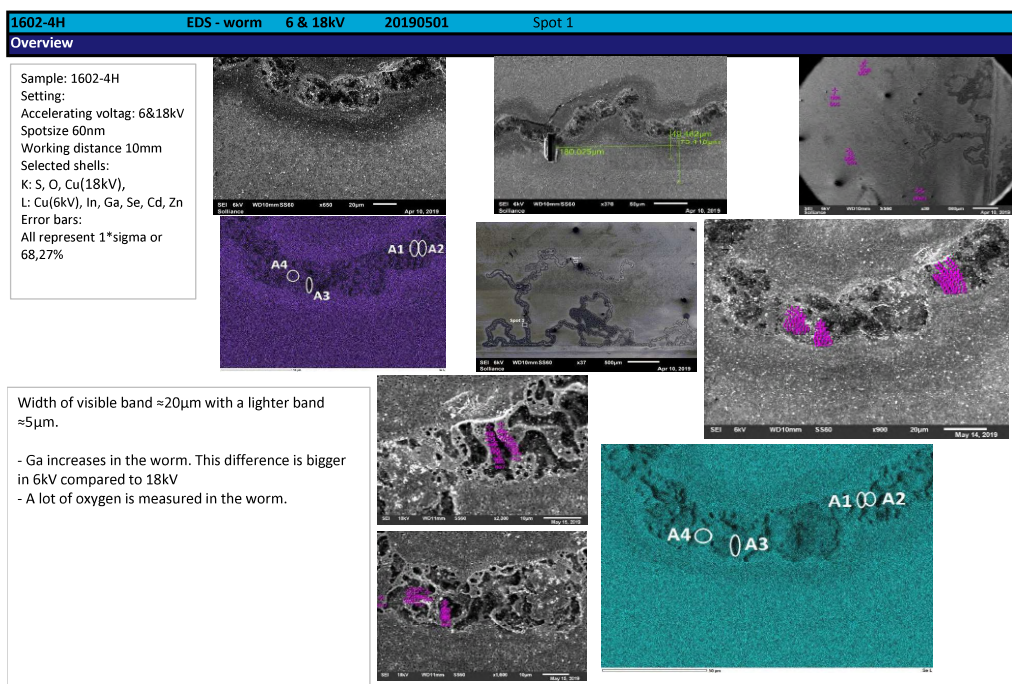
1602-4D EDS - edge 18kV 20190402 Spot 2									
At%									
Measurement	Cu	In	Ga	Se	Cd	S	Zn	O	
Bulk	22.1	17.8	6.6	49.9	0.0	2.3	0.0	1.2	
50	23.3	16.0	6.6	49.0	1.2	2.2	0.0	1.7	
30	24.0	15.8	6.5	48.1	1.3	2.7	0.0	1.5	
25	23.5	15.9	6.5	49.2	1.1	2.3	0.0	1.6	
20	23.8	15.8	6.5	48.6	1.2	2.4	0.0	1.8	
15	23.9	15.8	6.4	47.9	1.0	2.8	0.0	2.1	
10	24.3	15.8	6.2	47.1	1.3	3.7	0.0	1.7	
7.5	24.4	14.8	6.2	45.7	1.8	4.9	0.0	2.1	
5	20.2	13.7	5.5	43.2	7.6	6.4	0.0	3.3	
2	20.4	14.4	5.5	45.3	7.2	5.7	0.0	1.6	
Meas. GGI CGI S/Cd Se/CIg NGGI NCGI NS/CD NSe/CIg									
Bulk	0.27	0.91	0.00	1.07	1.00	1.00	1.00	1.00	
50	0.29	1.03	1.89	1.07	1.08	1.13	0.00	0.99	
30	0.29	1.08	2.07	1.04	1.08	1.18	0.00	0.97	
25	0.29	1.05	2.12	1.07	1.08	1.15	0.00	1.00	
20	0.29	1.07	2.04	1.05	1.08	1.17	0.00	0.98	
15	0.29	1.07	2.70	1.04	1.07	1.18	0.00	0.97	
10	0.28	1.10	2.83	1.02	1.05	1.22	0.00	0.95	
7.5	0.29	1.16	2.72	1.01	1.09	1.28	0.00	0.94	
5	0.29	1.05	0.84	1.10	1.07	1.16	0.00	1.03	
2	0.28	1.02	0.79	1.13	1.03	1.13	0.00	1.05	
Mass%									
Measurement	Cu	In	Ga	Se	Cd	S	Zn	O	
Bulk	18.0	25.1	5.8	49.7	nd	0.9	nd	0.5	
50	18.7	23.5	6.0	49.1	1.4	0.9	nd	0.5	
30	18.9	22.6	5.9	49.4	1.8	1.2	nd	0.2	
25	18.3	23.3	5.9	49.6	1.7	0.9	nd	0.3	
20	18.3	22.7	6.2	50.0	1.5	0.9	nd	0.4	
15	19.0	23.6	5.3	48.9	1.5	1.0	nd	0.7	
10	19.2	23.2	5.5	48.5	2.0	1.3	nd	0.3	
7.5	19.8	22.3	5.8	47.7	2.3	1.7	nd	0.5	
5	16.2	21.1	5.3	45.5	9.2	2.3	nd	0.5	
2	16.0	19.8	5.1	47.6	9.5	1.8	nd	0.3	
Standard deviation									
Meas. GGI CGI S/Cd Se/CIg NGGI NCGI NS/CD NSe/CIg									
Bulk	0.01	0.02	0.00	0.02	0.00	0.00	0.00	0.00	
50	0.01	0.04	0.25	0.03	0.04	0.04	x	0.03	
30	0.01	0.07	0.39	0.06	0.04	0.07	x	0.06	
25	0.01	0.04	0.46	0.04	0.05	0.04	x	0.03	
20	0.01	0.04	0.40	0.03	0.05	0.04	x	0.03	
15	0.02	0.05	0.36	0.05	0.06	0.06	x	0.04	
10	0.01	0.06	0.56	0.06	0.04	0.07	x	0.05	
7.5	0.01	0.06	0.55	0.03	0.03	0.07	x	0.03	
5	0.02	0.11	0.07	0.09	0.08	0.12	x	0.08	
2	0.02	0.06	0.05	0.07	0.08	0.06	x	0.06	





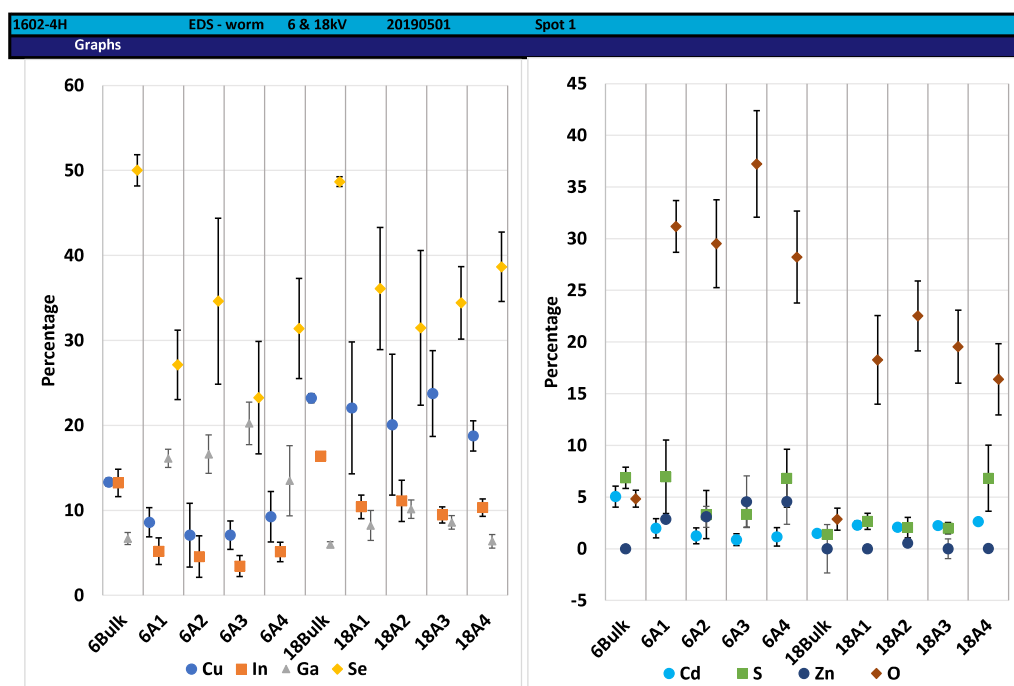
1602-4H EDS edge 18kV 20190402 Spot 1									
At%									
Measurement	Cu	In	Ga	Se	Cd	S	Zn	O	
Buk	23.2	16.4	6.0	48.7	1.5	1.4	0.0	2.9	Meas.
75	24.6	17.2	5.9	47.8	1.3	0.9	0.0	2.2	GGI
50	23.0	16.7	6.6	49.4	1.3	1.0	0.0	2.0	CGI
30	23.5	16.9	6.3	49.3	1.2	1.0	0.0	1.8	S/Cd
25	23.1	16.6	6.4	49.4	1.2	1.1	0.0	2.1	Se/ClG
20	24.9	16.6	5.7	46.2	1.5	1.3	0.0	3.8	NGGI
15	22.7	16.5	6.3	48.7	1.6	1.2	0.0	3.1	NCGI
10	23.0	16.1	5.9	47.8	2.4	2.1	0.0	2.7	NS/Cd
5	22.2	14.7	5.5	44.3	5.4	5.4	0.0	2.5	NSe/ClG
2	22.0	13.1	5.2	43.8	6.2	5.4	0.0	2.5	
Mass%									
Measurement	Cu	In	Ga	Se	Cd	S	Zn	O	
Buk	18.5	23.9	5.4	48.4	2.5	0.5	nd	0.8	Meas.
75	19.0	24.8	5.3	48.5	1.6	0.3	nd	0.6	GGI
50	17.2	23.5	6.2	50.8	1.7	0.5	nd	0.2	CGI
30	20.2	25.5	5.0	46.9	1.7	0.5	nd	0.4	S/Cd
25	17.9	23.5	5.9	50.0	1.9	0.5	nd	0.3	Se/ClG
20	20.0	24.2	5.1	48.7	1.3	0.5	nd	0.3	NGGI
15	18.0	24.0	5.3	48.7	2.5	0.5	nd	1.0	NCGI
10	22.8	24.2	4.4	43.9	3.1	0.9	nd	0.7	NS/Cd
5	17.2	21.9	5.1	44.7	8.4	2.3	nd	0.5	NSe/ClG
2	17.7	0.0	4.4	44.8	9.0	2.3	nd	0.2	
Standard deviation									
Measurement	Cu	In	Ga	Se	Cd	S	Zn	O	
Buk	0.01	0.05	0.37	0.02	0.00	0.00	0.00	0.00	Meas.
75	0.04	0.13	0.12	0.12	0.14	0.12	0.12	0.11	GGI
50	0.01	0.05	0.21	0.06	0.05	0.05	0.22	0.05	CGI
30	0.02	0.07	0.19	0.07	0.08	0.07	0.19	0.07	S/Cd
25	0.01	0.04	0.22	0.03	0.04	0.04	0.23	0.03	Se/ClG
20	0.03	0.20	0.21	0.14	0.12	0.19	0.22	0.13	NGGI
15	0.02	0.06	0.10	0.04	0.09	0.05	0.10	0.04	NCGI
10	0.02	0.11	0.13	0.08	0.06	0.11	0.13	0.07	NS/Cd
5	0.03	0.10	0.26	0.08	0.10	0.10	0.27	0.08	NSe/ClG
2	0.26	1.19	0.07	0.25	0.99	1.14	0.07	0.23	



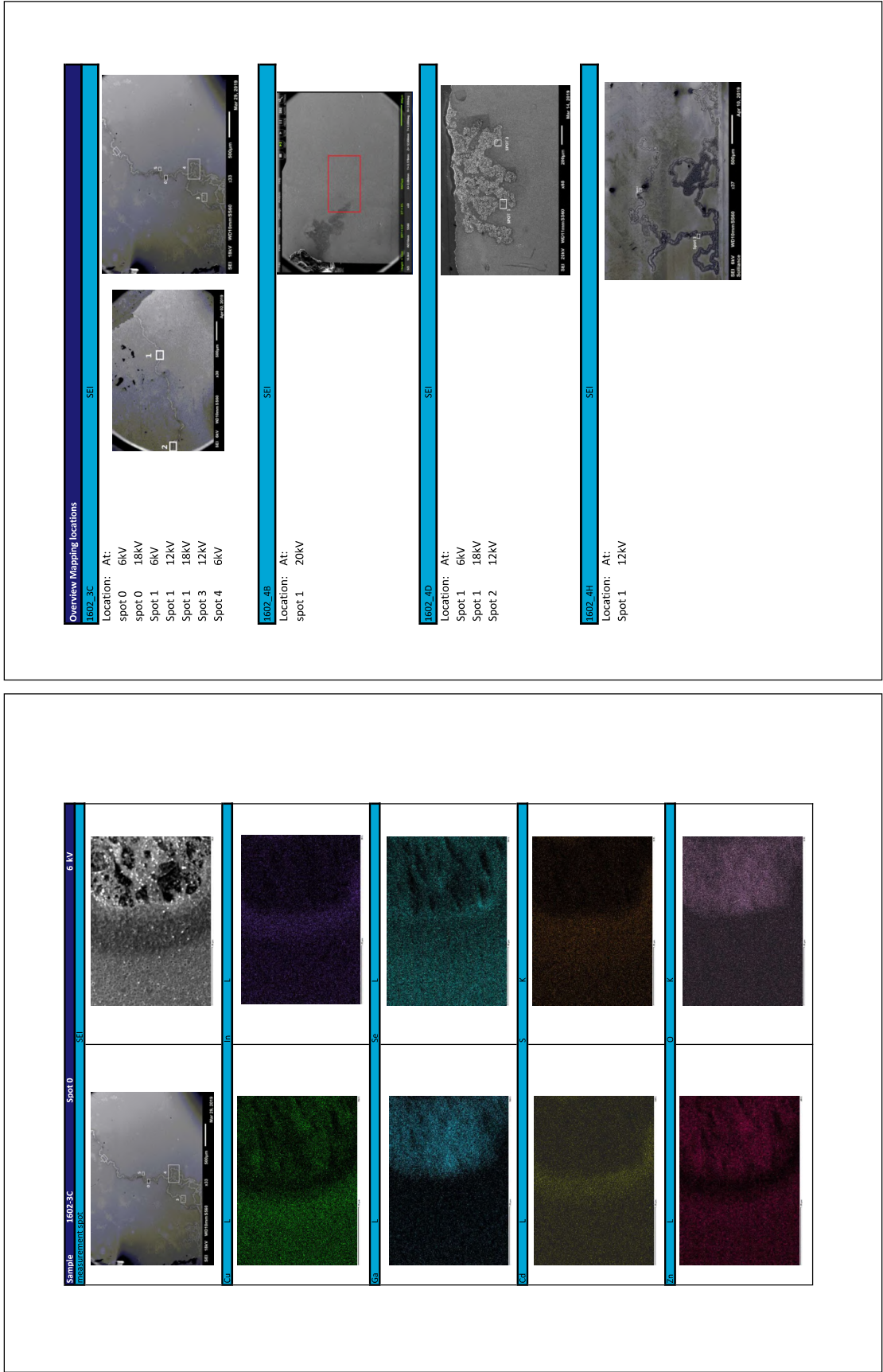


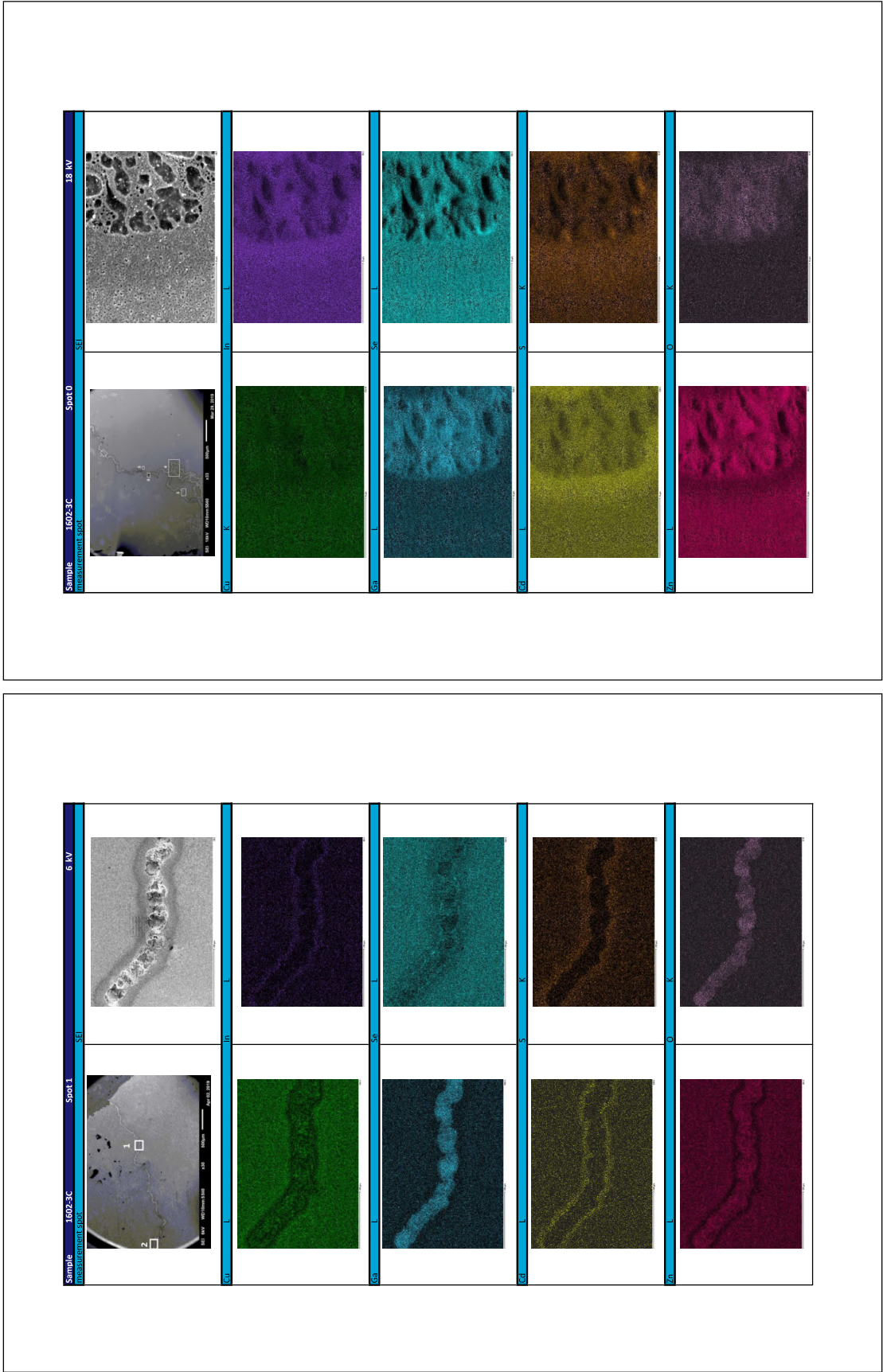
1602-4H		EDS - worm				6 & 18kV		20190501		Spot 1							
At%									Normalized ratio's								
Measurement	Cu	In	Ga	Se	Cd	S	Zn	O	Meas.	GGI	CGI	S/Cd	Se/CIG	NGGI	NCGI	NS/CD	NSe/CIG
6Bulk	13.3	13.2	6.7	50.0	5.0	6.9	0.0	4.8	6Bulk	0.34	0.68	1.42	1.51	1.00	1.00	1.00	1.00
6A1	8.6	5.2	16.1	27.1	2.0	7.0	2.9	31.2	6A1	0.76	0.41	4.10	0.91	2.26	0.60	2.89	0.60
6A2	7.1	4.5	16.6	34.6	1.2	3.3	3.1	29.5	6A2	0.79	0.35	3.76	1.29	2.36	0.52	2.65	0.86
6A3	7.1	3.4	20.2	23.3	0.9	3.3	4.6	37.2	6A3	0.86	0.31	4.22	0.76	2.54	0.46	2.98	0.50
6A4	9.2	5.1	13.5	31.4	1.2	6.8	4.6	28.2	6A4	0.72	0.54	14.32	1.16	2.13	0.80	10.11	0.77
18Bulk	23.2	16.4	6.0	48.7	1.5	1.4	0.0	2.9	18Bulk	0.27	1.04	0.97	1.07	0.79	1.53	0.69	0.71
18A1	22.1	10.4	8.2	36.1	2.3	2.7	0.0	18.3	18A1	0.44	1.22	1.17	0.93	1.31	1.80	0.83	0.62
18A2	20.1	11.1	10.1	31.5	2.1	2.0	0.5	22.5	18A2	0.48	0.96	1.00	0.81	1.43	1.42	0.70	0.54
18A3	23.7	9.5	8.6	34.4	2.3	2.0	0.0	19.5	18A3	0.48	1.33	0.88	0.84	1.42	1.96	0.62	0.55
18A4	18.8	10.3	6.4	38.7	2.6	6.8	0.0	16.4	18A4	0.38	1.13	2.70	1.10	1.13	1.66	1.90	0.73

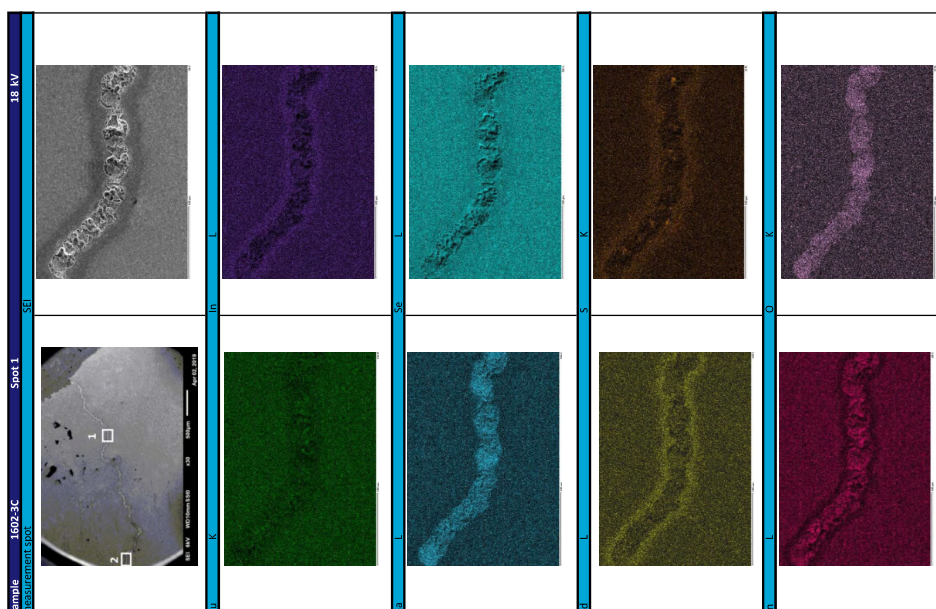
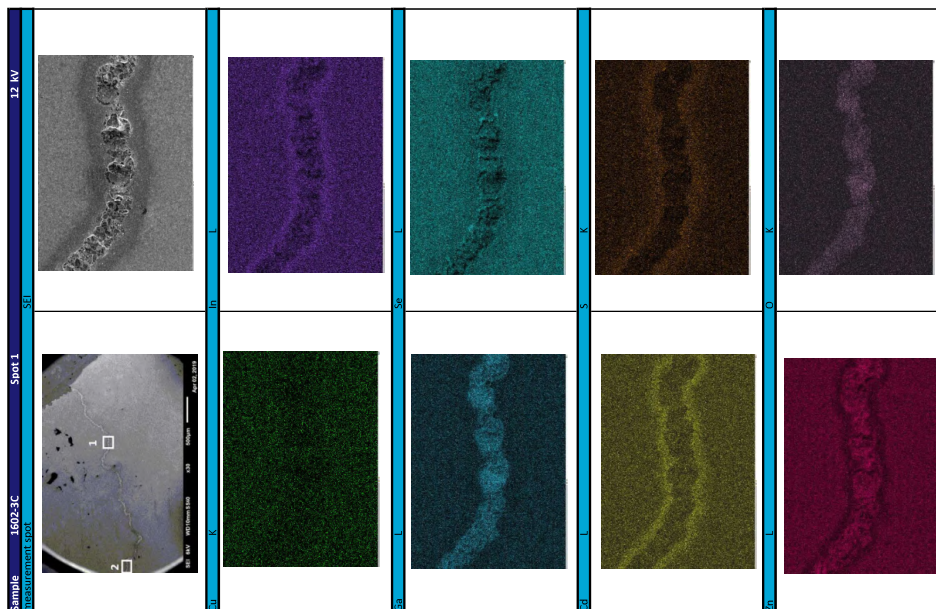
Mass%									Standard deviation								
Measurement	Cu	In	Ga	Se	Cd	S	Zn	O	Meas.	GGI	CGI	S/Cd	Se/CIG	NGGI	NCGI	NS/CD	NSe/CIG
6Bulk	11.6	19.5	5.2	51.1	7.6	3.7	nd	1.3	6Bulk	0.02	0.09	0.38	0.12	0.00	0.00	0.00	0.00
6A1	10.3	13.0	19.3	40.1	2.2	4.2	2.8	8.0	6A1	0.06	0.11	2.27	0.15	0.18	0.16	1.61	0.10
6A2	13.5	7.4	20.8	42.8	2.1	4.2	0.9	8.4	6A2	0.08	0.22	2.83	0.59	0.25	0.32	2.00	0.39
6A3	10.4	8.1	23.2	40.6	1.4	3.2	2.2	11.0	6A3	0.05	0.11	3.44	0.23	0.14	0.17	2.43	0.15
6A4	11.2	11.0	13.7	43.9	3.4	3.2	6.7	6.9	6A4	0.07	0.23	23.55	0.31	0.22	0.33	16.62	0.21
18Bulk	18.5	23.9	5.4	48.4	2.5	0.5	nd	0.8	18Bulk	0.01	0.05	0.37	0.02	0.03	0.07	0.26	0.01
18A1	12.0	15.9	12.9	49.0	3.0	0.9	nd	6.3	18A1	0.06	0.50	0.37	0.31	0.19	0.73	0.26	0.20
18A2	14.5	23.3	9.6	43.5	3.4	1.1	nd	4.6	18A2	0.08	0.46	0.49	0.32	0.23	0.68	0.35	0.21
18A3	19.9	16.7	9.2	45.2	3.6	1.1	nd	4.4	18A3	0.04	0.35	0.22	0.17	0.12	0.52	0.16	0.11
18A4	17.0	17.0	7.1	45.0	4.8	3.5	0.3	5.2	18A4	0.04	0.12	1.44	0.14	0.13	0.17	1.01	0.09

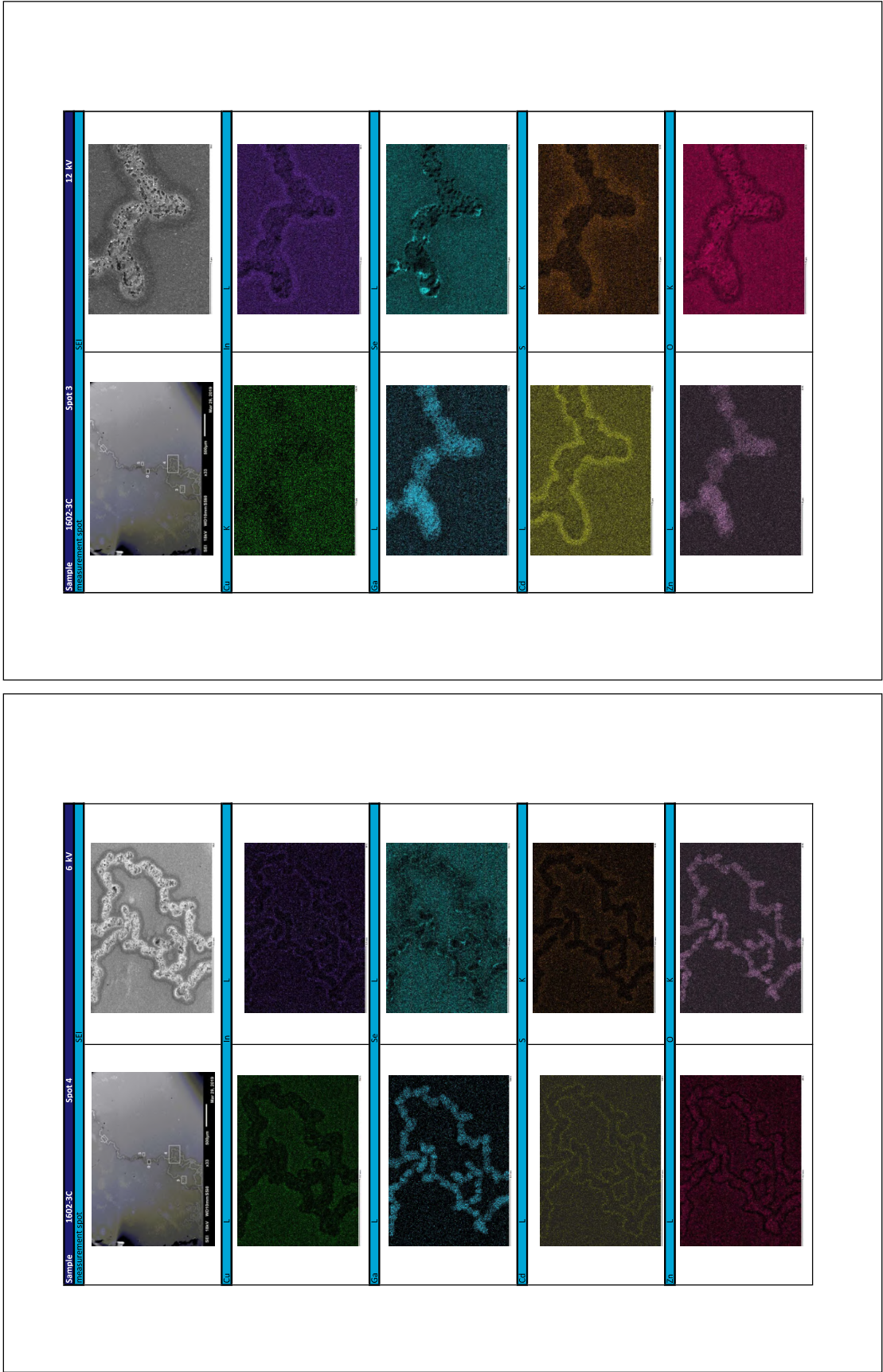


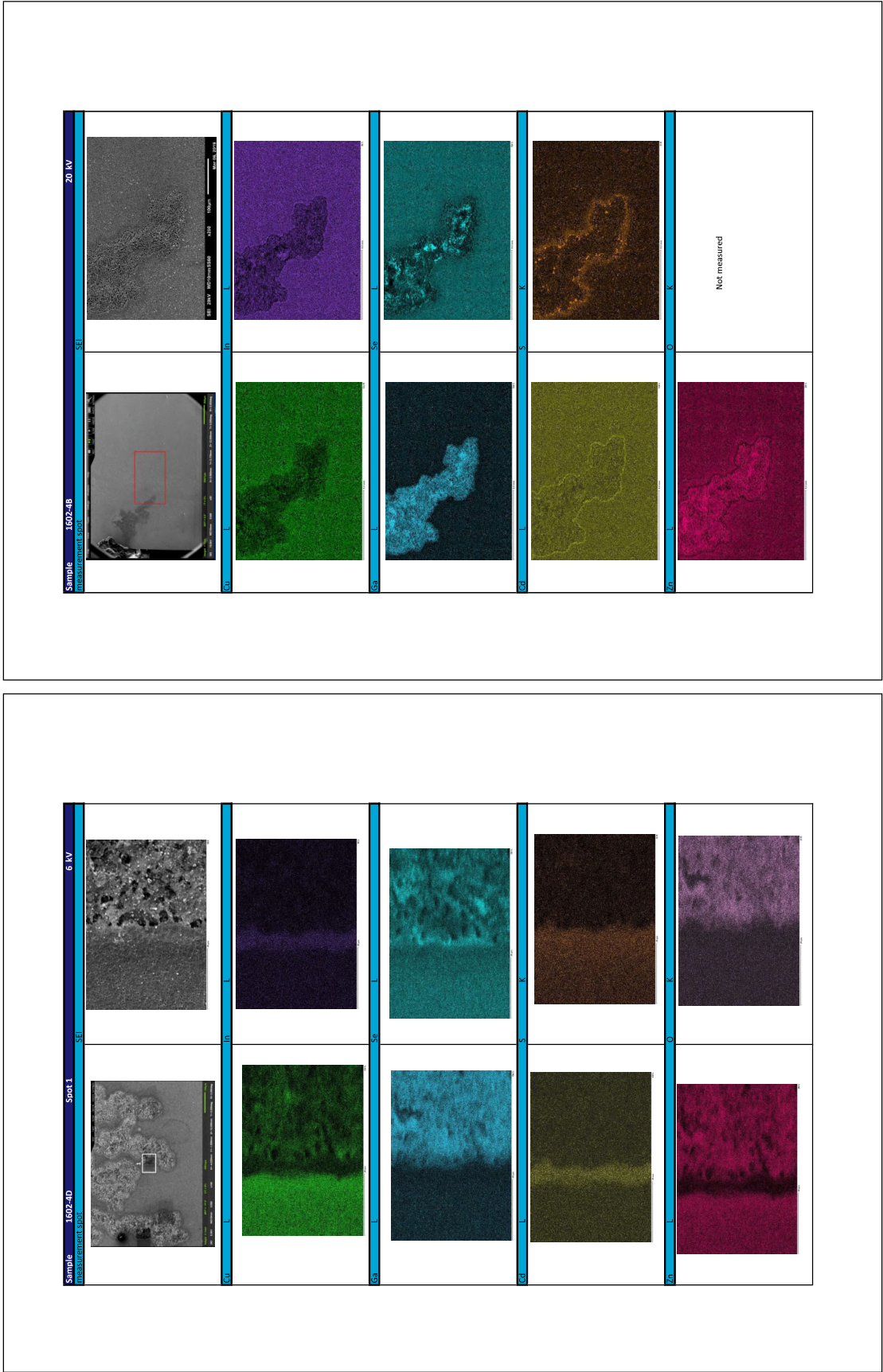
D.2. Nantes mapping

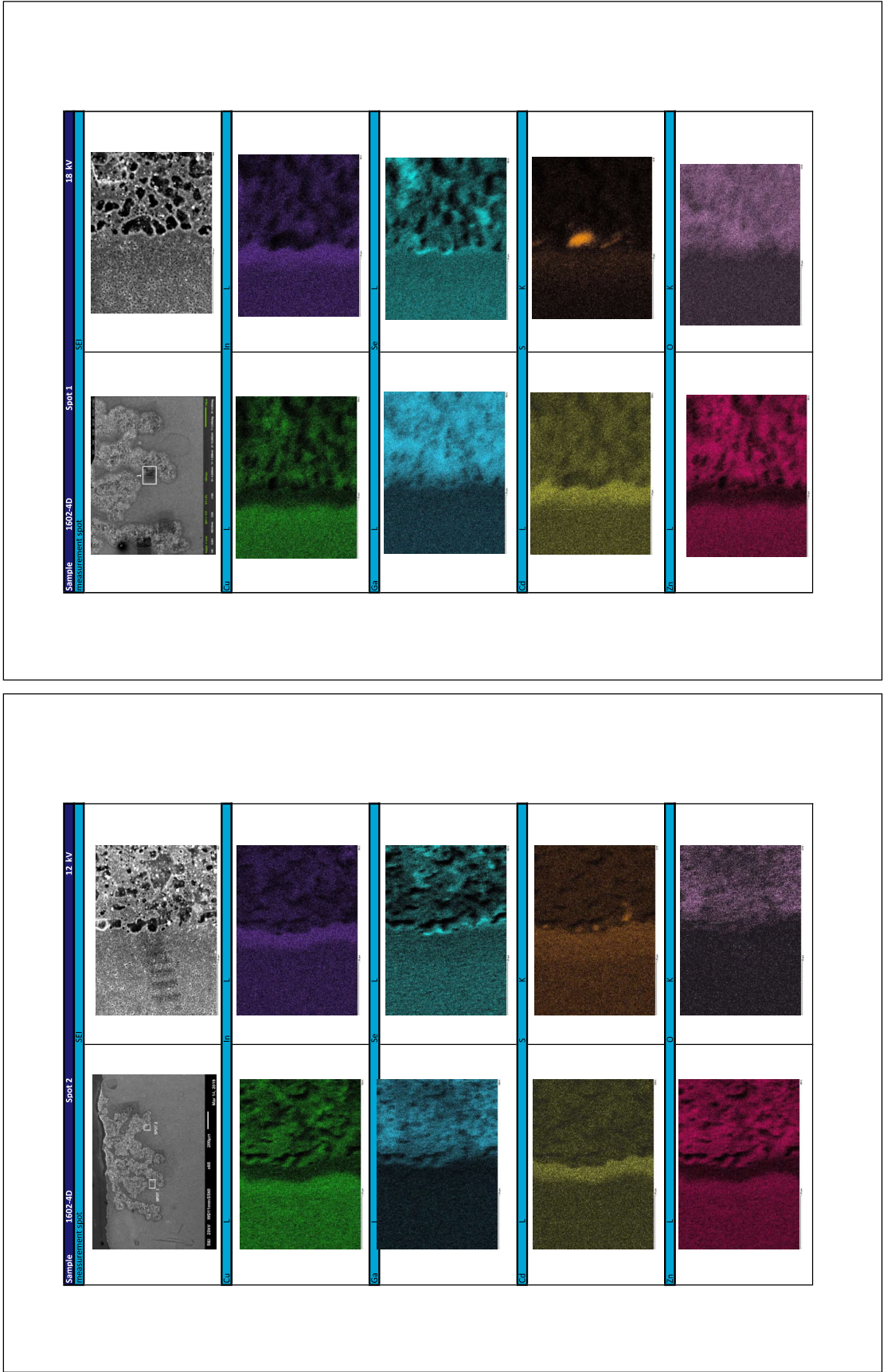


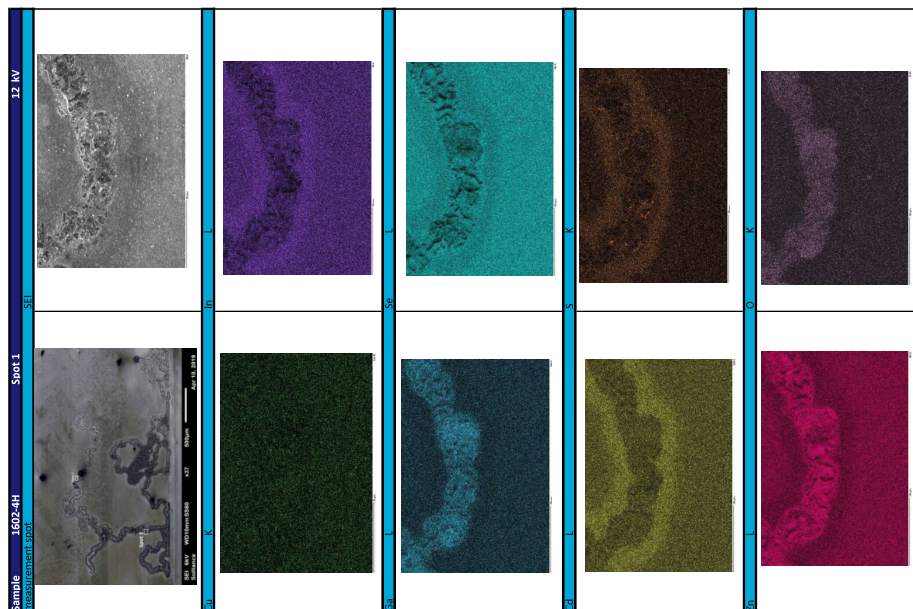










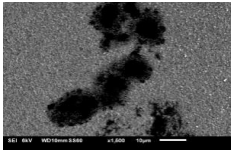
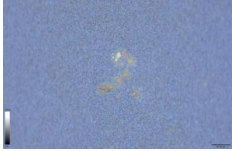
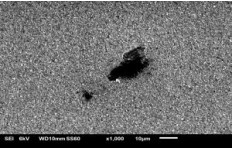

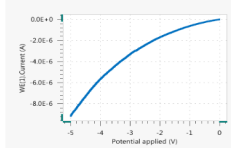
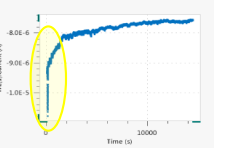
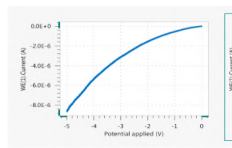
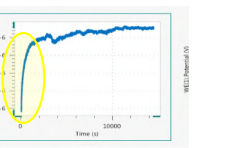
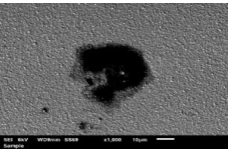
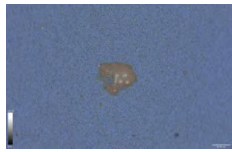
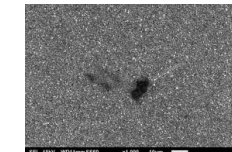

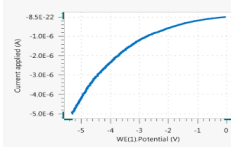
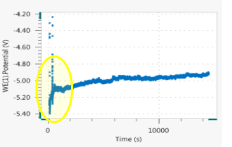
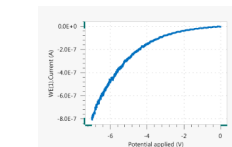
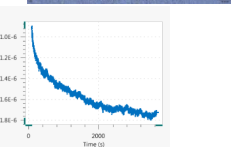
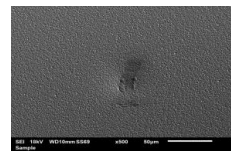
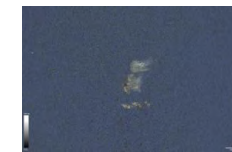
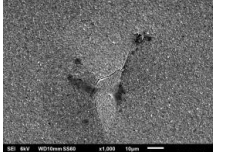

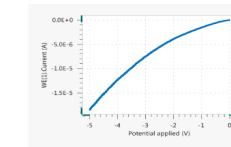
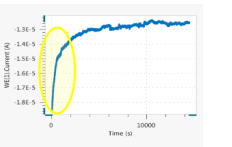
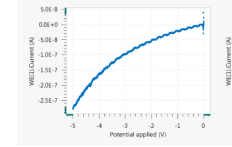
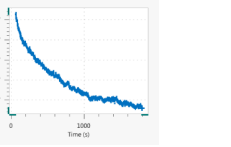


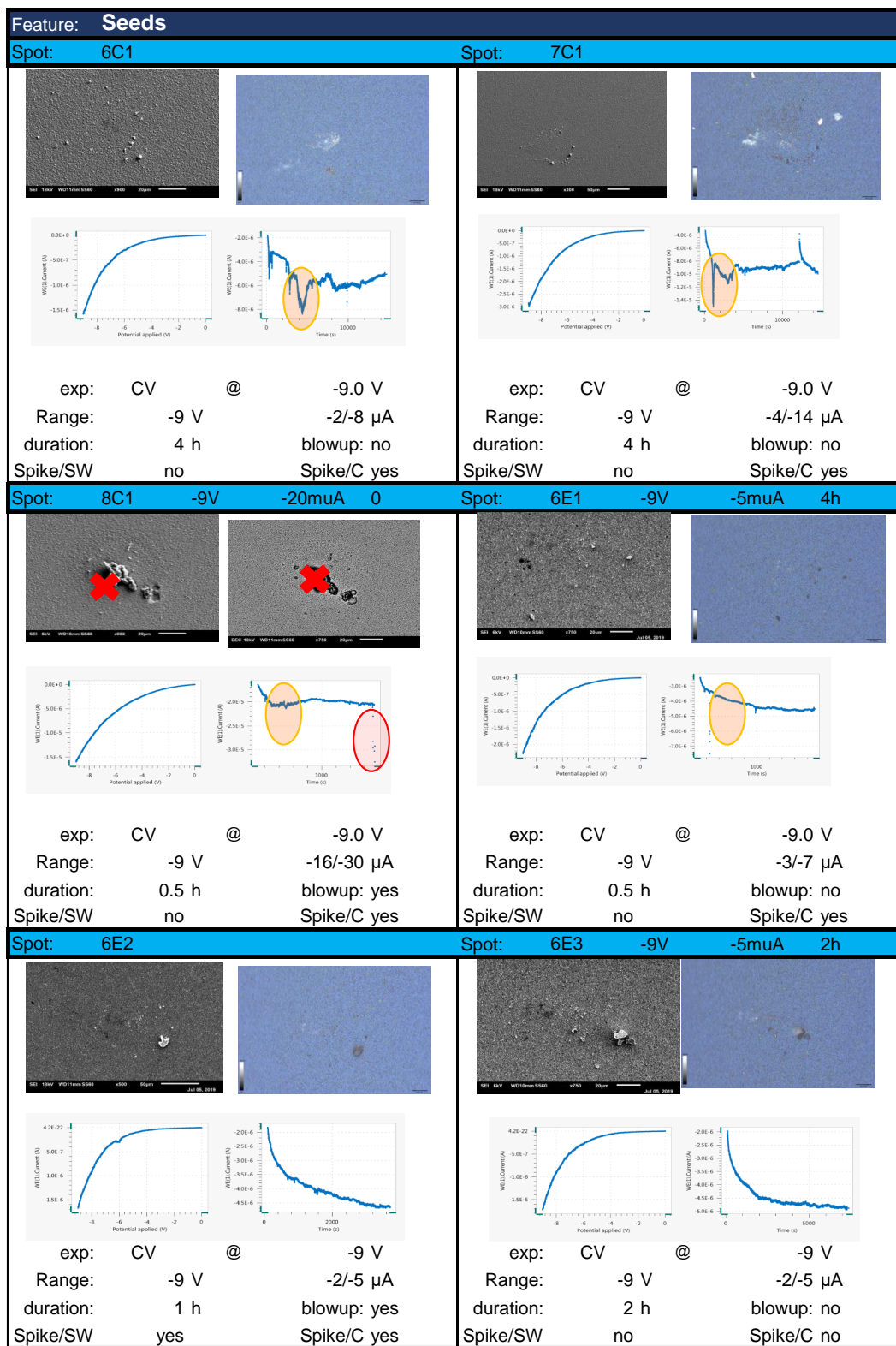
E

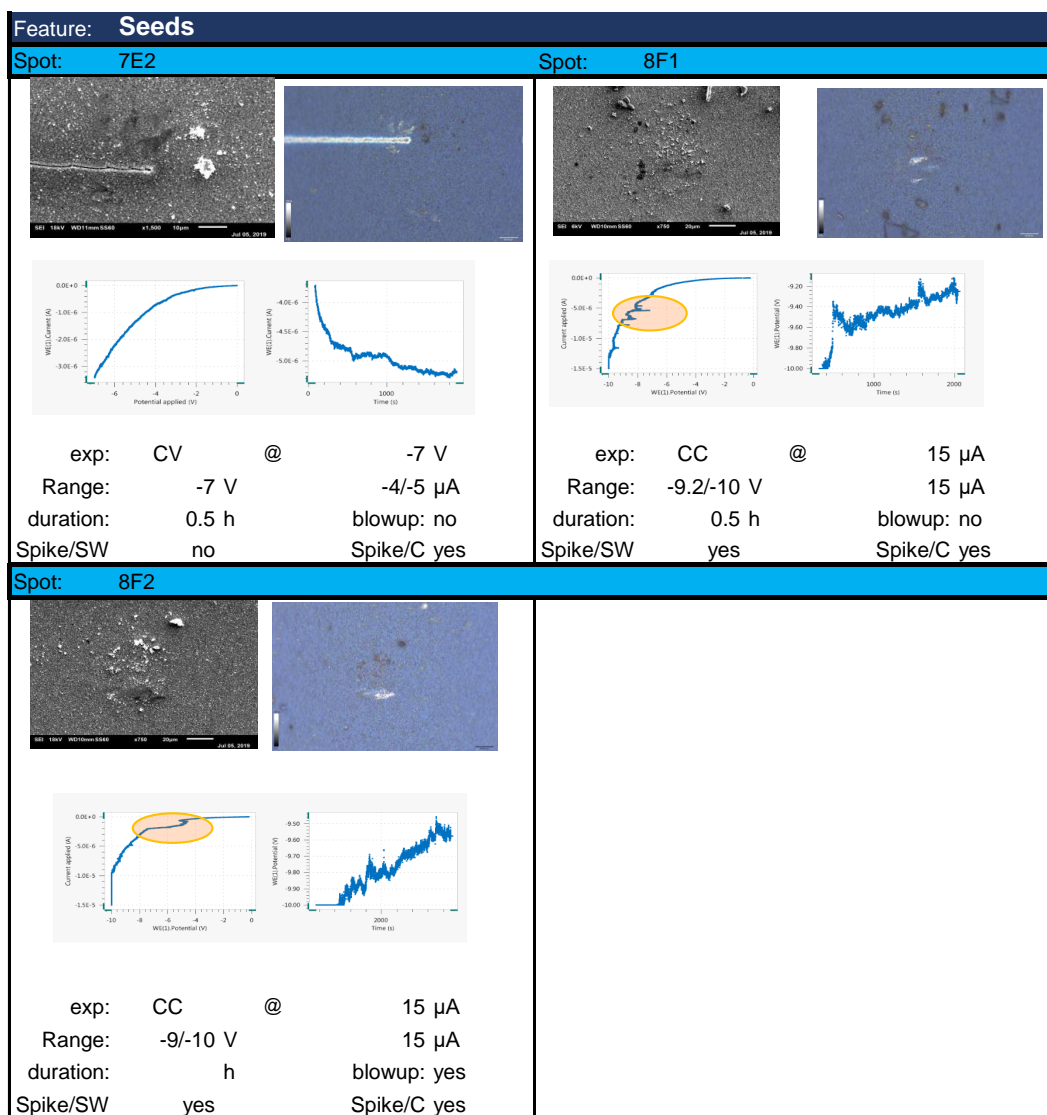
Point probe without AZO experimental
results

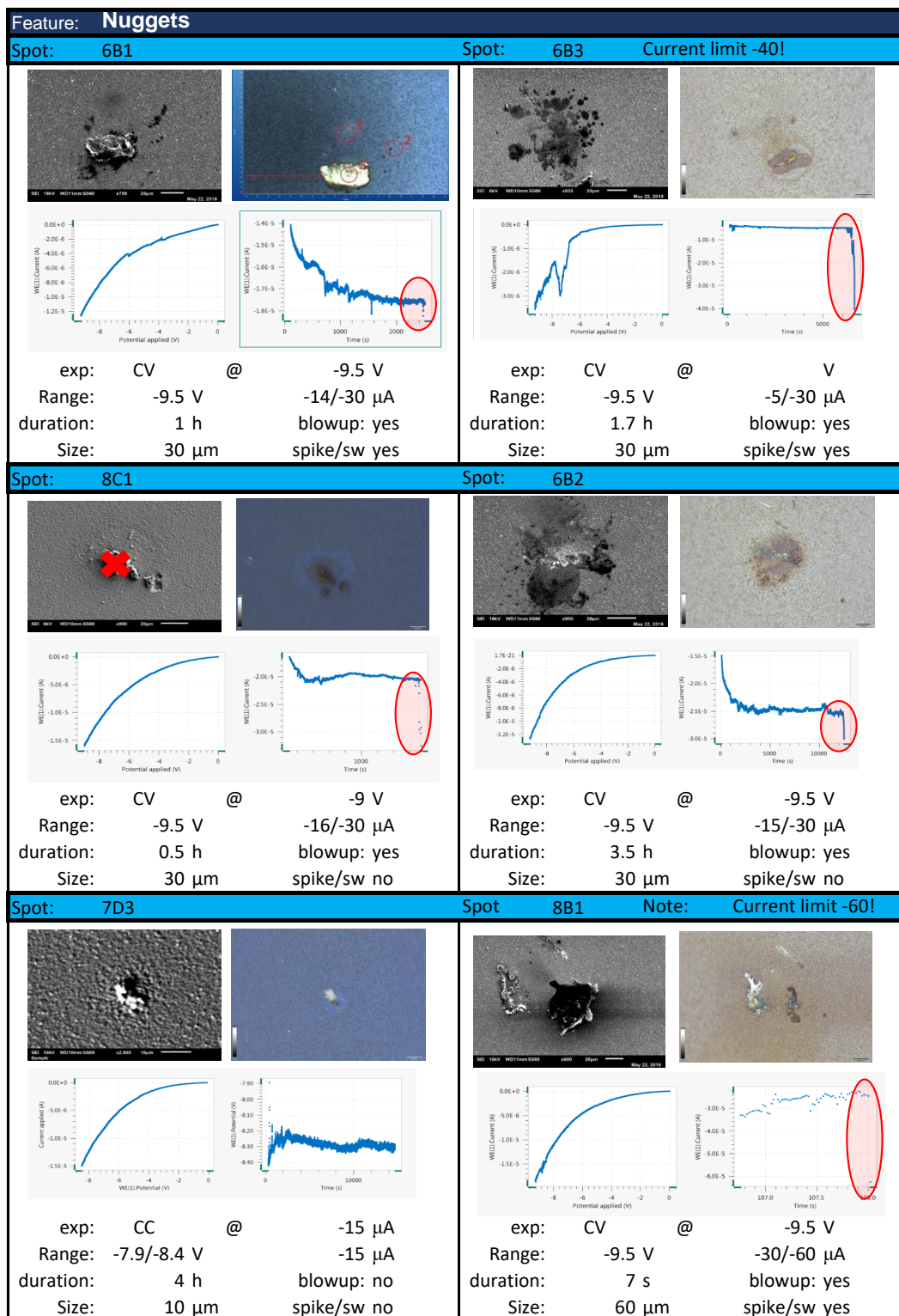
E.1. Feature categories

Feature categories

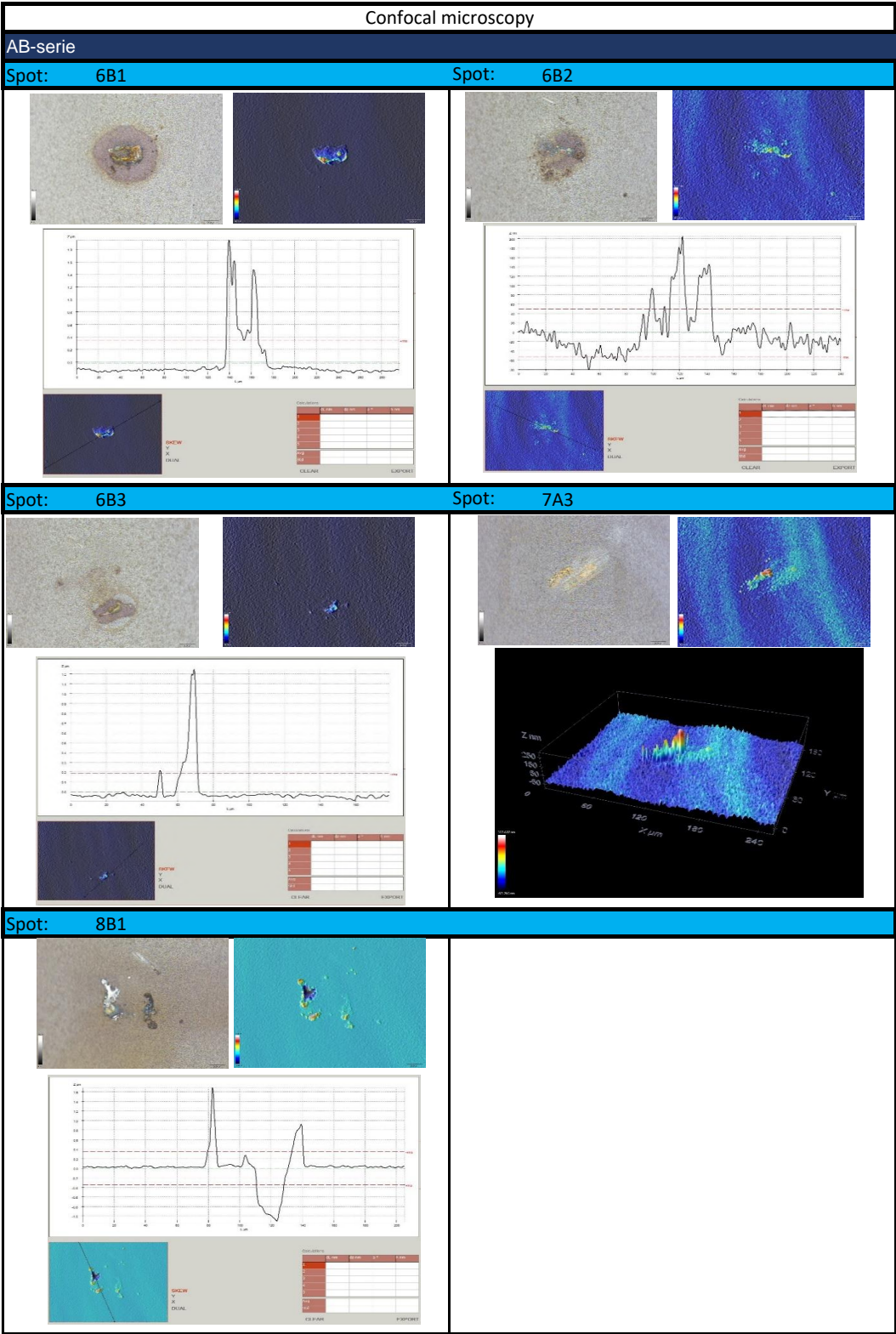
Features: Stains			
Spot: 9C3		Spot: 8C3	
			
			
exp: CV	@ -5 V	exp: CV	@ -5 V
Range: -5 V	-8/-11 μ A	Range: -5 V	-8.5/-6.5 μ A
duration: 4 h	blowup: no	duration: 4 h	blowup: no
Spike/SW no	Spike/C no	Spike/SW no	Spike/C no
Spot: 6D2		Spot: 7E3	
			
			
exp: CC	@ -5 μ A	exp: CV	@ -7 V
Range: -4.2/5.4 V	-5 μ A	Range: -7 V	-1/-2 μ A
duration: 4 h	blowup: no	duration: 1 h	blowup: no
Spike/SW no	Spike/C yes	Spike/SW no	Spike/C no
Spot: 7C3		Spot: 8E2	
			
			
exp: CV	@ -5 V	exp: CV	@ -5 V
Range: -5 V	-13 μ A	Range: -5 V	-0.3/-0.5 μ A
duration: 4 h	blowup: no	duration: 0.5 h	blowup: no
Spike/SW no	Spike/C yes	Spike/SW no	Spike/C no

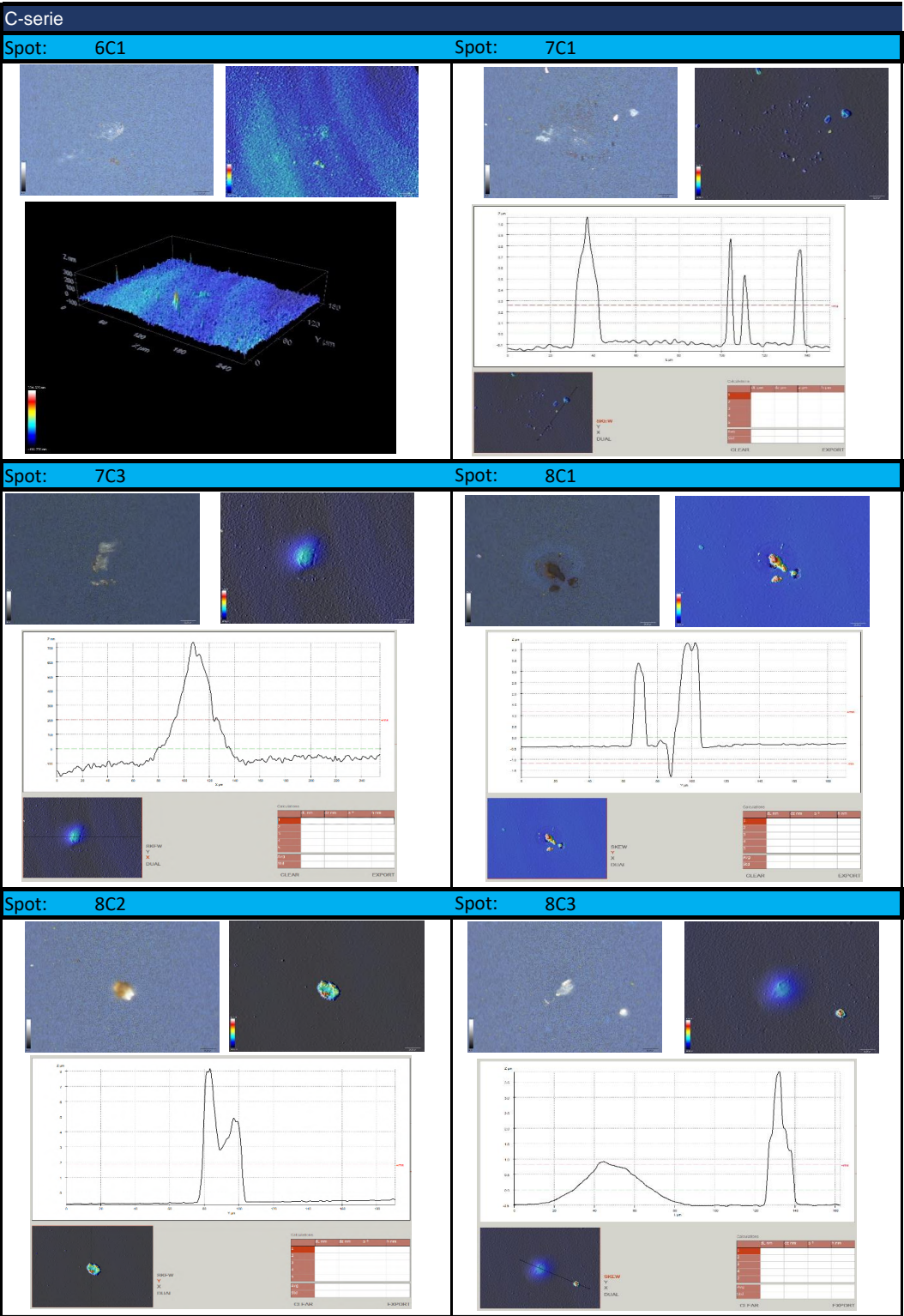


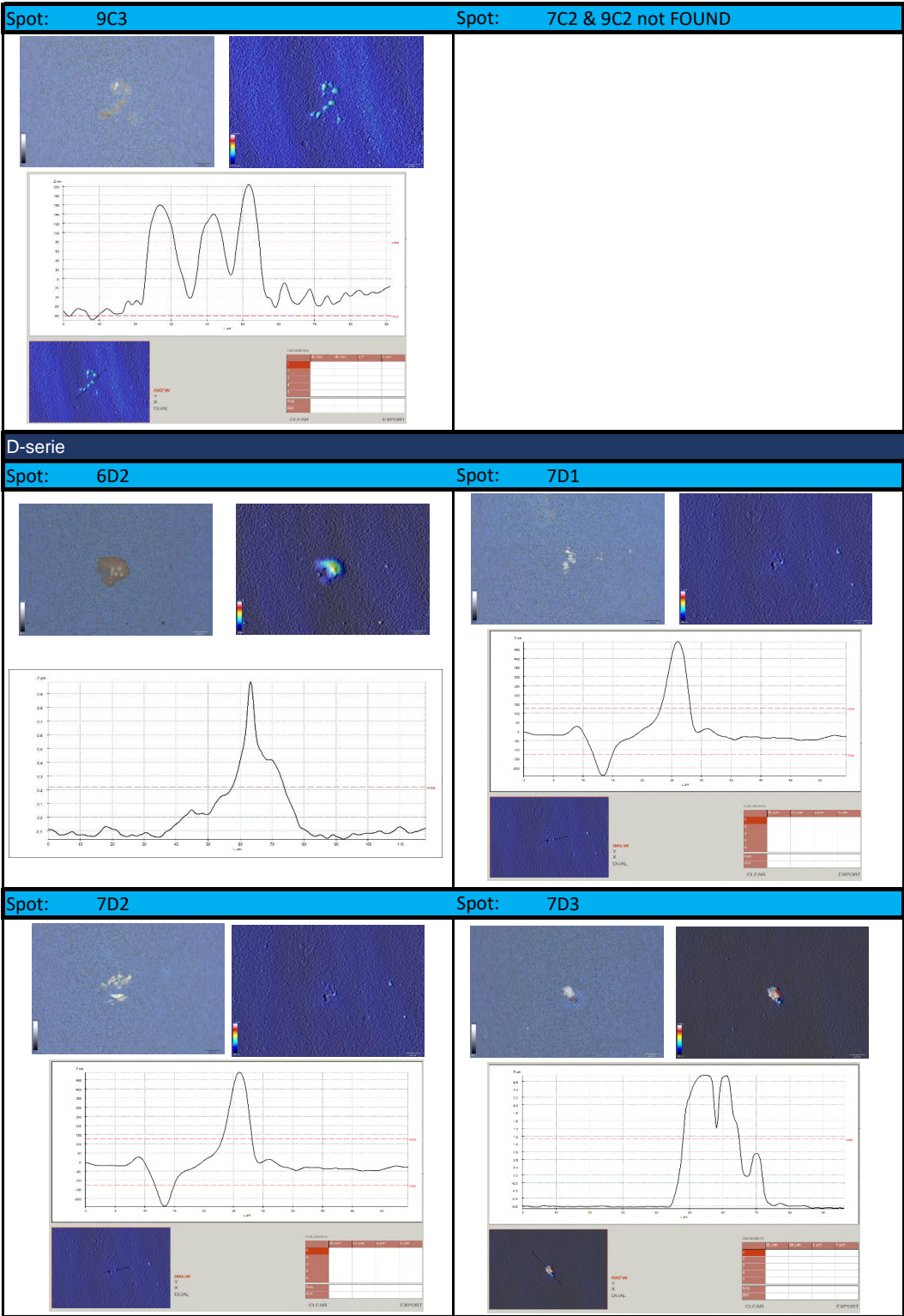


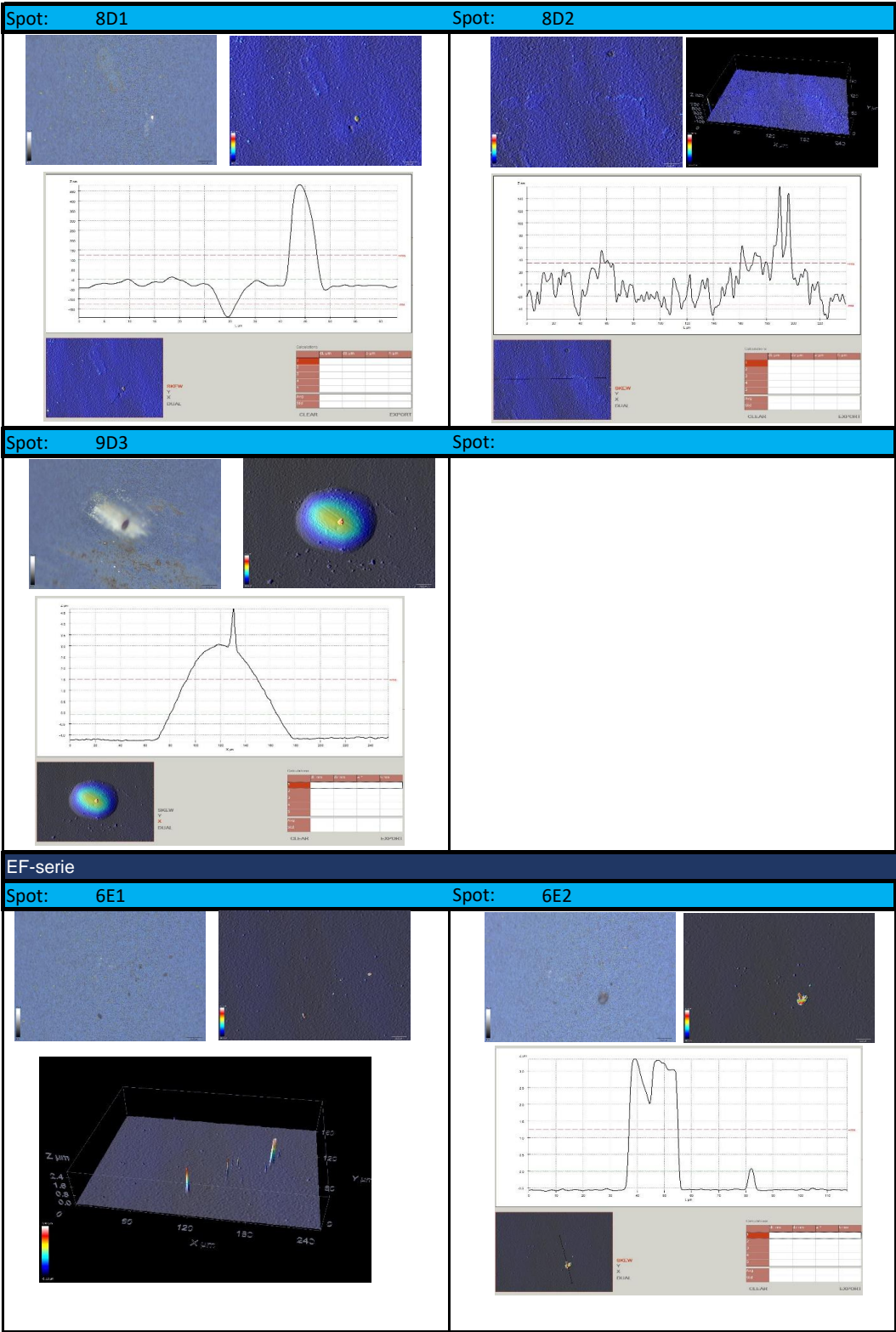


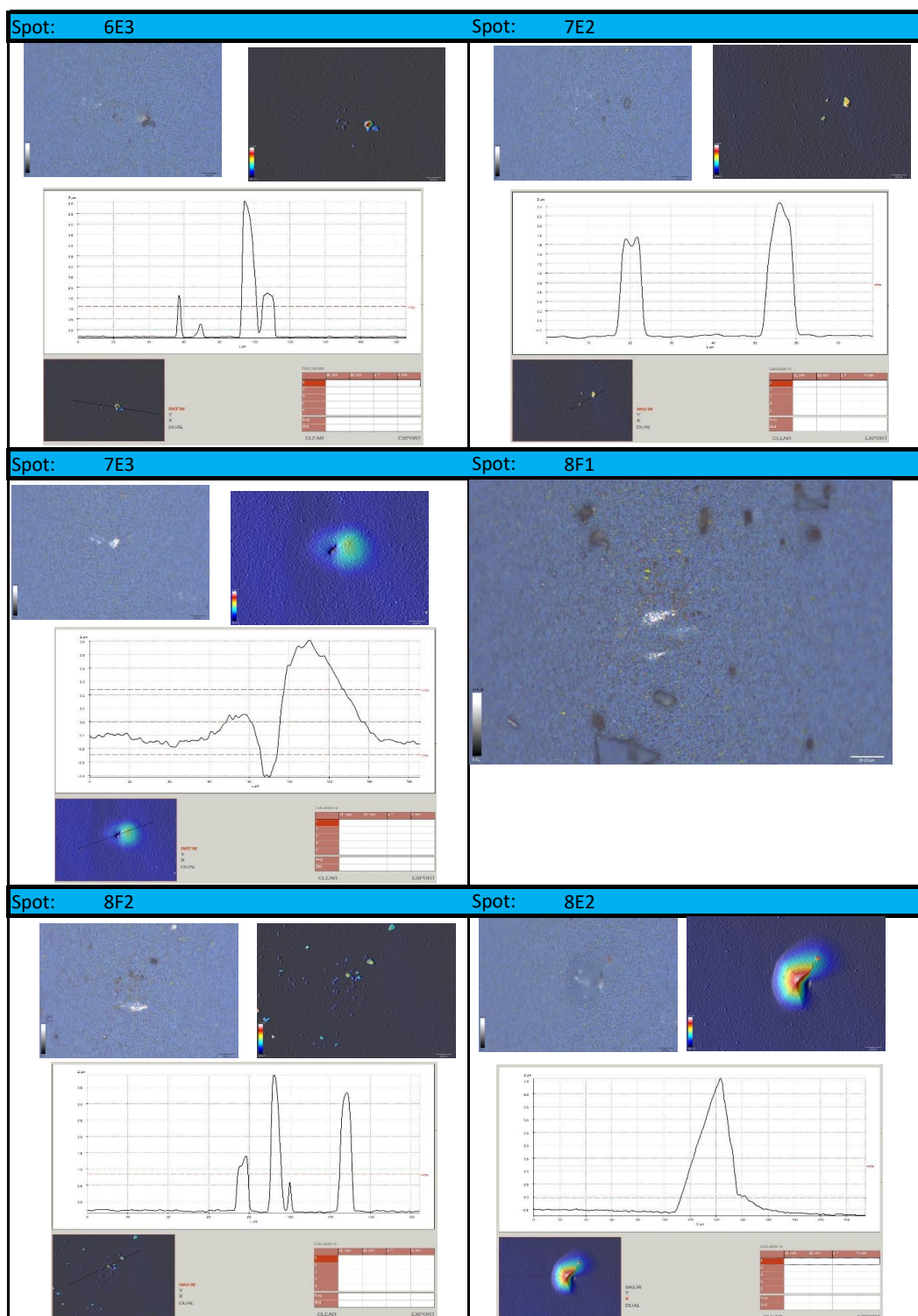
E.2. Confocal microscopy





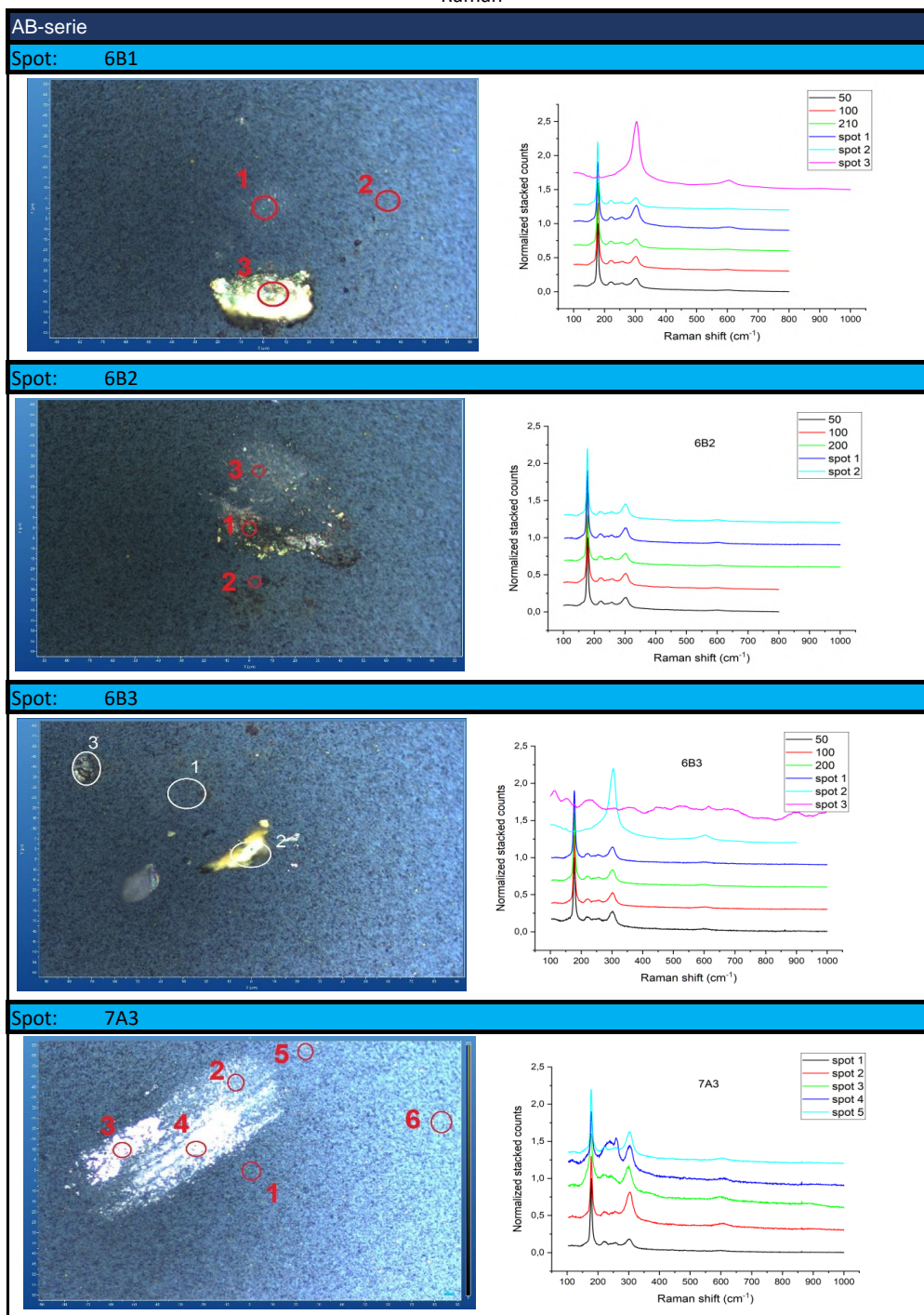


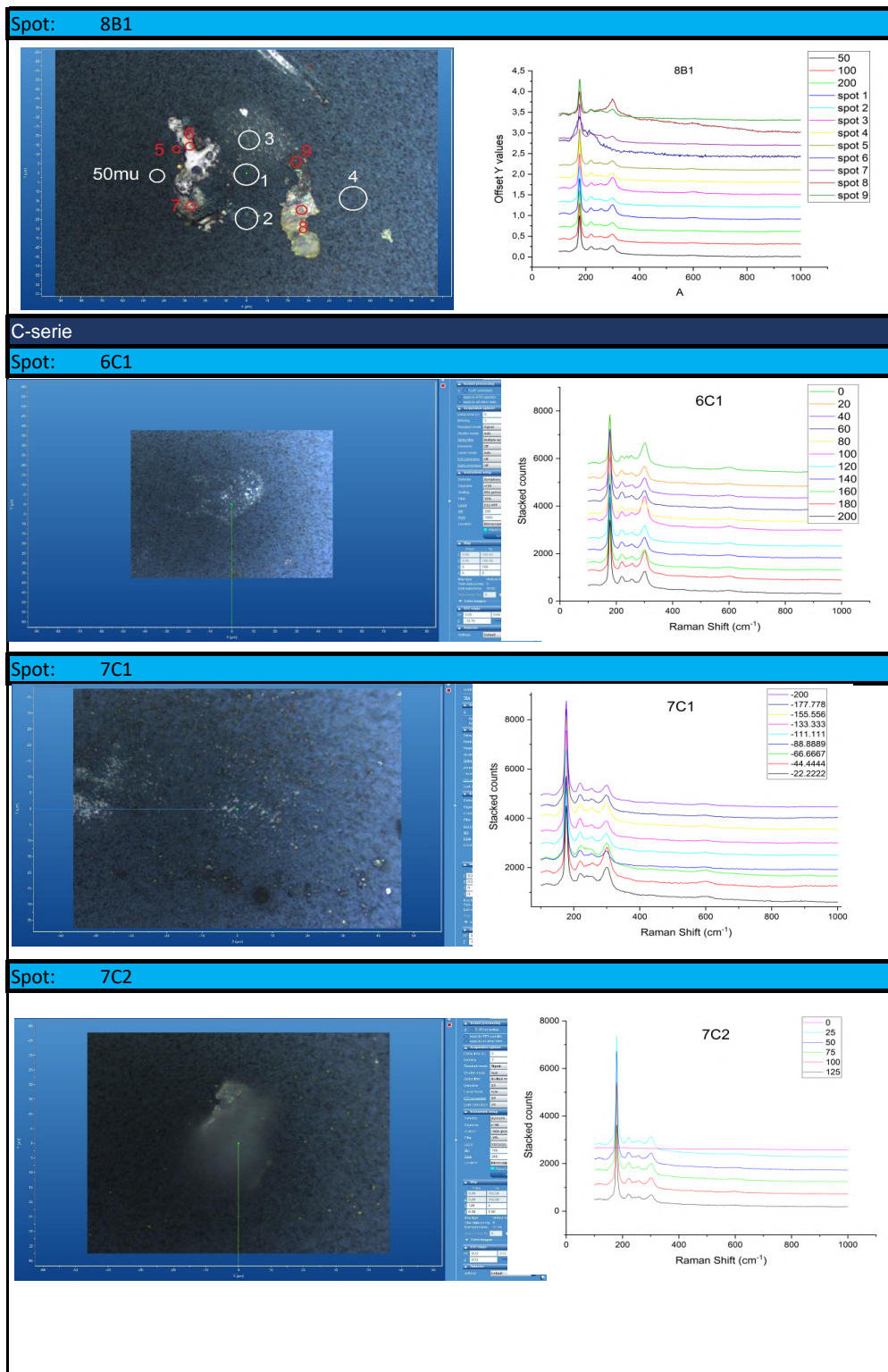


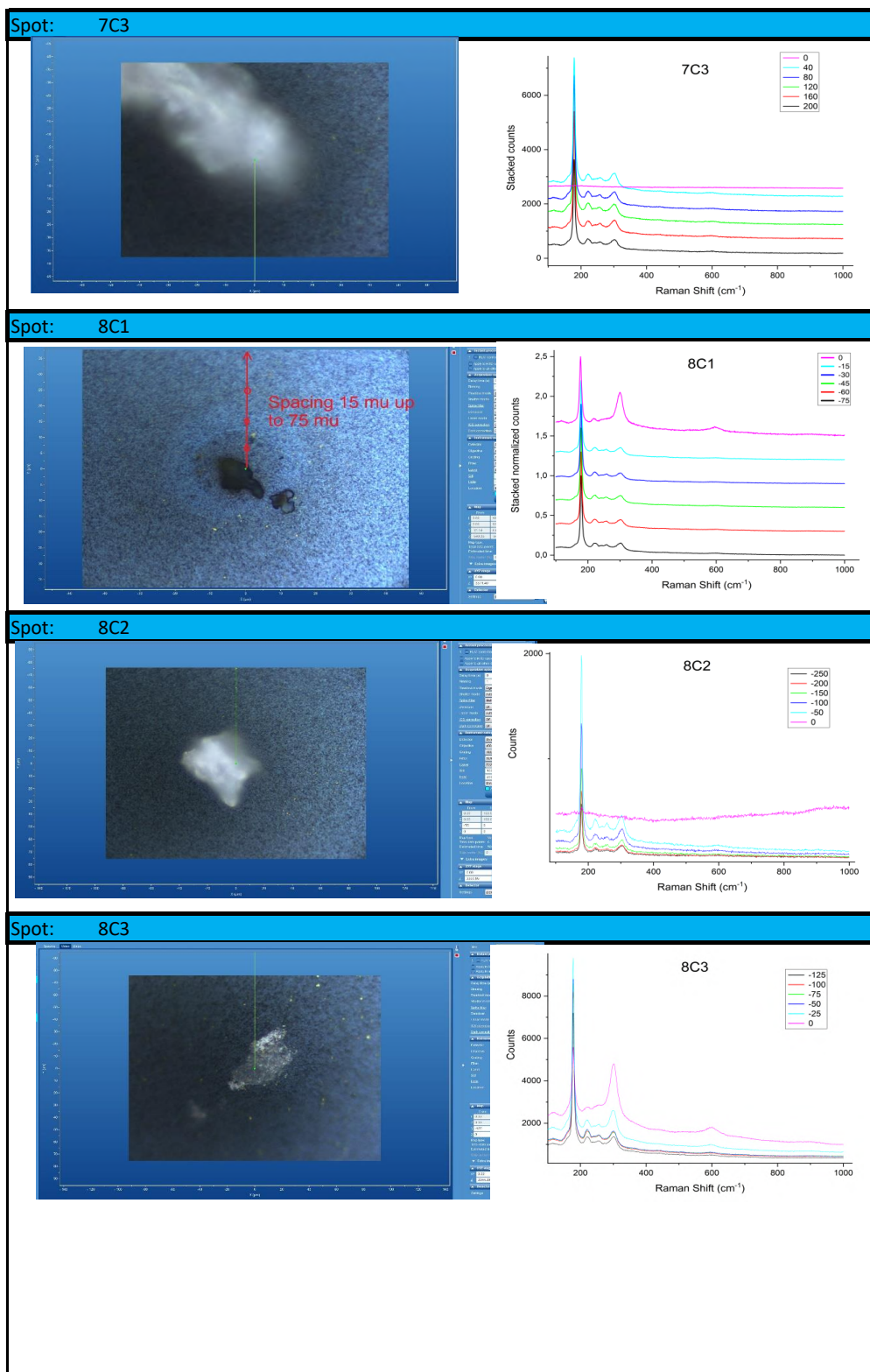


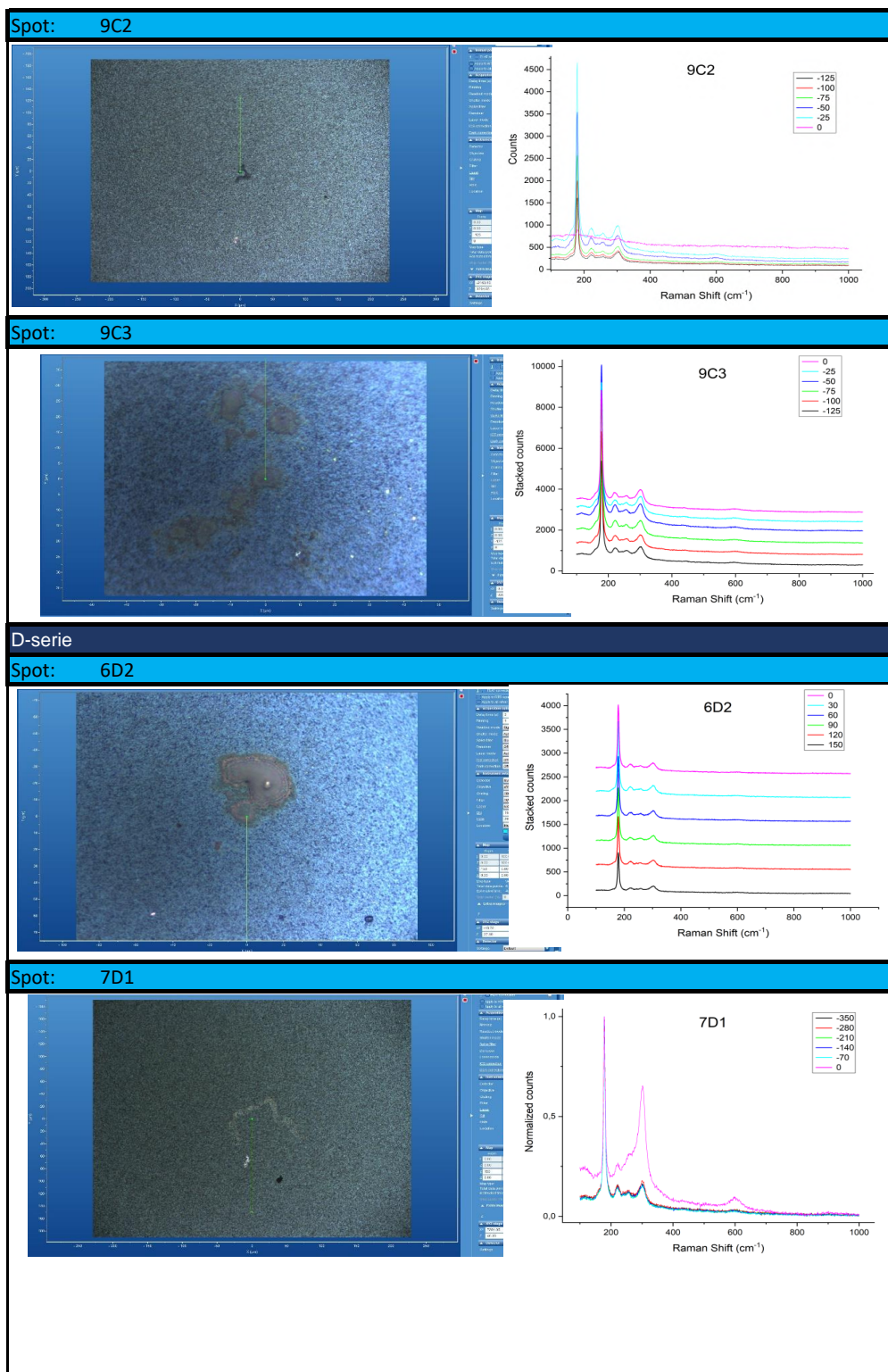
E.3. Raman spectroscopy

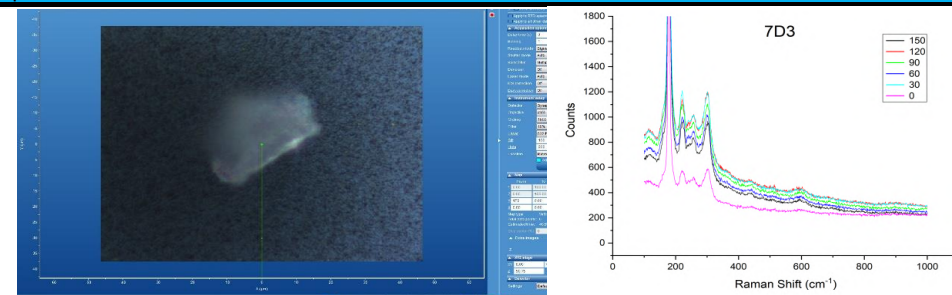
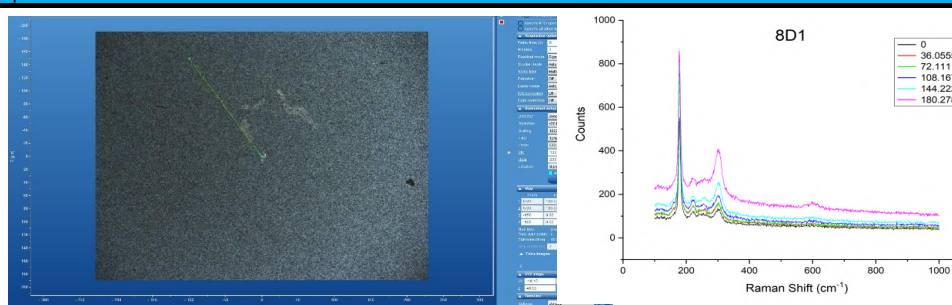
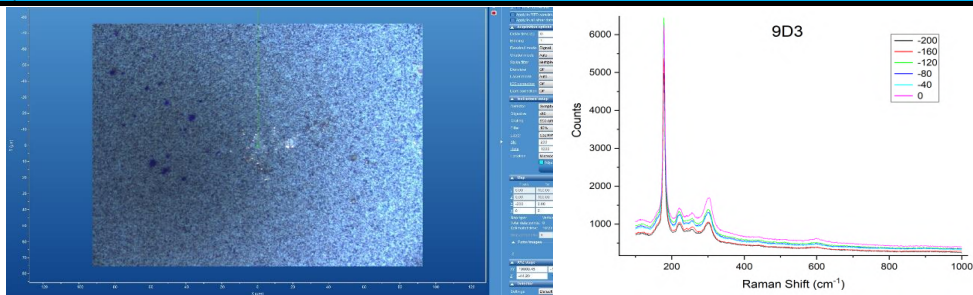
Raman









Spot: 7D3**Spot: 8D1****Spot: 8D2 not found****Spot: 9D3**

E.4. EDS

